Alma Mater Studiorum - Università di Bologna

DOTTORATO DI RICERCA IN
FISICA

Ciclo XXXI

Settore concorsuale: 02/A1
Settore Scientifico Disciplinare: FIS/01

DARK MATTER SEARCH WITH THE XENON1T EXPERIMENT: Background Predictions, Data Analysis and Final Results

Presentata da: Pietro Di Gangi

Coordinatore Dottorato
Prof.ssa Silvia Arcelli

Supervisore
Prof.ssa Gabriella Sartorelli

Correlatore
Dott. Marco Selvi

Esame finale anno 2019

To my families:
by blood, future and scientific.

Abstract

The search for dark matter (DM) is one of the most active fields in physics. Compelling astrophysical and cosmological evidences for DM existence have been attracting great theoretical and experimental efforts in the last decades, trying to shed light on the mysterious nature of dark matter. The XENON1T experiment is currently the most sensitive in the world for the direct search for WIMPs, the most investigated class of particles hypothesized to be the DM constituent. XENON1T employs a dual-phase (liquid-gas) time projection chamber (TPC) featuring 2.0 t liquid xenon (LXe) target mass. The detector is operated in the underground Laboratori Nazionali del Gran Sasso, in Italy, under 3600 meters-water-equivalent mountain rock shield. XENON1T aims at detecting WIMP elastic scattering off xenon nucleus, exploiting the light and charge observable signals produced by recoils in LXe. The WIMP search conducted with the XENON1T detector for a total exposure of 1.0 t·y is presented in this work.

WIMP interactions are extremely rare, hence an ultra-low and well characterized background is mandatory. Standard backgrounds for direct DM search experiments are electronic recoils (ERs), induced by gamma and beta particles emitted by external and intrinsic radioactive impurities or solar neutrinos, and nuclear recoils (NRs), from interactions of radiogenic neutrons or coherent neutrino-nucleus scattering. The backgrounds are studied with Monte Carlo (MC) simulations, through measurements on collected XENON1T data and modelling the detector signal response. The measured ER background for the XENON1T WIMP search amounts to $82^{+5}_{-3}(\text{syst}) \pm 3(\text{stat})\,(\text{t}\cdot\text{y}\cdot\text{keV})^{-1}$, in agreement with the rate and spectrum predicted by MC simulations. It is the lowest background level ever achieved in a direct detection DM experiment. The expectation value of the NR background is 1.5 ± 0.7 events in the 1.3 t fiducial LXe target volume where the data analysis for WIMP search is conducted. The profile likelihood analysis of data collected in 278.8 live-days finds no significant excess over background. The statistical inference on the WIMP-nucleon spin-independent cross section sets the world-best exclusion limit for WIMP masses above $8\,\text{GeV}/\text{c}^2$, with a minimum of $4.1 \times 10^{-47}\,\text{cm}^2$ at $30\,\text{GeV}/\text{c}^2$ and 90% confidence level.

The XENON Dark Matter Project will rapidly move towards the upgraded detector, XENONnT, with increased TPC (containing 6 t of LXe) and further reduced background. The XENONnT experiment will improve the sensitivity to WIMPs by one order of magnitude in 5 years of data acquisition.

Contents

Introduction

We know that we do not know, and there is nothing more fascinating. Physics is the infinite loop of human knowledge that strives for answers to find new questions to be answered. Our comprehension of fundamental physics continues to progress by leaps and bounds, as with the discoveries of the Higgs boson and the gravitational waves that recently marked new milestones for physics. Nonetheless, behind the scenes of breakthrough discoveries there is always a long journey made of collection of evidences or just hints about something that escapes our well written laws of physics, null experimental results, ingenious theoretical models proposing explanations for anomalies, new ideas too brilliant to be true. Our ultimate journey would be understanding the Universe, that is everything as far as we know, and for this reason most likely a never-ending dispenser of new "dark" sides to be investigated. Dark, yes. That is the word that currently dominates our knowledge of the Universe. We know that we do not know 95% of the energy content of the Universe, as the ordinary matter described by the Standard Model of particles contributes to less than 5%. The rest is "dark", precisely dark energy making up 68.5% of the Universe and dark matter accounting for the remaining 26.5%, where "dark" substantially means that their nature is still obscure to us. We will focus on the dark matter problem, while dark energy goes beyond the scope of this thesis.

Investigation about dark matter (DM) is nowadays one of the most attractive and therefore active fields of physics from both the theoretical and experimental points of view. In chapter 1 we outline the panorama of the dark matter quest. Compelling evidences supporting the hypothesis of the existence of a new form of invisible (dark) matter have been collected in the last decades. The first and most intuitive arguments come from gravitational effects at the galactic (or galaxy clusters) scale that luminous matter is not sufficient to explain (section 1.1.1). While postulating additional matter distribution seems the simplest solution to gravitational anomalies, modifications of the theory of gravity itself have been proposed without introducing new dark matter particles (section 1.1.3). However, the strongest evidence for massive DM particles arises from the cosmological scale (section 1.1.2), where DM is part of the successful ΛCDM cosmological model confirmed by precise measurements and it is needed to explain the early formation of structures of the Universe. Within the particle dark matter paradigm, a plethora of models and candidates beyond the Standard have been proposed (section 1.2). Among them the class of weakly interacting massive particles

(WIMPs) stands out as the most natural hypothesis (section 1.2.3), with mass and annihilation cross section typical of the weak scale ($\mathcal{O}(100\,\mathrm{GeV/c^2})$ and $\mathcal{O}(10^{-25}\,\mathrm{cm^3 s^{-2}})$, respectively). WIMPs attracted the largest part of experimental efforts in DM searches over the last decade. Three different and complementary approaches attempt to reveal a signal of DM presence (section 1.3): direct detection of galactic WIMPs scattering off targets in earth-based detectors (section 1.3.1), indirect DM detection through astrophysical radiation originating from DM annihilation or decay (section 1.3.2) and DM particles production with high energy collisions at accelerators (section 1.3.3).

Direct detection experiments demonstrated sensitivity to the lowest WIMP-nucleon cross section values, in particular for interactions independent on the target nuclear spin. The best results have been provided so far by xenon dual-phase (liquid-gas) time projection chamber (TPC) detectors. That technology is at the base of the XENON Dark Matter Project, which is currently leader in the field thanks to the largest operating liquid xenon (LXe) TPC in the world, XENON1T. The XENON DM Project, that started in 2007 with a small prototype XENON10 (containing 15 kg of LXe) and developed with the XENON100 experiment (161 kg of LXe), is described in chapter 2. The detection principle of a LXe TPC relies in the favourable properties of LXe as target medium for rare event searches and in the combined information of light and charge signals (called S1 and S2, respectively), which are observable following a particle recoil in the sensitive volume (section 2.1). Since 2016, the XENON1T detector is operational in the underground Laboratori Nazionali del Gran Sasso (LNGS), in Italy. The experiment, described in section 2.2, represents the first tonne-scale (with a total of 3.2 t LXe) and most sensitive DM detector in the world. The XENON Collaboration will rapidly move towards the upgrade called XENONnT (with about 8 t LXe) in 2019, aiming at improving the experimental sensitivity to WIMPs by an order of magnitude thanks to the larger target mass and enhanced background suppression (section 2.3).

A very large target mass and an ultra-low background level are key factors for the success of direct DM experiments. Alongside the background reduction strategies adopted in XENON1T, discussed in section 2.2.3, it is crucial to characterize, understand and model the residual background in the detector. Chapter 3 describes and discusses the background of XENON1T originated by electronic (ER) and nuclear (NR) recoils produced by known particles in the LXe target. Such background characterizes all direct detection experiments. The expected DM signature is a single low energy NR inside the TPC, where the recoil of a xenon nucleus is caused by a WIMP elastically scattering off a nucleon. This signal is exactly mimicked by neutrons and neutrinos undergoing elastic coherent scattering off nuclei (CNNS), which constitute the NR background (section 3.2). Low energy interactions of γ and β particles produce recoils of atomic electrons that yield a different partitioning of the energy into the light and charge observable signals. The ER background (section 3.1) can be therefore discriminated from NRs. However, given the higher rate and the non-null (though small) probability for an ER event to fall in the region of signal space where NRs are expected, the ER component is the main contributor to the XENON1T background.

The study of ER and NR backgrounds proceeds in three steps: Monte Carlo (MC) simulations of all the physical processes that can yield background events (based on the best knowledge before building the actual realization of the XENON1T detector), validation and matching of the expected background from simulation with actual measurements and constraints derived from real XENON1T data, and full modelling of the signal generation and propagation processes in order to produce background models in the experimentally observable signals space.

Sources of ER background are external gamma-rays emitted by radioactive decays in detector construction materials close to the LXe volume, beta-decays of intrinsic contaminants of xenon and solar neutrinos. The complete MC prediction of each contribution is described in section 3.1.1, while constraints derived from ancillary measurements with XENON1T data and the matching with the simulated ER spectrum are discussed in section 3.1.2.

Components of the NR background are muon-induced neutrons (section 3.2.1), which are suppressed by means of a Muon Veto system (section 2.2.4), neutrons stemming from radioactive impurities in detector materials (section 3.2.3) and CNNS neutrinos (section 3.2.2). CNNS induce an irreducible background for direct detection experiments, which can be tackled only with future directional detectors. Neutrons produced by spontaneous fission or (α, n) reactions can get deep inside the TPC undergoing multiple scatters along their path. With smaller probability, however, they can produce a single elastic scatter before exiting the fiducial volume (defined at the analysis level as an inner DM search LXe volume shielded from external backgrounds). Actual measurements of neutron background events is unlikely in XENON1T given the extremely low expected rate. Nevertheless, the XENON1T TPC is large enough to allow a measurement of multiple-site neutron scatters, which is exploited to put a constraint on the neutron background rate expected from MC simulations (section 3.2.5).

The detector response to both ER and NR interactions is carefully modelled through the description of the LXe microphysics and detector effects impacting on the propagation of S1 and S2 signals (section 3.3). The model parameters are then tuned on calibration data, collected during the XENON1T data taking period using an internally diffused low energy ER source and external neutron sources (section 2.2.5), to get the final description of the XENON1T signal response (section 3.3.3). The ER and NR background models for the WIMP search data analysis are built exploiting the signal response model to properly convert the recoil energy spectra predicted from MC simulations (section 3.4).

In chapter 4, the analysis of XENON1T data, collected in the first two science runs (named SR0 and SR1), for the search of WIMP-nucleon spin-independent interactions is presented. The analysis combines 32.1 (246.7) days in SR0 (SR1) for a total of 278.8 live-days, spanning more than one calendar year from 22 November 2016 to 7 February 2018 overall. A fiducial volume containing 1.3 t of LXe is optimized on the spatial distribution of backgrounds (section 4.3.1). Therefore, the exposure for this DM search amounts to 1 t·y. The fiducial volume selection is possible because the

dual-phase TPC technology allows a three dimensional reconstruction of the interaction vertex. Moreover, the position reconstruction, described in section 4.1.1, enables studies of position-dependent corrections (section 4.1.2) to properly take into account the light collection efficiency (for both S1 and S2 signals) and the electron lifetime (affecting the S2 signal amplitude due to depth-dependent survival probability of freed electrons in a recoil). The characterization of the detector's spatial response is carried out with periodical calibration runs where an intense ^{83m}Kr source of low energetic gammas is uniformly diffused inside the LXe reservoir. The time stability of light and charge signals is monitored exploiting mono-energetic lines present in the XENON1T ER spectrum at different energies (section 4.2). They include de-excitation gammas from metastable xenon isotopes activated during neutron calibrations (section 4.2.1), ^{83m}Kr gammas, high energy external gammas from detector materials and alpha decays of the intrinsic contaminant ^{222}Rn. With a good detector characterization in hand, selection criteria are established to reject known background events, to ensure data quality and to select the region of interest for the WIMP search (section 4.3). The final efficiency for DM signals, estimated from data control samples and from simulations, is the result of the signal acceptance loss due to each selection condition imposed to data (section 4.3.2).

XENON1T conducted a blinded data analysis, meaning that data in the most significant NR signal region (where WIMP signal is expected with highly reduced ER background contamination) are unveiled only at the very final stage, when the analysis method is fixed (in order to avoid any bias or fine tuning driven by the observed data of interest). Before data unblinding, the complete background and signal models need to be established as well (section 4.4). The XENON1T background includes two additional components besides the standard ER and NR backgrounds: "surface" events (section 4.4.1), happening at the TPC edges whose charge signal is partially trapped, and accidental coincidences of spurious S1 and S2 signals (section 4.4.2). The expected WIMP signal is derived from the analytical differential rate of recoils in the xenon target, under the standard assumption of isothermal galactic DM halo, convoluted with the detector response model to NR interactions (section 4.4.3). The complete prediction of background events for the 1 t·y WIMP search is presented in section 4.4.4.

The observed data in SR0 and SR1, after unblinding the signal region, are shown and discussed in section 4.5.3. The final result of the WIMP search is obtained through the statistical inference based on frequentist hypothesis test with the profile likelihood approach (section 4.5.1). The XENON1T likelihood function, described in section 4.5.2, features a four-dimensional parameter space as backgrounds and signal are modelled in the signal (S1,S2) space and also in the radial and vertical spatial coordinates. The constraint on the WIMP-nucleon spin-independent cross section is calculated with a Feldman-Cousins construction, which naturally switches from an exclusion upper limit to a confidence interval, in case of discovery. The conclusive results of the statistical inference on the full XENON1T dataset, presented in section 4.5.3, find no DM evidence and the world-best exclusion limits on WIMP-nucleon interaction are set.

Planned future noble-liquids detectors, including XENONnT, will continue scanning

the WIMP parameter space in the following years. The ultimate limitation for this class of experiments is represented by the CNNS background which is irreducible for non-directional detectors. In appendix A, we study the long-term projected discovery potential of xenon-based TPCs in the ultimate scenario, where the currently dominant ER and NR backgrounds are supposed to be suppressed by means of larger target masses and improved Xe purification techniques, and we evaluate the limitation due to the CNNS background.

Chapter 1

The search for dark matter

The ordinary baryonic matter accounts for less than 20% of the total mass budget of the Universe [1], the majority of existing matter being of unknown composition to date: that is what we call *dark matter*. Understanding the nature of dark matter is attracting large and growing efforts in the scientific community as it clearly represents one of the major open questions in physics. Progress in the knowledge about what dark matter actually is could shed light on fundamental aspects of the Universe, from large to small scales, from the evolution of galaxies to particle physics.

The existence of DM is well established among physicists as several convincing evidences of additional source of gravity beyond luminous matter were collected during the last century [2] (section 1.1). Simple arguments related to dynamics of galaxies and clusters, such as anomalous rotation velocity curves e.g., are the most direct and intuitive (section 1.1.1), even though observations linked to the cosmological scale (section 1.1.2) appear to be the strongest evidence of dark matter for many physicists. An alternative explanation of observed gravitational effects could in principle come from modified theories of gravity, introducing corrections to General Relativity with no need to postulate the presence of an unknown class of particles (section 1.1.3). Such a scenario cannot be excluded even though recent observations of the first gravitational waves have ruled out a large number of modified gravity models.

We have a much more precise idea about what dark matter is not than what it actually is. The field of proposed particles as DM components is ample with a large number of hypotheses in place to be tested experimentally. The only certainty is that standard model (SM) particles cannot fulfill all the properties required for dark matter. A plethora of models have been therefore proposed (section 1.2), making dark matter a golden channel for the search of new physics beyond the SM. The most popular candidates in recent times are called Weakly Interacting Massive Particles (WIMPs), a class of particles hypothetically subject to the weak force (section 1.2.3) which appears in models beyond SM in a pretty natural way and whose parameter space can be widely investigated with the current technologies. For such reasons WIMPs attracted most of the experimental efforts in the field and are the main physics channel also for the

XENON Dark Matter Project (chapter 2).

The number of experiments drawing their focus towards the discovery of dark matter has been steadily growing in the last decades. An overview of the different detection techniques employed and the current status of DM searches is presented in section 1.3. Experimental efforts in the astroparticle physics community aim at detecting non-gravitational interactions of DM with ordinary matter. The ground is explored by earth-based experiments looking for direct detection of faint signals produced by DM interacting with their target material (section 1.3.1) and by gamma-ray experiments which try to detect SM particles produced in DM annihilation processes (section 1.3.2). The latter approach is usually referred to as indirect detection technique and can be considered complementary to direct detection. Production of DM through collisions of SM particles with accelerators (section 1.3.3) is a further channel of investigation, where the signature would be missing energy-momentum [3]. Current colliders, led by LHC, are viable technologies to probe light dark matter candidates, in the lower end of the most popular mass ranges, while they are not competitive with direct detection experiments at larger masses.

1.1 Dark matter evidence

The earliest observations which led to the idea of dark matter existence can be traced back to the end of 19^{th} century, when the astronomical photography was invented. This allowed astronomers to start making considerations about the distribution of luminous objects in the sky. Several dark regions were noticed even in dense stellar fields. Since a uniform distribution of stars was expected, discussions about the nature of *dark vacant areas* and *dark structures* [4] began to develop in the astronomical community. Soon after the first attempts to understand the Milky Way structure from the dynamical perspective pointed to the presence of a possibly large number of invisible objects. Lord Kelvin estimated for the first time the amount of matter in the Milky way describing the galaxy as a gas of particles subject to gravity [5]. In 1904, he got to the conclusion that "many of our stars, perhaps a great majority of them, maybe dark bodies".

Ironically, the origin of the term "dark matter" is attributed to the French mathematician Henri Poincaré who was not convinced about the existence of "matière obscure", since the observed velocity dispersion of stars in the Milky Way was of the same order of magnitude obtained from Kelvin's estimate [6]. The first quantitative model for the dynamics of the stellar system in the galaxy is due to Jacobus Kapteyn in 1922 [7]. Thanks to his pioneering work, the problem of the local dark matter density was addressed by comparing the total gravitational mass with the number of visible stars. Even if no conclusive statements about the possible predominance of invisible matter over the luminous one were achieved in the following years, the concept of "dark matter" was slowly consolidating among astronomers.

It is 1933 when the Swiss-American astronomer Fritz Zwicky, in his study of redshift of extragalactic nebulae [8], noticed a very large dispersion in the apparent velocity of

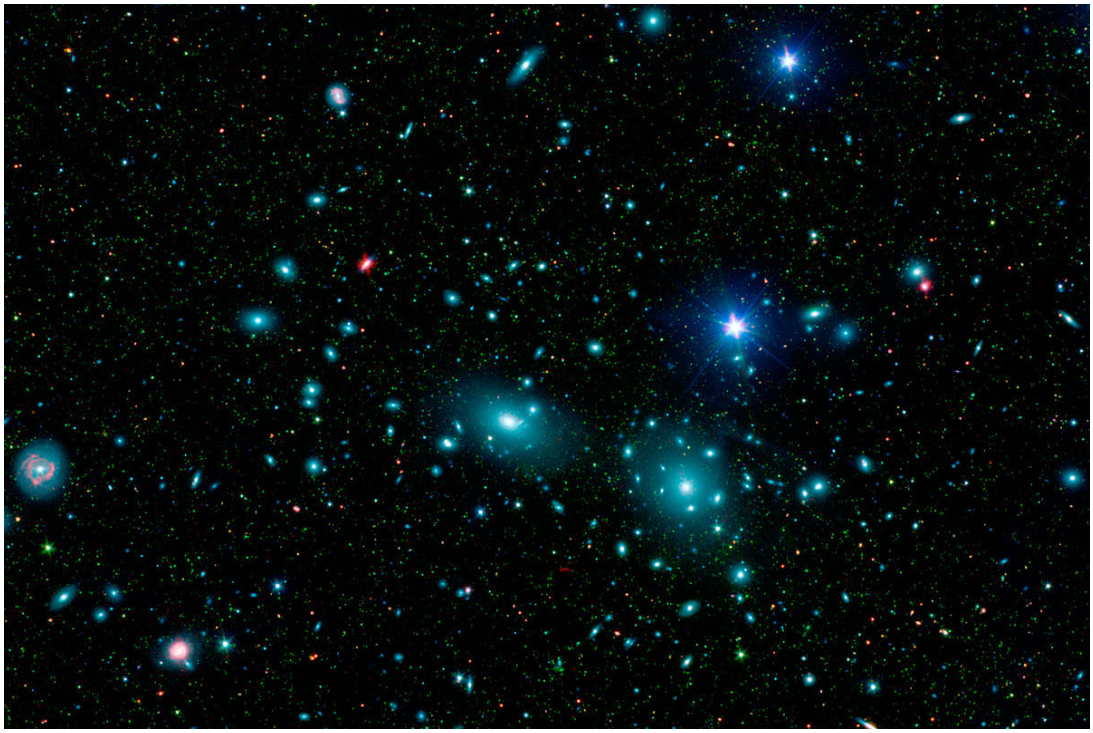

Figure 1.1: Mosaic of the Coma Cluster in long-wavelength infrared (red), short-wavelength infrared (green), and visible light. The Coma Galaxy Cluster is a nearly spherical cluster containing over one thousand galaxies, mainly elliptical and highly-flattened, about 15 billion years old. It is located in the Coma Berenices constellation at a mean distance from Earth of 99 Mpc. The Coma Cluster provided a major evidence of gravitational anomalies which can be explained with the presence of invisible mass. It is widely considered the first observational proof of dark matter existence. Image from NASA/JPL-Caltech/GSFC/SDSS.

galaxies within the Coma Galaxy Cluster (figure 1.1). He measured differences up to 2000 km/s among velocities of eight clusters, confirming a previous observation by Hubble and Humason two years earlier [9]. But Zwicky was the first to apply the virial theorem of thermodynamics to estimate the gravitational mass of a galaxy cluster to be compared with the mass inferred from the visible objects. His study resulted in the famous sentence: "if this would be confirmed, we would get the surprising result that dark matter is present in much greater amount than luminous matter". That is considered by many to be the first major evidence of dark matter existence.

1.1.1 Galactic and clusters scale

The mass of a galaxy cluster can be easily derived if galaxies are assumed bound by gravitational attraction[1], as shown by the illuminating works of Zwicky on the Coma

[1]Until the late 1950s, astronomers, including Zwicky himself, questioned the assumption of equilibrium for galaxy clusters, as a possible explanation of the observed discrepancy between the luminous and gravitational mass. But given the estimated age of the Universe and of the galaxies contained in

Cluster and Sinclair Smith on the Virgo Cluster [11] of 1936. The cluster is a system of N bodies whose equations of motion can be integrated to give $\frac{1}{2}\frac{d^2I}{dt^2} = 2K + U$, where $I = \sum_i m_i r_i^2$ is the moment of inertia in the center of mass frame and K and U are the kinetic and gravitational potential energy. If the cluster distribution is stationary, the moment of inertia I is null and $U = -2K$, which is known as the *virial theorem*. For a spherical distribution of galaxies, the potential energy is $U = \frac{GM^2}{R}$, with M and R the total mass and radius of the cluster. From the virial theorem the mass is given by

$$M = \frac{3R\langle v_{||}^2 \rangle}{G}\,, \tag{1.1}$$

as the velocity dispersion of galaxies $\langle v^2 \rangle$ corresponds to three times the dispersion of velocities along the line of sight $\langle v_{||}^2 \rangle$, which are the only measurable via redshift. Zwicky in his first redshift studies of the Coma Cluster measured an average velocity dispersion of approximately 1000 km/s, while he expected around 80 km/s from the virial theorem calculation by considering the total mass of the cluster as the product of the average mass of a galaxy ($10^9\, M_\odot$ as indicated by Hubble) and the number of observed galaxies (800). In a refined analysis of the Coma Cluster [12], Zwicky conservatively assumed that Coma contained 1000 galaxies within a radius of 2×10^6 light-years for a velocity dispersion of 700 km/s and solved for the cluster's mass. He obtained an average $4.5 \times 10^{10} M_\odot$ mass per galaxy to be compared with the average absolute luminosity of Coma's galaxies of $8.5 \times 10^7 L_\odot$, leading to a very high *mass-to-light ratio* of about 500. Zwicky actually overestimated this ratio because the relation between distance and redshift relied on the Hubble constant value of $H_0 = 558$ km/s/Mpc, the available estimate at that time. However, if we rescale Zwicky's result for the current measured Hubble constant $H_0 = 67.4 \pm 0.5$ km/s/Mpc [1] and if we use the modern estimates for the visible mass of Coma Cluster $M_{vis} = 1.6 \times 10^{14}\, M_\odot$ [13], the velocity dispersion of 1008 km/s [14] and the radius $R = 7.2 \times 10^7$ light-years [13], we get a virial mass of $M = 1.9 \times 10^{15}\, M_\odot$, leading to a one order of magnitude excess of mass which still represents a strong indication of dark matter.

Galaxies rotation curves Further clues for the presence of non-visible mass are present on the galactic scale from pretty straightforward dynamical considerations. We observe luminous objects, as gas clouds, stars, globular clusters, moving faster than what would be predicted by the newtonian gravitational attraction from all the other nearby visible objects. Measurements of the *rotation curves* of several spiral galaxies are certainly the most intuitive evidence of DM. In 1970s, much improved spectroscopic techniques allowed to extend observations to the edge of galaxies and therefore to compare spiral galaxies rotation curves predicted from photometry with those measured from the 21 cm radio observations. Thanks to the low absorption in the insterstellar

the cluster, such interpretation was in tension with the typical time scale for an unstable cluster to evaporate, which would have happened long time ago [10].

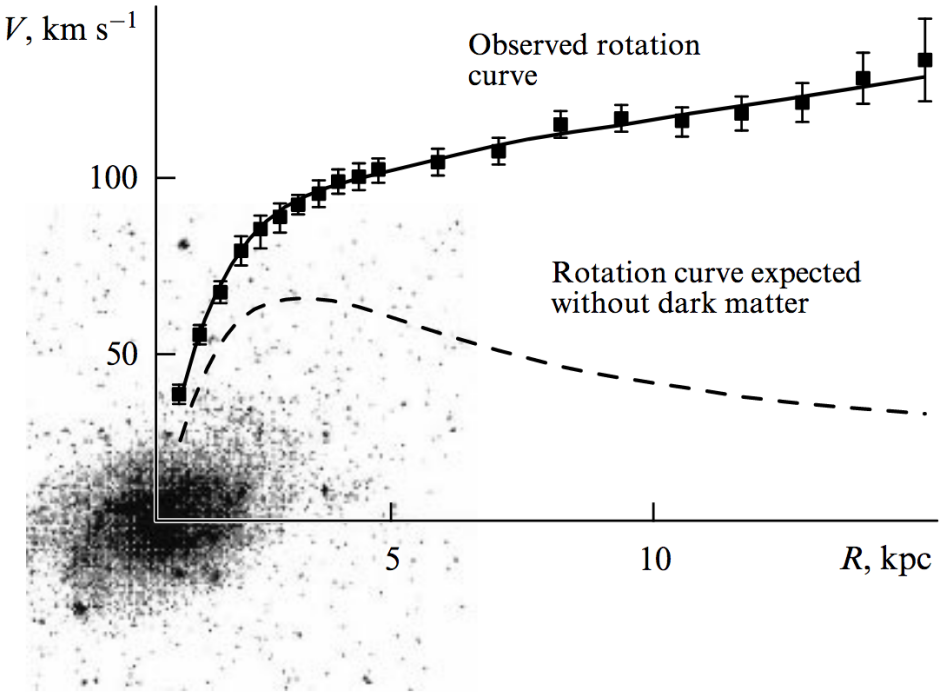

Figure 1.2: The observed rotation curve of the M33 (or NGC 598) galaxy. Dashed line is the expected rotation curve based on Kepler's law with the optical mass profile in the galaxy. The discrepancy suggests the DM dominance over luminous matter. Freedman derived a mass-to-light ratio as high as 20 at largest radii, based on data in [15]. M33 is a spiral galaxy distant 3×10^6 light-years from Earth, also known as Triangulum Galaxy. Plot from [16].

medium of the neutral hydrogen (HI) line, it is possible to measure the velocity of hydrogen clouds beyond the galactic optical disk. The earliest claim of a mass discrepancy in galaxies was derived from the rotation curve of M33 (see a modern illustration in figure 1.2) by Kenneth Freeman in 1970 [17]. The motion of objects in a spiral galaxy can be described as stable Keplerian orbit, whose rotational velocity v only depends on the distance r from the galactic center and the mass $M(r)$ inside the orbit, scaling like $v(r) \propto \sqrt{M(r)/r}$. Outside the optical disk of the galaxy, the (visible) mass distribution stays constant and the velocity should drop with radius as $v(r) \propto r^{-1/2}$. In most galaxies we observe, instead, an approximately constant rotational velocity in the outermost regions. To account for that, one must introduce a *dark halo* of invisible matter with a density profile $\rho \propto 1/r^2$, *i.e.* $M(r) \propto r$, which extends much beyond the distribution of luminous matter in the galaxy. One popular example of density distribution for DM halos is the Navarro-Franck-White (NFW) profile [18]:

$$\rho(r) = \frac{\rho_s}{(r/r_s)(1 + r/r_s)^2}\,, \tag{1.2}$$

where r_s and ρ_s are the characteristic halo radius and density. A recent study of a sample of 50 galaxy clusters (in a redshift range $0.15 < z < 0.3$) has shown that the

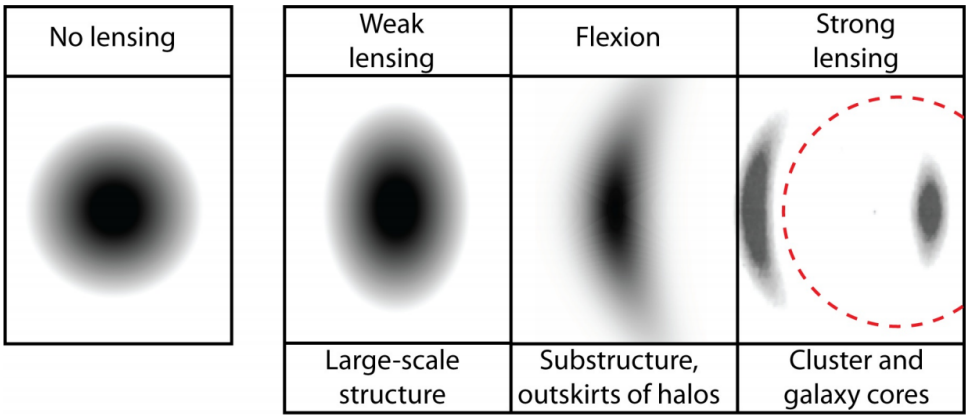

Figure 1.3: Image distortion induced in different regimes of gravitational lensing. An intrinsically circular object along the line of sight through the Universe is distorted into an ellipse by weak lensing shear with a typical axis ratio of $\sim 2\%$. Flexion curvature is typically introduced by nearer concentrations of mass. Strong gravitational lensing produces multiple images and giant arcs in directions close to the most massive galaxies of a cluster. Illustration from [20].

dark matter density profile derived from gravitational lensing measurements is perfectly fitted by the NFW distribution [19]. Such considerations on the presence of DM halos in most of known galaxies points to a lower bound on the DM mass density of $\Omega_{DM} \gtrsim 0.1$ (see section 1.1.2 for the current estimate of DM abundance in the Universe).

Gravitational lensing Many lines of research in astronomy related to dark matter are based on gravitational lensing effects, particularly suited to trace DM distribution in galaxies, clusters of galaxies and even larger scales. It is the most direct method to study DM through its gravitational influence on visible matter. A massive object that is interposed between the observer and a luminous source acts as a *gravitational lens*. Light rays are bended passing through the warped space-time of a gravitational field, analogously to what happens in case of optical refraction. This effect was actually the first experimental verification of general relativity when discovered in 1919 by observing the apparent motion of the stars in the Hyades Cluster while they passed behind the Sun during a solar eclipse [21]. Different flavours of gravitational lensing are exploited to trace matter distributions, depending of the strength and distance of the lens (see the illustration in figure 1.3). If a distant source is behind a dense concentration of mass, the light can travel along multiple paths and the object can eventually appear as an "Einstein ring" or in multiple locations. That is called *strong lensing* and can be used to reconstruct the distribution of mass in the lens. Hundreds of galaxies have been investigated through strong lensing, measuring their DM fraction and density profiles [22]. However, the majority of lines of sight do not cross strong gravitational lens, such as the core of galaxies and clusters of galaxies, and the light deflection can be very slight. That is the regime of *weak lensing*, where the distortion of a luminous

source can be approximated to a locally linear transformation of the sky. Observations of weak lensing are conducted, e.g., on almost aligned galaxies on the line of sight. Their intrinsic shapes are uncorrelated to first order and must average out as circular in absence of lensing. Due to the weak gravitational lensing effect, the average shape is an ellipse with a typical distortion of $\sim 2\%$ on the major-to-minor axis ratio, as first detected in the most massive clusters in 1999 [23]. Weak lensing signals from more than three hundred thousands galaxies revealed a typical DM halo of mass $1.4 \times 10^{12} M_{\odot}$ around galaxies with a stellar mass of $6 \times 10^{10} M_{\odot}$ [24]. The combination of weak and strong lensing has been used to probe the total mass of the Hubble Space Telescope SLACS survey of elliptical galaxies, resulting in required DM halos of $1.2 \times 10^{13} M_{\odot}$ for galaxies with luminous mass of $2.6 \times 10^{11} M_{\odot}$ [22]. Halfway between weak and strong lensing is *flexion*, a second-order effect measurable in the case the projected mass of a lens has a steep spatial gradient leading to the formation of an arc [25]. Flexion measurements are useful to reconstruct the mass around the bulk of galaxy clusters when the light deflection is too low for strong lensing and the cluster area is too small to perform a significant weak lensing analysis.

Bullet Cluster Evidence for dark matter in galaxy clusters found a spectacular example in the case of colliding clusters, as the famous Bullet Cluster (1E0657-558) shown in figure 1.4. Most of the baryonic mass of the clusters is in sparse intergalactic gas, which was heated to very high temperatures when the collision happened (recently on cosmological time scales). The consequent emission in the X-ray regime is so high that a clear image of the matter distribution of both clusters can be obtained with an X-ray telescope, like Chandra (the pink area in figure 1.4). That represents the distribution of the majority of ordinary matter, the intergalactic gas, which was shocked and decelerated in the collision, while the galaxies in the clusters proceeded on ballistic trajectories. The total mass of the Bullet Cluster can be reconstructed by weak lensing as both clusters have significant mass to act like gravitational lenses. The mass distribution mapped by imaging objects behind the clusters is shown in blue. An integrated analysis of the Bullet Cluster in 2004 [26] clearly showed the discrepancy between the distribution of ordinary matter with respect to the total mass. That was considered a "direct empirical proof of the existence of dark matter". Some tensions arose in the following years about the interpretation of the Bullet Cluster case. Numerical simulation based on the ΛCDM cosmological model could not reproduce the observation. However, computer models are still limited by several choices to be made on the physics to simulate, to approximate or to exclude in order to deal with the available computational power. In particular, technical decisions on the model box size and the resolution of features in the model seem to have a huge impact on the simulation outcome, pointing to the need of increasing both causing a yet unaffordable computational cost.

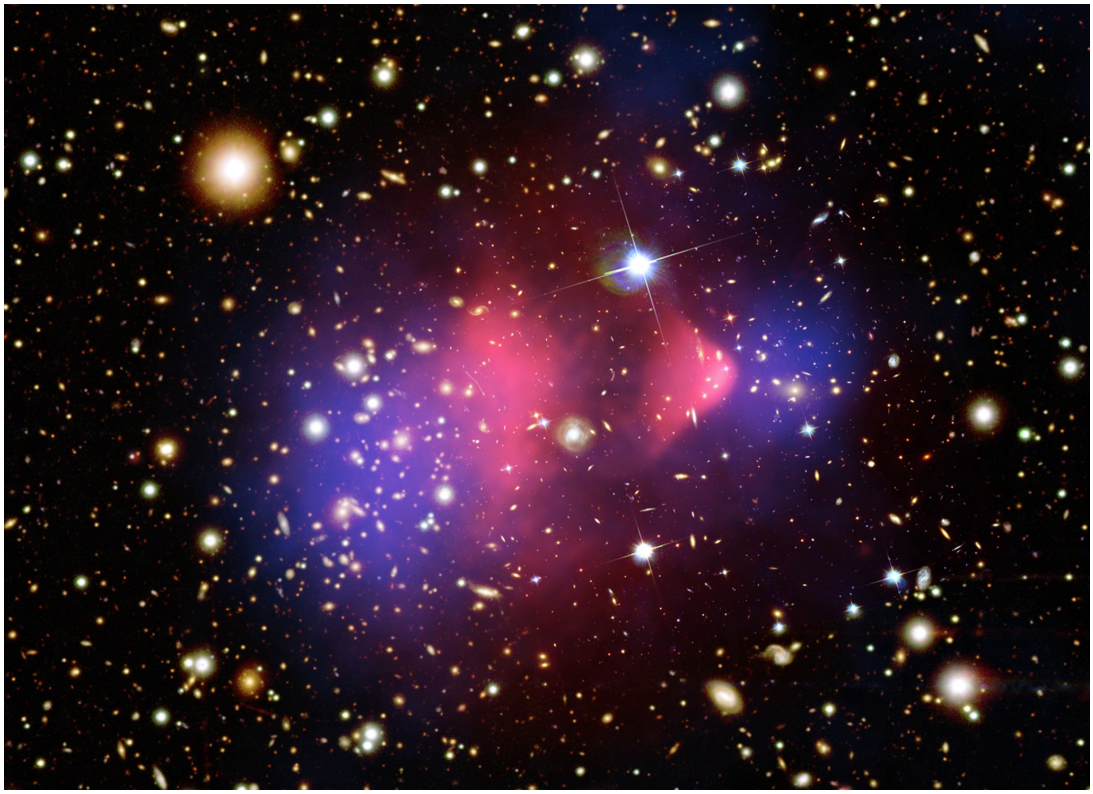

Figure 1.4: The Bullet Cluster as seen by the Hubble and Magellan optical telescopes. This is the remnant of the collision of a small "bullet" cluster that passed through a larger galaxy cluster. The X-ray image from the Chandra X-ray observatory is overlaid in pink, showing the density of hot gas in the two clusters which constitutes most of the (ordinary) mass. The region in blue represents the mass distribution reconstructed from weak lensing measurements. The clear discrepancy between the ordinary matter, slowed down and heated during the collision, and the total mass distribution, basically unaltered, is considered one of the most compelling evidences of DM existence and that its self-interaction and with ordinary matter is very weak. Picture from [26].

1.1.2 Cosmology

Dynamical anomalies in galaxies and clusters first led to the postulation of dark matter to account for unobserved mass. But to solve this kind of problems one could also invoke modifications to the laws of dynamics, as Einstein modified the newtonian gravity to explain the precession of Mercury's perihelion [27]. The same approach is followed by modified gravity models, which are consistent with galactic data [28] without any form of DM (even though many of these models have been ruled out by the recent observation of gravitational waves, see section 1.1.3). In this perspective, cosmological evidences for DM are much more specific and cannot be explained in terms of modified gravity scenarios.

CMB and ΛCDM model The rise of physical cosmology in the 1970's [29] brought a significant impetus to the DM hypothesis since it is an integral part of the ΛCDM model of cosmology, which is now the standard in the field. The success of such model mostly resides in its almost incredible consistency with cosmological observations over a huge range of distances (from Mpc to the Hubble scale) and times (from the present day to 10^9 years ago). In particular, ΛCDM can describe the Cosmic Microwave Background (CMB) temperature anisotropies, from which fundamental cosmological parameters are estimated with remarkable precision.

The accidental discovery of the CMB radiation by Penzias and Wilson [30] at Bell Labs in 1965, who actually needed Dicke, Peebles, Roll and Wilkinson to interpret the observed excess antenna temperature as the left-over radiation from the Big Bang [31] predicted by Gamov in 1948, set a milestone for the Hot Big Bang model of cosmology. The spectrum of CMB is a perfect black body with a temperature $T_0 = 2.7255 \pm 0.0006$ K [32] and is isotropic at the 10^{-5} level. Those are relic photons from the early Universe stage when temperature dropped to ~ 3000 K, allowing the recombination of electrons with protons and making the Universe transparent to photons as their energy was not sufficient to ionize hydrogen. The tiny temperature anisotropies of the CMB radiation are originated from quantum fluctuation of the inflation fields stretched during the inflationary epoch. High precision studies of the CMB anisotropies enable accurate testing of cosmological models and give stringent constraints on their parameters. As we observe almost gaussian temperature fluctuations, all the information contained in CMB maps can be compressed to a power spectrum through the expansions of anisotropies into spherical harmonics (where larger multiple moments ℓ correspond to smaller angular scales). The *Planck* collaboration recently released the final full-mission measurements of CMB anisotropies [1] with unprecedented precision, from which a cold dark matter density of

$$\Omega_{DM} h^2 = 0.120 \pm 0.001 \tag{1.3}$$

is inferred as well as a baryonic matter density $\Omega_b h^2 = 0.0224 \pm 0.0001$, meaning that DM is more than 5 times more abundant than baryonic matter. Moreover, the derived total matter density is $\Omega_m = 0.315 \pm 0.007$, the remaining 68.5% of the Universe content being in the form of Dark Energy Λ, the vacuum energy term of unknown nature introduced to account for the accelerated expansion of the Universe and its flatness [33].

Structure formation For many cosmologists, considerations about the structure formation in the Universe bring the strongest argument for DM existence. The structures present in the Universe are originated from initial perturbations in matter density that grew sufficiently to form the galaxies and clusters we observe. Perturbations can only grow during matter domination, after the radiation dominated epoch, proportionally to time as $\delta\rho/\rho \propto 1/z$. From the CMB anisotropies we know that initial perturbations were of the order of $\delta\rho/\rho \sim 10^{-5}$ at the recombination time, $z_{rec} \simeq 1300$. Perturbations in baryonic matter can start growing only after recombination, since the baryonic plasma is tightly coupled to radiation. And for the same reason, the size of initial

perturbations has to be equal to that of fluctuations in CMB radiation. Under the hypothesis that only baryonic matter exists, today's perturbations should be in the order of $(\delta\rho/\rho)_{rec} \times z_{rec} \sim 10^{-2}$. Nonetheless, structures are formed already in present time and perturbations in matter can be considered in non-linear regime: $\delta\rho/\rho \gtrsim 1$. To solve this contradiction, a non-baryonic form of dark matter has to be introduced in order to let the structure formation start prior to recombination [34]. Matter domination starts earlier in the presence of DM which was free to aggregate due to very weak self-interaction, as opposed to baryonic matter. Dark matter is needed as seed for structures formation, while baryons started aggregation at later times by falling into already existing gravitational wells.

1.1.3 Modified gravity paradigm

Although numerous indications form different fields and scales point to the existence of DM, such a mysterious form of matter has never been directly detected so far. What we discussed in previous sections are compelling but indirect evidences for additional unseen matter in the Universe, all relying on the common assumption that General Relativity (GR) holds as the ultimate theory of gravitation. Therefore, as an alternative to the introduction of more, "dark", mass, one could actually modify the theory of gravitation itself to explain the observed phenomenology of galaxies. That is the *modified gravity* paradigm, which developed in last decades as opposed to the dark matter interpretation. Einstein's GR has successfully passed every direct experimental test, but only up to small scales, such as planetary orbits, compared to galactic or cosmological scales. Alternative gravitational theories have then to reduce to GR at sub-galactic scale and solve the DM problem up to the cosmological scale.

The first significant attempt to reject the DM paradigm dates back to 1982 when Mordehai Milgrom proposed the *Modified Newtonian Dynamics* (MOND) [35] as "a possible alternative to the hidden mass hypothesis". The basic idea was pretty simple: Newtonian dynamics does not apply to objects with very low acceleration. Milgrom introduced a preferred scale of acceleration, in the order of the centripetal accelerations of gas clouds in the outskirts of disk galaxies ($a_0 \sim 10^{-10}$ m/s^2), to modify the second law of dynamics:

$$\tilde{\mu}(a/a_0)\vec{a} = -\vec{\nabla}\Phi_N \, . \tag{1.4}$$

The positive monotonic function $\tilde{\mu}$ tends to unity when $a \gg a_0$ and approximately equals its argument in the deep MOND regime ($a \ll a_0$), while Φ_N is the newtonian gravitational potential generated by the baryonic mass density. The MOND theory could very well explain the constant galactic rotation curves [36] and softens the mass discrepancy in galaxy clusters [36], even though a factor ~ 2 remains by applying the MOND analogue of the virial theorem. However MOND is an intrinsically non-relativistic model and insurmountable obstacles arise in attempts to extend it to relativistic formulations, like the need for a superluminal propagation of a scalar field [37]. A relativistic theory pinned on the MOND paradigm was proposed by Jacob Beken-

stein under the name of TeVeS theory [38]. Instead of introducing a new (superluminal) scalar field, TeVeS describes gravity by three different fields: the Bekenstein metric tensor $\tilde{g}_{\alpha\beta}$, a sclar field ϕ and the Sanders vector field A_α. The theory, based on a covariant action, reduces to MOND in the weak field limit, to GR for not tiny accelerations and to newtonian dynamics in the non-relativistic limit.

The modified gravity paradigm is explored also by other generalizations of GR not based on Milgrom's MOND. An example of alternative explanation to DM evidence comes from the $f(R)$ *gravity* theory [39]. In this case, Einstein's GR is extended by a family of modified gravity theories, each of them defined by a different function f of the Ricci scalar R (the curvature of the space-time manifold), relaxing the assumption of GR that the Hilbert-Einstein action for the gravitational field is linear in the Ricci scalar. Galactic and extragalactic anomalies can be solved by an accurate selection of these functions f, but with the requirement of a scale and time dependent gravitational constant.

Dynamical anomalies at the galactic scale can also be explained by the *Entropic (or Emergent) Gravity* (EG) theory recently proposed by Erik Verlinde [40]. Gravity is not a fundamental interaction anymore, but an entropic force emerging due to the increasing entropy linked to the information associated to mass distributed in space, under the assumption of quantum gravity's holographic principle. Though controversial in its fundamental aspects, EG successfully passed the first empirical tests from weak lensing measurements of the mass density of more than 30 thousands galaxies [41].

Constraints from gravitational waves observation The extraordinary detection of the first *gravitational waves* (GWs) not only marked a historical passage for modern physics, paving the way for a whole new sector such as multi-messenger astronomy, but it has immediately provided important experimental answers to the modified gravity paradigm. On August 17, 2017, the Advanced LIGO-Virgo experiments picked up a clear signal of gravitational waves from a binary neutron star merger in the NGC 4993 galaxy [42], named GW170817A. That was the fifth gravitational-wave detection, since the breakthrough discovery of the first GW from the coalescence of a binary black hole [43], happened on September 14, 2015. But GW170817A was the first ever gravitational wave observed in coincidence with an electromagnetic counterpart. About 1.7 seconds after the event registered by LIGO-Virgo, a short gamma-ray burst (GRB170817A) was recorded by the Fermi satellite from a similar location in the sky [44] and the GW source was observed throughout the entire electromagnetic spectrum in the following days. The NGC 4993 galaxy is approximately 1.3×10^{11} light-years away from the Milky Way and the time delay of less than 2 seconds between the GW and electromagnetic signals implies that GWs and light travel at the same speed within 1 part in 10^{15} [45]. This single observation improves previous constraints by 14 orders of magnitude and actually represents the first ever test of Einsten's weak equivalence principle (WEP), according to which photons and gravitons experience the same time delay (Saphiro delay) passing through a non-zero gravitational potential. As a conse-

quence, entire classes of theories of gravitation alternative to GR, with no dark matter postulation, have been ruled out in one go. Theories beyond GR plus a cosmological constant, such as *disformal theories* [46], require the presence of new dynamical fields which can mix with GW, modifying their speed by an effective refractive index other than 1. Hence the almost perfect simultaneity of GW170817A and GRB170817A excludes any cosmologically relevant scalar field in disformal theories of gravity [47–49]. Also T*e*V*e*S and the whole class of modified gravity models known as *MOND-like DM emulators* seems to be rejected since they violate the WEP as they couple ordinary matter to a modified metric tensor $\tilde{g}_{\mu\nu}$ (like the Bekenstein's tensor) while GWs couple with the standard $g_{\mu\nu}$ [50]. Moreover, we know that the time arrival on Earth of the light from the GW170817A event has been delayed by a few years due to the warped space-time along the line of sight, as derived from weak lensing measurements of DM density in that direction. Therefore, GWs must have experienced exactly the same time delay, providing a strong evidence for dark matter's effect on gravitational waves.

1.2 Particle dark matter hypotheses

The discussion of the "dark matter problem" leads to a first dichotomy between the particle DM and the modified gravity paradigms. From here onwards, we will stay under the former as this work comes in the context of the experimental direct search for particle DM. The second level question is then about the physical nature of the hypothetical dark matter particle, or particles. That is not a dichotomy of course, but an inquiry that faces a vast horizon of possibilities. There is no shortage of particle physics models which fulfil the requirements for explaining DM; with very different production mechanisms and within a huge range of particle masses, from 10^{-5} eV of axions to 10^{13} GeV like super heavy WIMPs (see section 1.2.2). Candidates for DM must be *stable* on cosmological time scale, otherwise they would have decayed by now, and they must have the *correct relic density* as in equation (1.3). To be "dark", they also must *interact very weakly with electromagnetic radiation*, being gravitational and (possibly) weak interaction the only interactions with whom they are coupled.

Dark matter plays a crucial role in the formation and evolution of structures in the Universe, as it accounts for a quarter of the total mass-energy budget of the Universe (see also section 1.1.2). The hypothesized primordial velocities of DM particles during the Inflation era, when DM decouples from the cosmological fluid, has a big impact on processes of structures formation. Three main scenarios can be distinguished based on DM velocity dispersion at decoupling: *hot dark matter* (HDM), for relativistic DM particles, *cold dark matter* (CDM), where DM is non-relativistic, and *warm dark matter* (WDM), which is the intermediate case.

Yakov Zeldovich proposed a top-down model of structure formation [51], in which relativistic DM implies that large structures were formed first in pancake-like shapes and then fragmented into smaller units. The primary candidates as DM particles in this scenario are Standard Model *relic neutrinos*. However, considerations about galaxies'

observed age and constraints on neutrinos' relic density reject the HDM hypothesis. Such a model is discussed in section 1.2.1, as well as baryonic matter which has been excluded to be the main contributor to the total DM budget in the Universe.

Nowadays, the CDM scenario is the most accepted and supported. DM particles slow down to non-relativistic velocities before decoupling and large structures are formed hierarchically from aggregation and clustering of small objects which collapsed first under their self-gravity, in the so-called bottom-up model. First evidences for CDM came in 1970s from N-body simulations of the formation of astrophysical structures by Ostriker and Peebles [52]. They could not reproduce spiral or elliptical galaxies starting with a matter distribution with total mass equal to the visible mass of the galaxies. But when they added a static and uniform distribution of matter, with mass from 3 to 10 times the total mass of the galaxy, they obtained recognizable structures. Numerous modern numerical simulations, e.g. Millennium Simulations [53, 54], under the CDM scenario show an excellent agreement with the observed matter distribution in the Universe. Moreover, astrophysical objects are produced in time scales in agreement with observations by the CDM N-body simulations, while in the HDM scenario the present structures can be reproduced but in a much longer time. The success of this kind of simulations (see figure 1.5) contributed, along with studies of CMB, to make ΛCDM the standard model of cosmology, whose key ingredients are the inflationary expansion of the Universe at early stages, the mysterious Dark Energy opposing to gravitational collapse to explain the current expansion, and cold dark matter to describe the formation and existence of astrophysical structures. A number of viable particle candidates for CDM arise naturally in theories beyond the SM. The main particle models are briefly discussed in section 1.2.2, with particular attention devoted to WIMPs in section 1.2.3, which is the most investigated class of candidates for CDM.

The CDM paradigm seems to predict galactic halos more centrally concentrated than what is currently observed. A better agreement with halo structures can be obtained with warm dark matter [55], while preserving the successful CDM predictions at larger scales. WDM leads to a top-down model for formation of small structures and bottom-up for larger ones. The best motivated candidate for WDM is *sterile neutrino*, a right-handed neutrino whose interaction is merely gravitational (see section 1.2.2).

1.2.1 Excluded candidates

The field of DM candidates is extremely wide and obscure. Our best knowledge on the fundamental nature of possible DM particles is actually about what they are not. When the number of hypotheses is so large, science usually advances by sifting the simplest ones first. The dark matter quest is no exception. One then starts asking himself if any of the known particles can account for the observed DM, before trying with more or less new particles. The answer to this question is no, DM has to be something else than anything included in the Standard Model. In this section we briefly discuss the main possibilities to explain DM with ordinary matter and why they are rejected.

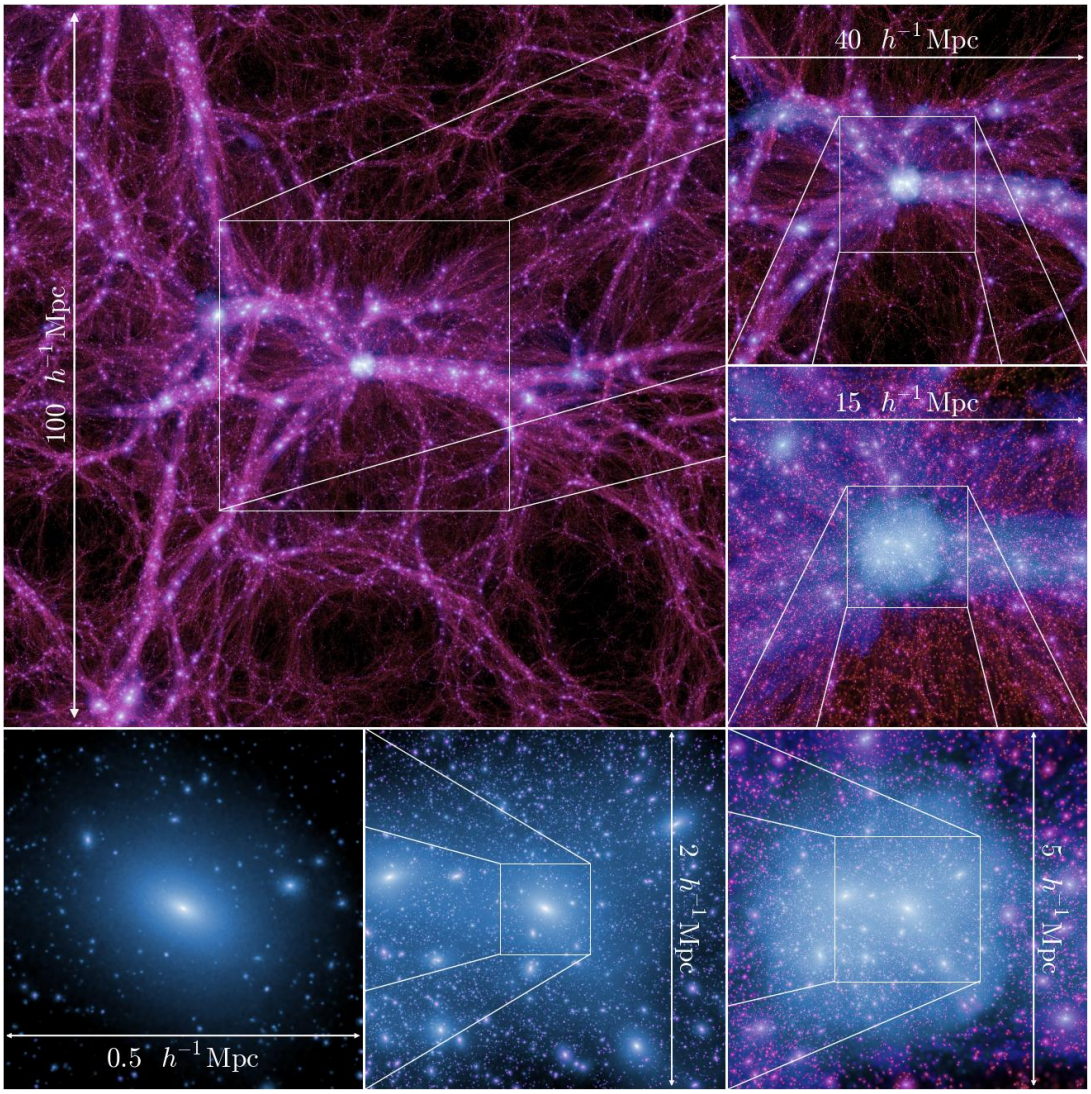

Figure 1.5: Millennium-II Simulation of dark matter evolution under the assumption of ΛCDM cosmology. A sequential zoom is shown starting from the large image (upper left), a slice through the full 100 h^{-1}Mpc simulation box at redshift zero, centered on the most massive halo in the simulation. This halo has similar mass to the one of the Coma Cluster. It is composed of 119.5 million particles, and contains approximately 36,000 resolved subhalos. Starting from the upper right and moving clockwise, subsequent panels zoom into the cluster region and show slices that are 40, 15, 5, 2, and 0.5 h^{-1}Mpc on a side. This simulation demonstrates excellent convergence in observed dark matter halos characteristics over an unprecedented range of scales, from halos similar to those hosting Local Group dwarf spheroidal galaxies to halos corresponding to the richest galaxy clusters. Image from [54].

Baryonic matter Ordinary matter, but non-luminous and therefore undetectable through direct observation was hypothesized as responsible for the mass contained in dark galactic halos. The class of such objects made of baryonic matter are called Massive Astrophyisical Compact Halo Objects (MACHOs). These include brown dwarf stars, cold clouds of molecular hydrogen, black holes of ∼100 solar masses. The MACHO project tested this hypothesis via microlensing measurements in the Large Magellanic Cloud concluding that MACHOs could contribute to DM but for less than 10-20% of the total DM amount in galactic halos [56]. The EROS-2 experiment, twice more sensitive, did not confirm MACHO's signals as it found no significant microlensing effects [57]. Baryonic matter could in principle still be a contributor to DM, but just in sub-dominant percentage as result from these searches.

Relic neutrinos Neutrinos were one of the first suggested candidates due to their "dark matter-like" properties: they are stable, interact with matter very weakly and are massive. In Zeldovich's HDM scenario, *relic neutrinos* forming the Cosmic Neutrino Background (CνB) [58] predicted by the Big Bang cosmology are the natural DM candidate particles. Neutrino's relic density is given by $\Omega_\nu h^2 = \sum_{i=1}^{3} m_i/93$ eV, where the sum is over the mass of the three neutrino flavours. The strongest constraint on the summed neutrino mass is provided by the latest Planck's data [59]:

$$\sum m_\nu < 0.12 \text{ eV} . \tag{1.5}$$

Such upper bound implies a limit on the relic density of $\Omega_\nu h^2 < 0.0013$ which is way too low to account for the estimated total DM density in equation (1.3).

As already mentioned, another argument against DM in the form of SM neutrinos comes from their relativistic nature and the subsequent top-down formation history of the Universe which is rejected by N-body numerical simulations. Moreover, the Milky-Way appears to be older than the Local Group [60] and we observe galaxies with redshift $z > 4$ [61], while the top-down evolution of the HDM scenario predicts late formation of galaxies, at redshifts $z \lesssim 1$ [62].

1.2.2 Non-baryonic dark matter

We excluded baryonic matter, Standard Model and relativistic particles. We need non-baryonic candidates, stable, only subject to gravitational and (perhaps) weak interaction and which are part of a new theoretical framework beyond SM. The DM required properties could be satisfied by a great variety of particles predicted in different theories, from minimal extensions of SM to String theory, form Supersymmetry (SUSY) to Extra-dimensions models. Great interest in the astroparticle physics community has been devoted to the class of WIMPs, among which SUSY particles appear natural candidates for DM (see section 1.2.3). In this section we briefly review all the other interesting, non-baryonic, viable solutions to the DM problem.

Axions Widely-discussed DM candidates are the *axions*, occurring in extensions of the SM solving the strong CP problem, and *axion-like particles* (ALPs), which are predicted by embeddings of the SM in String theory. Peccei and Quinn postulated a new global $U(1)_{PQ}$ chiral symmetry to address that QCD does not violate the CP symmetry [63]. The $U(1)_{PQ}$ symmetry is spontaneously broken by a Nambu-Goldstone boson, called axion, whose mass is constrained to $m_a = 2.6 \pm 0.3 \times 10^{-5}$ eV by numerical simulations under the assumption that it makes up all of the dark matter [64]. The relic abundance of axions strongly depends on assumptions made about the production mechanism. It is possible to find an acceptable range where axions' relic density is compatible with that of non-baryonic DM. They are also expected to interact extremely weakly with ordinary particles. Axions are then viable candidates for light dark matter.

Experimental searches are based on the Primakoff effect [65]: under an adequate magnetic field axions are converted into photons. The current strongest constraint on the axion-photon coupling strength was obtained by the CAST experiment at $g_{A\gamma} < 6.6 \times 10^{-11}$ GeV/c^2 [66] looking at solar axions. Observable signatures can rise also from the coupling to electrons through the axio-electric effect [67], analogue to the photo-electric process. The XENON100 experiment set the best limit on such interaction to $g_{Ae} < 7.7 \times 10^{-12}$ [68]. The ADMX experiment, dedicated to the search for axionic DM, recently demonstrated unprecedented sensitivity to axion-photon coupling [69] and promises to provide nearly definitive test of axions models in a wide range of masses.

Sterile neutrinos Singlet $SU(2) \times U(1)_Y$ *sterile neutrinos*, with no SM weak interaction, were proposed as DM candidates in 1994 by Dodelson and Widrow [70]. They are the natural choice in the warm dark matter scenario, but must have mass in the order of keV since lighter neutrinos forbids the formation of DM structures at large redshift [71]. Relic keV neutrinos ν_s can be detected if they mix with ordinary neutrinos via radiative $\nu_s \to \nu\gamma$ decays [72], which produce a flux of mono-energetic photons observable by X-ray satellites. Recent evidence for an X-ray line at ~ 3.5 keV was registered by the XMM-Newton satellite [73, 74] and interpreted as decaying DM. The existence of this line, however, was not confirmed by the Suzaku [75] and Hitomi [76] missions.

SUSY candidates Supersimmetry is the most popular extension of the SM as it addresses numerous phenomenological issues, like e.g. the hierarchy problem [77], the missing unification of gauge symmetries at high energies [78] or the fine tuning problem of Higgs boson mass [79]. SUSY is a space-time symmetry defined by supermultiplets consisting of a SM particle and its supersymmetric partner holding the same quantum numbers but the spin, differing by 1/2. Such a framework requires the postulation of many new particles among which several candidates for CDM can be found. Particular attention is dedicated to the *lightest supersymmetric particle* (LSP), since in SUSY models with R-parity conservation it is stable. All of the SM particles have R-parity equal to 1 and all their superpartners have $R = -1$. Thus, from R-parity conservation (first introduced to suppress the rate of proton decay), SUSY particles can only decay

into an odd number of superpartners. The LSP is, therefore, stable and can only be destroyed via pair annihilation, making it an excellent dark matter candidate.

The partners of neutrinos, named *sneutrinos*, have long been considered potential DM contributors. If their mass ranges between 550 and 2300 GeV, the relic density can be of the desired order for DM. However, the cross section of scattering on nucleons appears to be higher than exclusion limits set by DM direct detection experiments [80].

Gravitinos, the superpartners of graviton, are considered to be strongly theoretically motivated as in some SUSY scenarios they are the LSP. They interact only gravitationally, thus their observation is extremely difficult [81].

Another possible LSP in SUSY models is the *axino*, a Majorana chiral fermion superpartner of the axion, since its mass is strongly model-dependent, ranging form $\sim$ eV to $\sim 10^{15}$ GeV. Axinos are capable of acting as WDM [82] and, for quite low reheating temperatures at the end of Inflation, also as CDM [83]. They share similar phenomenologic properties with gravitinos.

The most studied and investigated DM candidates are, however, the *neutralinos*, the superpartners of neutrinos which are the LSP in R-parity conserving SUSY models. A more extended description of neutralinos is given in the following section.

Other particle DM models Superheavy DM particles, also known as *Wimpzillas*, are taken into consideration as non-thermal DM candidates [84], with masses from 10^{10} up to 10^{16} GeV. Such particles were initially proposed to explain the ultra-high energy cosmic rays, above the GZK cut-off ($\sim 5 \cdot 10^{10}$ GeV) at which the Universe becomes opaque to protons on cosmological scales. The decay or annihilation of superheavy DM are hypothesized as the production mechanism of so energetic protons [85].

In the context of Extra Dimensions theories, *Kaluza-Klein* (KK) excitations of SM fields also come as viable candidates for DM, in particular the lightest KK particle [86]. The idea of an Extra Dimensions model was carried out by Theodore Kaluza in 1921 [87] to include electromagnetism in a "geometric" theory of gravitation by adding new dimensions besides the 3+1 observed. The typical mass range of the lightest KK particle is 100-1000 GeV.

Many other examples of DM candidates arise from more or less exotic models, which include (in a not fully comprehensive list) *mirror particles* [88], *light scalar DM* [89], *DM from little Higgs models* [90], *charged massive particles* (CHAMPs) [91], *self-interacting DM* [92].

1.2.3 Weakly Interacting Massive Particles

The DM evidence and the strongest arguments about its properties made the generic class of WIMPs, and the lightest neutralino of supersymmetry among them, the best suited candidate as particle DM constituent, attracting the majority of efforts in experimental searches for DM during the last decades. WIMPs satisfy all the better established DM characteristics: it must be electrically neutral, non-baryonic, massive,

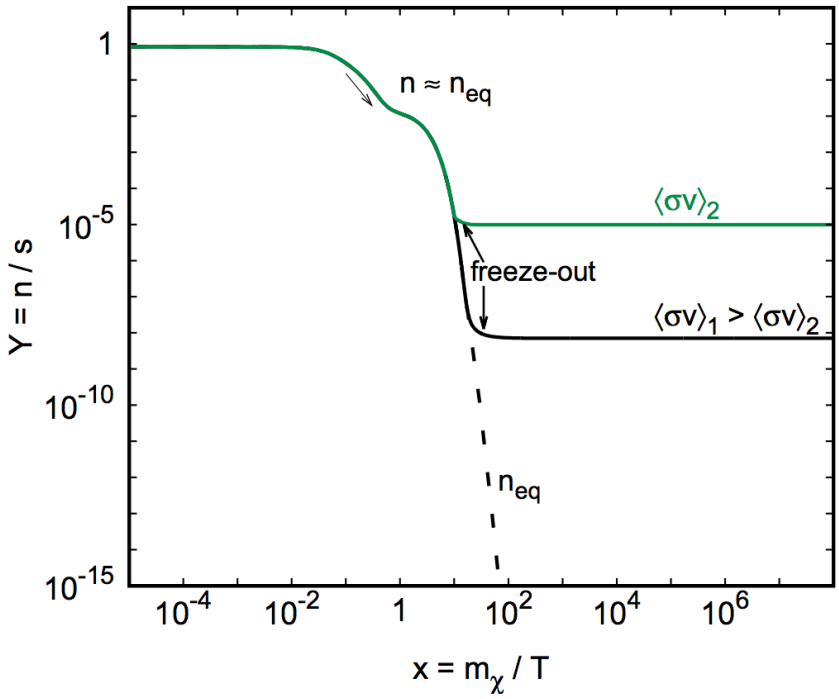

Figure 1.6: The DM yield, Y, as a function of $x = m_\chi/T$ for a standard freeze-out scenario. At freeze-out, the actual abundance leaves the equilibrium value and remains essentially constant; the equilibrium value, on other hand, continues to decrease so freeze-out is key to preserving high relic densities. Furthermore, the larger the annihilation cross section, $\langle\sigma v\rangle$, the lower the relic density. Plot adapted from [94].

cold at decoupling from primordial thermal plasma, with interactions not stronger than weak nuclear forces with ordinary matter and feeble self-interaction, and stable or extremely long lived (lifetime $\lesssim 160$ Gyr [93]). Moreover, the observed DM relic density is obtained from basic and generic considerations on the nature of WIMPs.

If they are stable, there is a cosmological relic abundance produced during the Big Bang. Assuming for such particles a mass m_χ, one has that for $T > m_\chi$ they were in thermal equilibrium while at temperatures below m_χ they decoupled and their abundance started to lower. Finally, when the expansion rate of the Universe became larger than the annihilation rate ($\Gamma_{ann} < H$, where H is the Hubble constant), the WIMP abundance "froze out", resulting in the current relic abundance (see an illustration in figure 1.6). The evolution of the WIMP density is described by the Boltzmann equation

$$\frac{dn_\chi}{dt} + 3Hn_\chi = -\langle\sigma_a v\rangle[(n_\chi)^2 - (n_\chi^{eq})^2]\,, \tag{1.6}$$

where n_χ^{eq} is the number density at the thermal equilibrium and $\langle\sigma_a v\rangle$ is the thermally averaged total annihilation cross section. For massive particles (non-relativistic limit)

and in the Maxwell-Boltzmann approximation, n_χ^{eq} is given by

$$n_\chi^{eq} = g\left(\frac{m_\chi T}{2\pi}\right)^{3/2} e^{-m_\chi/T} , \tag{1.7}$$

where g is the number of degree of freedom, m_χ the particle mass and T the temperature. As said, the "freeze-out" is verified for $\Gamma_{ann} = H$ that results in a temperature $T \simeq m_\chi/25$ [95]. Introducing the entropy density $s = 2\pi 2 g_* T^3/45$, where g_* counts the number of relativistic degrees of freedom, and using the conservation of entropy per co-moving volume, one finds

$$(n_\chi/s)_0 = (n_\chi/s)_f = \frac{H(T_f)}{\langle\sigma_a v\rangle s(T_f)} \equiv 100\frac{1}{g_*^{1/2} m_\chi M_P \langle\sigma_a v\rangle} , \tag{1.8}$$

where M_P is the Planck mass and the subscripts 0 and f denote the present and the freeze-out epoch, respectively. Thus, the relic density can be expressed as function of the annihilation rate:

$$\Omega_\chi h^2 = \frac{m_\chi n_\chi}{\rho_c} \equiv 3 \cdot 10^{-27} \frac{\mathrm{cm^3 s^{-1}}}{\langle\sigma_a v\rangle} , \tag{1.9}$$

which is independent from m_χ. The annihilation cross section of a new particle interacting at the weak scale can be estimated as: $\langle\sigma_a v\rangle \sim 10^{-25}$ cm^3 s^{-1}. Such value is close to the one derived from cosmological arguments. This strongly suggests that if a stable particle associated with the electro-weak scale interactions exists, then it is likely to be the dark matter particle. This coincidence, also known as the "WIMP miracle", has provided strong motivation for WIMP searches.

The neutralino The Minimal Supersymmetric Standard Model (MSSM) contains the smallest possible field content necessary to give rise to all the Standard Model fields. In MSSM, binos ($\tilde{B}$), winos ($\tilde{W}_3$) and higgsinos ($\tilde{H}_1^0$ and $\tilde{H}_2^0$) states mix into four Majorana fermionic mass eigenstates, called neutralinos. The four neutralinos are labeled as: $\tilde{\chi}_1^0$, $\tilde{\chi}_2^0$, $\tilde{\chi}_3^0$ and $\tilde{\chi}_4^0$. The first of them is the lightest one and it is referred as the *neutralino*, $\chi = \tilde{\chi}_1^0$.

The most relevant neutralino interactions for dark matter searches are self *annihilation* and *elastic scattering* with nucleons. At low velocities, the leading channels for neutralino annihilations are into fermion-antifermion, gauge bosons pairs and final states containing Higgs bosons.

All the possible annihilation processes are of interest for indirect dark matter searches (section 1.3.2), while direct detection techniques (section 1.3.2) are based on the elastic scattering processes. WIMP interactions with matter can be divided in two types: *spin-independent* (SI) and *spin-dependent* (SD). A scalar interaction, i.e. SI, with quarks can be expressed as

$$\mathcal{L}_{scalar} = a_q \overline{\chi}\chi\overline{q}q , \tag{1.10}$$

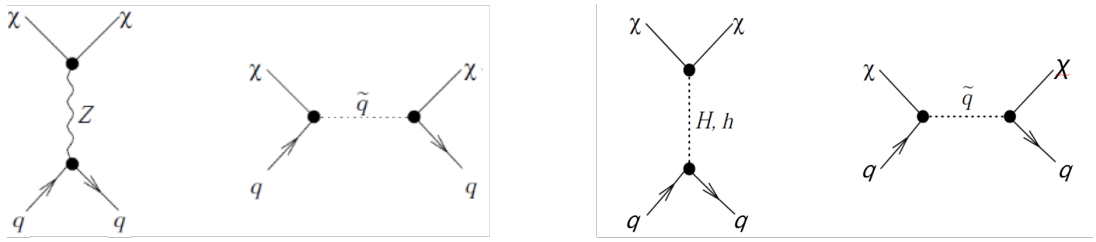

Figure 1.7: Feynman diagrams for (a) neutralino-quark scalar (*spin-independent*) elastic scattering interactions; (b) neutralino (*spin-dependent*) axial-vector interactions [96].

where a_q is the WIMP-quark coupling. The scattering cross section is given by

$$\sigma_{scalar} = \frac{4m_r^2}{\pi} f_{p,n}^2 \,, \tag{1.11}$$

where m_r is the reduced mass of the nucleon and $f_{p,n}$ is the coupling to protons and neutrons. The total scalar cross section for interactions with a nucleus, in the case of zero transfer momentum, is given by the sum over all the nucleons:

$$\sigma = \frac{4m_r^2}{\pi} \Big(Z f_p + (A - Z) f_n \Big)^2 \,. \tag{1.12}$$

A spin-dependent interaction, i.e. axial-vector interaction, between WIMPs and quarks can be expressed as

$$\mathcal{L}_{AV} = d_q \overline{\chi} \gamma^\mu \gamma_5 \chi \overline{q} \gamma^\mu \gamma_5 q \,, \tag{1.13}$$

where d_q is the generic coupling. The Feynman diagrams for both SI and SD neutralino interactions are shown in figure 1.7.

The cross section for SD interactions is given by [97]

$$\frac{d\sigma}{d|\vec{v}|^2} = \frac{1}{2\pi v^2} \overline{|T(v^2)|^2} \,, \tag{1.14}$$

where v is the WIMP velocity relative to the target and $T(v^2)$ is the scattering matrix element. At zero momentum transfer, one has

$$\begin{aligned} \overline{|T(0)|^2} = \frac{4(J+1)}{J} | &(d_u \Delta_u^p + d_d \Delta_d^p + d_s \Delta_s^p) \langle S_p \rangle + \\ &+ (d_u \Delta_u^n + d_d \Delta_d^n + d_s \Delta_s^n +) \langle S_n \rangle |^2 \,, \end{aligned} \tag{1.15}$$

where J is the total nuclear spin of the target nucleus, $\Delta_{u,d,s}^{n,p}$ are the fractions of the nucleon spin carried by a given quark and $\langle S_{p,n} \rangle$ are the expectation values of the total spin of protons and neutrons, respectively. For target nuclei with even numbers

of protons and neutrons, the total spin is equal to 0. Thus, for such nuclei, the spin-dependent cross section vanishes.

Another kind of interaction to be considered is the WIMP-quark vector:

$$\mathcal{L}_V = b_q \overline{\chi} \gamma_\mu \chi \overline{q} \gamma_\mu q \tag{1.16}$$

where b_q is the WIMP-quark vector coupling. The zero transfer momentum cross section can be expressed as [98],

$$\sigma = \frac{m_\chi^2 m_N^2 [2Zb_p + (A-Z)b_n]^2}{64\pi(m_\chi + m_N)^2}\,, \tag{1.17}$$

with $b_q = G_F(T_q^3 - 2e_q \sin^2\theta_W)/\sqrt{2}$, where G_F is the Fermi constant, T_q^3 and e_q are the weak isospin and electric charge of the quark q, respectively, and θ_W is the Weinberg angle.

1.3 Experimental efforts for dark matter detection

For nearly three decades the experimental search for dark matter has been continuing its intense activity with impressive and rapid progress. The compelling evidence of DM existence associated with the absence of a clear detection yet, has attracted a great interest in the field from different branches of physics, from astrophysics to particle physics. The experimental dark matter community is going through a great ferment of ideas and investments in new experiments and technologies. The search for DM is nowadays one of the major experimental challenges for physics and it is constantly growing in terms of results, number of dedicated experiments and involved scientists. Three distinct lines of research can be identified: direct or indirect methods to DM detection and production at high energy colliders (see figure 1.8).

Direct detection (DD) experiments search for low energy scattering of WIMPs off atomic nuclei in ultra-low background detectors, typically operated deep underground (see section 1.3.1). The indirect detection (ID) strategy, instead, searches for annihilation products of dark matter exploring possible excesses of standard particles, such as gamma rays, X-rays, neutrinos, positrons and antiprotons, over the astrophysical background (see section 1.3.2). More recently, also the LHC experiments are devoting increasing attention to DM by looking for emerging DM particles produced in high energy collisions, whose signature would be missing energy in the reconstructed event associated to familiar particles as quarks, gluons, photons or Z bosons (see section 1.3.3).

1.3.1 Direct WIMP searches

Direct detection searches for dark matter were born with the idea proposed by Goodman and Witten [98] that WIMPs could be detected by their collision with atomic nuclei in Earth-based experiments, following an earlier suggestion by Drukier and Stodolsky [99],

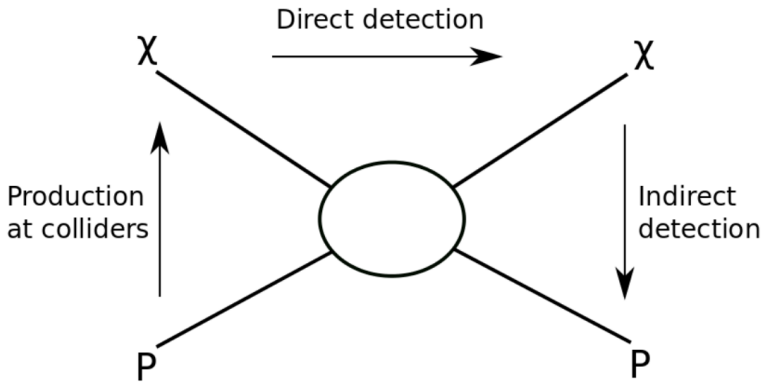

Figure 1.8: Schematic representation of the possible dark matter couplings to a particle P of ordinary matter. While the annihilation of DM particles (downwards direction) could give pairs of Standard Model particles, the collision of electrons or protons at colliders could produce pairs of dark matter particles (upward direction). Direct detection experiments search for elastic scattering of dark matter off ordinary target particles, typically baryons (horizontal direction).

in 1984, to detect solar and reactor neutrinos through their elastic neutral-current scattering off nuclei. Interestingly, such interaction of neutrino represents the ultimate background for non-directional direct WIMP searches (see section A.3), as experiments can not be shielded from the astrophysical and atmospheric neutrino flux which gives a signature indistinguishable from that of a WIMP.

The direct detection technique requires an ultra-low background, which is achieved by shielding the detector from environmental radioactivity and enhancing the radiopurity of detector elements, including construction materials and the target medium itself (see section 2.2.3 for a discussion on background reduction strategies adopted in XENON1T). In addition, methods of discrimination between WIMP and background recoils are employed to disentangle DM signals from residual background. An alternative DM signature can be provided by annually modulated signals due to Earth's motion through the DM galactic halo [100]. Efforts are also directed towards directional detection in future experiments, which will provide a DM specific signature distinguishable from neutrinos [101].

Interactions of WIMPs with target nuclei can be detected via scintillation light, produced by de-excitation of nuclei, charge from ionization of atoms or heat (phonons) in bubble chambers (crystal detectors). Usage of one or a combination of two observable signals characterizes different detector types, depending on the technique exploited to disentangle WIMPs from background nuclear (NR) and electronic recoils (ER), as illustrated in figure 1.9. This is possible due to the different signal response for a given recoil energy since nuclear recoils are more quenched than electronic recoils, i.e. produce less light and charge. WIMPs are expected to recoil only off nuclei, therefore ERs constitute a background, typically from external gamma radiation or β-decays that take place in the detector surrounding material or inside the target mass. Neutron interactions or

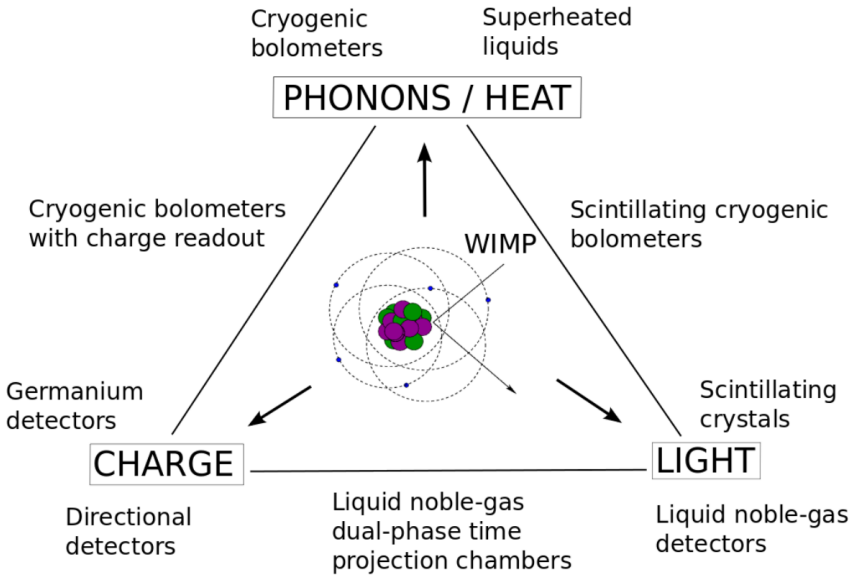

Figure 1.9: Schematic view of possible signals that can be measured in direct detection experiments depending on the technology in use. To measure the ionisation signal either germanium detectors or gases (low pressure, for directional searches) are employed, while scintillation can be recorded for crystals and for noble-gas liquids. To detect heat, the phonons produced in crystals are collected using cryogenic bolometers at mK temperatures. The heat signal is also responsible for nucleation processes in experiments using superheated fluids. Detectors which exploit the discrimination power by measuring two signals are positioned between the corresponding signals: scintillating bolometers for phonon and light detection, germanium or silicon crystals to measure phonon and charge, and dual-phase noble liquid detectors for charge and light readout.

α-decays, which can mimic the WIMP signal, are screened or rejected at the analysis level. Depending on the choice of signal detection technique, a variety of target material are employed in DD experiments.

Scintillating crystals The DAMA/LIBRA [102] experiment, operating at the LNGS underground laboratory, employs about 250 kg highly radio-pure NaI(Tl) crystals. With this approach, only the *scintillation light* is exploited and no discrimination between ER and NR is possible. The DM signature in such detectors is an annually modulated signal over the flat background. DAMA has been recording an annually modulated DM-like signal for two decades [103], with a significance level that currently reached 12.9σ [104]. However, the DM interpretation of these results is in strong tension with null results published by other experiments using different detection techniques and targets: XENON100 [105–107] and XENON1T [108, 109], LUX [110], PandaX-II [111] using liquid xenon (LXe) in dual-phase time projection chambers, as well as limits from detectors sensitive to low mass WIMPs like CDMSlite [112], a low ionization threshold cryogenic germanium detector, and XMASS [113], which is a single-phase LXe detector.

Other experiments using the same detection strategy of DAMA have been proposed, using NaI(Tl) crystals as well, trying to confirm or reject the annual modulation observed by DAMA: the COSINE experiment [114] at the Yangyang underground laboratory (Korea) and SABRE [115] which will employ twin arrays of NaI(Tl) detectors operating in both hemispheres, at LNGS and at the Stawell Underground Physics Laboratory (SUPL) in Australia, aiming at minimizing seasonal systematic effects.

Low threshold germanium detectors The *charge ionization signal* can be effectively measured with low-temperature and ultra-low background germanium detectors [116], that are particularly suitable for low mass WIMP search ($\lesssim 10\,\mathrm{GeV/c^2}$). The CoGeNT experiment, which uses such technique, claimed the observation of an annual modulation in its data [117]. Such signal had a 2.8σ significance and was not confirmed in later searches. The DM interpretation of the CoGeNT excess has also been disfavoured by other germanium detectors as CDEX [118] and MALBEK [119].

The charge signal can be exploited also by directional DM searches with gaseous detectors [120], like DRIFT [121], MIMAC [122] and DMTPC [123].

Cryogenic bolometers *Phonon signals* produced by WIMP-nucleus scattering in crystals provides another important experimental signature, particularly useful for light DM search because of the typically very low energy threshold achievable with this technology. Thermic background is kept under control by using cryogenic bolometers with additional charge or scintillation light readouts. The SuperCDMS [124] and EDELWEISS [125] experiments employ the former detection strategy, while CRESST [126] and COSINUS [127] combine phonon measurements with the light signal.

In 2013, CDMS-Si (with a silicon detector) reported the observation of 3 WIMP candidate events [128], with a rejection of the background-only hypothesis with 99.8% significance. However, such result was not confirmed by the same collaboration exploiting germanium crystals in the CDMS-II [129] and SuperCDMS [124] DM searches. An excess in two mass ranges, around 10 and $25\,\mathrm{GeV/c^2}$, over the expected number of events was also observed by CRESST-II [130] in 2011, with 4.2σ and 4.7σ significance respectively. Nonetheless, the same collaboration found that the excess was mainly due to a missing contribution to the assumed background model [131].

If superheated fluids are used instead of crystals, WIMP-nucleon interactions can be detected through the *heat signal* in bubble chambers. DM particles traversing the detector can be visualized thanks to the initiated process of bubble creation. The PICO experiment [132], that follows this detection strategy, set the strongest exclusion limits for the spin-dependent WIMP interaction on protons [133] among all the DD experiments.

Noble liquid dual-phase TPCs The most stringent constraints on the WIMP-nucleon spin-independent cross section are obtained by dual-phase (liquid-gas) time projection chambers (TPCs) utilizing liquid xenon as target material. The current best

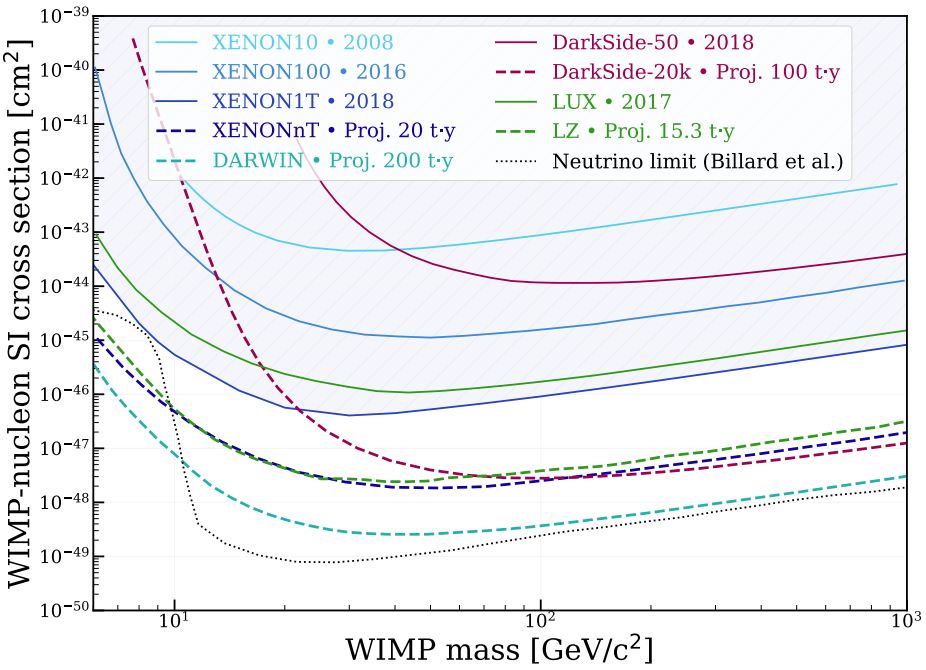

Figure 1.10: Limits on the WIMP-nucleon spin-independent cross section as a function of WIMP mass from direct detection searches with noble liquid dual-phase TPC detectors. The excluded WIMP parameter space is highlighted by a blue shaded region above the current world-best exclusion limit set by XENON1T [109] (discussed in this work). Results from previous experiments of the XENON Dark Matter Project, XENON10 [134] and XENON100 [105], are also drawn as solid blue lines of different tonality. Future projections of WIMP direct searches with noble-liquid detectors are shown through the expected sensitivities of the most competitive experiments (dashed lines): XENONnT (using LXe target) projection in 20 t·y exposure [135] (blue), LZ (LXe) in 15.3 t·y [136] (green), DarkSide-20k (LAr) in 100 t·y (magenta) and DARWIN (LXe) in 200 t·y. DarkSide-20k and LZ are enlarged and improved future detectors evolving from DarkSide-50 [137] (magenta solid) and LUX [110] (green solid), respectively. The neutrino discovery limit [138] is shown as dotted black line with grey shaded area beneath.

results come from the XENON1T experiment [109] (discussed throughout this work) that improved previous limits of LUX [110] and PandaX-II [111], shown in figure 1.10. This kind of technology allows to readout both the light and charge signals (as described in section 2.1). Thanks to the scalability of such detection systems, future multi-ton LXe experiments as XENONnT (see section 2.3), LZ [139] and DARWIN [140] are expected to improve the sensitivity to WIMPs by up to three orders of magnitude, approaching the so-called "neutrino floor" [138], where the CNNS background is expected to limit the sensitivity to WIMPs (see figure 1.10). Liquid Argon can also be used as target to build multi-ton TPCs, such as DarkSide [141] and ArDM [142].

LXe-based TPCs also provided competitive limits on the spin-dependent WIMP cross section, exploiting the ^{129}Xe and ^{131}Xe isotopes, with XENON100 [105] and LUX [143], while such interaction can not be investigated in LAr detectors due to the absence of non-zero spin target isotopes.

A detailed discussion about the experimental case of WIMP direct search with LXe dual-phase TPC is given in section 2.1.

1.3.2 Indirect detection experiments

Dark matter particles might be detected by observing their annihilation through the standard radiation emitted in such process. After decoupling from the other particles in the early Universe, the DM pair annihilation must be largely suppressed in order to yield the observed DM density, but self-annihilation could still be significant in present Universe. Hence, indirect searches look for excesses of Standard Model particles above the usual astrophysical background, that could be interpreted as DM annihilation products.

Gamma-ray telescopes A common end product of DM annihilation is gamma-ray emission with either a continuous spectrum produced by the decay, hadronization and final state radiation of SM particles generated from the annihilation, or with specific spectral features such as mono-energetic lines or internal bremsstrahlung gammas. This kind of searches are focused in astrophysical regions with high density of DM for an easier discrimination with respect to the gamma-ray background due to ordinary processes. The Galactic Center (GC) is probably the most investigated target for ID experiments since it is expected to be the brightest source of gamma-rays from annihilating DM [144], even though complex background must be faced. The strongest and most robust limits, however, come from dwarf spheroidal galaxies [145], from which less intense signal is expected, but free from the astrophysical backgrounds of GC. Galaxy clusters are promising targets [146], even if they suffer from large and poorly understood astrophysical backgrounds. The full sky is also exploited to set limits on annihilation summed over cosmological (and unresolved) DM halos [147], looking for spectral features in the isotropic gamma-ray background.

Direct gamma-ray observations are made with space telescopes, while ground-based observatories exploit the Cherenkov light produced by showers of secondary particles from the interaction of gamma-rays in the atmosphere. DM searches have been performed by the space telescope EGRET [148] and currently by Fermi-LAT [149], which uses pair conversion inside a tracking detector and an electromagnetic calorimeter. The most promising ground-based telescopes are the Imaging Air Cherenkov Telescopes (IACTs), including the currently running MAGIC [150], VERITAS [151], HESS [152] and the planned next-generation telescope CTA [153]. IACTs have higher energy threshold with respect to space detectors, but the effective area that can be observed is much larger.

Direct gamma-rays observation with space telescopes provides the strongest limits on the WIMP annihilation cross section up to masses of $\sim 1\,\mathrm{TeV/c^2}$, while IACTs are more sensitive at larger DM masses. Figure 1.11 shows recent limits and future projection on the WIMP annihilation to $b\bar{b}$ cross section. The strongest limits are pro-

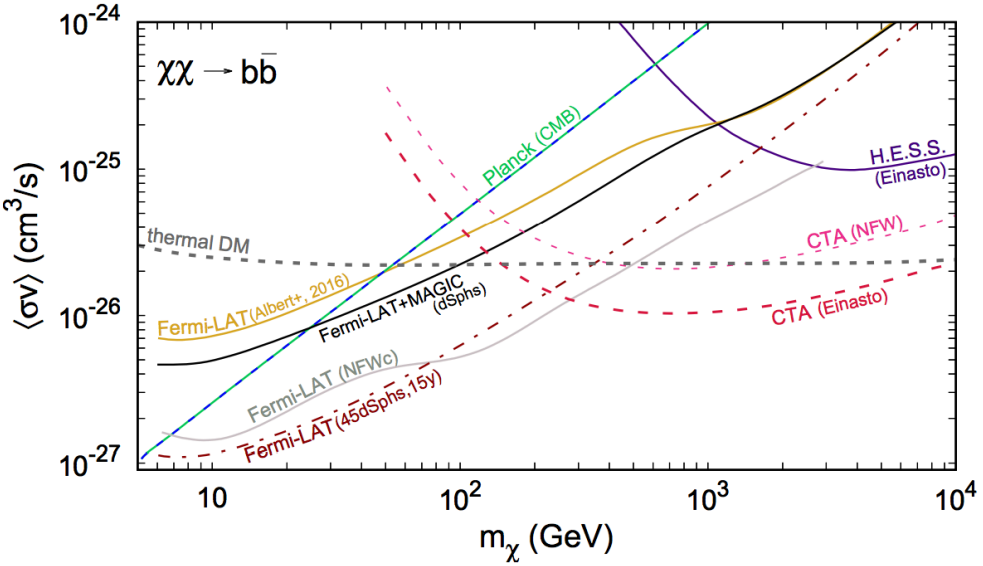

Figure 1.11: Limits on the annihilation cross section for DM particles annihilating into a $b\bar{b}$ pair. Currently the strongest limits correspond to the stacked analysis of dwarf galaxies from Fermi-LAT [156] (solid golden line), combined analysis of both Fermi-LAT and MAGIC [154] (solid black line) collaborations, HESS observations of the GC [155] (solid violet line). In the low DM mass regime the important limits come from the CMB analysis released by the Planck collaboration [157] which constraints the annihilation cross section around the time of recombination (dashed blue-green line). The future projections are shown for the stacked analysis of 45 dwarf galaxies and 15 years of data taking [158] (dash-dotted brown line), as well as for the CTA collaboration [159] based on different DM density profiles assumed: NFW (dashed pink line) and Einasto (dashed red line). The value of the annihilation cross section that corresponds to the thermal production of WIMP DM [160] is denoted with dotted gray line.

vided by the combined analysis of dwarf galaxies from Fermi-LAT and MAGIC [154] below $\sim 1\,\mathrm{TeV/c^2}$ and by observations of the Galactic Center from HESS [155], at larger masses.

Charged cosmic rays Cosmic rays measurements are complementary to gamma-rays in the indirect search for DM [161], as electrons, protons and light nuclei are expected to be produced jointly with γ-rays when DM particles annihilate or decay. Since an equal amount of matter and antimatter should originate from neutral DM annihilation, ID searches focus in particular on positrons, antiprotons, antideuterons, antihelium, etc., which have much less astrophysical background than the standard matter counterpart. The expected signature of DM-induced cosmic rays is a diffuse spectrum with a cut-off at energies close to m_χ or $m_\chi/2$ for annihilations or decays, respectively, where m_χ is the DM particle mass.

Searches for anomalies in charged cosmic rays are made with ballon-type detectors (HEAT [162], ATIC [163]), ground-based telescopes (Pierre Auger Observatory [164],

Telescope Array [165]) and experiments on satellites (PAMELA [166], AMS [167], Fermi-LAT [149]). An excess in the positron spectrum was observed by PAMELA [168] in 2008, subsequently confirmed by the other satellite telescopes Fermi-LAT [169] and AMS-02 [167]. Such observation could be consistent with DM interpretation, but could also be explained by astrophysical sources given the uncertain impact of magnetic field configurations on the positron trajectories [170].

Recently, an excess in antiproton flux has been measured by AMS-02 [171] which could be explained by DM annihilation. Further studies will come to shed light on all the observed anomalies with future searches with the CALET [172], DAMPE [173] and GAPS [174] experiments.

Neutrino telescopes Depending on DM models, neutrinos can be produced mainly in cascades of particles originating from DM annihilation or decay. DM-induced neutrinos can be searched in regions with large concentration of DM, such as the Sun, the Galactic Center, nearby galaxies, galaxy clusters and even the Earth itself. As DM particles accumulates inside celestial bodies, their annihilation products moving slower than the escape velocity are trapped while neutrinos are the only produced particles that always can escape and reach detectors providing a unique signature [175].

Water Cherenkov neutrino telescopes (ANTARES [176], IceCube [177], Super-Kamiokande [178]), thanks to impressive experimental progresses, are able to provide the current most stringent constraints on WIMP-nucleon spin-dependent cross section based on upper limits on the the neutrino flux from DM annihilation. Further improvement is expected from planned neutrino telescopes: BAIKAL-GVD [179], IceCube-PINGU [180], Hyper-Kamiokande [181] and KM3Net [182].

1.3.3 Dark matter production at colliders

In most DM scenarios, the WIMP coupling and mass range are close or just above the electro-weak symmetry breaking scale. Therefore, high energy colliders, LHC in particular, are viable experimental venues for DM detection through its production. The DM signature in hadron collisions would be a large amount of missing energy associated with the discovery of one or more visible particles in a channel characterized by highly energetic jets or leptons. However, if new visible particles are actually beyond the collider's reach, the detection strategy must involve the identification of an isolated object (jets, gauge bosons or leptons) accompanied by large missing momentum.

ATLAS [183] and CMS [184] experiments interpret constraints on production cross sections in terms of effective field theories [185, 186] and simplified models [187], in order to compare with observables in DD and ID DM experiments, such as WIMP-nucleon scattering cross section or thermal relic density. While collider constraints are not competitive to those from DD for the spin-independent WIMP-nucleon interaction, interpretation of LHC signals in terms of spin-dependent cross section [188], assuming an axial-vector mediated model e.g., are more powerful over a wide range of WIMP

masses. Connecting collider experiment's results on invisible particles to DM requires also DD and ID experiments and the comparison and contrast of these three different types of information will be of great help in understanding the DM nature.

Chapter 2

The XENON Dark Matter Project

Detectors using liquid xenon have demonstrated the highest sensitivities over the past years in the direct search for dark matter. The XENON Collaboration is leader in the field employing LXe-based dual-phase TPC technology (described in section 2.1), thanks to the DM Project started two decades ago and hosted at the Laboratori Nazionali del Gran Sasso (LNGS), the largest underground laboratory of the world under 3600 meters-water-equivalent mountain rock.

The first detector of the XENON Dark Matter Project was XENON10 [189], installed in 2005 and operational until 2007, featuring a total LXe mass of 15 kg, with 5.4 kg used as fiducial mass. The main goal of the experiment was to test the feasibility of a dual-phase detector (LXe/GXe) on the kg scale to detect dark matter interactions. In 2008, the XENON10 experiment published the results of the 58.6 days run, establishing world-record upper limits on both SI and SD WIMP-nucleon cross section, with minimum of $4.5 \times 10^{-44}\,\mathrm{cm}^2$ [190] and $5 \times 10^{-39}\,\mathrm{cm}^2$ [191] (coupling with neutron), respectively, for $30\,\mathrm{GeV/c}^2$ WIMP mass.

The good results achieved by XENON10 pushed towards the realization of a new and larger detector, XENON100 [192], based on the same detection principle. The LXe amount was increased to 161 kg, with 62 kg used as active volume in the TPC and the remaining as an outer active veto; the fiducial volume was chosen as 34 kg or 48 kg, depending on the background conditions in the various runs. The goal of this experiment was to lower the sensitivity by two orders of magnitude with respect to XENON10. Such result has been achieved with the larger target, but also thanks to a factor 100 of background reduction through an accurate screening and selection program for all detector construction materials.

The XENON100 experiment published the world-best upper limits on the spin-independent [193] and spin-dependent [194] coupling of WIMPs to nucleons in 2012 and 2013. No dark matter evidences have been found in the final exposure of 447 live-days of data taking [105], leading to 90% confidence level upper limits on the WIMP SI interaction at $1.1 \times 10^{-45}\,\mathrm{cm}^2$ for $50\,\mathrm{GeV/c}^2$ mass, while for SD WIMP-neutron (-proton) cross section upper limits were set at $2.0 \times 10^{-40}\,\mathrm{cm}^2$ ($5.2 \times 10^{-39}\,\mathrm{cm}^2$) for

$50\,\mathrm{GeV/c^2}$ WIMP mass.

XENON100 also explored and constrained other dark matter physics channels besides the main WIMP NR elastic scattering off nucleons, such as searches for axions [195], leptophilic DM [196] (WIMPs coupling with electrons), annual modulation [106, 107] (excluding DAMA signal), low mass WIMP [197] (using the ionization signal only), inelastic DM [198] (WIMP inelastic scattering off nuclei), high energy NRs in effective field theory approach [199], magnetic inelastic DM [200] (inelastic scattering of WIMPs with non-zero magnetic dipole moment), bosonic super-WIMP [201] (vector and pseudo-scalar DM particles).

To significantly improve upon the XENON100 experimental sensitivities, the XENON Collaboration has paved the way for the next generation of multi-ton scale DM detectors with XENON1T [202, 203] (section 2.2), operating a 3.2 t LXe detector (with 2.0 t active mass in the TPC). After setting the current most stringent constraint on the WIMP-nucleon SI cross section, with a minimum at $4.1\times10^{-47}\,\mathrm{cm^2}$ for $30\,\mathrm{GeV/c^2}$ WIMP mass, a fast upgrade towards XENONnT (section 2.3) will replace XENON1T in 2019, in order to employ about 8 t (6 t) total (active) LXe mass with the goal of one order of magnitude improvement in sensitivity.

2.1 Detection principle of a xenon dual-phase TPC

The detectors of the XENON DM Project are based on a *dual-phase TPC*, containing xenon in the liquid phase and, above it, a small gap of gaseous xenon. In this section the main properties of a xenon-based target (section 2.1.1) and the characteristics of detection signals achieved with the dual-phase TPC (section 2.1.2) are outlined, with focus on the discrimination between ER and NR interaction based on the combined information of light and charge signals.

2.1.1 Liquid xenon as target

The choice of LXe as active target for the direct detection of dark matter implies several advantages. An important property of a xenon target is represented by its self-shielding power against external background sources, thanks to its high density, equal to 2.96 $\mathrm{g/cm^3}$, and a relatively large triple point (161 K) [204], which is not extremely demanding from the cryogenic point of view. Moreover, since the WIMP cross section scales with A^2 of the target nucleus, the large xenon atomic number ($A = 131$), relatively to other noble gases, increases the expected WIMP interaction rate. Xenon has nine stable isotopes, while unstable ones are very short-lived. Hence, it is a rather pure material, which is a mandatory requirement for a search of very rare events like WIMP scatterings. Specifically, there are two isotopes with non-zero spin: ^{129}Xe (spin 1/2) and ^{131}Xe (spin 3/2), with isotopic abundance of 26.4% and 21.2% respectively. This allows to study also the dependence of the WIMP-nucleon cross section on the spin, thus providing more information about the dark matter nature.

After an electronic transition from an excited to the fundamental state, xenon emits scintillation light of 177.6 nm wavelength (VUV photons). Xenon is an excellent scintillator, since emits about 5×10^7 photons per keV deposited, but has also a good ionization yield, of about 6×10^7 electron-ion pairs per keV. Therefore, an interaction produces both a relatively large amount of charges and photons.

The xenon scintillation is ruled by de-excitation of excimers, excited xenon dimeric molecules (Xe_2^*), which are formed after recoil events through direct excitation or recombination of ionization products. In the direct excitation process an excited state Xe^* is promptly formed, leading to scintillation through the following scheme:

$$\begin{aligned} Xe^* + Xe &\rightarrow Xe_2^* \\ Xe_2^* &\rightarrow 2Xe + h\nu \, . \end{aligned} \tag{2.1}$$

After ionization in the xenon target, the Xe^+ ions can form a molecular state and a freed electron can recombine, producing scintillation at the end of the chain:

$$\begin{aligned} Xe^+ + Xe &\rightarrow Xe_2^+ \\ Xe_2^+ + e^- &\rightarrow Xe^{**} + Xe \\ Xe^{**} &\rightarrow Xe^* + \text{heat} \\ Xe^* + Xe + Xe &\rightarrow Xe_2^* + Xe \\ Xe_2^* &\rightarrow 2Xe + h\nu \, . \end{aligned} \tag{2.2}$$

Due to the different configuration of the energy levels of dimers and atoms, the photons emitted by dimers are not re-absorbed by the atoms making LXe transparent to its own scintillation light. The scintillation light in LXe has two decay components characterized by two different decay times: the singlet (S) and triplet (T) states of the excited dimers Xe_2^*. The fast scintillation component is due to the S state and its decay time can vary under intense electric fields. For instance, with a 4 kV/cm electric field, the decay times after the interaction of relativistic electrons with xenon atoms are: (2.2 ± 0.3) ns from the singlet states decays and (27 ± 1) ns from triplet states [205].

2.1.2 Observable signals

A particle interacting in LXe produces a prompt scintillation signal, called S1, and ionization electrons. The electrons can recombine, participating to the S1 signal, or can be drifted by an appropriate electric field towards the liquid-gas interface where they are extracted by a strong extraction field $\mathcal{O}(10$ kV/cm), and a second light signal, named S2, is generated by proportional scintillation in the gas. The S2 signal is delayed by the time occurring in the drift from the interaction site to the liquid-gas interface. A sketch of the signal production in a dual-phase TPC is shown in figure 2.1.

The bottom end of the TPC is defined by the cathode electrode (negatively biased), while at the top by the gate mesh (grounded). This region encloses the LXe sensitive volume used to detect the interactions and which is available for the electrons drift.

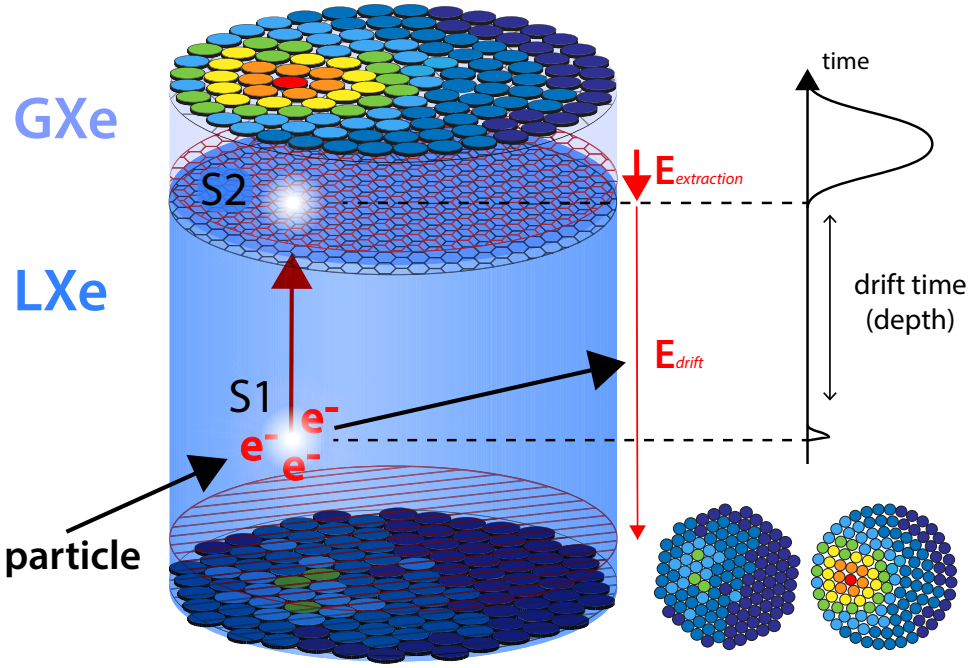

Figure 2.1: Schematic view of the working principle of dual-phase time projection chambers used in the XENON DM Project. The prompt scintillation signal S1 is measured by both PMT arrays. Ionization electrons are drifted from the interaction vertex towards the LXe/GXe interface under a uniform electric field. The S2 signal is formed via proportional scintillation triggered by electrons extracted in the gaseous region by means of an intense electric field established between the gate (electrode just below the liquid-gas interface, black) and the anode (electrode just above the liquid-gas interface, red). The localized pattern of the S2 signal in the top PMT array is used to reconstruct the (x, y) interaction position. The time delay between S1 and S2 informs about the z coordinate of the interaction vertex. The energy of the event is reconstructed from the combination of both S1 and S2 signals.

Along the vertical axis, equally spaced thin copper rings are properly distributed, together with the cathode and the gate mesh, to generate a uniform drift field. Above the gate electrode there is the anode, with LXe/GXe interface between them.

Two PMT arrays, one on top of the TPC, in the GXe region, and one at the bottom below the cathode, in LXe, are used to detect both light signals. A dual-phase TPC detector allows to reconstruct the vertex of an interaction in the sensitive volume in three dimensions. From the hit pattern of the S2 signal on the top PMTs, the (x, y) position is determined. The z coordinate is inferred from the time difference between S1 and S2 signals, since that is due to the electron drift time proportional to the depth in the TPC. The knowledge of the interaction point allows the selection of those events located in the inner part of the LXe, usually called fiducial volume (FV). Since the majority of background events are expected to be found at the edge of the TPC, the outermost volume is used as shield to remarkably reduce the background from external

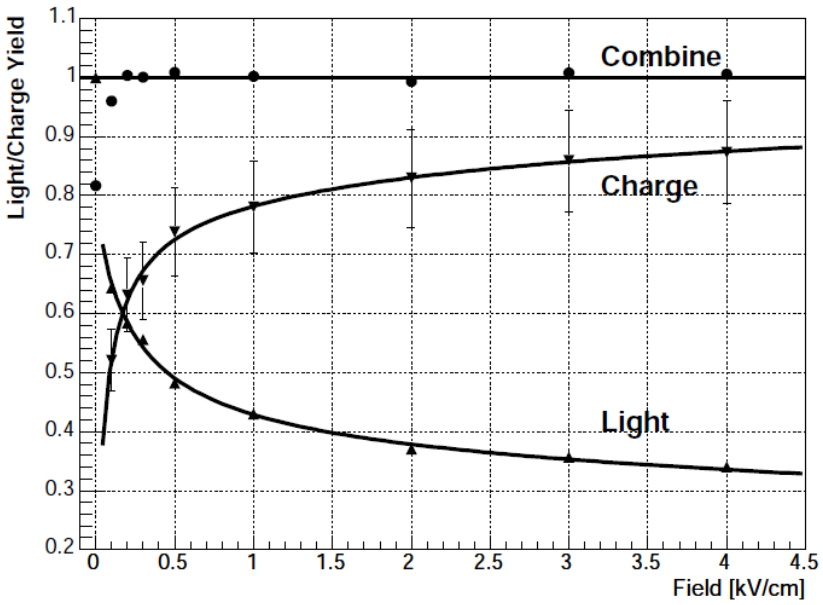

Figure 2.2: Measurements of light and charge yield in liquid xenon, derived from the S1 and S2 signal size respectively, using the mono-energetic 662 keV γ-rays from ^{137}Cs [206]. The anti-correlation holds at different electric drift fields. The charge yield increases with higher fields as the recombination of freed electron becomes less probable and more electrons participate to the S2 signal. This also implies that the S1 signal loses the contribution from the recombination process.

sources. Single scatters (expected from WIMPs) can be distinguished from multiple scatters thanks to the presence of more than one S2 signal in the event.

The combined information arising from the light (S1) and charge (S2) signal is exploited for ER background suppression, due to a different recombination process with respect to NRs. The ability to discriminate among different particles is essential since WIMPs are expected to produce NRs while most of the background radiation produces ERs. Particles with different Linear Energy Transfer (LET), dE/dx, have different S2/S1 ratio and this is exploited for discrimination. A NR has higher electron recombination rate with respect to ERs, due to higher LET. A higher recombination causes smaller S2 and larger S1, thus a lower S2/S1 ratio. This is due to the anti-correlation between ionization and scintillation signals, as experimentally observed (see figure 2.2). Hence, using the ratio of the signals S1 and S2 as discrimination parameter, it is possible to distinguish between the two types of recoil.

Figure 2.3 shows the separation between ER and NR events in the signal space achieved in the XENON100 experiment: S1 signals vs S2/S1 discrimination parameter (defined as $\log_{10}(\mathrm{S2/S1}) - \mathrm{ER}_{\mathrm{mean}}$). The distributions in the signal space space are usually referred to as ER and NR bands. The detector response to ER and NR events is studied through calibration sources of γ and β particles (for ER) or neutrons (for NR), in order to characterize the actual separation achieved. Typically, a $> 99\%$ ER rejection

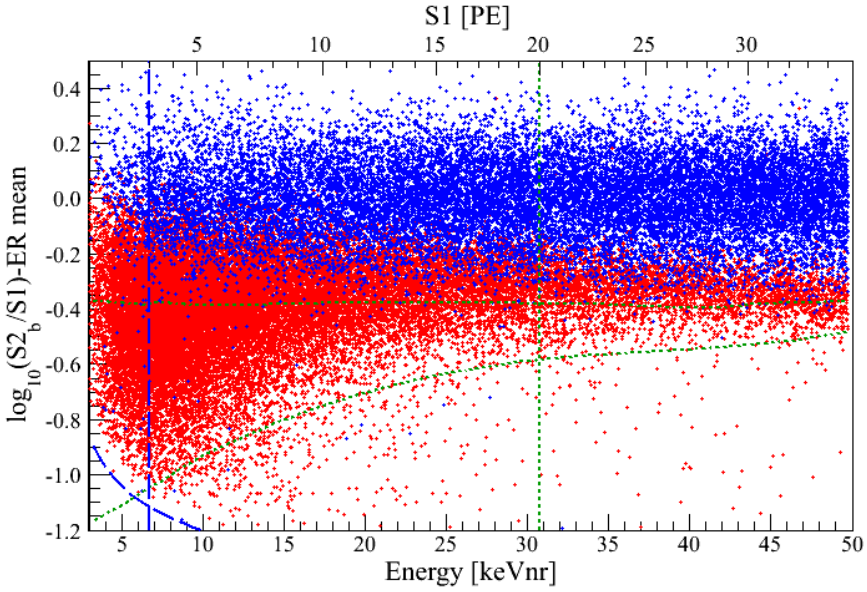

Figure 2.3: Distribution of the flattened discrimination parameter, $\log_{10}$(S2/S1), as function of the nuclear recoil energy (or S1 signal, upper x-axis) achieved with the XENON100 experiment [193]. The ER band (blue points), obtained from ^{60}C and ^{232}Th (γ-emitters) calibration data, is shown together with the NR band (red points), from ^{241}AmBe (neutron source) calibration. The y-axis is the "flattened" version of the S2/S1 distribution, considering $\log_{10}(\mathrm{S2/S1}) - \mathrm{ER}_{\mathrm{mean}}$, where $\mathrm{ER}_{\mathrm{mean}}$ is the mean of the ER band. In this way, one gets a flat ER band centered in zero and removes the energy-dependence of this discrimination parameter.

power is reached with 50% acceptance to NRs. Given the overlap between the ER and NR bands, in XENON100 a 99.5% ER discrimination corresponds to a 50% acceptance of NR events, while 99.75% ER discrimination gives 40% NR acceptance [193].

A detailed description of the properties of physics processes in liquid xenon, as well as signal propagation and detector efficiency, is given in section 3.3 with the full characterization of the XENON1T signal response model to ER and NR interactions.

2.2 The XENON1T experiment at LNGS

The XENON1T detector hosted underground at Laboratori Nazionali del Gran Sasso was brought operational in Spring 2016. The detector is filled with 3.2 t of LXe, of which 2 t are in the sensitive TPC volume. XENON1T is the largest LXe dark matter experiment in operation, with a sensitivity reach of $1.6 \times 10^{-47}\,\mathrm{cm}^2$ at $50\,\mathrm{GeV/c}^2$ with 2 t·y exposure [135].

The XENON1T dual-phase TPC (described in section 2.2.1) is installed inside a double-walled vacuum cryostat in the center of a large water tank. The tank serves as passive shield as well as a Cherenkov Muon Veto detector (see section 2.2.4). A three-floor building erected in Hall B of LNGS laboratory (shown in figure 2.4) accommodates all ancillary systems. These include the systems to cool, purify and store

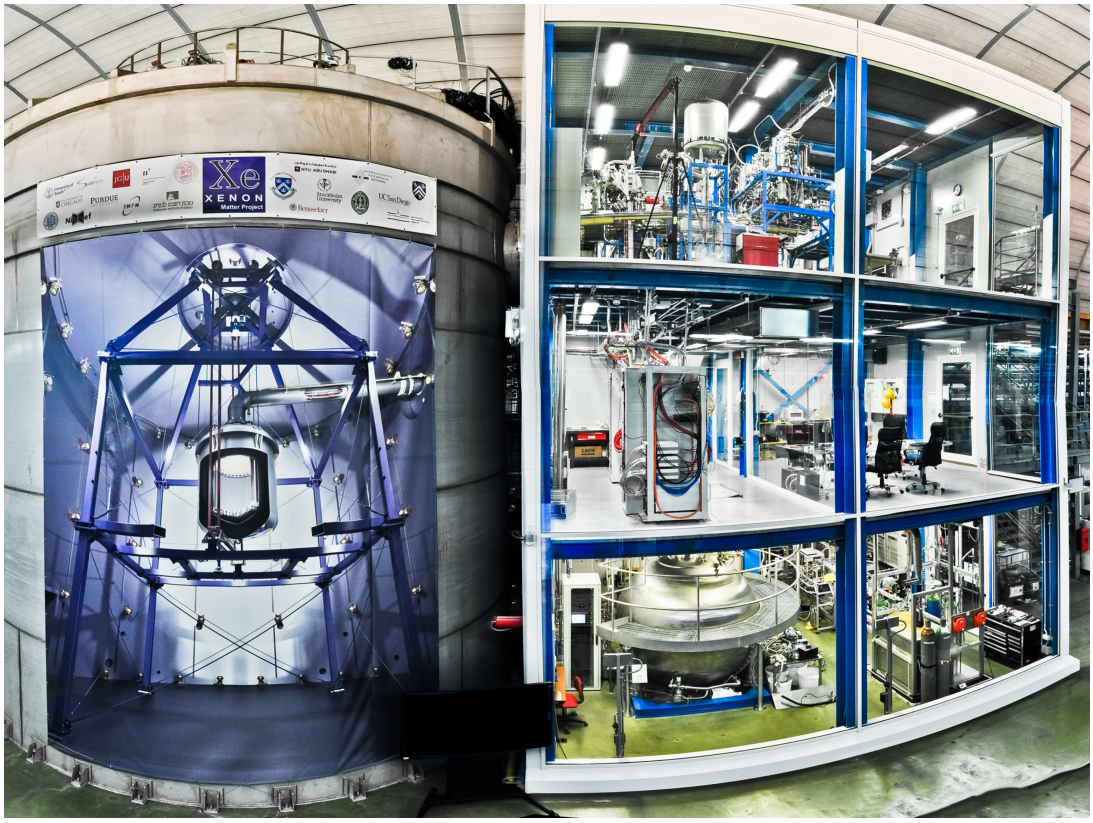

Figure 2.4: Picture of the XENON1T building placed at LNGS, the largest underground laboratory of the world: on the left, the Muon Veto water tank containing the TPC; on the right the Service Building which hosts the cryogenic and purification systems (top floor), the DAQ and slow control equipment (middle floor), the cryogenic distillation column and the emergency recovery system (ground floor).

the xenon gas (see section 2.2.2), the cryogenic distillation column for krypton removal (see section 2.2.3), the data acquisition system as well as the control and monitoring systems for the entire experiment. The TPC calibration systems are installed on the xenon purification system and on the top of the water shield (see section 2.2.5).

2.2.1 The XENON1T Time Projection Chamber

The cylindrical TPC of 97 cm height and 96 cm diameter, shown in figure 2.5, contains an active LXe target of 2.0 tonnes. It is enclosed in 24 interlocking and light-tight PTFE (polytetrafluoroethylene) panels, whose surfaces were treated with diamond tools in order to optimize the reflectivity for vacuum ultraviolet (VUV) light [207]. Due to the rather large linear thermal expansion coefficient of PTFE, its length is reduced by about 1.5% at the operation temperature of −96 °C. An interlocking design allows the radial dimension to remain constant while the vertical length is reduced.

To ensure drift field homogeneity, the TPC is surrounded by 74 field shaping electrodes made from low-radioactivity oxygen-free high thermal conductivity (OFHC) cop-

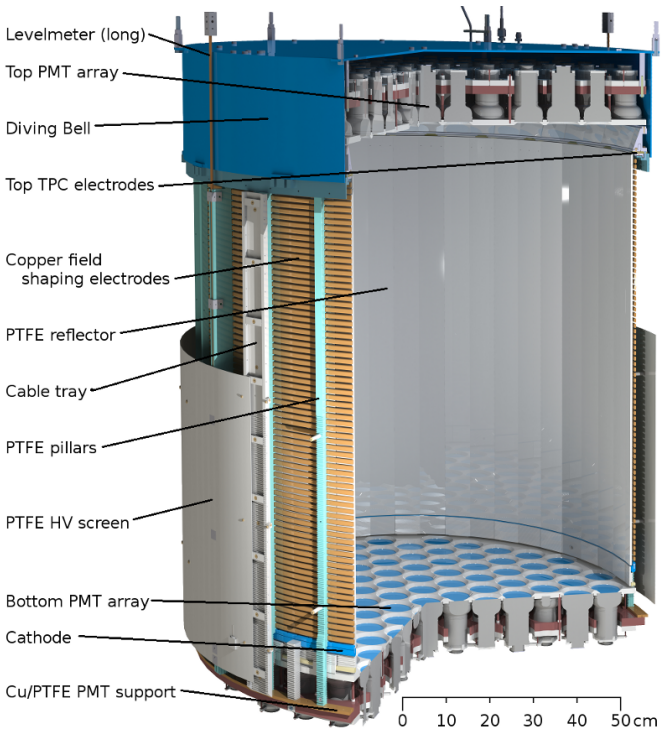

Figure 2.5: Illustration of the XENON1T TPC. It is built from materials selected for their low radioactivity, e.g., OFHC copper, stainless steel and PTFE. The top and bottom PMT arrays are instrumented with 127 and 121 Hamamatsu R11410-21 PMTs, respectively.

per and connected by two redundant resistor chains. Most S1 light is detected by the photo-sensors below the target. The electrodes were thus designed for S1 light collection by optimizing the optical transparency of the gate, the cathode and the bottom screening electrodes. The cathode is negatively biased, the anode is positively charged, the gate electrode is kept at ground potential and the screening electrodes can be biased to minimize the field in front of the PMT photocathodes.

A "diving bell" made of stainless steel, which is directly pressurized by a controlled gas flow, is used to maintain a stable liquid-gas interface between the gate and anode electrodes. It encloses the top PMT array. The height of the liquid level inside the bell is controlled via a vertically-adjustable gas-exhaust tube. Possible tilts of the TPC are measured by means of four custom-made parallel-plate-capacitive level-meters installed inside the diving bell, with a precision of $\sim 30\,\mu$m.

A total of 248 PMTs of 76.2 mm diameter are used to record the signals from the TPC. They are radially installed in the top array (127 PMTs) to facilitate radial position reconstruction, and packed as tightly as possible in the bottom array (121 PMTs) to maximize scintillation light collection efficiency. They feature an average room temperature quantum efficiency of 34.5% at 178 nm [208], a high photoelectron collection efficiency of 90% and are designed to operate stably in gaseous and liquid xenon at

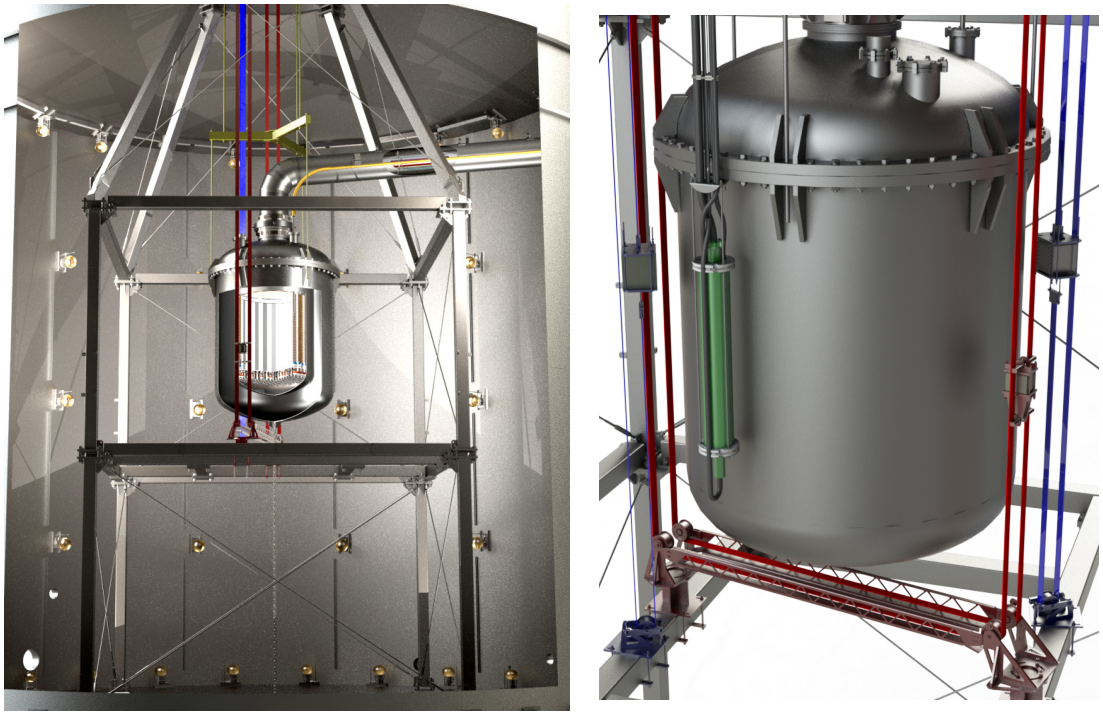

(a) (b)

Figure 2.6: (a) The stainless-steel cryostat containing the LXe TPC installed inside a 740 m^3 water shield equipped with 84 PMTs deployed on the lateral walls. The cryostat is freely suspended on a stainless-steel support frame, which can be converted into a cleanroom. The cryostat is connected to the outside by means of two pipes. The large vacuum-insulated cryogenic pipe carries all gas/LXe pipes and cables. A small pipe (yellow) is used for the cathode high-voltage. Also shown is the system for calibrating XENON1T. (b) The deployment system for external calibration sources. Two belts ("I-belts", blue) allow for vertical movement of sources inside their W-collimators, while one belt ("U-belt", red) reaches areas around the detector bottom. The DD-fusion neutron generator (green) can be vertically displaced along the cryostat.

cryogenic temperature [209, 210].

All installed PMTs were screened for their intrinsic radioactivity levels [211] and tested at room temperature and under gaseous nitrogen atmosphere at −100 °C. The PMTs with the highest quantum efficiency were installed at the center of the bottom array to maximize the light collection efficiency. Both arrays consist of a massive OFHC copper support plate with circular cut-outs for the PMTs. A single PTFE plate holds the individual PMTs and a PTFE reflector plate covers the areas between the PMT windows. Custom-developed low pass filters installed on each high voltage and return line reduce the electronic noise to sub-dominant levels.

The TPC is installed inside a double-walled, cylindrical stainless steel cryostat made of low radioactivity material [212]. The inner vessel is 1.96 m high and 1.10 m in diameter. Its inner surface, in direct contact with the liquid xenon, was electro-polished in order to reduce the emanation of radon. It is enclosed by an outer vessel of 2.49 m

height and 1.62 m diameter, large enough to accomodate the detector of the upgrade stage XENONnT as well (see section 2.3). The cryostat is installed in the center of the water Cherenkov detector (see figure 2.6a and section 2.2.4). The connections to the outside are made through a double-walled cryogenic pipe enclosing all the connections to the cryogenic system (cooling, purification, fast emergency recovery, diving bell pressurization) and the cables for the PMTs and auxiliary sensors.

2.2.2 Xenon handling systems

XENON1T follows the "remote cooling" concept that was successfully employed by XENON100 [192]. It allows for maintenance of the cryogenic system, which is installed far away from the TPC, while the detector is cold. The xenon gas inside the XENON1T cryostat is liquefied and kept at its operating temperature $T_0 = -96\,°\mathrm{C}$ by means of two redundant pulse-tube refrigerators (PTRs), each providing $\sim 250\,\mathrm{W}$ of cooling power at T_0. The xenon pressure inside the cryostat is kept constant by controlling the temperature of the active PTR cold finger using resistive heaters.

The cryogenic system interfaces with the cryostat through the vacuum-insulated cryogenic pipe. Xenon gas from the inner cryostat vessel streams to the cryogenic system, is liquefied by the PTR, collected in a funnel and flows back to the cryostat vessel, driven by gravity, in a pipe that runs inside the cryogenic tube. Another pipe carries LXe out of the cryostat, evaporates it in a heat exchanger, and feeds it to the xenon purification system. The purified xenon gas is liquefied in the same heat exchanger and flows back to the cryostat. The pipe that carries the purified LXe back to the cryostat is also used during the cryostat filling operation.

Electronegative impurities, such as water or oxygen, absorb scintillation light and reduce the number of ionization electrons by capture in an electron drift time dependent fashion. These impurities are constantly outgassing into the xenon from all detector components. Therefore, the gas must be continuously purified to reduce the impurities to the 10^{-9} O_2-equivalent level (ppb). The purification loop consists of a gas transfer pump, a mass-flow controller and a high-temperature rare-gas purifier (getter). The latter removes oxide, carbide and nitride impurities by forming irreducible chemical bonds with the getter material (zirconium). The purification system is also used to inject calibration sources into the detector, which are dissolved in the xenon gas (see section 2.2.5).

A new xenon storage system, called ReStoX, is developed to address the operational challenges posed by the first multi-ton LXe experiment: mainly fast TPC filling and Xe recovery. It consists of a vacuum-insulated stainless steel sphere with 2.1 m diameter ($4.95\,\mathrm{m}^3$ volume). Its volume and the wall thickness of 28 mm allow for storage of up to 7.6 t of xenon as a liquid, as a gas and even as a super-critical fluid (being capable to withstand pressures up to 73 bar).

All components of the gas handling system, their relative placement and connections are shown in figure 2.7.

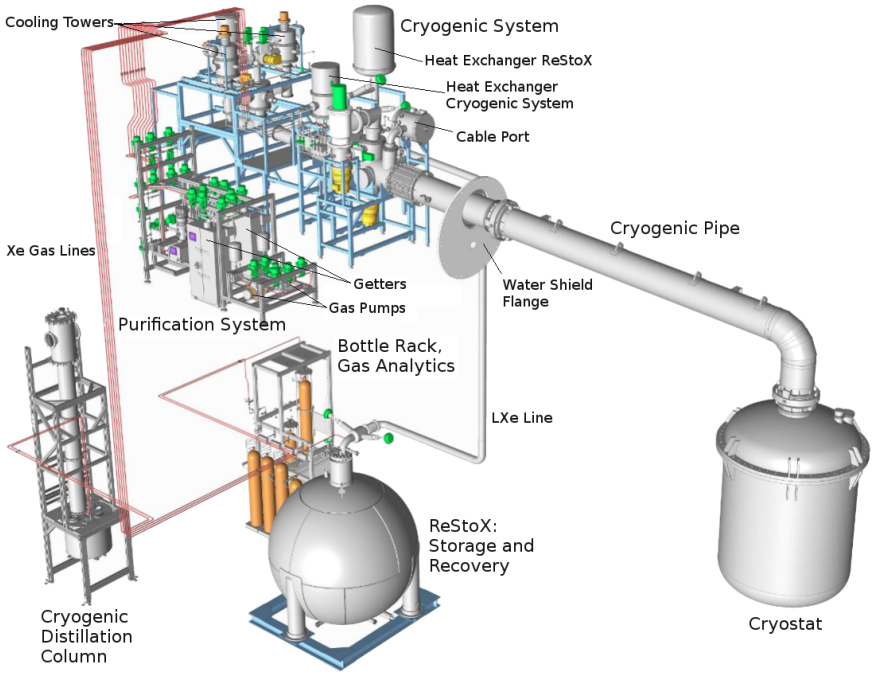

Figure 2.7: The gas-handling system of XENON1T consists of the cryogenic system (cooling), the purification system (online removal of electronegative impurities), the cryogenic distillation column (^{nat}Kr removal), ReStoX (LXe storage, filling and recovery), the gas bottle rack (injection of gas into the system) and gas analytics station (gas chromatograph). The cryostat inside the water shield accomodates the TPC.

2.2.3 Background reduction strategies

The standard background for DM direct detection experiments can be divided into electronic and nuclear recoils. The ER background originates from the radioactivity of the detector materials, sources intrinsic to LXe (beta-decay of ^{85}Kr, of ^{214}Pb from the ^{222}Rn decay chain, ^{136}Xe double-beta decay) and from solar neutrinos scattering off electrons. The NR background is due to neutrons, from spontaneous fission, (α, n) reactions and muon-induced interactions (spallations, photo-nuclear and hadronic interactions), and neutrinos, in particular those from the ^{8}B channel in the Sun, which can contribute to the NR background through coherent neutrino-nucleus scattering (CNNS). The study and characterization of these backgrounds are extensively discussed in chapter 3. In this section we describe the strategies adopted in XENON1T to reach the unprecedented low background level required by the XENON1T science goals [135], that include detector shielding, material selection and active removal of intrinsic radioactive contaminants of LXe.

Additionally, backgrounds are effectively reduced at the data analysis level: multiple scatter signatures are rejected based on the number of S2 peaks (see section 3.2.3), ER-like events are identified based on the event's S2/S1 ratio, and external backgrounds are reduced by volume fiducialization (see section 4.3.1), i.e. the selection of an inner

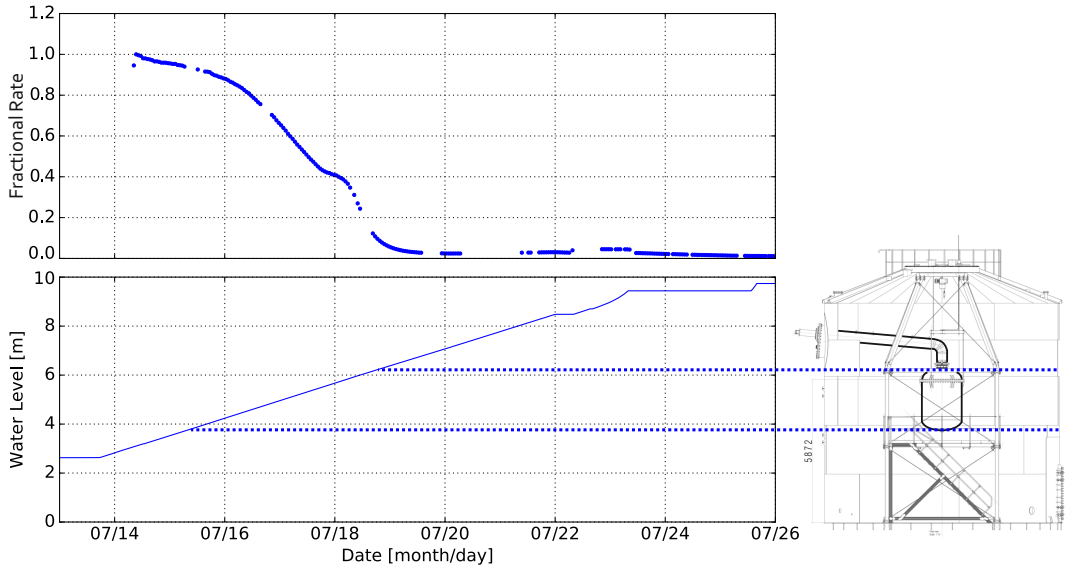

Figure 2.8: Event rate as a function of the water level in the MV tank, during the XENON1T commissioning phase. A gradual reduction of background rate (by more than two orders of magnitude) is observed as the water shield reaches the cryostat height and surrounds the detector.

detector region. However, fiducialization is not effective for target-intrinsic sources, such as the noble gases ^{222}Rn and ^{85}Kr, or the two-neutrino double-beta decay of ^{136}Xe. It is also not effective against solar neutrino-induced backgrounds.

Water shield and Cherenkov veto An active water Cherenkov detector [213], called Muon Veto (MV), surrounds the cryostat. It identifies both muons, that have a flux of $(3.31 \pm 0.03) \times 10^{-8}$ cm^{-2}s^{-1} with an average energy of ~ 270 GeV in Hall B of LNGS [214], and muon-induced neutrons by detecting showers originating from muon interactions outside the water shield. The water additionally provides effective shielding against γ-rays and neutrons from natural radioactivity present in the experimental hall. The suppression by a factor ~ 200 of the background rate measured in the TPC during the water filling of the MV tank is shown in figure 2.8. The XENON1T Muon Veto system is described in section 2.2.4. It allows to reduce the muon-induced background to a negligible contribution in XENON1T as discussed in section 3.2.1.

Detector materials screening In order to reduce ER and NR background events arising from radioactive decays in the detector components, all materials of the TPC, the cryostat and the support structure were selected for a low content of radioactive isotopes. Monte Carlo simulations were used to define the acceptable levels. The radioactivity measurements were performed using low-background high-purity germanium spectrometers of the XENON collaboration [215–217]. The most sensitive spectrometers, located at the LNGS underground laboratory, can reach sensitivities down to the µBq/kg level. In addition, standard analytical mass spectroscopy methods (ICPMS,

GD-MS) were employed at LNGS and at external companies. The measured radioactivity levels of the PMTs are summarized in [211] and that of all other materials and components in [212].

Most materials in contact with the liquid or gaseous xenon during standard operation were additionally selected for a low ^{222}Rn emanation rate. This includes most components of the TPC, the inner cryostat and its connection pipes, the cryogenic system with its heat exchangers and the purification system. The LXe storage vessel and the cryogenic distillation column are irrelevant sources of Rn-emanation as they are not continuously connected to the TPC. Even though the emanation rate is usually related to the ^{226}Ra content of a material, which is obtained by γ spectrometry, it must be measured independently since in most cases emanation is dominated by surface impurities. The measurements were performed according to the procedure described in [218] using the ^{222}Rn emanation facilities. To remove radioactive isotopes from surfaces, all TPC components were cleaned after production according to the dedicated procedures for each material type.

The TPC was assembled above ground at LNGS, inside a custom-designed cleanroom with a controlled particle concentration, using a movable transport frame. The double-bagged TPC (aluminized mylar), fixed to the transportation frame, was moved to the underground laboratory by truck and attached to the top flange of the inner cryostat, where a mobile soft-wall cleanroom was erected for this purpose.

Krypton distillation Natural krypton, which contains the β-decaying isotope ^{85}Kr ($T_{1/2} = 10.76\,\mathrm{y}$) is removed by cryogenic distillation, exploiting the 10.8 times larger vapor pressure of Kr compared to Xe at $-96\,^{\circ}\mathrm{C}$. In a cryogenic distillation column, the more volatile Kr will hence be collected at the top while Kr-depleted xenon will be collected at the bottom. Given a ^{nat}Kr/Xe concentration of $< 0.02\,\mathrm{ppm}$ in commercial high-purity Xe gas, a Kr reduction factor around 10^5 is required to reach the design goal of ^{nat}Kr/Xe$< 0.2\,\mathrm{ppt}$. To achieve this goal, a distillation column 2.8 m tall was built following ultra-high vacuum standards. The total height of the XENON1T distillation system is 5.5 m [219].

The Kr particle flux inside the column and the separation efficiency can be monitored using the short-lived isotope ^{83m}Kr as a tracer [220]. After installation at LNGS, a separation factor of $(6.4^{+1.9}_{-1.4}) \times 10^5$ was measured [219], reaching a concentration $^{nat}\mathrm{Kr/Xe} < 0.026\,\mathrm{ppt}$ and demonstrating that the system fulfills the requirements for XENON1T and for the future XENONnT. Such low concentrations are measured with a gas chromatography system coupled to a mass spectrometer (rare gas mass spectrometer, RGMS [221]). To allow for data acquisition with a fully operational dual-phase TPC while at the same time reducing the Kr concentration, the XENON1T collaboration has successfully established the online removal of Kr. After continuously operating in this mode for 70 days, with an initial measured ^{nat}Kr/Xe concentration of 60 ppb, a final concentration of 0.36 ± 0.06 ppt was measured by RGMS. This concentration is the lowest ever achieved in a LXe dark matter experiment. The average concentra-

tion during the first two XENON1T science runs is measured in 0.66 ± 0.11 ppt (see section 3.1.2).

Finally, the possibility for online removal of Rn was demonstrated by installing a shortened (1 m package material) version of the final cryogenic distillation column in reverse and lossless mode on XENON100. A radon reduction factor of > 27 (at 95% CL) was achieved [222]. Such operation has been shortly tested also in XENON1T (see section 3.1.2) and will be fully exploited for the XENONnT experiment.

2.2.4 Muon Veto

The Muon Veto system, built under the direct responsibility of the Bologna research group, consists of a tank of 9.6 m diameter and 10.2 m height filled with deionized water with a residual conductivity of 0.07 µs/cm. Operated as a Cherenkov detector, the water tank is instrumented with 84 PMTs of 20.3 cm in diameter with a bialkali photocathode on a borosilicate window (see figure 2.6a for an internal view of the tank and MV PMTs disposition). The quantum efficiency is $\sim$ 30% for wavelengths between 300 nm and 600 nm, and the mean gain is 6×10^6 for a bias voltage of 1500 V. The PMTs operate with a threshold that allows for the detection of single photoelectrons with $\sim$ 50% efficiency.

After optimization in a Monte Carlo study [213], the PMTs were deployed in five rings at the circumference of the water shield at different heights. The bottom ($z = 0$ m) and top ($z = 10$ m) rings consist of 24 evenly spaced PMTs, while only 12 PMTs are installed in the three rings at $z = 2.5$ m, $z = 5.0$ m, and $z = 7.5$ m height. To further enhance the photon detection efficiency, the inner surface of the water tank was cladded with reflective foil featuring a reflectivity of $> 99\%$ at wavelengths between 400 nm and 1000 nm [223]. In addition, a small fraction of $\sim$ 7.5% of the ultraviolet Cherenkov photons are shifted towards longer wavelengths in the reflection process thereby they better match the PMT sensitivity.

Each PMT is calibrated by illumination with blue LED light through a plastic fiber. The response of the full system can be also measured by light emitted from four diffuser balls mounted on the cryostat support frame.

The MV trigger operated for the XENON1T science runs demands the coincidence of 8 PMTs above a threshold of 1 PE within 300 ns. The measured trigger rate of 0.35 Hz corresponds to 144 muons/h and agrees with the expectations. The muon detection efficiency under these trigger conditions is obtained by means of a Monte Carlo simulation, taking into account all relevant signal creation and detection aspects (see section 3.2.1 for more details). Using the characteristics emission of Cherenkov light, the distribution of the signal arrival times on the 84 PMTs can be used to reconstruct the muon track through the water (see figure 2.9).

The distribution of time differences Δt between TPC events and their closest Muon Veto trigger during science runs shows a clear peak at $\Delta t < 1$ µs on top of accidental background. The peak population originates from muon-induced coincidence events

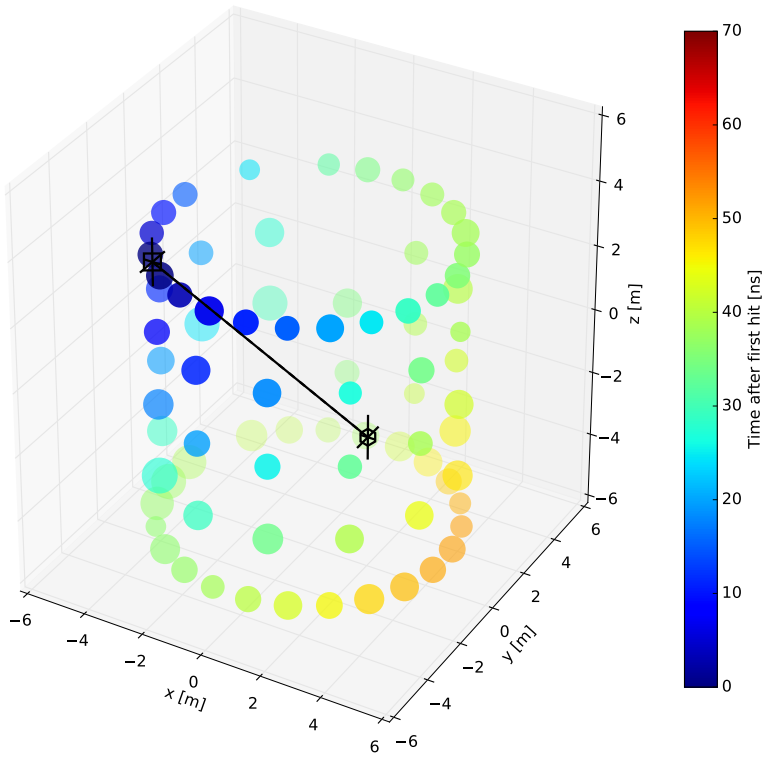

Figure 2.9: The arrival time information of light in the PMTs of the Muon Veto detector (color coded points) allows the approximate reconstruction of the muon track (black line) through the water shield. This example shows an event where the muon traversed the shield close to the TPC.

in the two detectors and can be vetoed with a simple time coincidence cut (see section 3.2.1). Since the muon veto trigger rate is small, the rate of accidental coincidences between the two systems ($R_{MV} = 0.35\,Hz$, $R_{TPC} \sim 5\,Hz$) is small during a dark matter run. This leads to a negligible loss ($\sim 0.04\%$) of live time even if only the Muon Veto trigger information is used to reject TPC events, without further analysis of the digitized Muon Veto PMT data.

2.2.5 Calibration systems

Calibrating and characterizing the detector response is crucial for any experiment. For XENON1T the main calibration systems are developed to study and monitor the PMTs functioning (LED source), to calibrate the spatial dependency of observable signals (^{83m}Kr source) and to model the response to physical interactions of NR (neutron sources) and ER (^{220}Rn) type (see section 3.3.3).

LED The PMT gains are calibrated by stimulating the emission of single photoelectrons from the photocathode by means of low-level light pulses from a blue LED. A total of four LEDs are simultaneously controlled by a 4-channel pulse generator. The

light is guided into the cryostat via four optical fibers. Bakeable synthetic silica fibers (600 µm) transfer the light to the cryostat. To reach uniform illumination of all PMTs and to minimize the calibration time, each of the silica fibers is split into six thin plastic fibers (250 µm) that feed the light into the TPC at various angular positions and heights around the field cage. A periodic external signal triggers the pulser and the TPC DAQ system. The LED calibration procedure is the only measurement which is not self-triggered.

Krypton-83m Due to the excellent self-shielding efficiency of LXe, the central target can only be calibrated with low-energy single scatter ERs from dissolved sources. XENON1T uses ^{83m}Kr ($T_{1/2} = 1.8\,\mathrm{h}$), the short-lived daughter of ^{83}Rb, which delivers mono-energetic conversion electron lines at 32.1 keV and 9.4 keV [224, 225]. The ^{83}Rb source is installed in the purification system to release the ^{83m}Kr into the TPC when required. While the noble gas Kr mixes very well with Xe, it was shown that no long-lived ^{83}Rb is emitted [226]. The uniformity and high intensity of the ^{83m}Kr source is ideal for spatial calibrations of the detector (see section 4.1).

Radon-220 The intrinsic source of the noble gas isotope ^{220}Rn ($T_{1/2} = 56\,\mathrm{s}$) is exploited to calibrate for low energy ERs. It is efficiently emanated by an electro-deposited ^{228}Th source ($T_{1/2} = 1.9\,\mathrm{y}$). The ^{220}Rn decay chain produces α, β and γ particles that are all useful for detector calibration [227], as demonstrated in XENON100 [228]. The β-decay of ^{212}Pb (12.3% branching ratio to the ground state, Q = 570 keV) delivers single scatter ERs in the dark matter region of interest. Due to the rather short half-life $T_{1/2} = 10.6\,\mathrm{h}$ of ^{212}Pb, which dominates the chain, the activity is reduced by a factor 6×10^4 within one week.

NR calibrations Neutrons with energies around 2.2 and 2.7 MeV from a Deuterium-Deuterium (DD) fusion neutron generator [229] are used to calibrate the detector response to NRs. By setting the generator voltage and current, the neutron flux can be tuned to the desired value. The generator was modified to achieve very low emission rates, around 10 neutrons per second in 4π under stable conditions, as required for reducing the rate of pile-up events. The generator can be displaced into three positions around the cryostat (see figure 2.6b), to achieve a uniform illumination of the target.

An external ^{241}AmBe source is also used to calibrate the NR response. It is installed in a collimator that can be deployed by means of belts from the top of the water shield to the cryostat. Two belts ("I-belt", blue in figure 2.6b) allow for moving the source vertically at two angular positions. Another belt ("U-belt", red) crosses below the cryostat at $\sim 20\,\mathrm{cm}$ distance from the central point. Such system is also used for γ sources (^{228}Th and ^{137}Cs) for external gammas calibration. The collimators, which are stored above the water level when dark matter data are acquired, constrain the particles to a cone with 40°-wide opening. This illuminates a central $\sim 1\,\mathrm{t}$ fiducial volume when located at half height of the TPC.

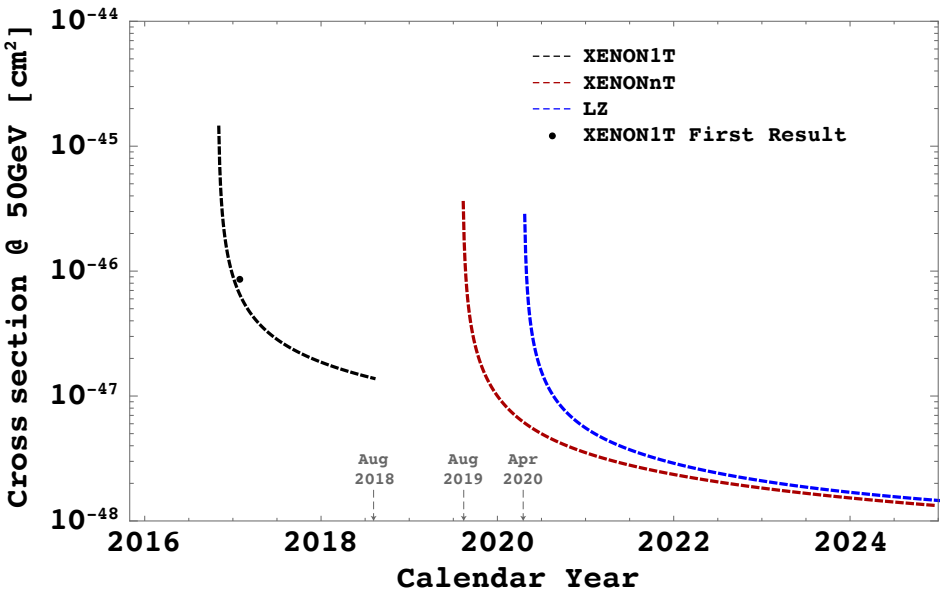

Figure 2.10: A comparison, as function of calendar year, of the projected sensitivity to spin-independent WIMP-nucleon interactions for a 50 GeV/c^2 WIMP for XENON1T (1 tonne fiducial mass), XENONnT (4 tonnes fiducial mass), and LZ (5.6 tonnes fiducial mass). Curves in this plot have been calculated using the official values that each experiment has estimated for WIMP energy range, NR acceptance, ER rejection and background. The black dot indicates the upper limit obtained in the analysis of the first XENON1T science run [108].

2.3 The XENONnT upgrade

XENON1T has been built with the capability to rapidly increase its sensitive target while further reducing the background from intrinsic sources. With XENON1T working as designed, the XENON Collaboration will pursue the detector upgrade called XENONnT, with a foreseen start by mid-2019. The new XENONnT inner detector will be placed in the same water shield and serviced by the same systems and infrastructure. The increased target mass, together with a further reduction of the intrinsic background, mainly achieved by careful material selection, active Rn-removal, improved detector/veto design and more efficient self-shielding, will allow an order of magnitude improvement in sensitivity, expanding the physics reach and discovery potential of the XENON program (see figure 2.10).

The XENON1T detector support structure was built for a heavier TPC to be placed in the same cryostat, replacing just the inner vessel. Similarly, the xenon cryogenics and purification systems as well as the recovery system were designed to handle a target mass scale-up to about 8 tonnes. Leveraging on these existing systems and overall infrastructure, thoroughly tested during XENON1T commissioning and operation, will allow for a fast upgrade to the new detector with 8 tonnes of LXe of which 6.0 tonnes are active. The design of the new detector will follow closely that of the current one,

with a modest ∼40% scale-up in diameter and drift length.

A few new systems will be installed to enable the handling and purification of the larger Xe mass and to achieve the required background reduction compared to XENON1T. The first one is an online radon removal system. The existing cryogenic distillation column built for XENON1T will reduce the ^{85}Kr background to the required level [219]. A new Rn removal tower relies on the same cryogenic distillation principle as for removing the krypton from xenon, but in a "reverse mode". The achievable reduction in the Rn concentration due to sources inside the cryostat depends essentially only on the purification cycle time with respect to the Rn lifetime, that is, on being able to remove the Rn faster than it can decay. It is therefore highly beneficial to have an online Rn removal system installed on a fast purification loop such as that of the cryogenic LXe purification system.

An additional storage system for the large amount of xenon used in XENONnT will be exploited. It will improve the safe handling of the xenon gas and increase the flexibility during detector operation. A new purification facility which works on the liquid phase will also be operated.

In addition, a veto detector to tag neutrons which first scatter inside the TPC, leaving a single scatter nuclear recoil signal, will be part of the upgrade. It will be realized doping with Gd-sulphate the 700 t of water in the outer shield. Neutrons, once exiting the cryostat, will be effectively captured on Gd and produce a gamma cascade of about 8 MeV in total. The Cherenkov light generated after neutron capture will be detected with 120 additional PMTs, same model of the ones used in the Muon Veto, but with higher quantum efficiency and reduced radioactivity, installed about 1 m far away from the cryostat and inside a newly built reflector.

The fast upgrade to XENONnT will enable the XENON program to lead the direct detection field in the next few years with a sensitivity to dark matter cross sections down to 10^{-48} cm^2 [135]. Figure 2.10 shows, as function of calendar year, the projected sensitivities to spin-independent WIMP-nucleon interactions for a 50 GeV/c^2 WIMP of XENONnT and the competitor Xe-based TPC LZ [230]. The time scale assumes an 80% livetime fraction for all experiments. The projected sensitivity is estimated for all experiments using Feldman-Cousins statistics.

The dominant background is expected to come from the internal sources ^{85}Kr and ^{222}Rn, as in XENON1T (see section 3.1). A measured radon level of $\sim$ 10 µBq/kg is achieved in XENON1T (see section 3.1.2). For XENONnT, levels of ^{222}Rn and ^{85}Kr ten times smaller than in XENON1T are required, namely 1 µBq/kg ^{222}Rn and 0.02 ppt of ^{nat}Kr/Xe. The ^{222}Rn requirements will be achieved by the online radon reduction technique, and by improving the cleanroom used for the TPC assembly, to reduce contributions from particulates. As far as ^{85}Kr is concerned, operation of the XENON1T distillation column has already demonstrated its capability to efficiently reduce krypton down to ^{nat}Kr/Xe$\leq$ 48 ppq at 90% confidence level [219]. Thanks to the neutron veto, the number of background events from neutrons will be reduced to about 1 event in the whole 20 t·y exposure.

Chapter 3

Electronic and nuclear recoil backgrounds in XENON1T

In the search for extremely rare events, crucial factors are how big can you make your target for particle interactions and how silent is your detector in order to recognize few signals over the events from known physics. We described how the background in XENON1T is reduced to the required level for a DM direct detection experiment in section 2.2.3. As important as the actual background level reached is how well you know your backgrounds, since their characterization allows the best disentanglement from DM signals pushing the sensitivity of the experiment. In XENON1T we distinguish two main categories of background: *electronic recoils* (ERs) mainly due to gamma and beta particles from radioactive decays, described in section 3.1, and *nuclear recoils* (NRs) dominated by neutron interactions, discussed in section 3.2. WIMPs are expected to scatter on nucleons, thus generating signals of NR type. Electronic interactions can be discriminated from NR with typical rejection efficiencies larger than 99% at 50% NR acceptance, as obtained in XENON100 [231]. However, given the high rate compared to other backgrounds, ERs still represent the largest background for XENON1T, with an average ER leakage fraction of about 0.3% in the NR region, below the NR median.

The study of backgrounds begins before the experiment is actually built, with Monte Carlo (MC) simulations that assess the prediction on the expected background rates and relevant distributions. The XENON simulation working group is conducted by the Bologna group, which is responsible for the XENON1T MC background studies. Each source of ER background for XENON1T is simulated and predicted rates and spectra are presented in section 3.1.1. As the detector starts operations, real data are available to provide constraints on some individual background sources and on overall properties. Measurements of the ER background level and the comparison with MC predictions are discussed in section 3.1.2. The XENON1T experiment demonstrates the lowest ER background rate ever achieved in Xe-based DM detectors (see figure 3.1).

Neutron interactions or *coherent elastic neutrino-nucleus scatterings* (CNNS or CEνNS) produce NRs which exactly mimic WIMP recoils. DM-nucleon cross section

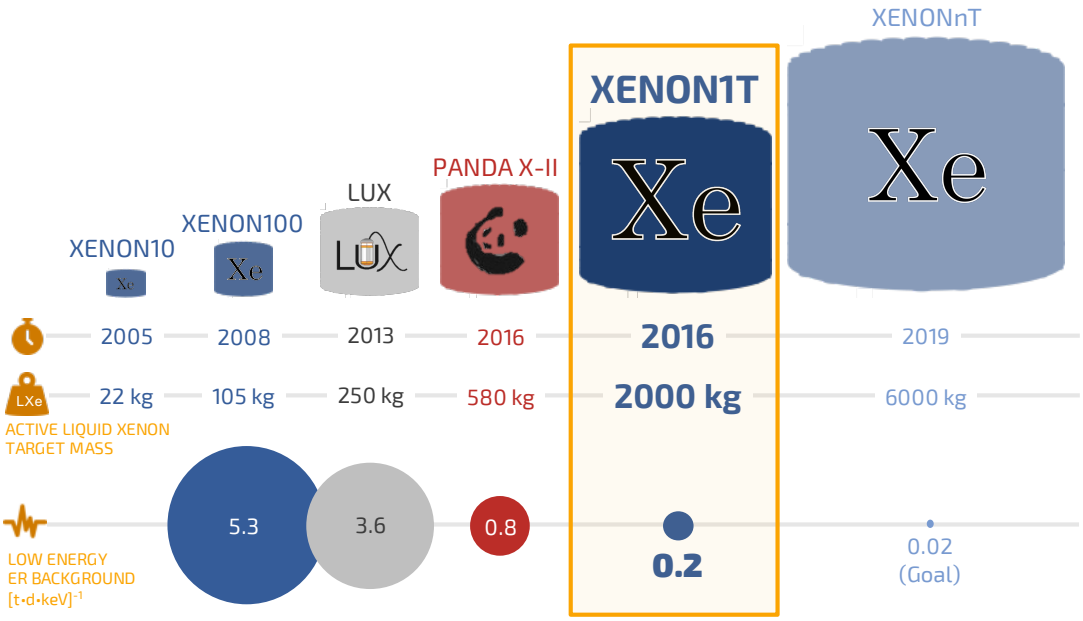

Figure 3.1: Evolution of LXe-based dark matter detectors. The experiments of the XENON DM Project are illustrated along with the current detectors of LUX and PANDA-X collaborations, also using xenon dual-phase TPCs. The time-line and the LXe active target mass used are shown. In the last row, the evolution in terms of ER background rate at low energy (in the WIMP search range, approximately (1, 12) keV) is sketched for XENON100 [105], LUX [232], PandaX-II [111] and XENON1T [109] along with the goal of XENONnT. Improved techniques to reduce external sources and intrinsic contaminants allowed to lower such background, which is the predominant one for this class of experiments. XENON1T proved a remarkable step forward in ER background reduction achieving the best ever rate of 0.2 events per tonne-day-keV (see section 3.1.2 for more details on this result). With the XENONnT experiment, we aim at a reduction of ^{222}Rn contamination by a factor 10 to further knock down the ER background.

is so low that at most one single scatter, if any, is expected in the target volume. The same consideration holds for CNNS (section 3.2.2), while neutrons can scatter multiple times inside the XENON1T fiducial volume, due to the $\sim$ 10 cm mean free path of typical MeV radiogenic neutrons emitted from detector materials. Only neutron single scatters contribute to background, but the predicted rate due to radiogenic neutrons is much higher with respect to CNNS, as resulting from MC simulations (see section 3.2.3). However, the neutron background rate is kept so low that its expectation value is typically less than 1 event in direct detection experiments (depending on the fiducial mass choice and exposure), which implies that direct measurement of such background is extremely unlikely. For the WIMP search with XENON1T presented in this work, the NR background has been constrained by actual measurements of neutron interactions: the observation of multiple NR scatters in the TPC is used to set a constraint on the expected single scatter rate based on the multiple-to-single scatter ratio estimated from MC simulations and calibration data (see section 3.2.5). Moreover, the simulations of NR background has been extended to include a class of events referred

to as *neutron-X*. These are events with an energy deposition in the partially sensitive LXe region below the cathode in addition to a standard single scatter inside the fiducial volume (see section 3.2.4). The neutron-X component introduces a distortion to the standard NR background model in a region restricted to the very bottom of the TPC volume. The full study and simulation of neutron-X in XENON1T is motivated by the improved modelling of all the backgrounds, extended also to spatial coordinates with the respect to previous XENON data analyses. This allows to utilize a larger fiducial volume and to improve the sensitivity despite getting more background events (whose overall distribution is peaked at the TPC edges). The XENON1T analysis presented in this work utilizes a fiducial volume extending down to 2.9 cm above the cathode, including therefore a region where the neutron-X distortion becomes appreciable.

Having characterized and studied the expected background rates, their spatial distributions and their energy spectra, the last step towards the final background prediction requires the accurate modelling of the detector response to both ER and NR, which is needed to convert recoil energies into S1 and S2 signals observable in real data (section 3.3). The response model includes the LXe microphysics (section 3.3.1), which describes how xenon reacts to ER and NR in terms of emitted light and charge, and the detector properties (section 3.3.2), where the efficiencies in photons and electrons propagation, signals generation and reconstruction are taken into account. Finally, the response model is fitted to ER and NR calibration data (section 3.3.3) in order to characterize the so-called ER and NR *bands*, i.e. the distributions of the two interaction types in the observable (S1, S2) space for the low energy range of interest for WIMP search. The ER and NR background models produced by convoluting the expected recoil spectra with the XENON1T signal response model are presented in section 3.4.

3.1 Electronic recoil background

Despite the world-leading ultra-low ER rate achieved with XENON1T (see section 3.1.2), electronic recoils are still one of the main background sources for WIMP search. The region of interest (ROI) to look for WIMP signals is typically below 100 photoelectrons (PE) of S1 signal size, where the spectrum of even high mass WIMPs ($\mathcal{O}(\mathrm{TeV/c^2})$) is almost entirely contained. The corresponding electronic recoil energy is less than $\sim$10 keV, meaning that only low energetic ERs, that are not accompanied by other interactions inside the fiducial volume, contribute to background.

One source of electronic recoils below $\sim$10 keV can be *X-ray photons* via photoelectric interaction. External sources of X-rays cannot lead to a background as they penetrate $\mathcal{O}(10\,\mu\mathrm{m})$ in LXe. X-rays can be produced by radioactive contaminants in the xenon itself that undergo electron capture, such as ^{127}Xe which is cosmogenically activated. However, this background is negligible for a xenon inventory stored underground for several months or years, like the one used in XENON1T, since ^{127}Xe has a 36 days half-life.

High energy γ*-rays* ($\mathcal{O}$(MeV)) emitted by radioactive contaminants in detector con-

struction materials surrounding the active LXe volume can produce low energy ERs via Compton scattering. If they escape the detector after only one Compton scatter, without depositing their entire energy, external γs can therefore contribute to the ER background. Such a background was dominant in XENON10 and XENON100, while the $<$10 cm penetration depth of MeV γ-rays in LXe [233] is small compared to the much bigger XENON1T TPC size. Hence, the external ER background is negligible in the inner core of the TPC and can be easily controlled by volume fiducialization (as described in section 3.1.1).

Another external source of ER background are solar *neutrino scatterings off electrons* of xenon atoms, which cause single low energy recoils given the weak cross section of neutrino processes. Contrary to external gamma sources, neutrinos yield a diffused background uniformly distributed in the TPC.

The neutrino contribution is subdominant with respect to diffused backgrounds due to intrinsic radioactive contaminations of xenon. The dangerous events originated inside the TPC are *β decays*, which produce the same signal as an electron recoil even if the moving electron is not produced by an actual collision. Beta decays of heavy elements, such as the typical residual contaminants of ultra-pure xenon (described in section 3.1.1), give rise to an almost flat spectrum below $\sim$10 keV as a consequence of their high kinematic endpoint energies. Intrinsic ER background, due to ^{136}Xe but mainly to ^{222}Rn and ^{85}Kr contaminations, is the dominant one for XENON1T. Since volume fiducialization is not effective in this case, it can only be fought with purification (distillation) efforts and by minimizing the emanation of contaminants into the xenon reservoir.

A detailed description of each contributor is given in the following section along with the study of the expected ER background in XENON1T from MC simulations. The observed background level and constraints on the specific contribution of ^{222}Rn and ^{85}Kr contaminants based on collected data are discussed in section 3.1.2.

3.1.1 Predictions from MC simulations

Every potential source of ER background has been studied before the installation of the XENON1T detector by an accurate GEANT4 [234] simulation of the detector itself (details of the GEANT4 XENON1T detector model are described in [135]) and of the physical processes involved. Recoil energies are converted into observable S1 and S2 signals based on a detector response model, taking into account the LXe emission model and detector optical properties, analogous to the final model fitted to real data (described in section 3.3). The level of radioactive contaminants present in the various detector components is taken from the results of a dedicated screening measurements campaign [212]. Assumptions are made to fix the concentration of intrinsic contaminants of xenon to perform the background simulations presented in this section. They are finally rescaled after the control measurements carried out during data taking operations to get the complete description of the ER background in XENON1T. The energy

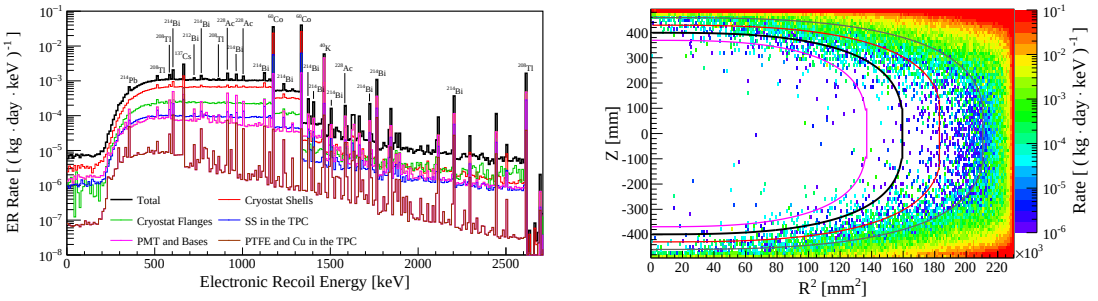

(a) **(b)**

Figure 3.2: Electronic recoil background originated from detector materials radioactivity: (a) recoil energy spectrum induced by different detector components; (b) position distribution of events inside the active volume, in the (1, 12) keV energy range. Solid lines delimit increasing super-ellipsoid fiducial volumes containing 800, 1000, 1250, 1530 kg LXe mass.

range considered is (1, 12) keV which approximately corresponds to the ROI in the S1 space of (3, 70) PE (while the ROI corresponds to (4, 50) keV for NR interactions due to the different light and charge yields).

Detector materials radioactivity The selection of each component used in the experiment is based on an extensive radiation screening campaign [212], using a variety of complementary techniques (see section 2.2.3) and dedicated measurements: Germanium (Ge) detectors and mass spectrometry techniques. For the gamma spectrometry with Ge, XENON has access to the most sensitive screening facilities: the Gator [215] and GeMPIs [217] detectors, placed underground at LNGS, and GIOVE [216] in Heidelberg. Ge detectors are sensitive to most of the dangerous radiogenic nuclides: ^{40}K, ^{60}Co, ^{137}Cs, those in the ^{232}Th chain and in the second part of the ^{238}U chain, ^{226}Ra and its daughters.

Based on the matrix of contamination level of detector materials from each of the radioactive isotopes, decays of such nuclides are simulated confined uniformly inside all components, such as stainless steel (SS) making up the inner cryostat and electrode rings, PTFE and copper of TPC, and the various parts of PMTs. The energy spectrum of background events in 1 tonne fiducial volume is shown in figure 3.2a. It is almost flat below 200 keV, due to Compton scatters, while at higher energies the various photoabsorption peaks of different lines are visible: 1460 keV from ^{40}K, 1173 and 1333 keV from ^{60}Co, 662 keV from ^{137}Cs, the 352, 609, 1120, 1765, 2204 keV lines from ^{238}U chain and the 583, 911, 969, 2615 keV lines from ^{232}Th chain.

The total background rate from materials in the (1, 12) keV energy range and in 1 tonne fiducial volume is $2.7 \pm 0.3\,(\mathrm{t \cdot y \cdot keV})^{-1}$. The uncertainty is obtained as a convolution of the one in measurements of the material contamination, the statistical uncertainty of the simulated MC samples and an additional 10% systematics to consider the potential differences in modelling the actual geometry of detector in slightly different

hypothesized configurations before the final design. The highest contribution of 61% is due to the SS shells and flanges of cryostat, particularly from the ^{60}Co contamination. PMTs contribute to 23%, SS components inside the TPC to 15%, while the contribution from PTFE and copper parts is just ∼1 %. This background is mainly confined to the top, bottom and lateral TPC edges as shown in figure 3.2b, while the inner core is protected thanks to the high self-shielding efficiency of xenon.

Radon-222 decay chain ^{222}Rn can emanate from the detector materials, or diffuse through the seals. Due to its relatively long half-life (3.8 days), it can diffuse in the LXe volume almost homogeneously. Considering its daughters, down to the long lived ^{210}Pb, the contribution to low-energy ERs comes from the β decay of ^{214}Pb onto the ground state of ^{214}Bi, with end-point at 1023 keV, where no other radiation is emitted. However, especially if the decay occurs close to the borders of the active region, decays on other energy levels are also potentially dangerous, since there is a finite probability that the accompanying gamma exits the detector without depositing energy and being detected. This is responsible for the slightly higher background rate from ^{222}Rn seen at larger fiducial masses in figure 3.3b.

The only other beta emitter in the chain (^{214}Bi), also potentially dangerous, can be easily removed looking at the time correlation with the α decay of its daughter, ^{214}Po, which occurs with a half-life of 164 µs. The isotope ^{220}Rn can also be emanated from detector materials, being a noble gas, but due to its 56 s short half-life the probability to diffuse in the active LXe volume is much lower than ^{222}Rn. A conservative assumption of a ^{220}Rn concentration of 0.1 µBq/kg still leads to a negligible background induced by its daughters.

Early measurements of radon emanation [235, 236] of materials in close contact with LXe (TPC and pipes), to be used for XENON1T, provided an estimation of ^{222}Rn contamination at about 10 µBq/kg, which is the value assumed in the MC simulations. The resulting ER background rate in the ROI and in 1 tonne fiducial mass amounts to $56 \pm 5\,(\mathrm{t \cdot y \cdot keV})^{-1}$, about 20 times larger than the contribution from external gammas. A 10% systematic uncertainty accounts for the uncertainties in the branching ratios of ^{214}Pb to the ground state.

Krypton-85 Commercially available xenon is contaminated by krypton with typical ^{nat}Kr/Xe concentrations of $\mathcal{O}$(ppm) as it is extracted from atmosphere. Natural krypton contains traces of the radioactive isotope ^{85}Kr, which is a product of nuclear fission and it is released in atmosphere mainly by nuclear fuel reprocessing plants. Its relative isotopic abundance in Europe has been determined by low level counting to be 2×10^{-11} [237]. ^{85}Kr is a beta emitter with half-life of 10.76 y and an end-point energy of 687 keV.

During XENON100 operations, a ^{nat}Kr/Xe concentration of (19 ± 4) ppt [mol/mol] has been achieved processing the gas through cryogenic distillation [231]. For XENON1T, thanks to a new high through-put and high separation cryogenic distillation column [219] (see section 2.2.3), the goal was set to a reduction of two orders of

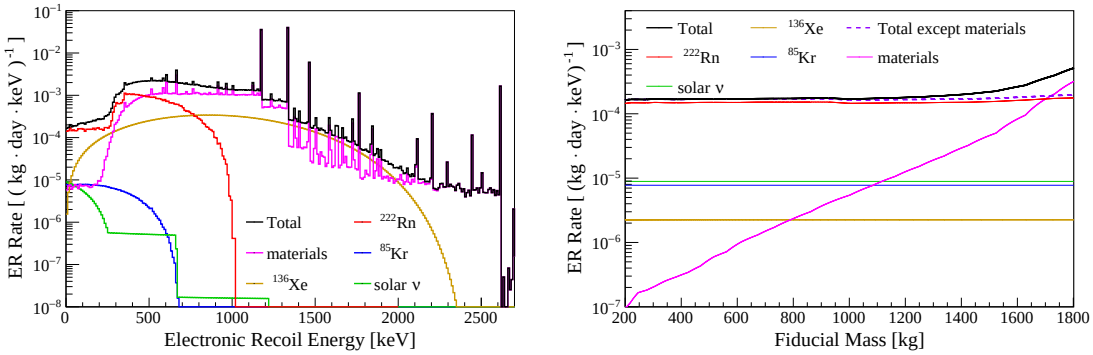

(a) **(b)**

Figure 3.3: Total ER background (black line), together with the separate contributions: detector materials (purple), 10 µBq/kg of ^{222}Rn (red), 0.2 ppt of ^{85}Kr (blue), solar neutrinos (green) and ^{136}Xe double-beta decay (brown). On the left, the recoil energy spectrum up to few MeV. The plot on the right shows ER background rate as a function of the fiducial mass contained in progressively larger super-ellipsoid fiducial volumes.

magnitudes. Simulations of background induced by ^{85}Kr shown in figure 3.3 assume 0.2 ppt of ^{nat}Kr/Xe. The resulting rate in the ROI is $2.8 \pm 0.5\,(\mathrm{t \cdot y \cdot keV})^{-1}$, similar to the ER background from materials in the 1 tonne fiducial mass selection. The 20% uncertainty is mainly due to the uncertainty in the shape of the beta spectrum at low energies [238].

Xenon-136 double-beta decay Natural xenon contains 8.9% of ^{136}Xe which is a double-beta emitter with Q-value 2458 keV and half-life of 2.17×10^{21} y [239]. The double-beta decay spectrum, shown in figure 3.3a (brown line), is obtained through the DECAY0 code [240]. The average background rate in the energy region (1, 12) keV is $0.8 \pm 0.1\,(\mathrm{t \cdot y \cdot keV})^{-1}$. Based on the current accuracy in the knowledge of the low energy part of the ^{136}Xe double-beta spectrum [241], such background estimate comes with a 15% rate uncertainty.

Solar neutrinos Solar neutrinos from all the nuclear reactions in the Sun [242,243] are considered, taking into account neutrino oscillation $\nu_e \rightarrow \nu_{\mu,\tau}$ with survival probability of electron neutrinos of $P_{ee} = 0.55$ [244] and the reduced cross section for $\nu_{\mu,\tau}$. Neutrinos from *pp* reaction contribute to 92%, ^{7}Be to 7%, *pep* and all the others sources with less than 1%. The average background rate in the ROI amounts to $3.25 \pm 0.07\,(\mathrm{t \cdot y \cdot keV})^{-1}$, close to the level of ERs from materials and ^{85}Kr. An uncertainty of 2% is quoted, as the result from combining ∼1 % error in the *pp* neutrino flux and ∼10 % from ^{7}Be [242], plus ∼2 % uncertainty in the oscillation parameters [244]. Neutrinos easily pass through the Gran Sasso mountain, hence the induced background is expected to be uniformly distributed in the sensitive volume given their very long penetration depth.

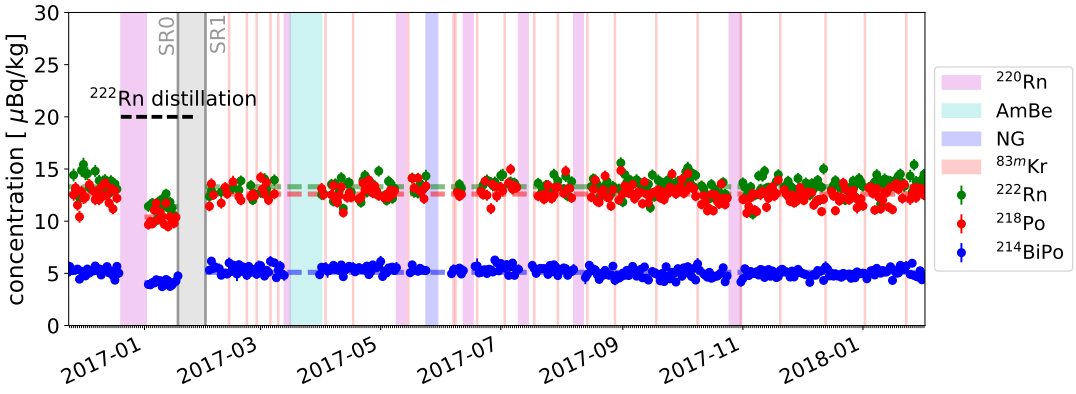

Figure 3.4: The measured concentration of ^{222}Rn and ^{218}Po α decays and of ^{214}BiPo delayed coincidences of β followed by an α decay. Rates are monitored on a daily basis over the XENON1T first and second science runs, with the exception of days dedicated to ^{220}Rn and neutron calibration (AmBe and NG) runs indicated with colored areas, as well as ^{83m}Kr calibrations. During radon distillation, measured concentrations of all the three isotopes lowered by ∼20 %. After distillation the rates went back to the nominal values. ^{218}Po and ^{214}BiPo concentrations give an upper and lower limit on ^{214}Pb activity (the β-emitter responsible for the highest contribution to low energy ER background).

3.1.2 Background measurements and matching with simulations

The Monte Carlo simulations of the expected ER background in XENON1T rely on assumptions made about the concentration of intrinsic contaminants ^{222}Rn and ^{nat}Kr in the xenon reservoir. With the detector in operation, in-situ measurements of such concentrations are available to estimate the actual purity level achieved. The related background predictions can be then accordingly adjusted to get the complete description of the ER background we have in XENON1T. Moreover, the final rates expected from each contributor, presented in table 3.1, adopt the 1.3 tonnes fiducial volume choice (described in section 4.3) made for the WIMP search, based on sensitivity optimization with the final models of each background component in the signal and spatial spaces.

Radon-222 decay chain The relevant concentration for ER background studies is the one of ^{214}Pb in the fiducial volume. Alpha decays occurring in the ^{222}Rn can be easily tagged in data analysis given their clear signature at high energy ($\mathcal{O}$(MeV)) and their relatively high rate. This provides a way to estimate the activity of the decay chain from which the ^{214}Pb concentration can be constrained. In particular, we can monitor the rate of α decays of ^{222}Rn (5.5 MeV) and its daughter ^{218}Po (6.0 MeV), and the delayed coincidence of ^{214}Bi (β decay) and ^{214}Po (7.7 MeV α). The β emission of ^{214}Pb occurs in between ^{218}Po and ^{214}BiPo decays, whose rates provide an upper and lower limit respectively on the ^{214}Pb activity. The reason why the two rates can differ is that daughter isotopes can stay positively charged after the parent decay and they can consequently be pulled out the fiducial volume by the TPC electric field.

The activities measured day-by-day during the two science runs (SR0 and SR1) of

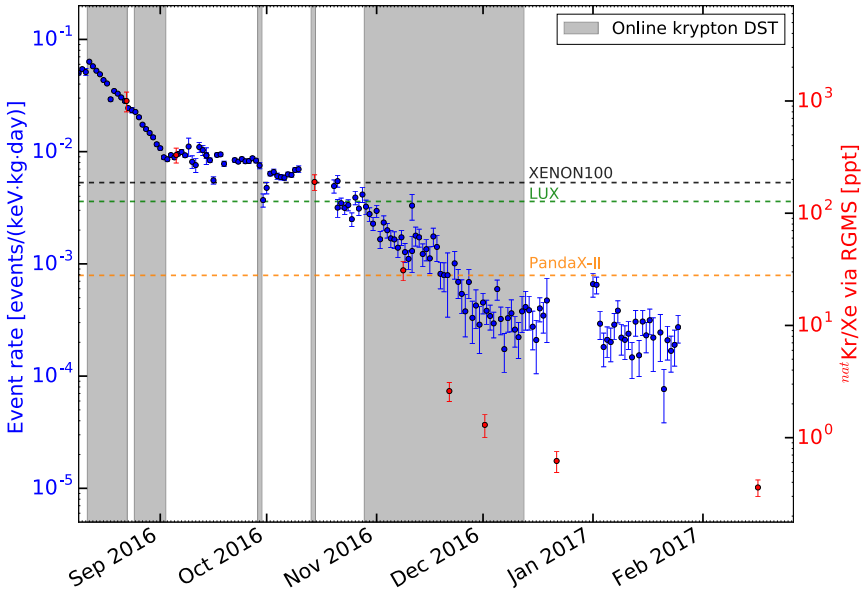

Figure 3.5: The evolution rate of low energy ER background events, in the energy range (0, 200) keV inside 1 tonne fiducial volume is shown from the first XENON1T commissioning operations to the end of SR0. RGMS measurements of ^{nat}Kr/Xe concentration are shown in red. The gray bands identify operation times of the cryogenic krypton distillation system. Horizontal dashed lines mark the background level of the most competitive Xe-based DM detectors: XENON100 [105] (black), LUX [232] (green) and PandaX-II [111] (orange). By the end of 2016 (corresponding to the begin of the first DM search run), ^{85}Kr concentration was reduced to a subdominant contribution to the ER background, dominated by ^{214}Pb β decays thereafter.

XENON1T are shown in figure 3.4. The rates of ^{222}Rn, ^{218}Po and ^{214}BiPo are found stable (within 10%) over SR0 and SR1, with a decrease by ∼20 % observed at the time when the krypton cryogenic distillation column was operated in reverse mode to remove radon. Excluding the radon distillation period (a small fraction of the complete exposure of SR0+SR1), the observed concentrations are: 13.3 ± 0.8 µBq/kg (^{222}Rn), 12.6 ± 0.8 µBq/kg (^{218}Po) and 5.1 ± 0.5 µBq/kg (^{214}BiPo). The assumption of 10 µBq/kg as ^{214}Pb concentration (yielding a $56 \pm 5\,(\mathrm{t \cdot y \cdot keV})^{-1}$ background rate) is then well inside the upper and lower limits, which implies a background rate between 71 ± 8 and $29 \pm 4\,(\mathrm{t \cdot y \cdot keV})^{-1}$, where uncertainties are the combination of statistical ones from data analysis and 10% systematics from simulations (mentioned in the previous section).

Krypton-85 The concentration of natural krypton ^{nat}Kr/Xe has been reduced through cryogenic distillation [219] by more than three orders of magnitude since the XENON1T commissioning, reaching a minimum value of 0.36 ± 0.06 ppt in the end of SR0 [108]. Rare-gas mass spectrometry (RGMS) [221] measurements on samples extracted from the detector allow a regular monitoring. Figure 3.5 shows the RGMS measurements overlaid with the low energy ER background rate evolution. The latter exactly follows the ^{nat}Kr/Xe drop in coincidence with periods when the cryogenic dis-

Background component	Rate $[(\mathrm{t}\cdot\mathrm{y}\cdot\mathrm{keV})^{-1}]$	Relative contribution [%]
^{214}Pb	56 ± 6	75%
^{85}Kr	7.7 ± 1.3	10%
Detector materials	8 ± 1	11%
Solar ν	2.5 ± 0.1	3%
^{136}Xe $2\nu\beta\beta$	0.8 ± 0.1	1%
Total (MC prediction)	75 ± 6	
Total (measured)	82^{+5}_{-3} (sys) ± 3 (stat)	

Table 3.1: The XENON1T ER background rates in the low energy region (1, 12) keV of interest for WIMP search and inside the 1.3 t fiducial volume. The contribution from each component is estimated through MC simulations. Collected XENON1T data provide constraints on the ^{214}Pb and ^{85}Kr abundance in the LXe reservoir. An average ^{nat}Kr/Xe concentration of 0.66 ± 0.11 ppt is achieved. The background rate from ^{214}Pb assumes a concentration of 10 µBq/kg, compatible with the lower and upper bounds derived from ^{218}Po and ^{214}BiPo rate measurements in XENON1T data. Using the two boundary values, the resulting total ER background rate would be 48 ± 5 and $90 \pm 8\,(\mathrm{t}\cdot\mathrm{y}\cdot\mathrm{keV})^{-1}$.

tillation column was operated (gray areas in figure 3.5). The two trends separate when the ^{214}Pb-dominated regime is reached and ^{85}Kr becomes a sub-dominant contribution to the ER background. During SR0 and SR1 an average natural krypton concentration ^{nat}Kr/Xe of 0.66 ± 0.11 ppt is measured, with RGMS measurements coming with a 17% systematic uncertainty [245].

The actual ^{85}Kr abundance can be derived from data with high concentration of krypton in the beginning of XENON1T operation. Corresponding to RGMS ^{nat}Kr/Xe concentration of 1000 ± 170 ppt, present in the commissioning phase before Kr distillation through the column, the measured ER background rate below 200 keV amounts to $(11.2 \pm 0.2) \times 10^3\,(\mathrm{t}\cdot\mathrm{y}\cdot\mathrm{keV})^{-1}$. From MC simulations, the induced background rate per ppt ^{nat}Kr/Xe is $14\,(\mathrm{t}\cdot\mathrm{y}\cdot\mathrm{keV})^{-1}$ under the assumption of isotropic ratio $^{85}\mathrm{Kr}/^{\mathrm{nat}}\mathrm{Kr} = 2 \times 10^{-11}$ [mol/mol] [237]. By comparing the two rates we derive $^{85}\mathrm{Kr}/^{\mathrm{nat}}\mathrm{Kr} = 1.65 \times 10^{-11}$, which starting from the 0.66 ± 0.11 ppt measured ^{nat}Kr/Xe concentration gives a predicted low energy ER background rate of $7.7 \pm 1.3\,(\mathrm{t}\cdot\mathrm{y}\cdot\mathrm{keV})^{-1}$.

Summary of the ER background rate in XENON1T The MC prediction of the intrinsic contaminants contribution to the ER background rate is rescaled based on the ^{222}Rn and ^{85}Kr concentration measurements discussed above.

The induced background from detector construction materials in the 1.3 t fiducial volume used for the WIMP search is $8 \pm 1\,(\mathrm{t}\cdot\mathrm{y}\cdot\mathrm{keV})^{-1}$, almost tripled with respect to the quoted rate in 1 t fiducial volume, i.e. $2.7 \pm 0.3\,(\mathrm{t}\cdot\mathrm{y}\cdot\mathrm{keV})^{-1}$.

A refined description of the neutrino-electron interaction, considering the effect of xenon atomic binding [246] instead of assuming the scattered electron as free, is finally considered and results in a decrease of the event rate in the (1, 12) keV energy range by 24%. This leads to an ER background rate due to solar neutrinos of $2.47 \pm 0.05\,(\mathrm{t}\cdot\mathrm{y}\cdot\mathrm{keV})^{-1}$.

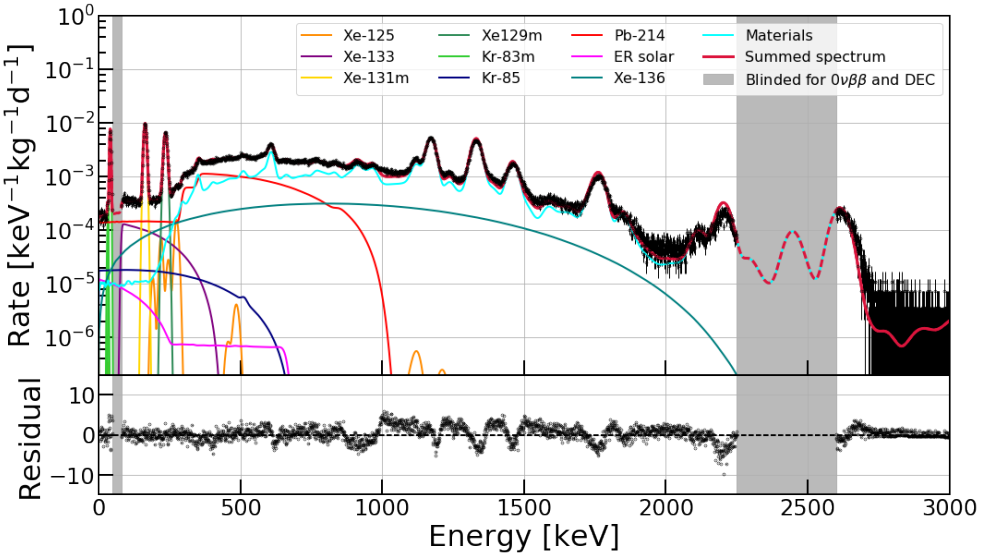

Figure 3.6: Matched background data energy spectrum (1 keV bins) in 1 tonne fiducial volume for the entire SR1 exposure. A 21 parameter fit (with fixed ratios between isotopes in each detector material) is performed in the energy range between 3 and 3000 keV, with the intervals (50, 80) keV and (2250, 2600) keV kept blinded for DEC and $0\nu\beta\beta$ searches. XENON1T data are in black, spectra of the different background sources are drawn in various colors. Besides the low energy ER background components described in this section, also ^{125}Xe and ^{133}Xe isotopes are included as well as the metastable ^{129m}Xe, ^{131m}Xe (activated during neutron calibration runs) and ^{83}Kr (injected for calibrations of the TPC spatial response).

Summing up all the components, including $0.84 \pm 0.13\,(\mathrm{t \cdot y \cdot keV})^{-1}$ from the ^{136}Xe $2\nu\beta\beta$-decay, the predicted ER background rate is $75 \pm 6\,(\mathrm{t \cdot y \cdot keV})^{-1}$ in the (1, 12) keV ROI and inside the 1.3 t fiducial volume. Table 3.1 summarizes the expected rate of each component and their relative contribution to the total XENON1T ER background. If the lower and upper bounds on the estimated ^{214}Pb concentration are taken into account, we obtain total ER rates of 48 ± 5 and $90 \pm 8\,(\mathrm{t \cdot y \cdot keV})^{-1}$, respectively.

XENON1T dark matter search data over the whole 1 tonne-year exposure provide the most accurate measurement of the ER background rate: the observed rate is stable at the level of

$$82^{+5}_{-3}(\mathrm{syst}) \pm 3(\mathrm{stat})\,(\mathrm{t \cdot y \cdot keV})^{-1}, \tag{3.1}$$

which represents the lowest background achieved in a DM detector to date. Such a rate is moreover in agreement with the expectation from MC simulations within uncertainties. The measured ER rate is extracted by fitting the ER background model in the observable space to DM search data and corrected for efficiency. The shape of ER background model (see section 3.4.1) comes from the fit of the ER band model to ^{220}Rn calibration data and the related systematic uncertainty is driven by the ER energy scale parametrization through the photon yield and recombination fraction.

Matching the spectral shape of ER background A deeper understanding of the XENON1T ER background also at higher energies is of great relevance for other interesting channels besides the standard WIMPs, such as neutrinoless doube-beta decay or double-electron capture (DEC), for example. For this scope one wants to match the background description built with MC simulations to the spectrum of real ER data ranging up to few MeV. The fit of the MC spectrum to the XENON1T ER data is shown in figure 3.6. The matching is performed through χ^2-minimisation, keeping fixed the ratios between radioactive isotopes contaminations in detector materials, based on screening measurements [212]. The MC spectra are smeared according to the observed energy resolution in the XENON1T detector (see section 4.1.3). A very good matching is achieved at low energies, while larger discrepancies are found at higher energies. On the data side, a shift of high energy peaks from their true position is observed due to pathologies in the signal reconstruction processor as it is optimized for low energy events and further investigations and tuning are needed for MeV electronic recoils.

3.2 Nuclear recoil background

Single interactions with xenon nuclei in the TPC produce nuclear recoils indistinguishable from that of a WIMP recoil, contrary to electronic recoils which can be discriminated from WIMP signals through their larger S2/S1 ratio. Particles that can cause NRs in the target LXe are neutrons and neutrinos undergoing CNNS.

Fast neutrons are more penetrating than γ-rays in LXe, their mean free path being of the order of tens of cm. Shielding the inner LXe volume aginst neutrons is then more difficult and their probability to undergo just a single scatter in the active target mass is higher than γs. Neutrons emitted by radioactive contaminants in detecor materials, referred to as *radiogenic neutrons*, have energies $\mathcal{O}$(MeV) and can therefore enter the TPC producing a low energy elastic nuclear recoil mimicking WIMP signals. They are the dominant NR background source for XENON1T as obtained from MC simulation studies (see section 3.2.3). An indirect constraint on the radiogenic neutrons rate based on XENON1T data comes from the measurement of multiple NR low energy interactions (see section 3.2.5).

Additionally, *cosmogenic neutrons* with energies extending to tens of GeV are produced by muons along their path through the rock into the underground laboratory and through the materials that surround the detector. They also represent a potential source of NR background but can be reduced much more easily with respect to the one induced by radiogenic neutrons as cosmogenic ones are mainly produced in the laboratory cavern rock. They are thus shielded by about 4 m of water, which is also instrumented as a Cherenkov detector to tag crossing muons and muon-induced showers. The expected background from this source is negligible for XENON1T, as described in section 3.2.1.

Astrophysical *neutrinos* contribute to the NR background (see section 3.2.2) through CNNS, a process predicted by the Standard Model difficult to detect but recently ob-

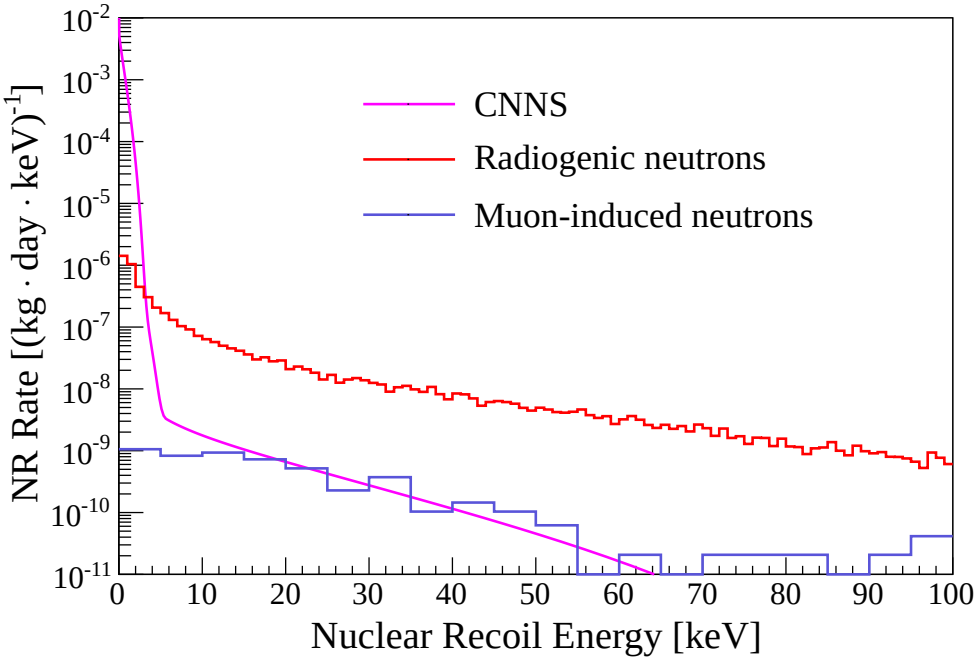

Figure 3.7: Recoil energy spectrum of NR backgrounds in 1 tonne fiducial volume. The region of interest for NR WIMPs is approximately (4, 50) keV, where the dominant background contribution comes from radiogenic neutrons emitted from detector construction materials (red). Coherent neutrino-nucleus scattering (CNNS), shown in magenta, contributes to background at energies close to the XENON1T threshold. Neutrons induced by the incoming muon flux in the underground experimental hall at LNGS (purple) are reduced to a negligible contribution thanks to the XENON1T Muon Veto sub-detector.

served for the first time by the COHERENT experiment [247]. This is an irreducible background for experiments with no possibility to measure the direction of the recoil track, like noble liquid TPCs. CNNS will represent the ultimate limitation to the WIMP sensitivity of direct detection experiments [138] (see section A.3 for the study of WIMP discovery potential under the ultimate scenario where CNNS is the only source of NR background).

3.2.1 Muon-induced neutron background

High energy neutrons are produced by the interaction of cosmic muons with the rock and concrete around the underground laboratory and with the detector materials. An estimate of the muon-induced neutron flux in the LNGS cavern is $\sim 7.3 \times 10^{-10} (\mathrm{cm}^2 \cdot \mathrm{s})^{-1}$ for >10 MeV neutrons, under conservative assumptions on the muon-induced neutron yield [248]. Such neutrons, whose energy ranges up to $\mathcal{O}$(GeV), can penetrate even through large shields and reach the sensitive part of the detector, mimicking a WIMP interaction. To protect XENON1T from this kind of background, the detector is built inside a cylindrical water tank, 9.6 m in diameter and 10.2 m in height, which acts as

Cosmogenic neutrons rate [y^{-1}]	"Muon" events	"Shower" events	Total
Without MV cut	9×10^{-3}	0.021	0.03
Tagging efficiency	99.5%	43%	
Residual background rate	5×10^{-5}	0.012	0.012

Table 3.2: Cosmogenic neutron background rate in (5, 50) keV and in 1 tonne fiducial volume. Rates and relative tagging efficiencies for the two possible classes of events, with muon crossing the water tank or not, are also reported. Considering the effect of both the water passive shielding and the active veto, the surviving neutron background is negligible for XENON1T.

a shield against external neutrons and gammas. Moreover, the tank is instrumented with 84 PMTs to tag the track of the muon, and of its induced showers, through the detection of Cherenkov light produced in water. The entire system is called Muon Veto (MV).

Events observed in the TPC happening in coincidence with a trigger from the MV detector can be then recognized and removed from the XENON1T exposure. The MV trigger, used for the XENON1T science runs, requires 8-fold PMT coincidence of signals whose amplitude is above a 1 photoelectron threshold within a 300 ns time coincidence window. The performance of the MV system is studied via GEANT4 modelling and simulation of muon events producing high energy neutrons that reach XENON1T. Details about the MC model of production, propagation and interaction of muon-induced neutrons can be found in [213]. Two classes of events are distinguished to characterize the tagging efficiency of MV: "muon" events, where the muon crosses the water tank, and "shower" events, in which the neutron comes inside together with the associated particle shower but the muon does not enter the water tank. The tagging efficiencies of MV are evaluated through MC simulation and are found to be 99.5% and 43% for "muon" and "shower" events respectively, under the trigger conditions set for the XENON1T DM search runs [249]. We cut TPC events if a MV trigger is registered in a 5 ms time interval around it, from 2 ms preceding the TPC event to successive 3 ms. The acceptance of the MV cut is evaluated in 99.75%, given the observed 0.45 Hz MV trigger rate. The residual cosmogenic neutron background rate in the NR region (5, 50) keV and in 1 tonne fiducial volume is 1.2×10^{-2} events per year, two orders of magnitude lower than the background from radiogenic neutrons and therefore negligible. The MV cut reduces the background rate by a factor 2.5, as can be deduced from table 3.2. The NR energy spectrum of muon-induced neutron in XENON1T is shown in figure 3.7 (blue line).

3.2.2 Coherent elastic neutrino-nucleus scattering

The expected NR background contribution due to CNNS is estimated following the approach developed in [138]. We consider solar neutrinos (from all the various chains), diffuse supernovae (DSN) and atmospheric neutrinos. The most relevant contribution, in the (4, 50) keV energy region of interest for WIMP search, comes from the ^{8}B and

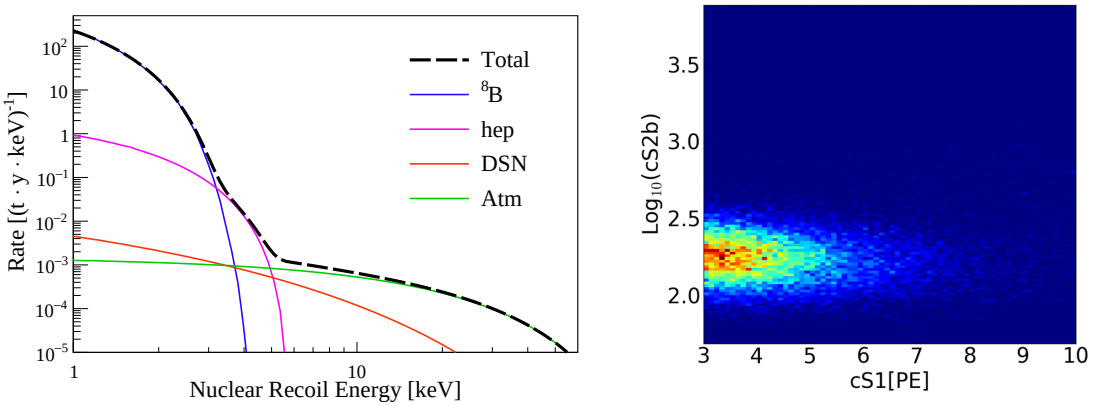

(a) **(b)**

Figure 3.8: The XENON1T NR background due to coherent neutrino-nucleus elastic scattering. (a) Recoil energy spectrum in xenon of CNNS (total rate in black dashed line) in the energy region of interest for WIMP search. The contribution of the main neutrino sources, solar ^8B and *hep* ν, diffuse supernova (DSN) and atmospheric (Atm) ν, are shown in solid lines. (b) Spectral shape of the CNNS background model in the observable (S1, S2) signals space (corrected S1 and bottom S2 are the signals used for the XENON1T DM search data analysis, see chapter 4). The color scale is linear and in arbitrary units. The CNNS is confined to very low energies, close to the 3 PE analysis threshold.

hep neutrinos from the Sun, while the event rate from higher energy neutrinos (DSN and atmospheric) is orders of magnitude smaller, as shown in figure 3.8a. The integral event rate above 4 keV is very small ($< 0.02\,(\mathrm{t}\cdot\mathrm{y})^{-1}$). However, due to the very steep energy spectrum of CNNS (e.g. the rate above 1 keV is $\sim 90\,(\mathrm{t}\cdot\mathrm{y})^{-1}$), it is relevant to estimate the event rate below the experimental NR energy threshold. Indeed, the relatively high rate of below-threshold CNNS NR events yields a non-negligible rate in the (3, 70) PE ROI defined in the observable S1 signal space. The reason is that Poissonian fluctuations in the generated signal (see section 3.3.1) allow to detect part of the low energy events since the number of photons emitted and detected is very low for such events.

The rate normalization of the CNNS background is constrained mainly by ^{8}B solar neutrinos flux, known with 14% precision [243]. Moreover, the Standard Model CNNS cross section is rescaled by a factor 0.77 accordingly to the recent results from COHERENT [247], which directly observed this process for the first time with neutrinos produced at a spallation neutron source. On top of the neutrino flux uncertainty of 14%, the final CNNS background model in the observable space also takes into account the uncertainty of about 21% from COHERENT [247] and of about 15% from the signal response model at the low energy region of most interest for neutrino scatters (see sections 3.3 and 3.4.2). The resulting relative rate uncertainty for solar neutrino scatters induced NR background is 29%. The shape in the observable signal space of the CNNS background model for XENON1T is shown in figure 3.8b, while the spatial distribution is uniform. Note that data analysis uses corrected (for detector related effects) S1 and

S2 signal variables (see section 4.1), indicated by cS1 and cS2 (or $cS2_b$, for the fraction of S2 signal observed by bottom PMTs). The derived CNNS background rate is $0.05 \pm 0.02\,(\mathrm{t \cdot y})^{-1}$ in the (3, 70) PE ROI for WIMP search.

3.2.3 Radiogenic neutrons

The presence of ^{238}U, ^{235}U and ^{232}Th in the detector materials generates neutrons in the MeV energy range through spontaneous fission (SF), mainly from ^{238}U, and (α, n) reactions induced by α particles emitted along the decay chains. Radiogenic neutrons represent the major contribution to the XENON1T NR background. For heavy nuclei, the high Coulomb barrier suppresses the (α, n) process. Therefore the neutron production is almost exclusively due to spontaneous fission. The highest (α, n) yields are from light materials, such as PTFE and the ceramic stems of PMTs. To make predictions about the neutron background expected in the DM search ROI we make use of MC simulations with the GEANT4 toolkit [234]. As radiogenic neutrons can have a quite large scatter multiplicity along their path in the large XENON1T TPC, it is important to characterize the detector's capability in separating two close scatters. This is studied with waveform simulations, exploiting a custom-developed waveform simulator for XENON1T (called FAX) which simulates raw signal waveforms to be fed to the same signal processor used on real data. The waveform simulator includes data-driven models of the scintillation light pulse shape, of the electrons diffusion during drifting, of the time profile of electron amplification, of the afterpulses caused by residual gas in PMTs, of the single electron generation by photoionization impurities and of the electronic noise. Results from simulations are then validated against a data-driven estimation based on neutron calibration data. The radiogenic neutrons background model is finally updated with the inclusion of the neutron-X contamination (section 3.2.4) which became relevant as an enlarged fiducial volume was chosen for WIMP search with respect to the 1 tonne LXe mass used in the analysis of the first XENON1T science run [108]. Given the large uncertainties involved in neutron background simulations, described in this section, the background rate induced by radiogenic neutrons is constrained by the measurement of multiple NR scatters (section 3.2.5).

Modelling the XENON1T multiple scatter resolution When a particle scatters twice inside the detector, the prompt S1 signals are merged, while due to the drift time multiple S2 peaks can be observed if the interactions occur at different z positions. In XENON1T, the large detection volume gives a powerful tool to remove a large portion of neutron background by cutting out multiple scatters. The selection of single scatters applied to XENON1T data is based on the amplitude of the largest and second largest S2 signal ($S2_{\mathrm{second-largest}}$) recorded in the event. For real multiple scatters, the other S2s can be as large as the main S2, while S2 noise orginated by PMT afterpulses or photoionization [250] comes with smaller amplitudes. In the low energy range of interest

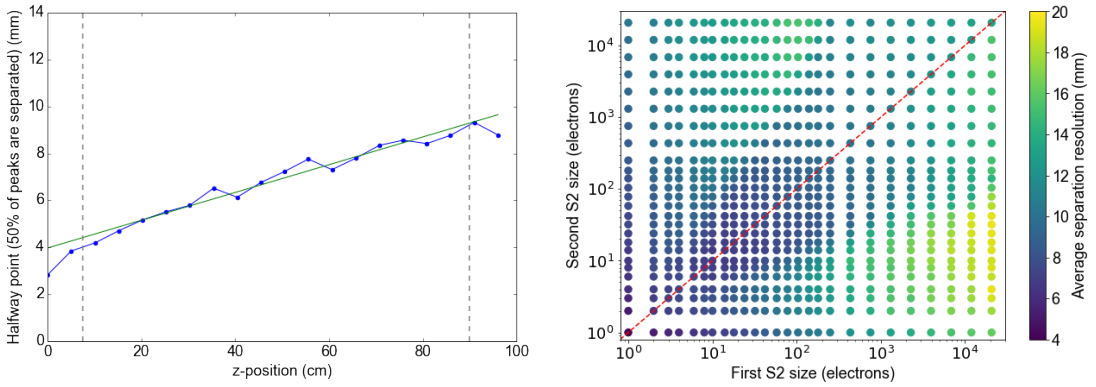

(a) **(b)**

Figure 3.9: Simulated z-, first S2- and second S2-dependent double scatter resolution defined as the minimum separation in the z coordinate between two scatters whose S2s are resolved by the XENON1T event reconstruction processor with 50% efficiency. (a) Dependency from depth in the TPC of equally sized S2 signals (with 42 electrons generated in the interaction site). Dashed vertical lines indicate the range of the linear parametrization of the resolution z dependency, where $z = 0$ is the cathode position and higher z values are deeper in the TPC. (b) Double scatter resolution as a function of the S2 size (expressed in terms of free electrons produced at the interaction point) of the first and second signal, averaged over z.

for WIMP search, the cut to reject multiple scatters is defined as

$$\mathrm{S2}_{\mathrm{second-largest}} < 0.00832 \cdot \mathrm{S2}_{\mathrm{main}} + 72.3, \tag{3.2}$$

which provides an ∼85 % rejection power on neutron calibration data with 99% acceptance of single scatters, established on ^{220}Rn ER data. The same cut is applied to MC simulations of NR background to ensure the same efficiency as the single-site scatter selection made on real data.

Nonetheless, two scatters happening at the same TPC depth yield two S2 signals which are seen as just one merged S2 at the event reconstruction step of data processing. The XENON1T multiple scatter resolution has therefore to be taken into account in the NR background prediction from MC simulations of neutron interactions. The resolution for double-site scatters is a function of the z coordinate, but also of the first S2 (not necessarily the largest) and the second one. Couples of S2s of different amplitudes are generated with the XENON1T waveform simulator from different z positions, varying their separation along z. They are then fed to the data processor to study if they are resolved or classified as a single S2. An inspection of the resolution as a function of z shows that a linear approximation is good for most S2 size combinations (see figure 3.9b), with larger Δz separation required for deeper interactions, whose S2s are more spread in time due to the ample electron cloud diffusion in the drift. The dependency from the signals amplitude of the minimum Δz separation at which 50% of events get reconstructed as separated S2s is shown in figure 3.9a, averaged over all possible z depths in the TPC. The three dimensional map, with resolutions ranging

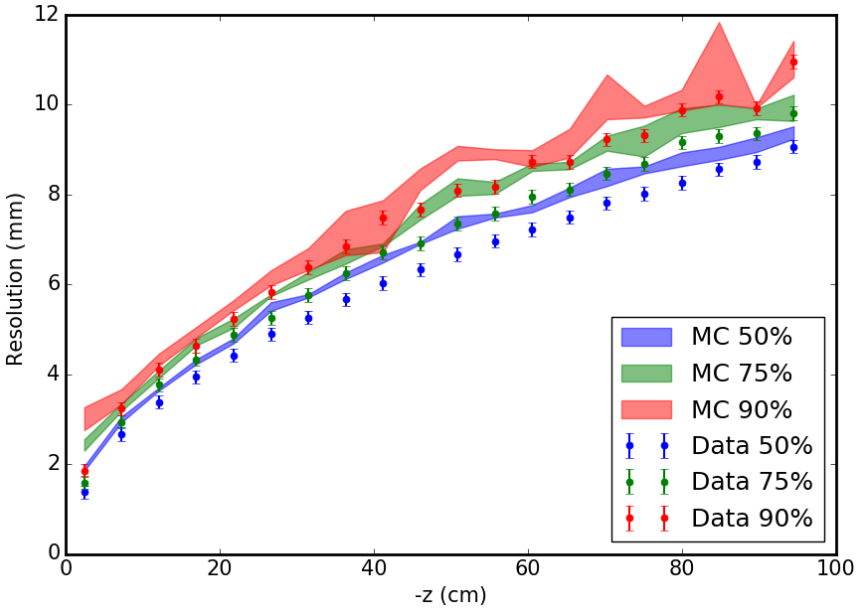

Figure 3.10: Validation of the simulated multiple scatter resolution against ^{241}AmBe calibration data. The data-driven resolution is estimated analysing multiple NR scatter events and looking for missing population at very small Δz separation between the main and the second largest S2. The resolution obtained from simulated ^{241}AmBe data is overlaid as filled bands representing the uncertainty in the estimation. The resolution defined as the minimum separation at which S2s are resolved with 50%, 75% and 90% efficiency is shown in different colours. A good agreement is found, with a slightly more conservative resolution obtained from simulation with respect to the data-driven method by ∼0.5 mm (∼8 %).

from ∼3 mm to ∼20 mm for very large S2s, is applied to simulated data to correctly cluster interactions with not sufficient z separation.

The resolution map derived from simulations is validated against neutron calibration data. Multiple scatters in data are explored in z slices and the exponential distribution of the Δz separation between the main and the second largest S2 is evaluated looking for a missing population at the smallest distances. The separation efficiency is estimated by the under-population of identified double scatters with respect to the exponential extrapolation down to zero separation. The comparison between the obtained resolution as a function of z, at 50%, 75% and 90% separation efficiency, and results from ^{241}AmBe neutron simulations (figure 3.10) shows a slight overestimation (∼8 %) from simulated data, meaning that by assuming the simulated multiple scatter resolution map we stay on the conservative side.

MC simulations of radiogenic neutron background Neutron yields in the detector materials are estimated using the SOURCES-4A software [251]. The neutron production rates for all the relevant detector materials are considered taking into account also chain disequilibrium. Detailed description of neutron yields used for each material

Radiogenic neutron background rate [y^{-1}]							
Component	^{238}U	^{235}U	^{226}Ra	^{232}Th	^{228}Th	Total	Percentage
PMTs Stem	$1.1 \cdot 10^{-1}$	$5.7 \cdot 10^{-2}$	$6.1 \cdot 10^{-2}$	$8.2 \cdot 10^{-5}$	$5.8 \cdot 10^{-2}$	0.290	33%
PMTs Base	$3.9 \cdot 10^{-2}$	$4.6 \cdot 10^{-3}$	$3.2 \cdot 10^{-2}$	$1.8 \cdot 10^{-4}$	$1.2 \cdot 10^{-2}$	0.087	10%
PMTs Quartz	$5.5 \cdot 10^{-2}$	$1.6 \cdot 10^{-3}$	$2.0 \cdot 10^{-3}$	$6.7 \cdot 10^{-6}$	$1.7 \cdot 10^{-3}$	0.060	7%
PTFE	$2.1 \cdot 10^{-2}$	$1.3 \cdot 10^{-2}$	$6.0 \cdot 10^{-2}$	$3.6 \cdot 10^{-4}$	$5.7 \cdot 10^{-2}$	0.142	16%
Shell (SS)	$8.7 \cdot 10^{-2}$	$1.5 \cdot 10^{-3}$	$6.5 \cdot 10^{-3}$	$9.5 \cdot 10^{-6}$	$2.4 \cdot 10^{-2}$	0.118	13%
Flange (SS)	$9.4 \cdot 10^{-3}$	$1.4 \cdot 10^{-4}$	$7.3 \cdot 10^{-3}$	$1.9 \cdot 10^{-6}$	$5.5 \cdot 10^{-2}$	0.071	9%
Bell (SS)	$3.2 \cdot 10^{-2}$	$5.4 \cdot 10^{-4}$	$6.5 \cdot 10^{-4}$	$5.7 \cdot 10^{-7}$	$2.1 \cdot 10^{-3}$	0.035	4%

Table 3.3: NR background rate induced by radiogenic neutrons in 1 tonne fiducial volume and in the (3, 70) PE region of interest for WIMP search in the S1 signal space. Components not listed in this table account for approximately 10% of the total XENON1T neutron background budget. The percentage contribution of each component refers to the total background rate.

and radioactive isotope can be found in [135]. A hundred million neutrons for each of the detector materials listed in table 3.3 (which account for ∼90 % of the total neutron contribution) are simulated with GEANT4. Close recoils in z are clustered according to the XENON1T multiple scatter resolution and the single scatter selection cut (both discussed in the previous paragraph) is applied to simulated data. At this stage of MC studies, the conversion of deposited energy into light and charge signals is carried out exploiting the XENON1T NR response model derived from the first science run [108] based on the underlying signal generation approach described in [135] and analogous to the model presented in section 3.3[1]. PMT components are the major contributor to NR background, inducing 50% of the total low energy neutron background budget in 1 tonne fiducial volume. Stainless steel cryostat parts account for 22%, while the TPC PTFE is responsible for 15% of the neutron background. The uncertainty associated to the background rate prediction is established at 50%, based on the uncertainty in the SOURCES-4A [252] code and the difference between the GEANT4 and MCNP particle propagation simulation codes [253]. The recoil energy spectrum in 1 tonne FV is shown in figure 3.7. The spatial distribution is mainly confined close to the TPC edges (see figure 3.11), similarly to ER background from detector materials.

3.2.4 Neutron-X contamination

Neutrons originating from bottom PMTs have a sizeable probability to scatter in the region between the TPC cathode and PMTs, referred to as the below-cathode (BC) region. The scintillation light from these scatters is detected but electrons are lost because the electric field in the BC region drifts them away from the active volume. Such events, with at least one scatter in the BC region and a single scatter in the TPC volume are called *neutron-X* events and have a lower S2/S1 ratio than normal NR

[1]The final radiogenic neutron model used to make the background prediction for the DM search of the combined SR0 and SR1 (described in section 3.4.2) is derived through the NR response model based on the whole XENON1T dataset (see section 3.3).

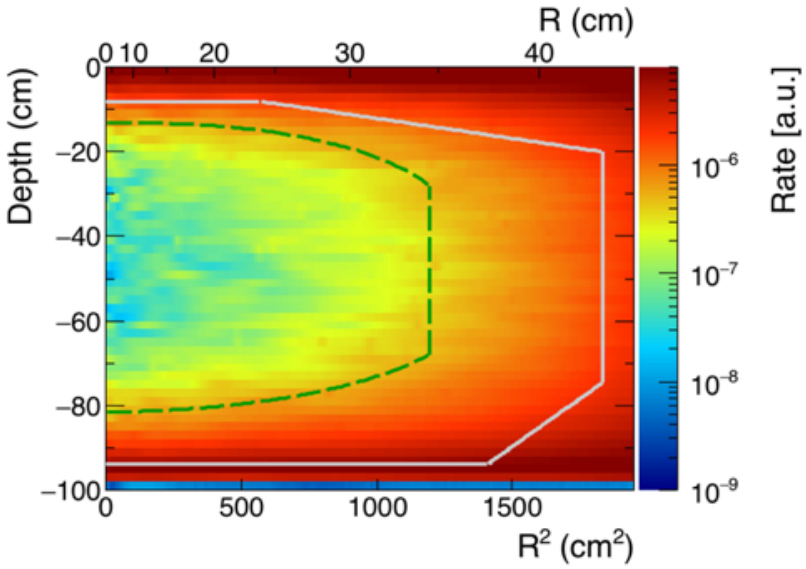

Figure 3.11: Spatial distribution of the XENON1T NR background induced by radiogenic neutrons emitted from detector construction materials as a function of TPC radius squared and depth along the z coordinate. The final 1.3 tonnes fiducial volume is drawn as a grey solid line, while the green dashed line delimits a reference 0.65 t volume with highly reduced background rate due to neutrons.

scatters. An example of the topology of such events can be visualized in figure 3.12, where two simulated background events due to a neutron emitted from a bottom PMT are shown: a neutron-X event with a low energy deposition BC (figure 3.12a) and a normal single scatter inside the FV (figure 3.12b). The plots are produced with an event display plugin to GEANT4 simulated events that I developed, helping the visualization of tracks of produced particles, their type and their interactions within the physical volumes defined in the XENON1T GEANT4 detector model.

Taking into account the BC interaction in events that contribute to the NR background, i.e. producing a single NR scatter inside the fiducial volume, implies a two-fold distortion of the "normal" neutron background (where interactions BC are neglected). For the neutron-X fraction of the whole neutron events sample, the S1 signal is increased by the scintillation light emitted BC, meaning that in-TPC NRs below threshold can be pushed inside the (3, 70) PE ROI and other events can be pushed above the 70 PE upper bound. Besides the impact on the final radiogenic neutron background rate, also the (S1, S2) energy spectrum is distorted as the neutron-X events ending up in the ROI will have an abnormally small S2 signal size with respect to normal scatters with the same S1 signal amplitude.

Investigating the neutron-X population The extension of the fiducial volume used in the combined SR0+SR1 DM search [109], from 1 tonne, defined in the analysis of SR0 [108], to 1.3 tonnes, motivated investigations of the neutron-X population which

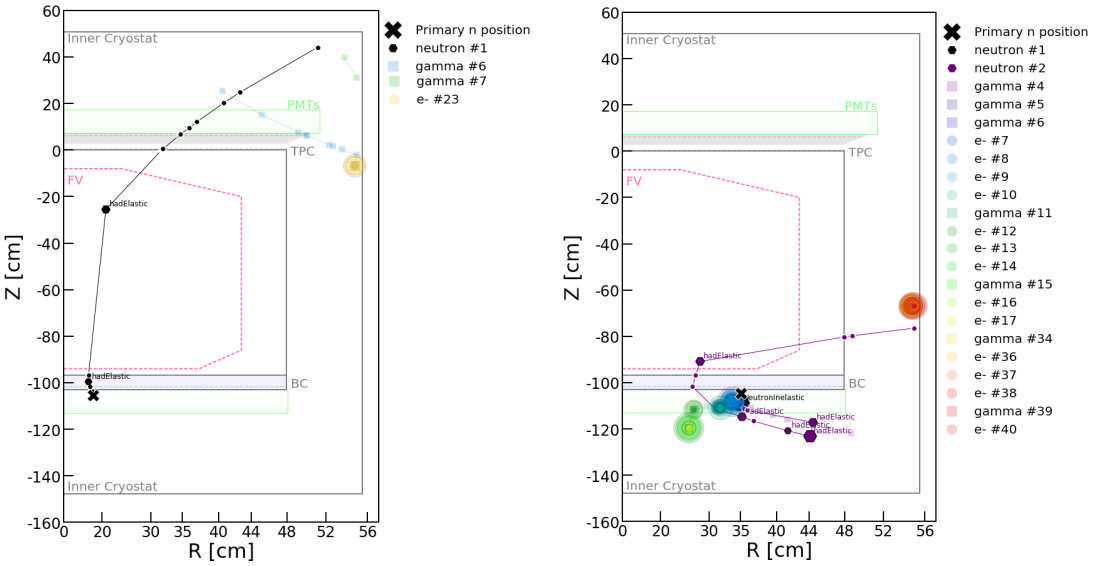

Figure 3.12: XENON1T event display of GEANT4 simulation of radiogenic neutron background originated from the bottom PMT array. (a) A neutron-X event, with additional low energy recoil in the below-cathode (BC) region, originated by a primary neutron with energy of 4.8 MeV. (b) A normal NR single scatter inside the fiducial volume from a 5.5 MeV neutron (in this case the NR in the FV is not caused by the primary neutron, but from a secondary neutron produced through neutron inelastic scattering outside the TPC). The custom developed event display shows a point for all physical interactions (points with black outline) or if the particle is transported through a different detector component with no energy deposition (points with white outline). In this simulation only neutrons, gammas, electrons and positrons are shown (which are the typical particles present in simulated events started by a neutron). The size of each point is proportional to the deposited energy. Neutron interactions with non-null energy deposition are labelled with the corresponding GEANT4 physical process name. The position of the primary particle (neutron) in the simulation is marked by a black cross. Only interactions in the sensitive xenon volumes (both liquid and gaseous) are stored and visualized. The 1.3 tonnes fiducial volume is drawn as pink dashed line.

was neglected in the previous analysis. From MC simulations, we find that ∼18 % of radiogenic neutron events, at any energy, multiplicity and in the whole active volume, include at least one interaction in the 6.2 cm gap between the bottom PMT array and the cathode, the BC region. The highest neutron-X contamination is observed for the events induced by neutrons emitted from PMTs (∼32 %), as especially those originating from bottom PMTs clearly have the largest probability to interact BC with respect to neutrons coming from any other initial position. Lower neutron-X fractions are present in events arising from cryostat neutrons (∼9 %) and from the Bell (∼2 %), which is positioned over the top of the TPC.

Neutron-X events are mostly located in the lowermost region of the TPC just above the cathode, as shown by figure 3.13a, for simulated radiogenic neutrons from PMTs. Energy depositions BC can be distinguished in NRs, due to neutron elastic scatters, and ERs, due to gamma or electron interactions originated from a neutron inelastic

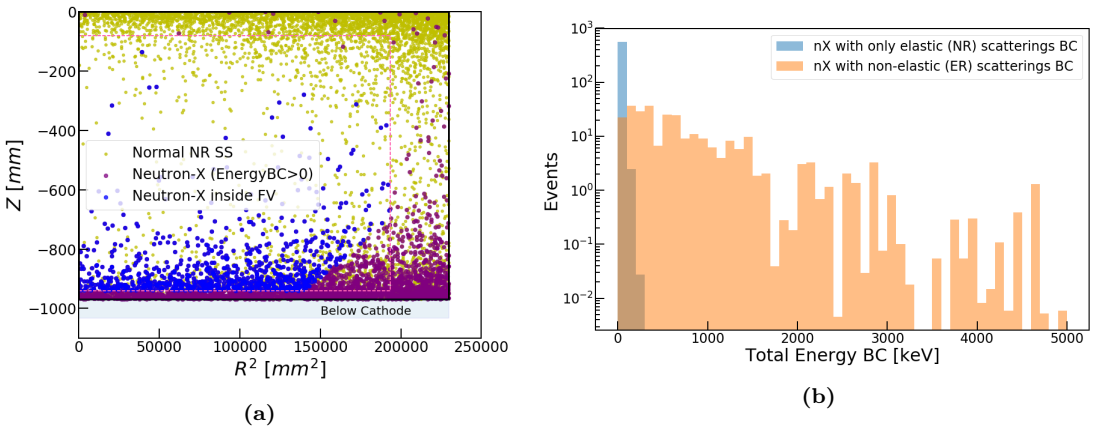

(a) (b)

Figure 3.13: GEANT4 simulation of neutron-X events originated by neutron emission from PMT components. (a) Position distribution in the TPC of single scatter events in the (0,50) keV energy range. Neutron-X events, which have additional interactions in the below-cathode (BC) region, are shown in the whole TPC active volume (purple points), with scatters inside the 1.3 tonnes fiducial volume colored in blue. Normal neutron single scatters are also drawn (yellow points). The pink dashed line delimits the maximum radius and z range of the fiducial volume. (b) Energy spectrum of recoils in the below-cathode region for neutron-X events with deposited energy in the TPC below 50 keV. In light blue, the spectrum for events where only NRs happen BC. The distribution of deposited energy BC for events with at least one ER interaction is shown in orange.

scattering or neutron capture. An elastic scattering BC is present in 85% of neutron-X events, while contribution from ERs originated from neutron inelastic scatters and neutron capture is 38% and 6% respectively. We refer to *elastic* neutron-X for purely nuclear recoils happening BC and to *non-elastic* neutron-X if at least one of the BC interactions is of electron recoil type. Since ERs have a larger light yield than NRs, most of non-elastic neutron-X events have a summed S1 (from BC interactions plus the NR in the fiducial volume) higher than the upper bound of the S1 ROI. The spectrum of deposited energy in interactions BC is shown in figure 3.13b for both elastic and non-elastic neutron-X events. Non-elastic interactions contribute in one-third of the simulated neutron-X and just $\sim$1 % of them has low energy ERs ($\lesssim$ 10 keV), due to γ compton scatters or absorption of X-rays produced by a photo-ionization outside the BC region. Consequently, only purely elastic neutron-X events can contribute to the NR background in the WIMP search ROI.

Impact on the neutron background model Given that background neutron-X events are only those with one or more nuclear recoils BC, the signal response for below-cathode interactions can be modelled as for normal NRs in terms of light signal, while the charge signal is not generated. The relative ratio and spectral difference in (S1, S2) distributions between normal neutron scatters and neutron-X events are taken into account in the simulation for building the final model of NR background induced by radiogenic neutrons (see sections 3.3 and 3.4). In the 1.3 tonnes fiducial

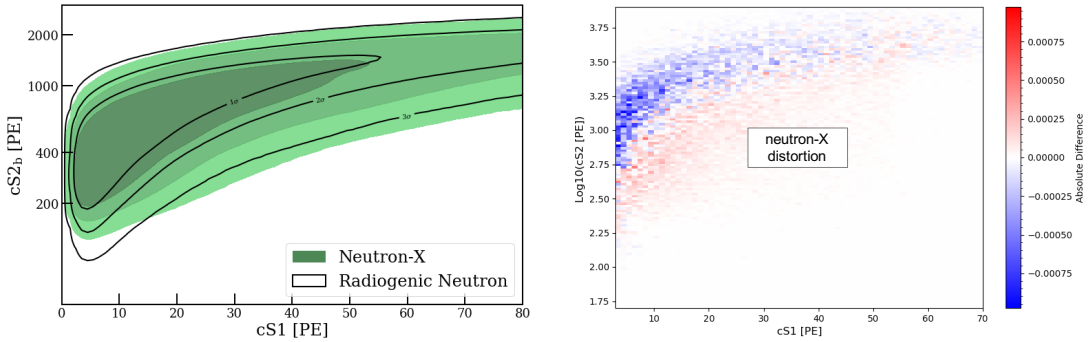

(a) (b)

Figure 3.14: Distortion of the NR background spectral shape induced by the 13.6% neutron-X contamination of the total background due to radiogenic neutrons. (a) Distribution of neutron background in the observable signal space. The black contours show the 1, 2 and 3σ quantiles for normal single scatter from radiogenic neutrons. The distribution of neutron background including the neutron-X population is depicted by green shaded regions representing the 1, 2, 3σ contours (from darker to lighter). (b) Variation bin-per-bin, in the (cS1, $\log_{10}$cS2$_b$) space, when neutron-X events are properly modelled with additional contribution to the S1 signal size from below-cathode interactions. Some events are removed since their S1 is pushed outside the (3, 70) PE ROI. Other events that produce a recoil in the fiducial volume with S1 amplitude less than 3 PE are moved inside the ROI. The overall variation of the background rate in ROI is -12%.

volume, the resulting NR background rate including proper treatment of the neutron-X fraction is lower by 12% with respect to the predicted rate ignoring below-cathode energy depositions, meaning that more events are pushed outside the (3, 70) PE ROI in S1 than those moved inside. No significant pattern is observed in the spatial distribution of removed and added events due to the neutron-X distortion of S1. The residual neutron-X contamination over the total radiogenic neutrons background in the ROI amounts to 13.6%. The most important effect is the distortion of the energy spectrum due to neutron-X in the NR background model, shown in figure 3.14. The neutron-X population is removed from the bulk of the normal neutron scatter spectrum (the so-called NR band) and it expands downwards due to the smaller S2/S1 ratio.

3.2.5 Constraint from multiple scatter analysis

Multiple neutron scatter events in DM search data and NR calibration data can be used to constrain the predicted neutron background rate from MC simulations, which is affected by a quite large 50% uncertainty. Derivation of the constraint on neutron single scatter rate relies on the estimated multiple-to-single NR scatter ratio from both simulations and calibration data.

Data analysis searching for multiple NRs in the 1.3 tonnes fiducial volume is conducted on all DM search data (SR0+SR1), selecting events up to 100 PE in the corrected S1 signal. The same selection criteria used for DM search (see section 4.3.2) are applied, apart those designed to remove multiple scatter events. In particular, the reverted cut

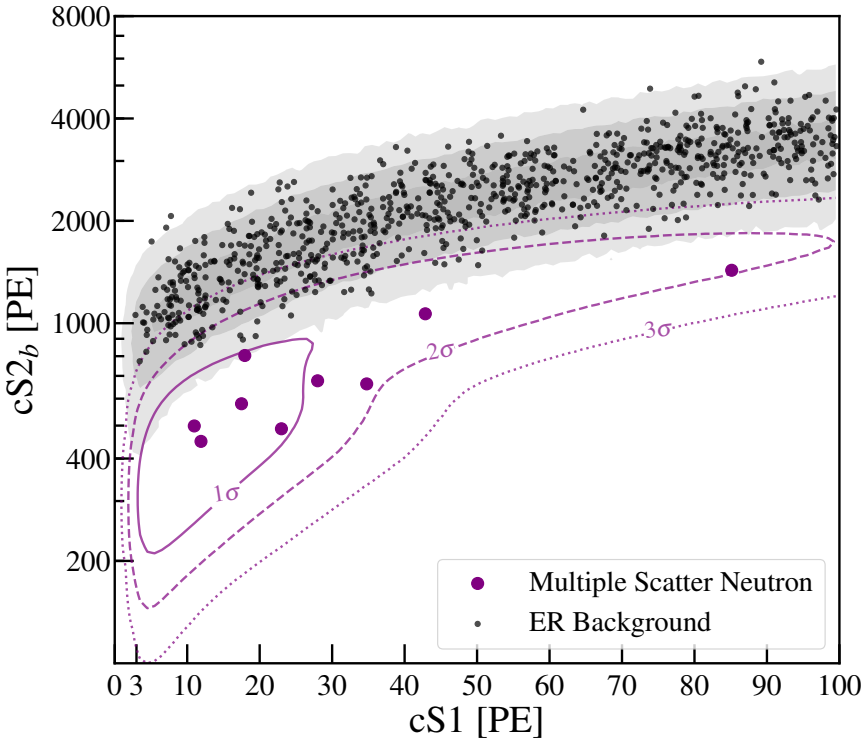

Figure 3.15: Distribution of neutron multiple scatter events in the discrimination space. The grey bands represent the single scatter ER model 1 and 2 σ quantiles. The NR model for multiple scatters is depicted as purple contours. Purple points are the nine identified neutron multiple scatters within the 1.3 tonnes fiducial volume in the XENON1T DM search data. The respective cS1 and cS2$_b$ signal sizes refer to the main interaction of each event, i.e. to the largest S2 peak. In black points the XENON1T ER background data.

in equation 3.2 is used to select muliple-site recoils in the dataset. Finally, cutting away events above the 2σ upper bound of the NR band for multiple scatters (which is derived from the NR response model described in section 3.3, but fitted on multiple scatters events in calibration data) ensures that the selection does not include ERs. Nine events survive the multiple neutron scatter selection. One event is found in the first science run and the remaining 8 events show up in SR1. Their distribution in the signal space, through the S1 and S2 of the main interaction, is shown in figure 3.15, while the spatial distribution of the main and secondary scatters is in figure 3.16. Releasing the NR requirement, four more multiple scatters are identified of electronic recoil type.

The observation of 9 events is compatible with the prediction from MC simulations of 6.4 ± 3.2 multiple scatter events in the 1.3 tonnes fiducial volume and in the XENON1T combined SR0+SR1 exposure of 278.8 days. A factor $\sim$5 higher rate of multiple with respect to single scatters is estimated from simulations of radiogenic neutrons. The multiple-to-single scatter ratio can be evaluated also from neutron calibration data by applying the same multiple scatter selection aforementioned. The estimated ratio

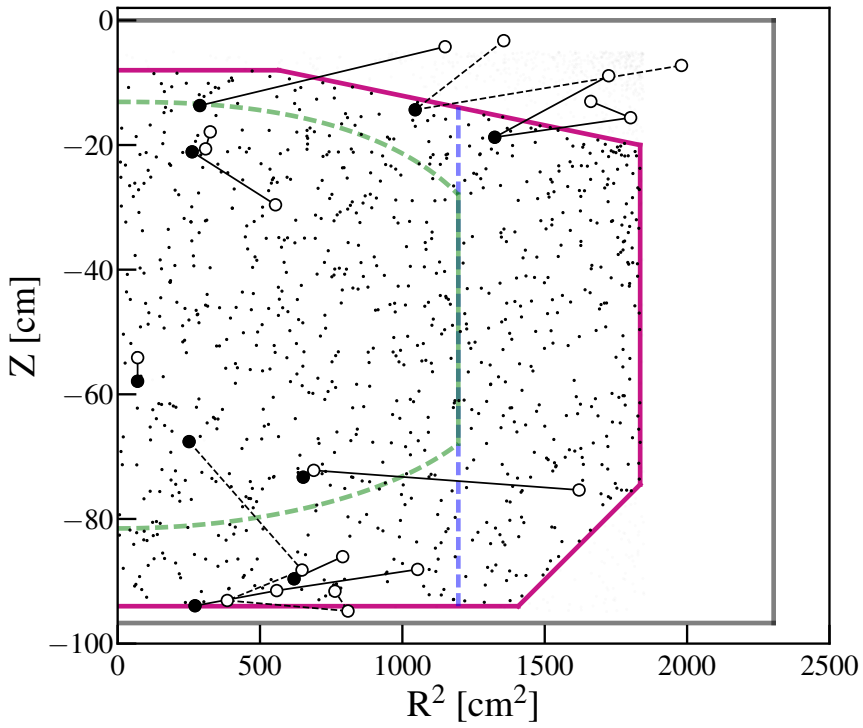

Figure 3.16: Position in the TPC of the identified nine neutron multiple scatters in XEONON1T DM search data. For each event, the chain of scatter points is linked by lines (dashed line are present when two chains overlap). Only one solid circle per event is shown, located at the reconstructed position of the largest S2 signal. There is at least one hollow circle for each event, drawn in the reconstructed position of the secondary S2s. Smaller dots are single scatter ER background in the 1.3 tonnes fiducial volume (purple line).

from analysis of ^{241}AmBe and neutron generator calibration data is lower than the multiple-to-single ratio derived from simulated calibration data by a factor 0.6 and 0.7 respectively. The larger discrepancy is conservatively taken into account in the derivation of the constraint to the single scatter radiogenic neutron background.

A likelihood function is defined to include all the available information about the rate of neutron scatters in XENON1T (both single and multiple). The number of multiple scatter events $\mu_{\rm ms}$ is parametrized through the multiple-to-single scatter ratio R and the number of single scatters μ_{ss} (the number of multiple scatter is given by $\mu_{\rm ms} = \mu_{ss} \cdot R$):

$$L(\mu_{\rm ms}) = \text{Poiss}(9|\mu_{\rm ms}) \cdot \text{Gaus}(\mu_{\rm ms}|\mu_{\rm ms}^{\rm MC}, \sigma_{\rm MC}) \cdot \text{Uniform}(\text{R in } [\text{R}_{\rm Data}, \text{R}_{\rm MC}]), \quad (3.3)$$

where the first term is the Poissonian probability of observing the 9 multiple scatter events with $\mu_{\rm ms}$ expectation value, the second one is the gaussian constraint from the MC prediction with $\mu_{\rm ms}^{MC} = 6.4$ and $\sigma_{\rm MC} = 50\%$ and the last term is a uniform PDF defining the allowed range for the multiple-to-single scatter ratio within the upper and lower estimations from data and simulations. The final constraint on the XENON1T single scatter neutron background is extracted by profiling out the multiple-to-single

scatter ratio R and comparing the likelihood contour and central value to the original MC prediction. A scaling factor of $1.48^{+0.90}_{-0.55}$ is obtained to be applied on the single scatter rate prediction derived from MC simulations of the radiogenic neutron background. Such a factor is applied to the normalization of the final XENON1T neutron background model (section 3.4.2) and provides the relative rate uncertainty, which for simplicity is taken symmetric with the average interval width of 49%.

3.3 Detector response model to ER and NR interactions

The modelling of the XENON1T response to electronic and nuclear recoils is based on a simulation which takes into consideration detailed characterizations of detector systematics, as well as a comprehensive modelling of the electron-ion recombination process in LXe. By modelling and fitting the detector response simultaneously for ER and NR, shared detector uncertainties can be treated coherently and all available information is used to constrain uncertainties.

3.3.1 Liquid xenon microphysics

The intrinsic signal response model in LXe follows the approach used in the NEST model [254,255], including the recombination fluctuation [256]. Energy deposited in LXe goes to three forms: thermalization of the recoiling particle, excitation and ionization of xenon atoms. The thermalization energy loss is undetectable in the XENON1T detector. The deposited energy ε can be reconstructed through the average sum (total number of quanta N_q) of number of excimers N_{ex} and ion-electron pairs N_i:

$$\langle N_q \rangle = L\varepsilon/W, \tag{3.4}$$

where L is the Lindhard factor expressing the fraction of energy loss to thermalization and W ($13.7 \pm 0.2\,\text{eV}$ from a global fit [254]) is the average energy required in LXe to create either an excimer or ion-electron pair. Negligible energy is lost to thermalization in an ER as the mass of the recoiling electron is much smaller than the xenon nucleus. In NRs, the recoiling xenon atom leaves kinetic energy through elastic scattering off surrounding atoms (thermalization), resulting in a Lindhard factor of 0.1-0.2 in LXe. The field- and energy-dependence of the Lindhard factor is parametrized following the NEST model [255]. The loss of deposited energy to heat in NRs leads to Poissonian fluctuations of the reconstructed energy:

$$N_q \sim \text{Poiss}\left(\langle N_q \rangle\right). \tag{3.5}$$

The division of the quanta expressed by the excimer-to-ion ratio N_{ex}/N_i is related to the excitation and ionization cross sections of recoiling particles on xenon atoms. For ERs, it is assumed to be constant, and is given a uniform prior ranging from 0.06 to 0.20 [254]. For NR, it is parametrized as a function of deposited energy and electric

field F, following [255]:

$$N_{ex}/N_i = \alpha F^{-\zeta}\left(1 - e^{-\beta\varepsilon}\right), \tag{3.6}$$

where α, β and ζ are tuned parameters in the model. This leads to the binomial fluctuations of N_{ex} and N_i:

$$\begin{array}{rcl} N_i & \sim & \text{Binom}\left(N_q, \frac{1}{1+N_{ex}/N_i}\right), \\ N_{ex} & = & N_q - N_i. \end{array} \tag{3.7}$$

The electrons have a probability $1-r$ to escape the cloud of ion-electron pairs, depending on both the deposited energy and the electric field applied:

$$\begin{array}{rcl} N_e & \sim & \text{Binom}\left(N_i, 1-r\right), \\ N_\gamma & = & N_i - N_e, \end{array} \tag{3.8}$$

where N_γ and N_e are the number of photons generated by ion-electron recombination and of escaping electrons, while r is the recombination fraction. Due to detector effects, such as field non-uniformity and intrinsic fluctuations [256], the recombination fraction r has fluctuations and is modelled as Gaussian:

$$r \sim \text{Gauss}\left(\langle r\rangle, \Delta r\right), \tag{3.9}$$

where Δr is the recombination fluctuation, modelled as energy-independent. The mean recombination fraction $\langle r\rangle$ is described by the Thomas-Imel (TI) box model [257]:

$$\langle r\rangle = 1 - \frac{1 + N_i\varsigma}{N_i\varsigma}. \tag{3.10}$$

For NRs, the TI box model associated with the Lindhard factor has been shown to match data well [255]. The recombination fluctuation was shown to be subdominated by the statistical fluctuations [258] induced by equations (3.5) and (3.7), and is set to 0 for NR in the signal response model. For the parametrization of NR recombination fraction $\langle r\rangle_{nr}$, equation (3.8) with additional field dependence of ς is used:

$$\varsigma = \gamma_{nr} F^{-\delta_{nr}}, \tag{3.11}$$

where γ_{nr} and δ_{nr} are parameters tuned to match data, with constraints from the NEST global fit [255].

For low energy ERs, several recent measurements [256, 260, 261, 263] indicate that the TI box model cannot fully describe the recombination process. A modified TI box model is therefore used to parametrize the ER recombination fraction $\langle r\rangle_{er}$:

$$\langle r\rangle_{er} = \left(1 - \frac{\ln(1 + N_i\varsigma)}{N_i\varsigma}\right) / \left(1 + e^{-(\varepsilon - f_0)/f_1}\right), \tag{3.12}$$

$$\varsigma = \gamma_{er} e^{-\varepsilon/\omega_{er}} F^{-\delta_{er}}, \tag{3.13}$$

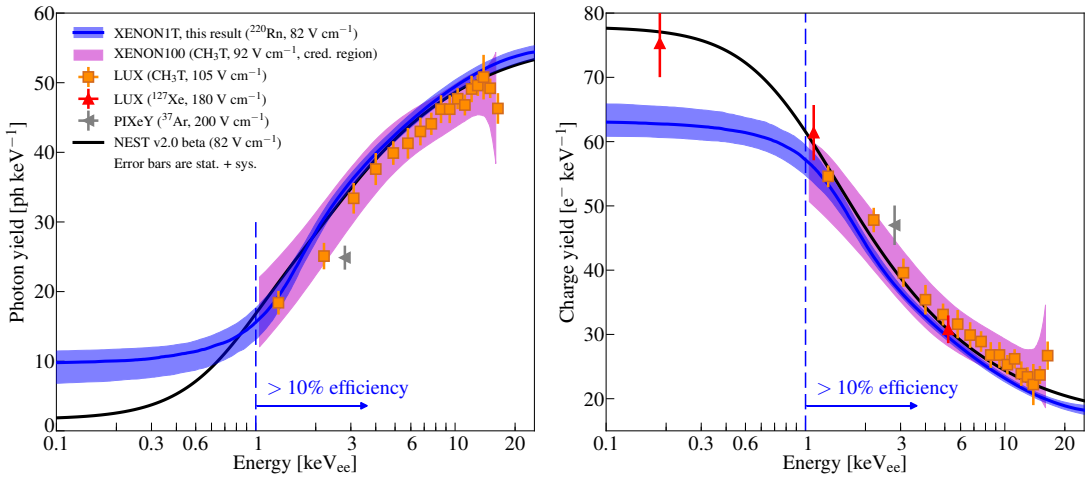

Figure 3.17: Mean photon and charge yields of ER in the XENON1T calibration data fit is shown in blue. The blue solid line and shaded region represent the point estimation and 15%-68% credible region, respectively, of the posterior. The measurements from [256, 259–261] are shown along with the best fit of NEST v2.0 beta [262]. The vertical dashed blue line indicate the energy threshold for XENON1T ER calibration, below which the detection efficiency drops to less than 10%.

where the Fermi-Dirac term in equation (3.12) and the exponential term in equation 3.13 was added to the TI box model in order to account for the deviation of measurements in <3 keV and >10 keV energy ranges, respectively. Similarly to NRs, the field dependence of the ER TI box parameter ς follows a power law as introduced in NEST [255]. The adjustable parameters f_0, f_1, γ_{er}, ω_{er}, and δ_{er} are not given other constraints than the matching of the signal response model to XENON1T data. Figure 3.17 and 3.18 show the mean photon and charge yields as a function of energy for ER and NR, respectively, as well as related measurements. The mean photon $\langle N_\gamma/\varepsilon\rangle$ and charge yield $\langle N_e/\varepsilon\rangle$ are defined as:

$$\begin{aligned} \langle N_\gamma/\varepsilon\rangle &= \frac{1}{W}\frac{\langle r\rangle + N_{ex}/N_i}{1+N_{ex}/N_i}, \\ \langle N_e/\varepsilon\rangle &= \frac{1}{W}\frac{1-\langle r\rangle}{1+N_{ex}/N_i}. \end{aligned} \tag{3.14}$$

The calibration of low energy ER in XENON1T is performed using an internal ^{220}Rn source [108]. The calibrated ER sample using β-decays from a ^{220}Rn source is analogous to the dominant ER background from ^{214}Pb β decays in the low energy region (<10 keV). However, the response model built for ER in XENON1T is not in principle applicable to γ-induced ER, that at sufficiently high energy may interact with the inner-shell electrons. When this happens, the vacancy in the inner shell results in either X-ray fluorescence, which further ionizes the surrounding xenon atoms, or Auger electrons. Consequently, γ-induced ER can have multiple β particles instead of one as in β-induced ER. The binding energies for K- and L-shell electron in xenon are about 34.6 keV and 4.8 − 5.5 keV, respectively. According to the NIST database [271], the corresponding X-rays have mean free paths of about 10 µm and 0.4 µm, respectively. The effect on the recombination of electron clouds separation at this scale is not well

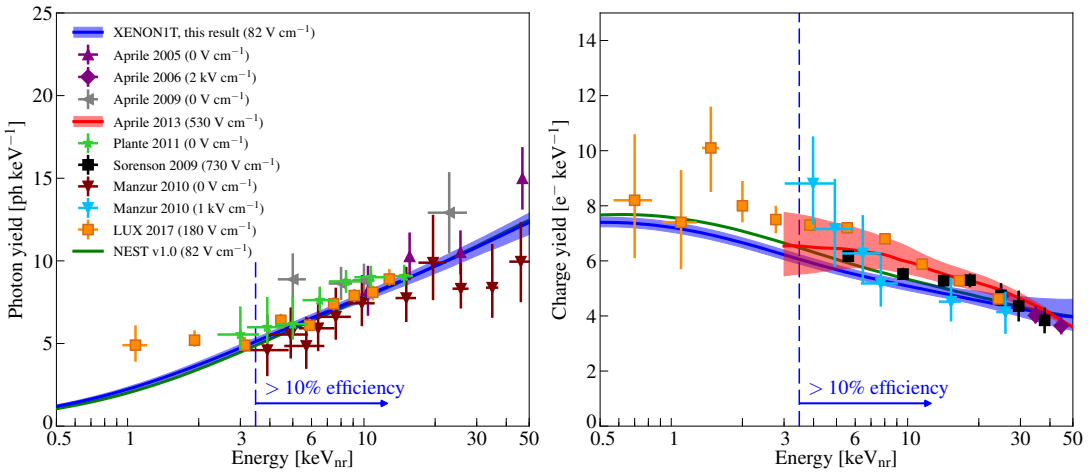

Figure 3.18: Mean photon and charge yields of NR in the XENON1T calibration data fit is shown in blue. The blue solid line and shaded region represent the point estimation and 15%-68% credible region, respectively, of the posterior. Data points are from fixed-angle neutron scattering measurements [264–270]. Results of XENON100 [258] using data-MC matching on ^{241}AmBe calibration method are shown with the red solid line and shaded region. The best fit from NEST [255] is shown with the green solid line. The vertical dashed blue line indicate the energy threshold for XENON1T NR calibration, below which the detection efficiency drops to less than 10%.

understood yet.

3.3.2 Detector signal reconstruction

Besides the intrinsic response of LXe, detector reconstruction effects on the total response are modelled. Detector features bring non-negligible contributions to the bias and fluctuation of the reconstructed scintillation (S1) and charge (S2) signals. More specifically, the spatial dependence of S1 and S2, the double photoelectron emission (DPE) of PMT photocathode [272, 273], the position reconstruction uncertainty, the reconstruction efficiency, bias and fluctuation of the signal, and the acceptance of data selection in the analysis are taken into account in the model.

Following the generation of photons and electrons in an energy deposition through the recombination (equation 3.8), photons are detected by the PMTs with a light collection efficiency ϵ_L. Electrons are drifted to the gas-liquid interface in the electric field and are extracted under the stronger gas field, amplifying the electron signal with the gas gain G. Both ϵ_L and G are spatially dependent and related to the energy scale parameters g_1' and g_2' by:

$$\begin{aligned} g_1'(\vec{x}) &= p_{dpe} \cdot \epsilon_L(x,y,z), \\ g_2'(x,y) &= \epsilon_{ext} \cdot G(x,y), \end{aligned} \tag{3.15}$$

where p_{dpe} is the average DPE probability of PMTs [272, 273] and ϵ_{ext} is the extraction efficiency which is assumed to be constant. The number of hits detected by a PMT N_{hit}

and photoelectrons generated from the PMT photocathode N_{pe} can be written as:

$$\begin{array}{rcl} N_{hit} & \sim & \text{Binom}\left(N_{ph}, g_1'(\vec{x})\right), \\ N_{pe} - N_{hit} & \sim & \text{Binom}\left(N_{hit}, p_{dpe}\right). \end{array} \tag{3.16}$$

In addition to the (x,y) dependence caused by the charge amplification, S2 signals depend on z position due to electrons attaching to impurities as the electrons drift. The number of electrons that survive the drifting and extraction N_{ext} are:

$$N_{ext} \sim \text{Binom}\left(N_e, e^{-z/(\tau_e \cdot \nu_d)} \epsilon_{ext}\right), \tag{3.17}$$

where τ_e and ν_d are the electron lifetime and electron drift velocity, respectively. The total proportional scintillation light detected by PMTs N_{prop} can be approximated as:

$$N_{prop} \sim \text{Gauss}\left(N_{ext}G, \sqrt{N_{ext}}\Delta G\right), \tag{3.18}$$

where ΔG is the spread of the gas gain. For simplicity, we consider $\Delta G/G$ a constant in the model.

The uncorrected S1 and S2 signals are constructed from N_{pe} and N_{prop}, respectively, amplified by PMTs, digitized and selected by the XENON1T clustering and classification software [274]. To account for biases and fluctuations in this process, the uncorrected S1 and S2 are written as:

$$\begin{array}{rcl} S1/N_{pe} - 1 & \sim & \text{Gauss}\left(\delta_{s1}, \Delta\delta_{s1}\right), \\ S2/N_{prop} - 1 & \sim & \text{Gauss}\left(\delta_{s2}, \Delta\delta_{s2}\right), \end{array} \tag{3.19}$$

where δ_{s1} (δ_{s2}) and $\Delta\delta_{s1}$ ($\Delta\delta_{s2}$) are the bias and spread, respectively, of the S1 (S2) reconstruction. The reconstruction bias and fluctuations are estimated using a waveform simulation including a realistic scintillation pulse shape, charge amplification model, electronic noise, PMT single PE spectrum, PMT after pulses, and impurity photoionization.

The S1 and S2 are corrected for their spatial dependence based on the reconstructed positions $\vec{x}_r$. The z position of an event is reconstructed using the time difference between S1 and S2 signals, and has relative higher resolution than the (x, y) position which is reconstructed through the S2 hit pattern on PMTs at top array (see section 4.1.1). We assume the reconstruction fluctuations along x and y axes are identical. The reconstructed position of x_r can be written as:

$$x_r \sim \text{Gauss}\left(x, \sigma_p\right), \tag{3.20}$$

where σ_p is the position reconstruction resolution, which depends on both S2 area and the position of event. The corrected S1 (cS1) and S2 (cS2) are derived based on the reconstructed position:

$$\begin{array}{rcl} \text{cS1} & = & \text{S1}\frac{g_1}{g_1'(\vec{x}_r)}, \\ \text{cS2} & = & \text{S2}\frac{g_2}{g_2'(x_r, y_r)} e^{z/(\tau_e \cdot \nu_d)}. \end{array} \tag{3.21}$$

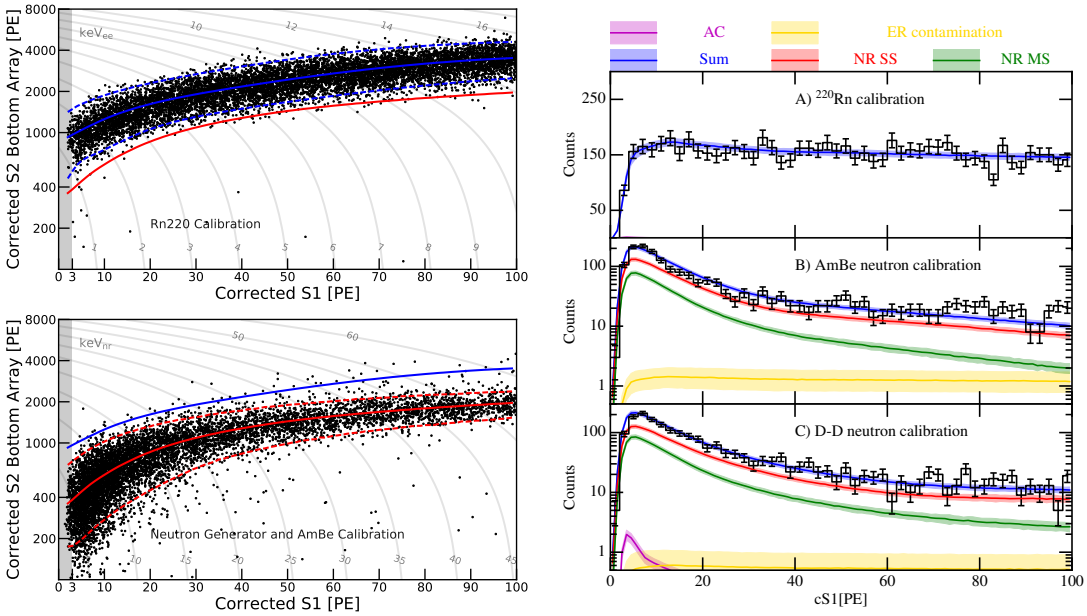

(a) (b)

Figure 3.19: (a) The XENON1T ER (top) and NR (bottom) bands. In the top panel, the ER median line (solid blue) is drawn together with the 2σ contours and the NR median (solid red). Data points are low energy ER calibration data from ^{220}Rn source. The bottom panel shows the NR model, with median and 2σ quantiles (solid and dashed red lines respectively). Data points are from neutron calibrations with ^{241}AmBe and D-D fusion neutron gun sources. The derived ER and NR energy scales are shown in grey lines in the respective plots. (b) cS1 projection of the signal response model fitted to calibration data. Solid lines represent the median of the posterior, and the shaded regions show the 15.4% to 84.6% credible regions of the posterior. The accidental pileup (AC, magenta), ER contamination (yellow), single-site (red), and multiple-site NR scatter (green) components are considered in the complete model.

Selection criteria were applied to data to ensure the purity of the sample and to optimize the signal-to-background ratio for the dark matter search (see section 4.3). The detection efficiency loss arises from the software reconstruction efficiency of S1s, and from the S1- and S2-related event selections. The efficiencies for these are considered as functions of N_{hit}, S1 and S2, respectively, in the signal response model. In addition, the selection of single-site scatters applied to actual data (described in section 3.2.3) is also implemented in the simulation in order to accurately address the acceptance of single-site scatters and the rejection power against multiple-site scatters.

3.3.3 Fit to calibration data

The signal response model is constrained using the calibration data from ^{220}Rn, for ER, and ^{241}AmBe and D-D generator, for NR (see figure 3.19a). With the calibration fit, the response model is used to construct WIMP signal and background models for the statistical inference of dark matter search data [108, 109]. The fit is performed simultaneously using all available XENON1T calibration data taken during the first

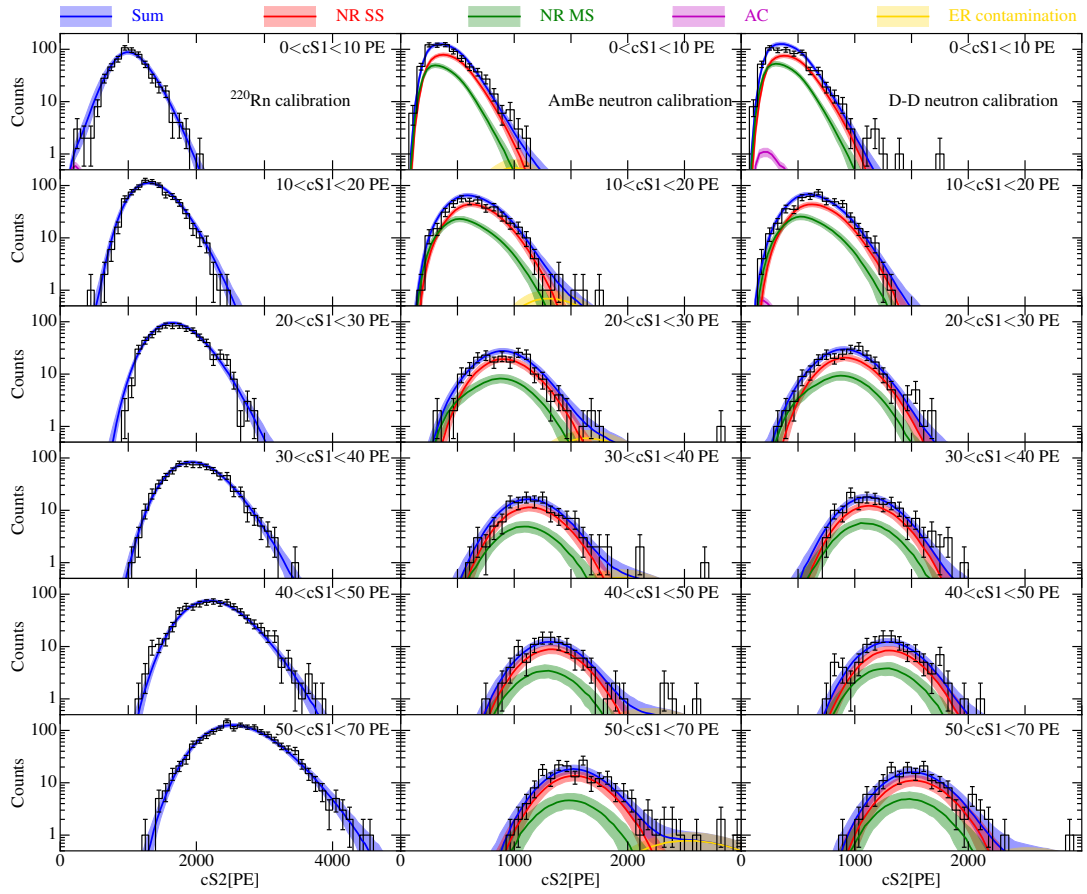

Figure 3.20: The cS2 spectra in different cS1 ranges of the ^{220}Rn ER, ^{241}AmBe and D-D fusion neutron calibration data (black), and the fitted signal response model (blue). Solid lines and shaded regions are the median and 1σ credible regions of each model component posterior (with same color code of figure 3.19b).

(SR0) and second (SR1) science data taking periods. The test is based on the binned likelihood for distributions in Log_{10}(cS2/cS1) versus cS1, using the data in the 1 tonne cylindrical fiducial volume defined in SR0 [108]. The likelihood is sampled using the affine invariant Markov Chain Monte Carlo (MCMC) [275]. The model fitted to ER and NR calibration data includes also accidental S1-S2 coincidences (AC, see section 4.4.2) and multiple-site scattering events passing the single scatter selection.

The fit to the cS1 spectrum of each calibration data sample is shown in figure 3.19b. Figure 3.20 shows the cS2 spectra in different cS1 ranges together with the posterior of the tested signal response model. The matching between the signal response model to the calibration data is good, with the goodness of fit p-values for cS2 spectra comparison in different cS1 ranges all above the 5% threshold set for an acceptable fit. The derived XENON1T ER and NR models in the bi-dimensional signal space are shown in figure 3.19a through the medians (solid lines) and the 2σ quantiles (dashed) overlaid to

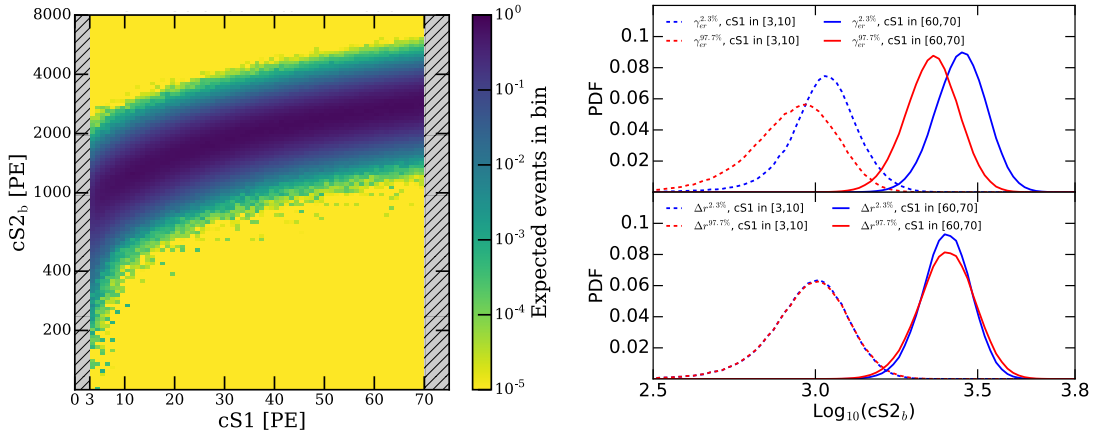

Figure 3.21: The XENON1T ER background model in the WIMP search ROI. (a) ER background distribution in the (cS1, cS2$_b$) observable signal space derived from nominal signal response model to ER interactions. (b) Change in Log$_{10}$(cS2$_b$) distributions as γ_{er} (top panel) and Δr (bottom panel) varies, from the 2.3% percentile to 97.7%th percentile of the signal model posterior, in different cS1 ranges.

the calibration data points. Under the obtained models, the fraction of ERs that leak in the NR reference region, defined between the median and -2σ contour of the NR distribution, is estimated to be 0.3%.

3.4 Background models in the observable space

The XENON1T ER and NR background models in the observable signals space (cS1, cS2$_b$) are built based upon the signal response models illustrated in section 3.3. The obtained ER and NR response models are employed to translate the expected recoil energy spectra derived from the MC simulations discussed in sections 3.1 and 3.2 into the final background models within the WIMP search ROI defined by the intervals (3, 70) PE of cS1 and (50, 8000) PE of cS2$_b$ signal size.

3.4.1 ER background model

The energy distribution of ER background is assumed to be uniform in the ROI due to the dominance of ^{222}Rn contribution. The uncertainties of the (cS1, cS2$_b$) distribution for the ER background is dominated by the uncertainties of γ_{er} in equation (3.13) and the recombination fluctuation Δr in equation (3.9). The effects of varying γ_{er} and Δr are to shift the mean and change the spread, respectively, of the ER distribution in cS2$_b$. Figure 3.21b shows the variation of the ER distributions on Log$_{10}$(cS2$_b$) in different cS1 ranges. The distributions are produced by the signal response model with the other nuisance parameters marginalized to the point estimation (median posterior)

after the fit to calibration data. The γ_{er} and Δr distributions are computed at 2.3%, 6.7%, 15.9%, 30.9%, 50.0%, 69.1%, 84.1%, 93.3%, 97.7% percentiles of the posterior after the calibration data fit.

The ER background distribution in the signal space at the nominal values of γ_{er} and Δr is presented in figure 3.21a. The ER background is uniformly distributed in the fiducial volume due to the dominant contribution of the intrinsic contaminant ^{222}Rn. The ER background prediction in the ROI within the 1.3 tonnes fiducial volume and for the combined (SR0+SR1) livetime of 278.8 days (for a total 0.99 t · y exposure) is

$$627 \pm 18 \text{ events.} \tag{3.22}$$

The ER expectation value is derived from the fit of the ER model in figure 3.21a to DM search data. The residual ER background in a NR signal reference region, defined between the median and -2σ quantile of 200 GeV/c^2 WIMP signal distribution, amounts to 1.62 ± 0.30 events, corresponding to a rate of 2.12 ± 0.39 events per year in the 1.3 tonnes FV.

3.4.2 NR background model

The XENON1T NR background model is composed by the contributions of radiogenic neutrons and neutrinos undergoing CNNS. The neutron background component induced by muons is neglected as its expected rate is approximately two orders of magnitude lower than the one due to neutrons from radioactive contaminants in detector materials. The models of both NR background sources, obtained convoluting the expected recoil energy spectra with the XENON1T NR response model, are shown in figure 3.22 (note that the same colorbar normalization is used in figures 3.21a and 3.22 for easy comparison).

For the XENON1T DM search presented in this work, the expectation value of the neutron background derived from MC simulations, with the complete treatment of the neutron-X component and taking into account the constraint derived from the observation of neutron multiple scatters in data, amounts to

$$1.43 \pm 0.66 \text{ events} \tag{3.23}$$

in the ROI and inside the 1.3 tonnes fiducial volume, i.e. 1.87 ± 0.86 events per year. The spatial distribution of the neutron background is derived from MC simulations and it is shown in figure 3.11. Inside the 0.65 tonnes core volume (green dashed line in figure 3.11) 0.26 ± 0.13 NR events due to radiogenic neutrons are expected. The rate uncertainty comes from the combination of 50% from MC simulation prediction and the measurement of multiple scatters as discussed in section 3.2.5. The rate uncertainty propagated from the NR response model amounts to 15% (3%) for 6 (200) GeV/c^2 WIMPs. The spectral shape of the neutron background is very similar to the expected NR spectrum induced by WIMPs of mass $\gtrsim 100$ GeV/c^2. Thus, the 3% uncertainty from the NR response model is negligible for the prediction of the radiogenic neutrons

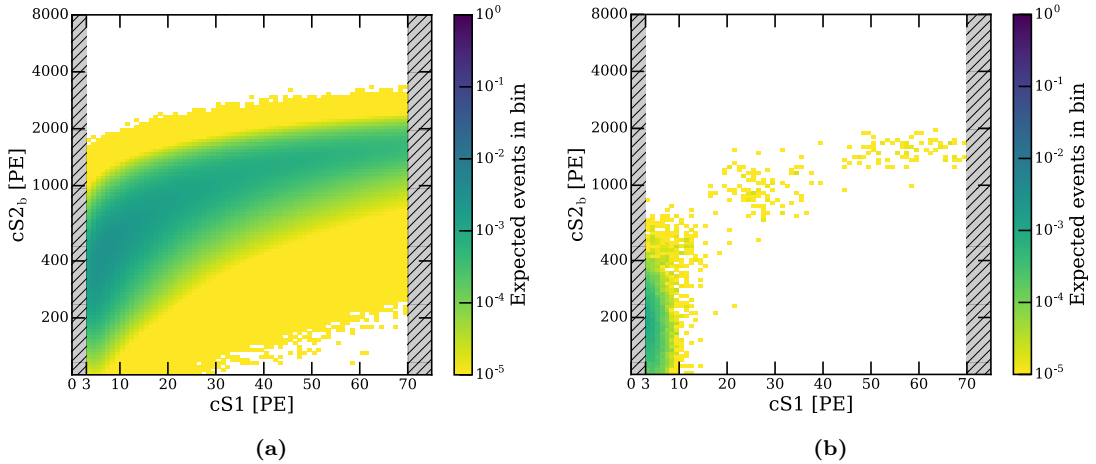

Figure 3.22: The XENON1T NR background model derived from nominal signal response model to NR interactions, in the (cS1, cS2$_b$) observable signal space. (a) Radiogenic neutron background distribution, including the neutron-X population. (b) Coherent neutrino-nucleus elastic scattering background distribution.

background level. The NR background from radiogenic neutrons is almost 30 times higher with respect to the one induced by neutrinos with CNNS, which is

$$0.05 \pm 0.02 \text{ events}, \tag{3.24}$$

where a total 29% uncertainty combines the 15% from the NR model (as the CNNS spectrum is almost identical to a 6 GeV/c^2 WIMP) and the indetermination on neutrino flux and CNNS cross section (as discussed in section 3.2.2).

The complete XENON1T background model includes also a surface background, due to inward reconstructed events at the TPC wall with reduced charge signal, and the contribution from accidental S1-S2 pile-ups. Such backgrounds and their models are presented in section 4.4 along with WIMP signal models.

Chapter 4

XENON1T data analysis and WIMP search results

The dark matter search discussed in this work combines data from the two science runs of the XENON1T experiment. The first science run (SR0) spanned from 22 November 2016 to 18 January 2017, when an earthquake of magnitude 5.7, occurred in central Italy, temporarily interrupted detector operation. After a brief period of maintenance, the second science run (SR1) started on 2 February 2017 and continued until 7 February 2018, marking over one year of stable data-taking operation. Accumulated live time of DM search data is 32.1 (246.7) days in SR0 (SR1) for total 278.8 live-days in the combined exposure (see figure 4.1), corrected for insensitive time periods due to dead-time of data acquisition system (7.8% and 1.2% in SR0 and SR1), Muon Veto triggers or down-time (1.2% overall) and high energy events that induced large photo-ionization and delayed electron extraction activity (4.4%). XENON1T is the most sensitive detector to date and set the world-best upper limit on the WIMP-nucleon spin-independent cross section for WIMP masses above $6\,\mathrm{GeV/c^2}$ with a minimum of $4.1 \times 10^{-47}\mathrm{cm}^2$ at $30\,\mathrm{GeV/c^2}$ [109], as will be presented in this work.

The XENON1T data analysis work flow is presented in this chapter, from reconstruction and characterization of detector's signals (see section 4.1) towards the statistical inference approach adopted to interpret the observed dataset (see section 4.5). The detector response to physical interactions in the active LXe target is calibrated during the time span of the science runs. Internal ^{220}Rn and external neutron sources are deployed to calibrate the low energy ER and NR, respectively, whose modelling was discussed in section 3.3. The dependency of recorded signals from the interaction position across the TPC is characterized with internally diffused ^{83m}Kr calibration source, that allows to study the position reconstruction performances upon which a set of corrections to the observed S1 and S2 signals is based. The presence of mono-energetic lines (at higher energy with respect to the ROI for DM search) in the XENON1T background spectrum provides the mean to assess the experimental energy scale, reconstructed from the combined information of the corrected S1 and S2 signals, and to monitor the stability

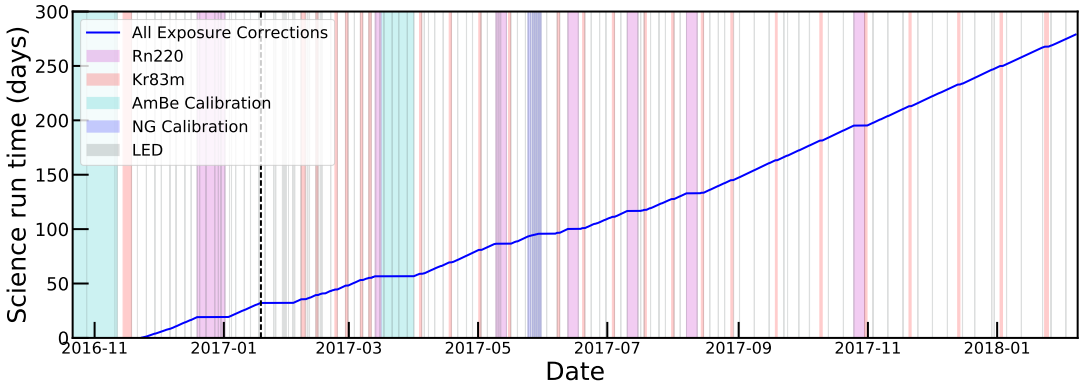

Figure 4.1: XENON1T live time in the first two dark matter search runs, SR0 (whose end is indicated by a grey dashed vertical line) and SR1. The collected exposure, corrected for dead-times due to insensitive detector conditions, is shown as a blue line. Periods indicated by colored boxes refer to data collected in the presence of various calibration sources: ^{220}Rn for low energy ERs [228] (17.1 days, magenta), ^{83m}Kr for spatial corrections [225] (every ∼2.5 weeks, red), LED to monitor PMT gains [276] (∼2 times a week, grey), ^{241}AmBe [203] (30.0 days, cyan) and D-D fusion neutron generator [229] (1.9 days, blue) for NRs.

of signals over time (see section 4.2). The selection criteria imposed to data, including the fiducial volume definition, data quality cuts and single scatter events selection, are discussed in section 4.3 as well as the resulting acceptance to DM signal. The XENON1T ER and NR background models were presented in section 3.4. The complete background model also features two sources of non-standard interactions which are modelled with data-driven approaches: accidental coincidences of spurious S1 and S2 signals and surface events happening at the TPC edges (in the PTFE lateral reflectors) whose charge signal is partially trapped at the surface. The final background predictions for the XENON1T 1 tonne×year DM search are presented in section 4.4 along with the adopted WIMP signal model. The results obtained with the profile likelihood analysis (outlined in sections 4.5.1 and 4.5.2) on the collected DM search data are finally discussed in section 4.5.3.

4.1 Detector characterization and signal reconstruction

Events from the XENON1T detector are reconstructed processing the raw waveforms of each PMT, recorded by the DAQ system, through a custom-developed data processor software, named Processor for Analyzing XENON, PAX (described in [203]). A sophisticated waveform simulator (called FAX) has been developed for optimization of software algorithms used in PAX, such as PMT hit finding in raw waveforms, clustering and peak classification. In addition, FAX is used to estimate the XENON1T event reconstruction efficiency and bias. The reconstruction of interactions' vertex position (discussed in section 4.1.1) is a crucial feature of the dual-phase TPC technology for background suppression through active volume fiducialization but also for position-

dependent corrections to both S1 and S2 signals (see section 4.1.2). XENON1T utilizes periodical calibrations with ^{83m}Kr, which is the ideal source to characterize the spatial dependency of detector response as it rapidly (within 1 hour) diffuses in the LXe target and provides high-statistics peaks at 9 and 32 keV (which are often reconstructed as a merged 41.5 keV line). The complete characterization of the detector response to known mono-energetic gamma lines (external gammas from detector materials or induced during calibration runs) allows to reconstruct the actual energy deposited by an interaction from the observable S1 and S2 and to estimate the energy resolution of the experiment (see section 4.1.3), which is crucial to explore new physics channels whose expected signal is a peak in the observed energy spectrum.

4.1.1 Position reconstruction

The position of interactions occurring in the active TPC volume (specifically between the cathode, at the bottom, and the grounded gate electrode, at the top) is reconstructed in three dimensions. The z coordinate is determined by the time difference between the prompt S1 and the delayed S2 signal due to the drift of freed charges under the electrical field.

The position in the (x, y) plane is obtained from the pattern of hits on the top PMT array of the delayed and amplified S2 signal. A total number of 15 PMTs, out of 127, in the top array are excluded from the data analysis (as can be seen from figure 4.2b) due to vacuum leaks, low single photoelectron (SPE) acceptance or impulsive light emission (flashing). In particular, one PMT switched off during SR0, showing low SPE acceptance, has been recovered for SR1 (after reducing its self-trigger threshold), while another PMT operative in SR0 was excluded in SR1 due to flashing. In the bottom PMT array, which has no influence on position reconstruction, 20 (1) among the 121 PMTs were turned off during SR0 (SR1).

Several position reconstruction algorithms have been developed and tested for XENON1T. Two of them, Neural Network (NN) and Top Pattern Fit (TPF), provide the best results in terms of position resolution. The NN algorithm is developed based on the Fast Artificial Neural Network library (FANN) [278], while the TPF algorithm [279] makes use of a maximum likelihood technique based on the measured S2 hit pattern in top PMTs. The NN and TPF algorithms give similar position resolution of $\sim$2 cm at very small S2 signals (200 PE); NN is chosen for the (x, y) reconstruction in the XENON1T combined (SR0+SR1) DM search.

Position reconstruction algorithms are trained with MC simulations of the PMT hit patterns caused by known initial positions of electron extraction. The optical simulations are performed using the XENON1T detector model [135, 280] developed with the GEANT4 toolkit [234]. Optical parameters, such as refractive index, PTFE reflectivity, xenon absorption length and Rayleigh scattering length are tuned by matching the light collection efficiency between ^{83m}Kr calibration data and simulated optical photons. Training samples for position reconstruction are large amounts ($\mathcal{O}(10^5)$) of uniformly

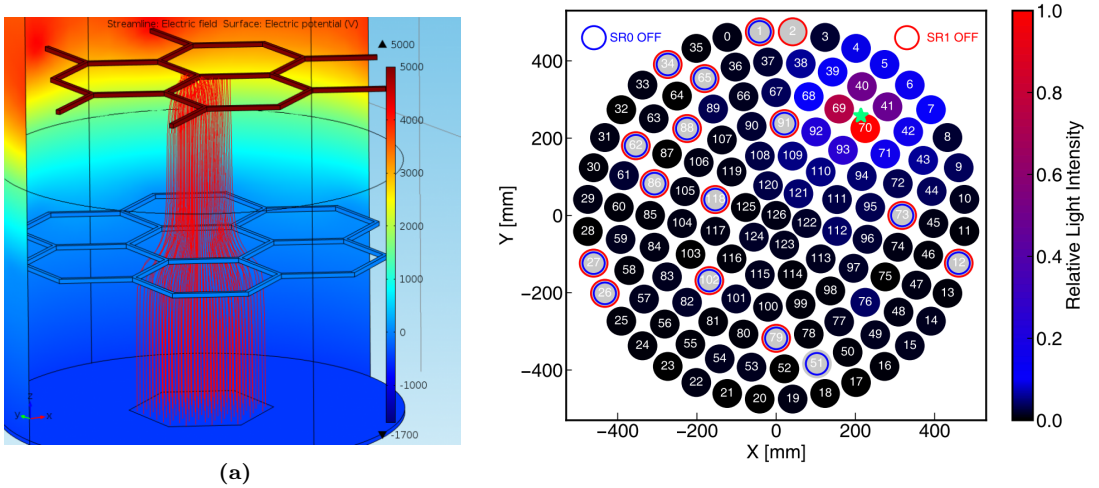

(a) (b)

Figure 4.2: (a) Simulation of electric field streamlines between the gate (grounded and immersed in liquid xenon, ∼2.5 mm below the liquid-gas interface) and the anode hexagonal mesh (with positive high voltage, in the gaseous region ∼5 mm above the gate mesh) performed with the COMSOL Multiphysics software [277]. The proportional scintillation S2 signal is originated right below the anode, whose hexagonal cells opening diameter is about 4 mm. (b) Example of the S2 hit pattern on top PMTs for a simulated S2 event showing how the proportional scintillation light distributes across the active PMTs (those switched off during SR0 and SR1 are indicated by a hollow circle of blue and red color, respectively). The origin of simulated optical photons is marked with a green star.

distributed S2 events in the gaseous amplification region, generated within a hexagonal mesh-like structure that reproduces the realistic S2 generation just below the anode hexagonal electrode mesh, as suggested by simulations of electric potential in that region (see figure 4.2a). Figure 4.2b shows the hit pattern on the PMTs of top array from a single simulated event whose original position in the (x, y) plane is marked with a green star.

The position reconstruction error, defined as the distance between the true and the reconstructed position, depends on the S2 size, being larger for low energy signals. The resolution derived from MC simulations is ∼4 mm for S2$\gtrsim$2000 PE and worsen up to ∼10 mm for 200 PE S2s. Moreover, the position resolution worsens toward the TPC lateral edges up to a factor ∼2 at the maximum radius (47.6 cm). The effect of dead PMTs is seen for radii larger than 41 cm reducing the precision of reconstructed position. Photon reflection on the lateral PTFE panels in the GXe gap also affects the position reconstruction error, in particular around $r = 45$ cm. In the future XENONnT TPC a non-reflective lateral wall in the GXe region will be used to alleviate this issue.

The performance of position reconstruction is also evaluated with data-driven approaches. The resolution can be derived from the two-step scatter produced by gamma emission of the ^{83m}Kr calibration source or from the ^{214}BiPo beta-alpha decay coincidence (also exploited to constrain ^{214}Pb concentration as discussed in 3.1.2). The metastable krypton subsequently decays to the ground state in two steps by emitting

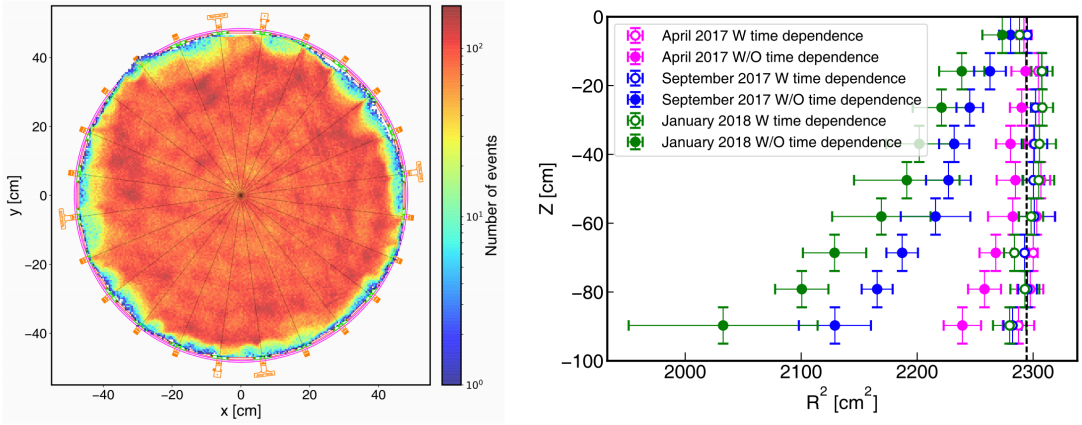

(a) (b)

Figure 4.3: Impact of drift electric field distortion on position reconstruction. (a) Reconstructed (x, y) position of ^{83m}Kr events before correcting for the electric field distortion. The revealing bite structure coincides with the 24 sliding PTFE reflectors (red) which form the TPC wall along with fixed PTFE reflector panels (green). Pillars (orange) to fix the PTFE reflectors and field shaping rings (pink) to uniform the drift electric field are also shown. (b) Reconstructed (r^2, z) position of the TPC edge (from ER background data) in three different time periods during SR1. Filled circles are edge positions before adding time-dependence to the position correction in April 2017 (magenta), September 2017 (blue) and January 2018 (green). Hollow circles indicate the edge position after adding the time-dependence. The TPC wall is drawn as a vertical black dashed line.

a 32.1 keV gamma and then a 9.4 keV conversion electron (with 154 ns half-life). The double S1 structure is resolved thanks to the short width of S1 pulses in XENON1T, while the two S2s are distinguished only for events in the top layer of the TPC, where the S2 signal is narrower due to the smaller diffusion. The mean free path of the 9.4 keV gamma is about 10 µm, thus the location in LXe of the two ^{83m}Kr transitions can be assumed coincident. Therefore, the difference of reconstructed position between the two lines can give an estimate of the position resolution. Analogously, the ^{214}Po alpha decay (with 164 µs half-life) has a range in LXe of ∼50 µm, producing then a second S2 after the ^{214}Bi β in the same position. The inferred reconstruction errors from both methods are compatible and give a resolution of ∼5 mm for large S2s and ∼2 cm at 200 PE.

Correction for electrical field distortion Electron attachment on PTFE has been observed during XENON1T operation. Based on NN algorithm, reconstructed positions of events produced by the homogeneously distributed ^{83m}Kr calibration source reveal a "bite" structure, as shown in figure 4.3a, that coincides with the 24 PTFE reflector panels making up the TPC wall. Such an effect leads to a non-axially symmetric electric drift field and to inward biased field lines at the TPC edge. Together with electric field leakage through the cathode electrode, charge attachment on PTFE panels is responsible for non-uniform drift field that challenges the position reconstruction. A three-dimensional correction in the (r, z, ϕ) space has to be applied to the distorted

reconstructed positions, particularly at the bottom of the TPC due to the larger drift length along inward biased field lines. A data-driven method is preferred with respect to a complete 3D electrical field simulation considering that the electron attachment mechanism is not well understood yet and the extremely time-consuming calculations required. A position correction map binned in 180 ϕ sectors and 40 z slices and finally interpolated to ensure continuity, is derived from the observed non-uniformity in the spatial distribution of ^{83m}Kr events. The correction map is also validated against ^{131m}Xe events, from the xenon isotope activated during neutron calibrations (see section 4.2.1), which are also expected to be uniformly distributed. Moreover, the corrected positions of neutron interactions produced by the external sources (^{241}AmBe and neutron generator) show good consistency with the simulated distributions.

As electrons keep building up on PTFE panels, a more severe electric field distortion is observed in later stages, which requires the implementation of a time-dependent position correction (see figure 4.3b). The time evolution of the induced bias on reconstructed positions is evaluated through ^{83m}Kr calibrations that are performed periodically (approximately twice per month) during the XENON1T science runs. The reconstructed TPC edge is also evaluated on background data by Gaussian fitting to the radial distribution of the outermost events, which are due to external gammas from detector materials. As shown in figure 4.3b, the reconstructed TPC edge, before the time-dependent correction, moves inwards with time as result of the continuous charge accumulation on the PTFE wall. Viable improvements to reduce such charge up in XENONnT are minimizing the region at the TPC edges with electric field lines closing on the PTFE wall and allowing for electrodes to touch the external surface of the side reflector.

4.1.2 Signal corrections

The size of the detected raw S1 and S2 signals is dependent on the event location in the detector. The detection efficiency of photons generated at the interaction site (S1) and in the gaseous xenon phase (S2) varies across the detector due to geometrical effects, variations of the thickness of the gaseous amplification region, electron attachment to electronegative impurities in LXe and electric field inhomogeneities. The corrections applied to S1 and S2 for such detector effects are described in this section.

S1 light collection efficiency The correction for geometrical effects impacting on the light collection of S1 signal is derived using ^{83m}Kr calibration data. The light collection efficiency (LCE) is determined by measuring the 32.1 keV line in discrete (r, ϕ) regions in slices of z. The LCE correction map, shown in figure 4.4a, is calculated by comparing the observed S1 signal amplitudes in each spatial bin with the average across the TPC and finally interpolating between bins. The corrected S1 signal is then defined as

$$\mathrm{cS1} = \frac{\mathrm{S1}}{\mathrm{LCE}(x, y, z)}. \tag{4.1}$$

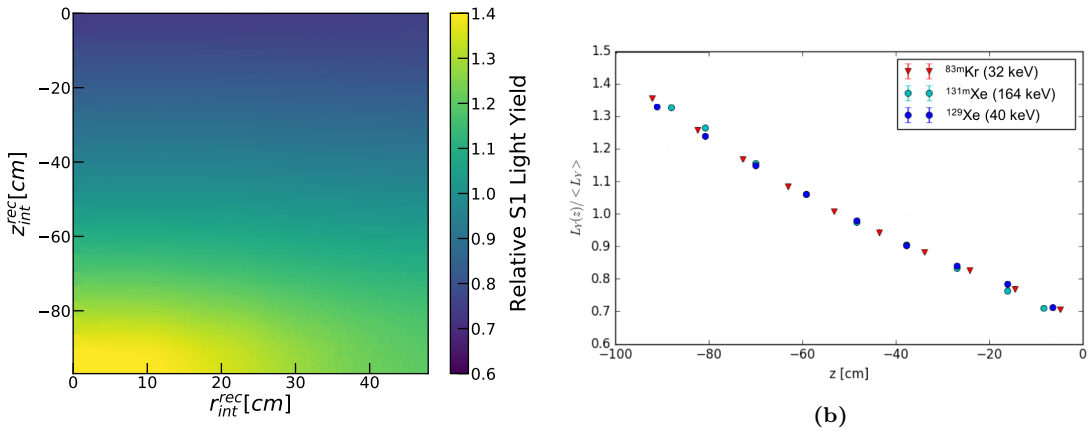

Figure 4.4: The XENON1T S1 light collection efficiency, defined as the relative S1 signal yield across the TPC volume with respect to the average. (a) Azimutally averaged LCE map, as a function of the reconstructed interaction vertex, exploited for position-dependent correction of S1 signals in XENON1T. The variation, up to a factor ∼2 is mainly caused by solid-angle effects and light reflection. (b) LCE profile along the z coordinate. The high-statistic measurement with ^{83m}Kr calibration data (red) is compared with xenon activation lines available after neutron calibrations. In particular, the 39.6 keV de-excitation line, due to neutron inelastic scattering off ^{129}Xe, and the 163.9 keV internal transition of ^{131m}Xe, activated through thermal neutron capture on ^{130}Xe or inelastic scattering of ^{131}Xe, are exploited. Error bars are not shown here as they are smaller than the data points size.

The LCE is smaller at the top of the TPC due to internal reflection occurring at the liquid-gas interface, resulting in larger photon absorption as the path length increases when moving closer to the anode. A decreasing LCE towards the TPC lateral edge is consequence of solid-angle effects. The largest variation, of a factor ∼2, is along z. Consistency is observed in the comparison with the LCE estimated from mono-energetic lines of activated xenon isotopes [281] during neutron calibration runs (see figure 4.4b), when available. The uncertainty on the LCE map is estimated in each volume bin normalized to the mean LCE and it is smaller than 1%.

Electron lifetime The loss of ionization electrons due to attachment to electronegative impurities in the LXe (H_2O, O_2, etc.) is described by the electron lifetime τ_e. The initial number of electrons created at the interaction site is exponentially reduced during the drift-time needed to reach the liquid-gas interface. This effect is the most important correction for S2 signals and is highly dependent on the impurity concentration in the target. Since the xenon is continuously purified, the electron lifetime is a parameter changing over time and has to be monitored regularly. The LXe purity could in principle also impact on the S1 signals via light absorption on impurities (primarily H_2O). However, the attenuation length of the scintillation light was always much larger than the detector dimensions, even during detector commissioning (> 10 m). The electron lifetime is evaluated by measuring the combined S2 from the two consecutive

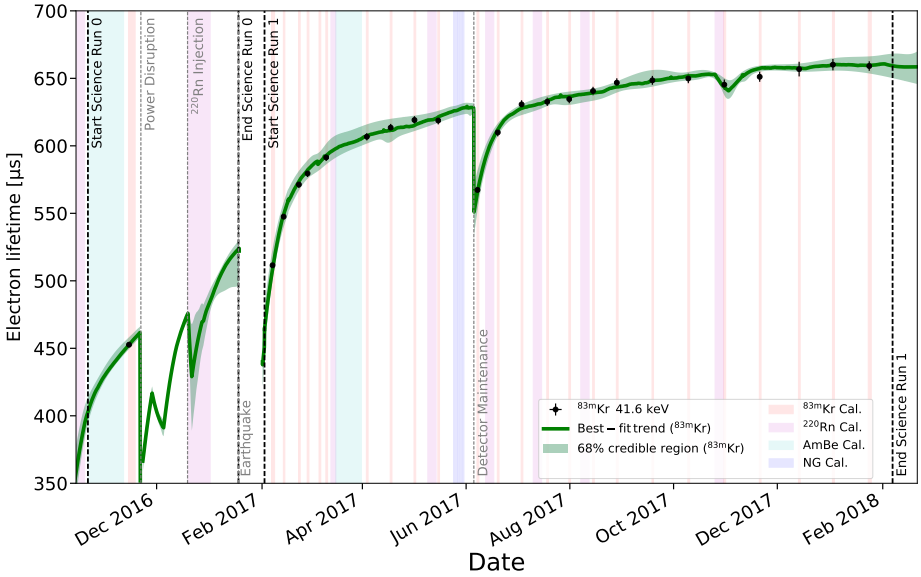

Figure 4.5: Electron lifetime evolution during the two XENON1T science runs. The green line and shaded region show the best fit of the electron lifetime model and its uncertainty, respectively. Data points are from measurements made with ^{83m}Kr calibration runs. Steady improvement up to ∼650 µs is obtained through continuous recirculation and purification of xenon. Drops are related to detector maintenance operations or power outages.

^{83m}Kr decays (41.5 keV line) as a function of electron drift time. Figure 4.5 shows the result of τ_e versus time, during the two science runs of XENON1T. In order to gain a continuous function of the electron lifetime evolution, measurements are fitted by a model that takes into account variations of the estimated impurity concentration (under the assumption that O_2 has the dominant impact on τ_e) based on slow control parameters, like xenon cooling power and recirculation flow to the purification system. The electron lifetime trend is also verified using mono-energetic alpha decays from the ^{222}Rn chain, daily observed in background data. During SR1, τ_e levelled off to about 650 µs corresponding to an oxigen impurity concentration of ∼0.5 ppb, limited by outgassing materials and the flow in the purification loop.

S2 amplification and LCE The proportional scintillation signal S2 is produced very localized in the gas region confined by the liquid-gas interface and the anode electrode, which features a distance of about 7.5 cm from the top PMT array. The partition of the S2 signal onto the two PMT arrays is almost double on the top, with only a few sensors contributing from the top PMT array and a uniform distribution over the bottom PMT array due to solid angle coverage.

Considering electron lifetime corrected S2 signals, two effects determine a varying

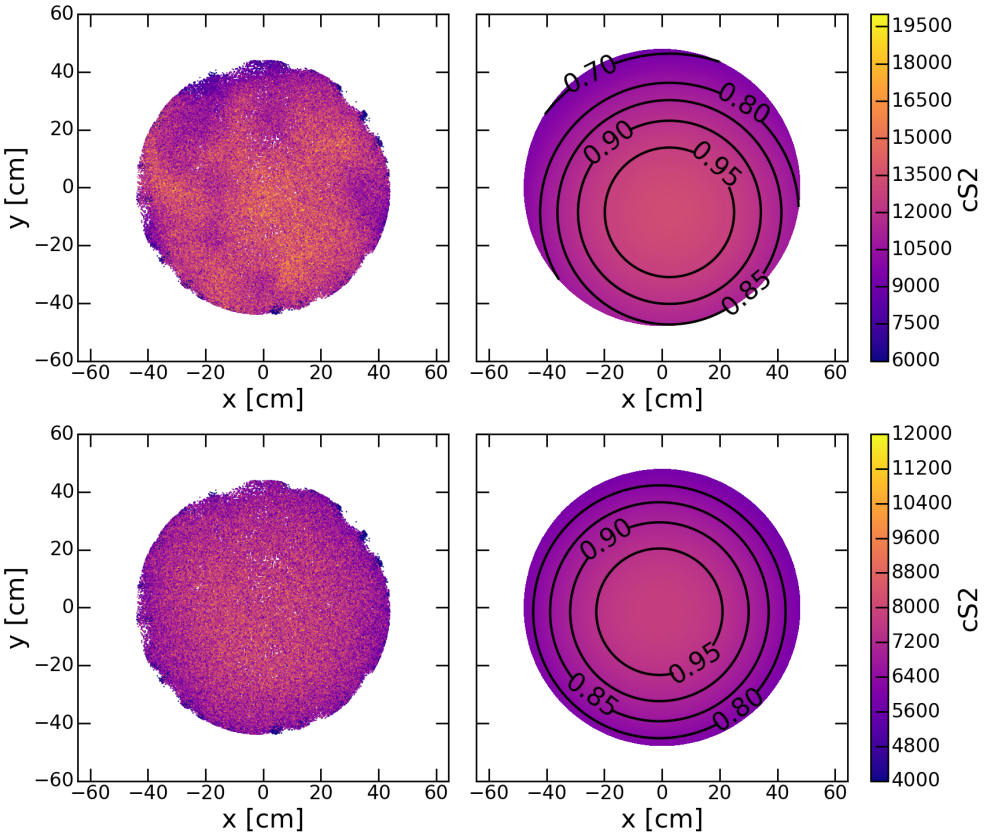

Figure 4.6: S2 signal distribution in the (x, y) plane of the 41.5 keV line of ^{83m}Kr observed by the top (top panel) and bottom (bottom panel) PMT array. The color scale shows the size of S2s corrected for the electron lifetime. On the right panels, the result of a bi-dimensional quadratic fit to the data (in the left panels) is shown together with contour levels indicated by black circles.

amplitude of the observed signal across the (x, y) plane for mono-energetic events. Different extraction field intensity caused by electrode warping and tilt results in large-scale variations of S2s, while small-scale differences are primarily induced by non-functioning PMTs in the top array. Different PMT gains do not play a role since those are accounted for at the processor level. For measuring anisotropies in the amplification gain and the light collection efficiency for the proportional scintillation S2 light, the 41.5 keV signal from ^{83m}Kr is exploited. Figure 4.6 shows the spatial (x, y) distribution of data together with the measured electron lifetime corrected S2 amplitude (in color scale) observed by the top and bottom PMT arrays. To account for the large-scale variations, the S2 sizes are fitted by a bi-dimensional quadratic function depending on x and y such that the corrected S2 signal is given by

$$\mathrm{cS2} = \mathrm{S2} \times \frac{1}{e^{-t_d/\tau_e}} \times \left(1 - b\frac{(x-x_0)^2 + (y-y_0)^2}{r_0^2}\right), \tag{4.2}$$

where $1/e^{-t_d/\tau_e}$ is the electron lifetime correction and $r_0 = \sqrt{x_0^2 + y_0^2}$. The fitted

quadratic functions to the top and bottom PMT arrays are shown on the right panels of figure 4.6. The extraction efficiency is approximately 20-30% lower at the edge of the detector compared to the center. This effect is primarily induced by anode sagging that causes a distortion of the electric field at the liquid-gas interface and therefore impacts on the electron extraction efficiency. Moreover, the displacement of the best-fit x_0 and y_0 from zero, in particular for the top array, suggests a slight tilt of the gate electrode resulting in a larger gas gap for negative values of y. After applying this first stage to correct for large-scale variations, residual anisotropies are accounted for by fitting cS2 distributions in bins of r and ϕ. For the bottom PMT array, very small variations, up to 5%, between adjacent bins are found, while small-scale corrections to the cS2 signal observed by the top array reach a 14% level due to the smaller solid angle which increases the impact of non-functioning PMTs.

The final S2 correction map combines all these effects. The less significant impact of small-scale distortions in the bottom PMT array motivated the usage of the bottom S2 signal ($\mathrm{cS2}_b$) throughout the WIMP search in order to minimize uncertainties from reconstructed position of events.

4.1.3 Energy scale

The parameters describing the detector efficiency in detecting light and charge signals are the primary scintillation gain $g1 = \mathrm{cS1}/n_\gamma$ and the secondary scintillation gain $g2 = \mathrm{cS2}_b/n_e$, where n_γ and n_e are the number of photons and electrons produced by an interaction in LXe and the observables cS1 and $\mathrm{cS2}_b$ are corrected for position-dependent effects (as described in section 4.1.2). For electronic recoils, almost all the energy is converted into light and freed charge, thus the energy of the interaction can be reconstructed using the combination of S1 and S2 signals:

$$E = \left(\frac{\mathrm{cS1}}{g1} + \frac{\mathrm{cS2}_b}{g2} \right) \cdot W, \tag{4.3}$$

where $W = 13.7 \pm 0.2\,\mathrm{eV}$ is the average energy required to produce one quanta (photon or electron) [282]. To calibrate the energy scale, sources producing mono-energetic lines of known energy can be deployed outside the detector, injected into the liquid xenon or activated during neutron calibrations. In a highly sensitive experiment such as XENON1T, even the low residual radioactivity of detector materials can be exploited for calibration. High energy γ-rays from ^{60}Co in the stainless steel cryostat or from ^{40}K in the PMTs can penetrate far enough into the detector to use them for this purpose. By fitting the anti-correlation between the measured light and charge yields from various radioactive sources, one obtains g_1 and g_2 (see figure 4.7). The light and charge yields of each mono-energetic line are evaluated by means of elliptical fits in the (cS1, $\mathrm{cS2}_b$) space and dividing the observed signal amplitudes by the known energy of absorbed gammas.

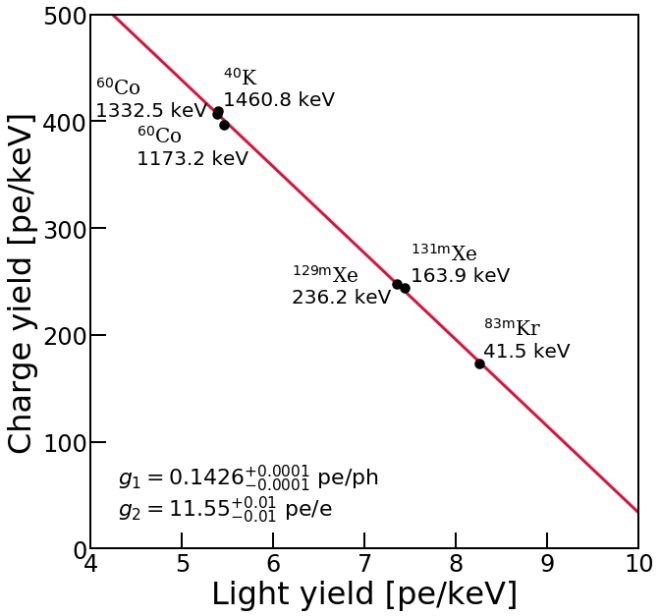

Figure 4.7: Mono-energetic gamma peaks in XENON1T exploited to extract the detector response parameters $g1$ and $g2$. The light and charge yields of ^{83m}Kr (injected for calibration runs), ^{129m}Xe and ^{131m}Xe (activated during neutron calibrations) and external gamma lines (from detector materials radioactive contaminants) are fitted with the linear anti-correlation in equation (4.3). Extracted values of $g1$ and $g2$ are reported in the inset with only the statistical uncertainty from the fit.

The estimated values for g_1 and g_2 for XENON1T are

$$\begin{aligned} g_1 &= 0.1426 \pm 0.0001\,(\text{stat}) \pm 0.0017\,(\text{syst})\,\text{PE/ph} \\ g_2 &= 11.55 \pm 0.01\,(\text{stat}) \pm 0.24\,(\text{syst})\,\text{PE/e}, \end{aligned} \tag{4.4}$$

whose uncertainty is dominated by systematics mainly derived from the evaluation of g_1 and g_2 in different sub-volumes of the TPC. As evident from figure 4.7, an excellent linearity is observed with XENON1T, from tens of keV up to few MeV. The energy resolution, shown in figure 4.8, is evaluated from the broadening of observed cS1 and $cS2_b$ signals for all the identified peaks in the XENON1T ER spectrum. The resolution improves at higher energies and its parametrization is obtained as

$$\frac{\sigma}{E} = \frac{31.0 \pm 0.4}{\sqrt{E}} + (0.37 \pm 0.03), \tag{4.5}$$

where gamma lines above 1.5 MeV are excluded from the fit since the event reconstruction is not yet optimized for relatively large energies (as discussed in section 3.1.2).

4.2 Time stability of signals

The XENON1T detector has been continuously running over 1 calendar year during the two dark matter search runs, with the exception of the $\sim$ 10 days interruption

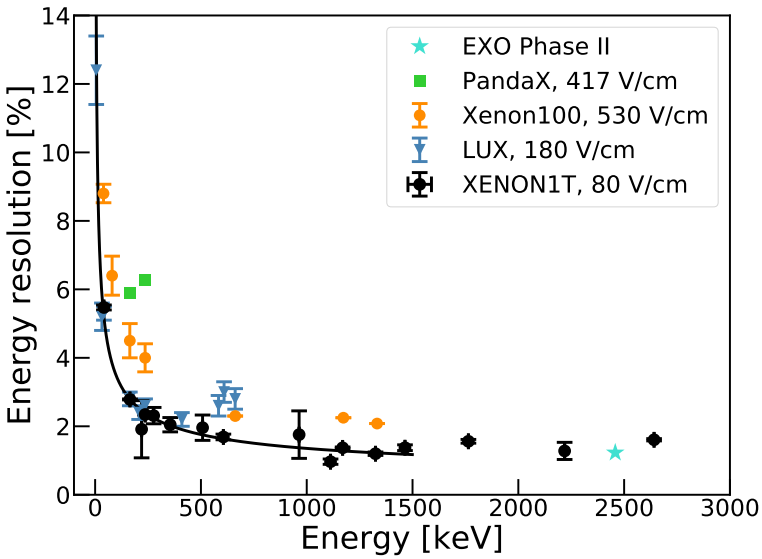

Figure 4.8: Energy resolution of the XENON1T detector. Black data points are measured mono-energetic gamma lines present in background or calibration data: ^{83m}Kr (41.5 keV), ^{131m}Xe (136.9 keV), ^{125}Xe (221.6 keV), ^{129m}Xe (236.1 keV), ^{125}Xe (276.6 keV), ^{214}Pb (351.9 keV), ^{208}Tl (510.8 keV), ^{214}Bi (609.3 keV), ^{228}Ac (968.0 keV), ^{214}Bi (1120.3 keV), ^{60}Co (1173.2 and 1332.5 keV), ^{40}K (1460.8 keV), ^{214}Bi (1764.5 and 2204.1 keV), ^{208}Tl (2614.5 keV). For comparison, measurements from EXO Phase II [283] (cyan), PandaX [111] (green), XENON100 [192] (orange) and LUX [284] (blue) are shown.

between SR0 and SR1 caused by an earthquake. It is therefore important to monitor the time stability of detector parameters and of the observed S1 and S2 signals, as instabilities can potentially introduce a bias in the data analysis and would eventually require appropriate modelling and corrections (one example is the significant impact on position reconstruction of charge accumulation at the TPC wall).

In the combination of the two XENON1T science runs, the LXe temperature and GXe pressure is successfully kept constant at $-96.0\,^{\circ}$C and 1.94 bar, respectively, both with RMS below 0.02%. The LXe level is mantained at 2.5 mm above the gate electrode, with observed fluctuations in sensor reading of 2% RMS. As already mentioned in section 4.1.1, a total of 35 (36) PMTs are excluded from the analysis of SR0 (SR1). The PMT gains are monitored weekly with a pulsed LED configured to produce signals of few photo-electrons using the model independent approach described in [276]. For the majority of PMTs, gains are stable within 2% with fluctuations dominated by statistical uncertainty in the gain measurements. The gain of some PMTs is found to be decreasing during the science runs. This is the case of PMTs affected by vacuum leaks, all showing an increasing afterpulse rate [285] by 1-2% during SR1. A Fermi-Dirac function is exploited to model the time evolution of the gain for 19 PMTs showing such a behaviour. Single electron (SE) peaks can be selected from data since they occur after large signals as a consequence of impurities or exposed metal photo-ionization, or delayed extraction of charge from the liquid-gas interface. The SE gain, i.e. the amplitude of S2 signals

per single electron, is extremely sensitive to variations of pressure in GXe, liquid level and the extraction electric field. It is monitored over time and a stability at 2.5% RMS is found in SR0 (mainly due to $\mathcal{O}(0.1\,\text{mm})$ liquid level variations), while the SE gain is stable within 0.2% during SR1.

The possible evolution over time of light and charge yields can be monitored through mono-energetic signals present in the detector across the science run duration either continuously (such as external gammas and alphas from ^{222}Rn), in occasion of calibration runs (^{83m}Kr) or for a limited period following neutron calibrations (activated xenon isotopes). All these sources are exploited to measure the stability of S1 and S2 signals in the long SR1 that lasted 371 days overall (see section 4.2.2). During the brief SR0 (58 calendar days), the signal stability was monitored with the 164 keV gamma line of ^{131m}Xe, activated by a ^{241}AmBe calibration run just before SR0, which was the lowest mono-energetic peak available (see section 4.2.1).

4.2.1 Gamma rays from activated xenon

Gamma rays from decay of xenon metastable states, such as ^{129m}Xe and ^{131m}Xe, which emit gamma rays at 236.1 keV and 163.9 keV [286], respectively, are generally exploited as reliable and precise calibration sources for LXe detectors [281]. They can be produced by thermal neutron capture on ^{128}Xe and ^{130}Xe, or by fast neutron inelastic scattering on ^{129}Xe and ^{131}Xe. In XENON1T they are activated during calibration runs in which an external source of neutrons, either ^{241}AmBe [203] or D-D fusion neutron gun [229], is deployed beside the cryostat. The activation of metastable states results in a spatially uniform activity in the XENON1T TPC. Thanks to their half-lives of 8.9 (^{129m}Xe) and 11.8 days (^{131m}Xe), activated xenon isotopes are suitable sources to monitor the light and charge yields over few weeks following neutron calibrations. Besides the spatial uniformity and the high intensity, as can be seen in figure 4.9a, another advantage of using ^{131m}Xe and ^{129m}Xe is that they offer gamma lines of relatively low energy compared to the external gammas ($\mathcal{O}$(MeV)). A lower energetic ER peak in XENON1T is the 41.5 keV line from ^{83m}Kr, which is present only during the calibration runs (that typically last few hours) due to its short half-life of 1.83 hours.

For the SR0 data taking, a ^{83m}Kr calibration was performed few days before the start of the science run. To monitor the signal stability during SR0, the 163.9 keV gamma line of ^{131m}Xe is therefore used, which is made available by an ^{241}AmBe calibration run as evident from the measured ^{131m}Xe event rate shown in figure 4.9b. Events are selected with double-Gaussian fit in the corrected signals space (cS1, cS2$_b$), as in figure 4.9a, and binned in time to ensure enough statistic for the evaluation of the light and charge yield. As the activity of ^{131m}Xe decreases with time, less data are available in final days of SR0, which requires a more coarse time binning. No data are available for a period of two weeks during the science run, when a low energy ER calibration with injected ^{220}Rn (orange interval in figure 4.10) prevents the identification of a clean ^{131m}Xe peak. Light and charge yield are stable throughout SR0 at 0.6% and 0.9% level, respectively,

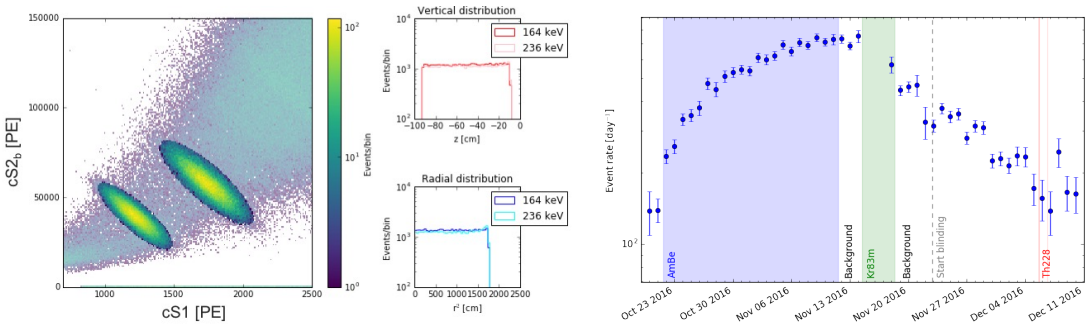

(a) **(b)**

Figure 4.9: (a) Activated metastable xenon lines in XENON1T data. In the left panel, the selection of mono-energetic gamma peaks of ^{131m}Xe (163.9 keV) and ^{129m}Xe (236.1 keV) through elliptical fits in the observable signal space. In the right panels, the vertical (top) and radial (bottom) distribution of both peaks along the TPC volume showing spatial uniformity. (b) Event rate of ^{131m}Xe gamma line (blue points) in early stages of the first XENON1T science run. The metastable isotope is activated mainly via neutron capture on ^{130}Xe during the ^{241}AmBe calibration campaign (blue interval), when the event rate of the 163.9 keV de-excitation gamma raises. The residual activity extends during SR0 data taking (whose start is indicated by the grey dashed line) with an exponential fall with fitted half-life of 12.2 ± 0.5 d, compatible with the expected 11.8 d [286].

and show local variations $<2\%$ as presented in figure 4.10.

4.2.2 Monitoring signal stability with mono-energetic lines

In the much longer SR1 time span, compared to SR0, regular ^{83m}Kr calibrations are available throughout the run, while events from xenon activation lines (^{131m}Xe and ^{129m}Xe) are present only in the first half of SR1 because the neutron calibrations were performed on March and May 2018. Several sources, of different energy and nature, are exploited to monitor the signal stability over SR1. At the lowest energy, ^{83m}Kr decays give a measurement approximately every two weeks. It is possible to measure the prompt scintillation S1 signal of both the emitted gammas of 32.1 and 9.4 keV from the two-step decay of ^{83m}Kr to the ground state. Exploiting the fraction of events with non-resolved S1 peaks, the light yield from the combined 41.5 keV line can be also monitored. Conversely, the two S2s can be resolved only for transitions happening at the very top of the TPC and only the charge yield at 41.5 keV can be measured in extended volumes. The time evolution of signals at higher energies is evaluated through gamma lines originated from radioactive contaminants in detector materials. Specifically, the 1.8 and 2.2 MeV gamma lines of ^{214}Bi and the 2.6 MeV gamma of ^{208}Tl are monitored on a monthly basis. A very high rate source that allows a finer time binning comes from α-decays of ^{222}Rn, from which light and charge yield of 5.5 MeV alpha interactions are evaluated day-by-day over the entire SR1.

The combined result from all the different sources is shown in figure 4.11 in terms of the relative deviation from the mean of the corrected S1 and S2$_b$ signals as a function

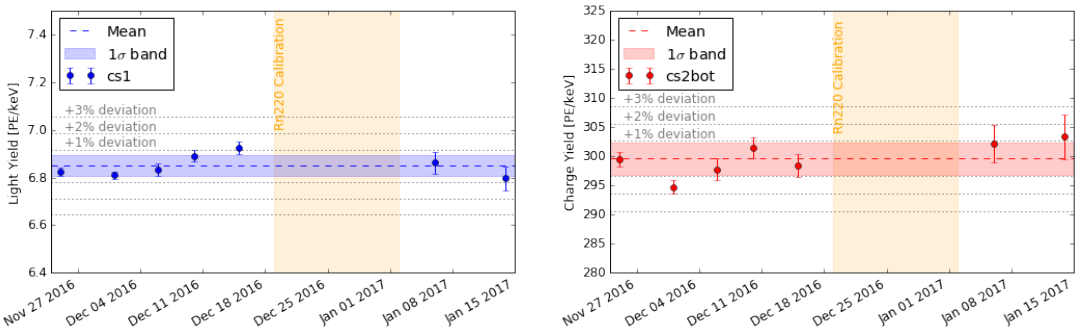

Figure 4.10: Time stability of light (left panel) and charge (right panel) signals during SR0 evaluated from corrected S1 and $S2_b$ amplitudes of the 163.9 keV ^{131m}Xe line. The activated xenon line is the lowest energy gamma peak present in background data during the short time span of SR0. No data are available during the ^{220}Rn calibration (orange interval) since the ^{131m}Xe cannot be clearly selected. The colored horiziontal dashed line and band represent the average signal yield and the 1σ deviation, respectively, derived from the measurements (points) over the SR0 duration. The light (charge) yield is stable at 0.6% (0.9%).

of time. Good consistency is found among measurements of the various mono-energetic peaks considered. The light yield stability is estimated at the 0.16% and 0.18% RMS level from ^{83m}Kr and ^{222}Rn measurements, respectively. Higher variability results from the monitored charge yield evolution, with 1.4% (1.2%) RMS obtained from ^{83m}Kr (^{222}Rn). All the sources show a slight increase of charge yield causing an overall variation during the whole SR1 of about 5%. Several hypothesis to explain the increasing trend of charge yield are being explored as it is not yet fully understood. From waveform simulations, that take into account the increasing afterpulse rate observed in some PMTs, one obtains indication for an induced charge yield increase of 1.5 % over the SR1 duration, which however would be just a partial contribution. A steady decrease of the liquid level can cause larger S2s as consequence of a bigger amplification gap, but no significant decreasing trend from sensor reading is observed. Effects or artifacts related to electric drift field distortion and electron lifetime correction are excluded by measurements of the charge yield in different sub-volumes, where the same trend is observed. Variation of the extraction field could in principle be caused by slow shifting of the anode towards the gate electrode or charge accumulation at the liquid-gas interface, however no verifications of such hypothesis are currently available.

Despite the charge yield is not fully stable during SR1, the size of the observed increase is still within the systematic uncertainties in the determination of the signal response to ER in the energy range of interest for WIMP search. When an effective correction is applied to $cS2_b$ signals based on the charge yield trend in figure 4.11, no significant difference in the ER band model derived from both background and ^{220}Rn calibration data is obtained. Such a correction is therefore not applied, as the impact of the charge yield increase is negligible for the WIMP search data analysis.

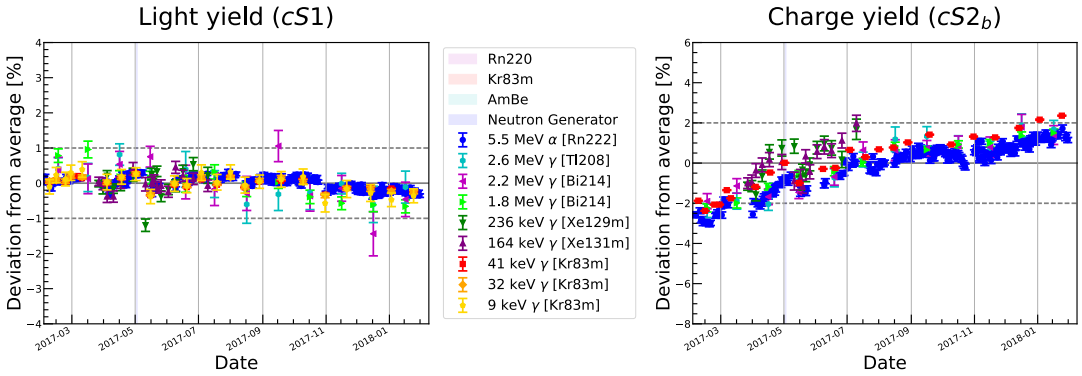

Figure 4.11: Relative deviation from the mean of light (left panel) and charge (right panel) yield during the second long XENON1T science run. The signal time stability is monitored with different sources of mono-energetic lines: ^{83m}Kr (9.4, 32.1 and combined 41.5 keV) during the bi-weekly calibration runs, ^{131m}Xe (163.9 keV) and ^{129m}Xe (236.1 keV) from April to August 2018 following neutron calibrations with ^{241}AmBe and neutron generator, external gammas of ^{214}Bi (1.8 and 2.2 MeV) and ^{208}Tl (2.6 MeV), alpha decay of ^{222}Rn (5.5 MeV). The RMS deviation for the average light and charge yield is 0.16% (0.18%) and 1.4% (1.2%), respectively, from ^{83m}Kr (^{222}Rn) data.

4.3 Data selection and efficiency

The XENON1T data for dark matter search are selected imposing boundary criteria on several parameters to ensure data quality and reject non-physical events or known backgrounds. The region of interest, where we look for WIMP-nucleon spin-independent interactions, is defined in the observable signal space as cS1 $\in$ (3, 70) PE and cS2$_b$ $\in$ (50, 8000) PE. The single scatter selection of equation (3.2), discussed in section 3.2.3, is applied in order to reject multiple-site interactions that are not expected by WIMPs. From all the studies performed on single scatter events in the ROI to characterize the detector response and to define data selection criteria, the data in the NR signal region are excluded. A blinding cut below the -2σ boundary of ER band and above the -4.5σ NR band quantile is imposed to avoid any possible bias in decisions about data analysis methods.

An internal fiducial volume containing 1.3 t of the total 2 t active LXe target mass in the XENON1T TPC is used for this analysis, whose dimensions and shape definition are discussed in section 4.3.1. Selection criteria to reject badly-reconstructed events at the data processing level drive the detection efficiency, which describes how sensitive is the experiment to physical interactions, in particular to those producing very feeble (S1) signals. Further selections are imposed at the analysis level in order to discard low quality data and to ensure the correct coupling of S1 and S2 peaks within the event time window. The description of the selection criteria adopted in the XENON1T data analysis, together with the resulting acceptance loss to WIMP signal, is given in section 4.3.2.

A small fraction of events is discarded without considering any of their properties due to operational conditions during data taking. If at least one channel in the data

acquisition system is unable to collect events, no data are recorded. This rejects anomalous long signals emitted by single PMTs keeping the relative channel busy. Events in coincidence with Muon Veto triggers are also removed, as well as time intervals in which the MV is inactive due to operational reasons. The pulse rates of each channel are scanned to look for sudden, drastic increases due to emission of light flashes from a PMT that is sometimes observed in XENON1T phototubes. In that case, the short time periods of enhanced pulse rates are removed from the exposure. After high energy background events, delayed S2 signals can reduced the detector's sensitivity to low energy interactions for several milliseconds. Therefore a condition is imposed to discard events occurring within a certain time window after a previous one, whose length depends on the amplitude of the S2 signal in the precedent event. These selection conditions remove time periods of data and are, therefore, taken into account as corrections to the exposure time and not included in the cut acceptance calculation. The consequent livetime reduction in the combined exposure of SR0 and SR1 amounts to $\sim$7.5 %.

4.3.1 Fiducial volume definition

The fiducial volume (FV) used for the DM search with XENON1T data is optimized by considering the spatial distribution of all background components (see section 4.4). The maximum radius of FV is chosen to be 42.84 cm in order to leave $\lesssim$ 100 surface background events (see section 4.4.1) that constrain the normalization of this component in the likelihood fit to unblinded data. A larger radius would introduce a too tight constraint on the tail of the radial distribution of surface events with respect to the extrapolation from the bulk of this population at the edge of the TPC. The z region is restricted between -8 cm[1], to exclude mis-reconstructed events from the gas region, and -94 cm, since below the electric field is less uniform.

The shape of FV is thereafter optimized based on the expected spatial distribution obtained from the background models restricted to the (cS1, cS2$_b$) portion of signal space where the WIMP signal has the highest significance, i.e. below the ER band median where the signal-to-background ratio extracted from the normalized models is higher. The optimization is performed only for the z dimension, maintaining azimuthal symmetry, since the backgrounds are modelled in their radial distribution and the XENON1T likelihood function features a dependency on r (see section 4.5.3). Upper and lower bound in z are defined in radial bins so that the sum of all backgrounds in the aforementioned energy region of interest is uniform within 10% across z. In this way, background contributions from radioimpurities in detector materials are kept sub-dominant with respect to the intrinsic ^{214}Pb background that induces uniformly distributed ERs inside the FV. The obtained shape, shown in figure 4.12, cuts away the top and bottom corners where external backgrounds are predominant. In order to take into account also the background from radiogenic neutrons that mainly occurs at

[1]The coordinate system is chosen so that the gate electrode corresponds to $z = 0$ and negative values to increasing depth towards the cathode, the bottom edge, that is at $z = -97$ cm.

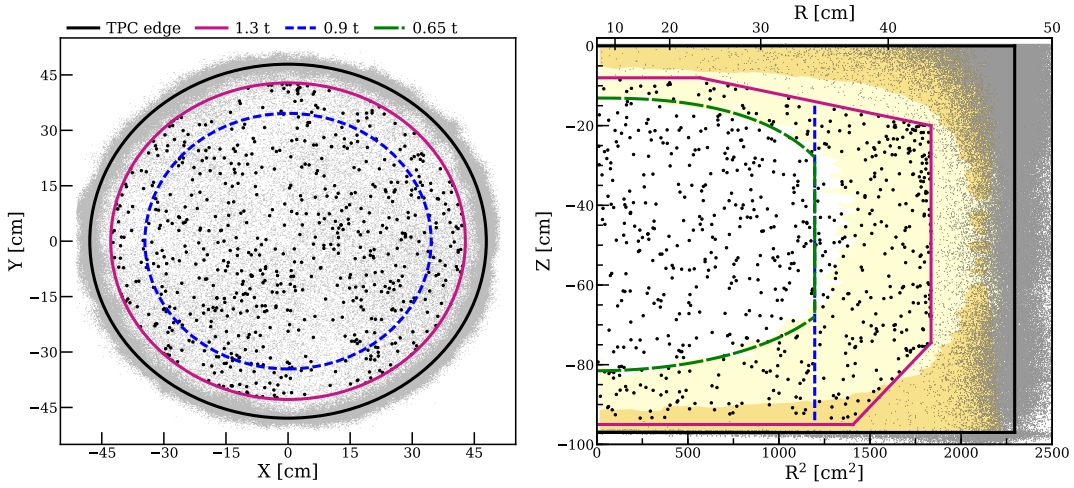

Figure 4.12: The XENON1T fiducial volume (magenta line) containing 1.3 t LXe mass in the (x, y) projection, left, (the maximum radius is drawn) and in the (r^2, z) space, right. The TPC boundary (black line), maximum radius of a reference 0.9 t mass (blue dashed), and core 0.65 t mass (green dashed) are also shown. Yellow shaded regions display the 1σ (dark), and 2σ (light) probability density percentiles of the neutron background model. The reconstructed position of background events in the energy region of interest for DM search (excluding event in the NR blinded region) is drawn as black points inside the 1.3 t FV and as smaller grey dots outside.

extreme z, the fiducial volume is segmented into two bins. The inner core mass (delimited by green dashed line in figure 4.12) is optimized based on the neutron background distribution in bins of r and z and contains a $\sim$80 % lower neutron rate compared to the total fiducial volume.

The LXe mass actually contained in the FV is determined with two different approaches: from the ratio of ^{83m}Kr calibration events in the selected volume with respect to the total sensitive volume and from geometrical considerations. The two values are combined and their difference is taken as systematic uncertainty on the obtained estimate of 1.30 ± 0.01 t for the total FV and 0.65 ± 0.01 t for the inner core LXe mass.

4.3.2 Detection efficiency and selection criteria

Detection efficiency Event detection in XENON1T is established by requiring that all events must contain a valid S1 and S2 pair and that the S1 signal is seen by at least 3 PMTs in coincidence within 100 ns. The event detection efficiency, shown as the green curve in figure 4.14, is estimated through FAX waveform simulations of S1 and S2 peaks of different amplitude, and is dominated by the S1 detection efficiency. A data-driven method, where small S1s are simulated via bootstrapping single PMT hits from relatively large S1s (from 20 to 100 PE) in data, is consistent with the detection efficiency estimated from simulations.

Data quality cuts Conditions are imposed to remove events that are either falsely reconstructed, members of known background populations, or generally of low quality. If an event contains a large fraction of signals ($>300\,\mathrm{PE}$) prior to the primary S2 (excluding the primary S1), it is deemed noisy and removed.

In addition, if the S1 signal is completely dominated by a single channel exhibiting an abnormally large signal, it is assumed to be the product of a PMT malfunction and thus removed.

Events where the primary S1 and S2 are not the largest peaks of their type are also rejected to suppress the effects of pile-up, double scatters, or improper interaction pairing.

S2 events are always produced at the gate position and have a fixed fraction of light collected in the top PMT array of around 63%. A selection condition requires this fraction to be respected in order to suppress signals that are mis-reconstructed or contain contributions not coming from the original S2.

Reliable S2 position reconstruction is ensured by demanding that the reconstructed S2 positions exhibit a sufficiently high likelihood given their top-array hit pattern. The likelihood for a given position is computed using simulated per-PMT light collection efficiency maps. Events with low likelihood may be combinations of multiple S2s or events that are reconstructed in the wrong (x, y) position, often due to inactive PMT channels. The latter case is especially critical for the lowest energy S2s and is the target of a further selection condition that removes events where the reconstructed position using two independent algorithms (Neural Network and Top Pattern Fit, see section 4.1.1) is sufficiently different.

Finally, since single electron S2s can be mis-classified as S1s, potentially contributing to low energy accidental coincidences (see section 4.4.2), it is required that the S1 must not have shape properties compatible to SE S2s.

The acceptance of this class of selection criteria, referred to as data quality cuts, is shown in figure 4.13 (red line).

S1-S2 pairing A few selection conditions that demand the correct pairing of S1 and S2 are applied to ensure that the PAX processor has identified a valid interaction, within the event time window defined around a trigger, and that it has reconstructed the interaction correctly.

The width in the time domain of the S2 peak is dependent upon the depth of the primary interaction due to diffusion of the electron cloud. Using calibration data sources, a diffusion model is built in waveform simulations and used to generate a large dataset extending across the full energy spectrum. If the observed spread of the S2 peak is incompatible within the 99% quantile of the expected width based on the diffusion model, the event is rejected.

Due to geometrical effects of photons reflecting on PTFE surfaces of the TPC, reflections at the liquid-gas interface and absorption by opaque components (e.g. electrode grids), the S1 hit pattern is heavily influenced by the three dimensional location of the

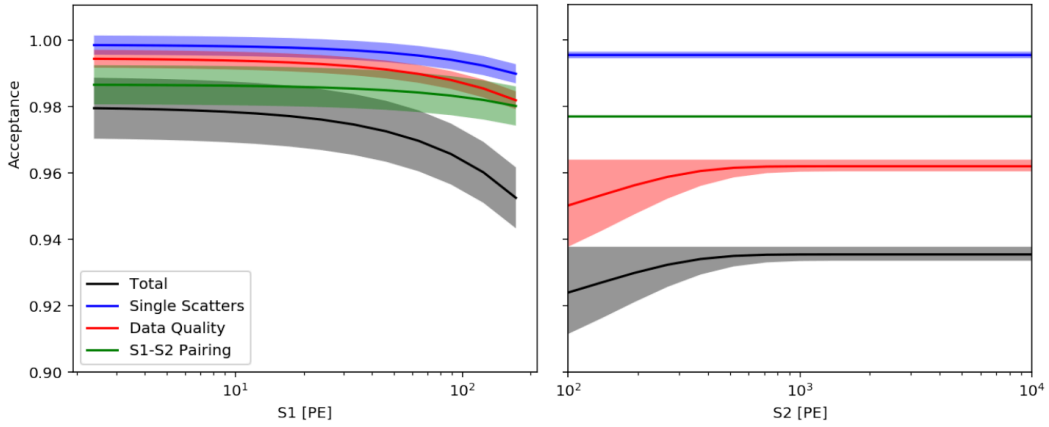

Figure 4.13: Acceptance of data selection criteria (black) versus the raw S1 (left panel) and S2 (right panel) signals, with the specific contribution of the single scatter selection (blue), data quality (red) and S1-S2 pairing (green). The uncertainty of the estimations is displayed as shaded region. The total acceptance is higher than 92% over the full analysis range.

primary interaction inside the TPC. Since the (x, y) position is extracted from the S2 and the z coordinate is computed from the drift time, compatibility of the S1 pattern with the reconstructed position represents a completely independent confirmation of the correct interaction pairing. The fraction of light seen in the top PMT array is determined at each position in the target volume using Monte Carlo simulations. For a given event in data, a binomial distribution is constructed based on the total number of photons detected in the event and the expected fraction that should be detected in the top array (based on the simulations). If the actual fraction detected falls into the extreme tails of the binomial distribution (p-value < 0.001) the event is removed.

The S1 hit pattern across all active PMT channels is also checked for likelihood given the interaction position, similarly to the condition previously described for S2 peaks.

The green line in figure 4.13 shows the acceptance as a function of S1 and S2 for the described selection criteria.

Signal efficiency The signal efficiency (or acceptance) of all the selection conditions, defined as the fraction of true WIMP signals that survive the selection cuts, is estimated with a combination of simulations and calibration control samples. The acceptance of the single scatter selection together with the two classes of cuts discussed above is shown in figure 4.13 as a function of the raw S1 and S2 signals. The combined acceptance is on average ∼96 % on S1 and ∼93 % for S2. It is primarily influenced by the data quality, impacting mostly the S2 acceptance, and by the S1-S2 pairing criteria, while the single scatter selection has a >99% acceptance.

The total XENON1T signal efficiency as a function of the nuclear recoil energy scale (derived from the model described in section 3.3) is shown in figure 4.14. That includes

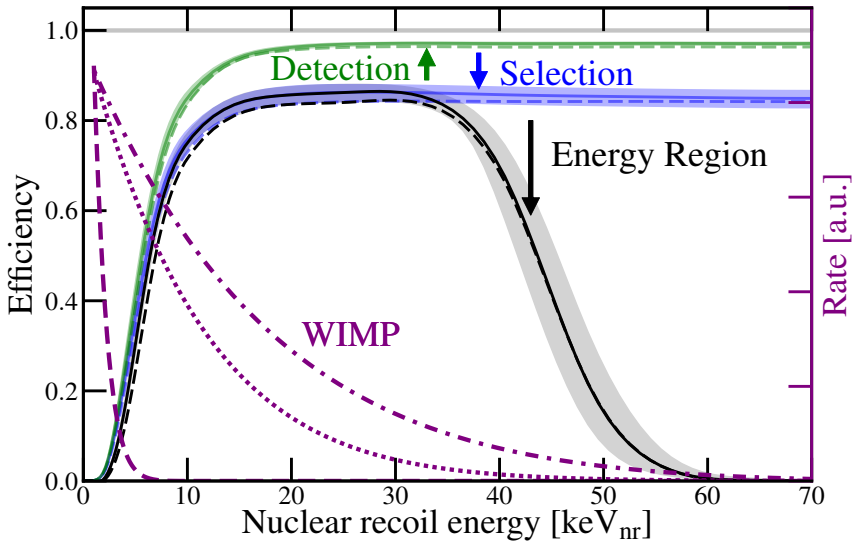

Figure 4.14: Total efficiency curve of XENON1T (black), including the energy ROI selection, for SR0 (dashed) and SR1 (solid) as a function of true NR energy (keV$_{nr}$). The efficiency of S1 detection (green) and the combination with selections (blue) are shown. The shaded bands show the 68% credible regions for SR1. The expected spectral shapes (purple) of 10 GeV/c^2(dashed) 50 GeV/c^2(dotted) and 200 GeV/c^2(dashed dotted) WIMPs are overlaid for reference.

the detection efficiency (green), which limits the sensitivity to extremely low energy events, the acceptance of all the data selection criteria (blue), including single scatter, data quality and S1-S2 pairing conditions, which drive the efficiency above ∼10 keV. The upper bound of the analysis range (cS1 = 70 PE) defines the limit of the efficiency at higher energies (black line). The overlaid NR energy spectra of WIMPs of 10, 50 and 200 GeV/c^2(purple) indicate how much the acceptance loss at very low energy affects the sensitivity to light (more) or heavy WIMPs (less).

4.4 Background and signal models

The XENON1T data analysis is performed in a "blinded" way, meaning that the collected data in the most sensitive region to WIMP signal in the analysis space are kept secret until the background and signal models are built. The blinded box in the (cS1, cS2$_b$) space, shown as a blue area in the left panel of figure 4.15, is defined between -2σ quantile of the ER distribution and -4.5σ quantile of the NR band.

Standard interactions in the XENON1T TPC can be modelled combining knowledge of LXe and detector-related responses with MC simulations, as for the ER (see section 3.4.1) and NR (see section 3.4.2) background models. For background events where the knowledge of the response is incomplete or missing, data-driven methods have to be developed to model the events and make predictions in the blinded WIMP signal box. This is the case for two other relevant background components in XENON1T:

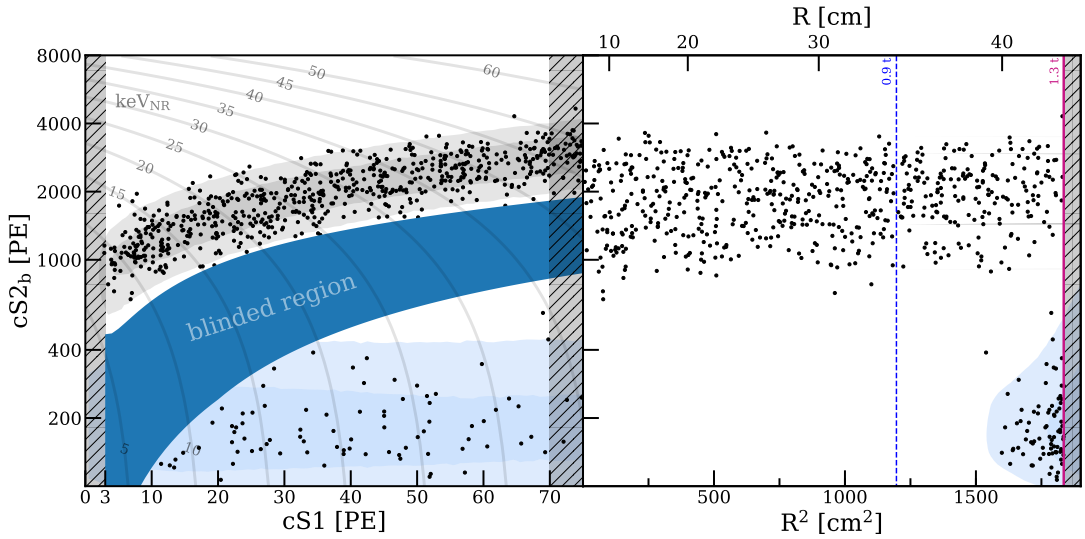

Figure 4.15: The XENON1T collected data over SR0 and SR1 in the observable signal space (cS1, $cS2_b$), left panel, and in their radial distribution versus $cS2_b$, right panel. The blinded region is shown as blue shaded area in the signal space, defined between -2σ quantile of the ER distribution and -4.5σ quantile of the NR band over the full range of cS1. Background data (black points) in the not blinded portion of the ROI are shown. The two main background models outside the blinded region, ER (grey) and surface background (light blue), are drawn as shaded areas (1σ, darker, and 2σ contour, light). From the radial distribution, it is evident how much the surface background is confined to the outermost layers of the TPC.

surface events (described in section 4.4.1) and accidental S1-S2 coincidences (discussed in section 4.4.2). The adopted WIMP signal model is presented in section 4.4.3. The final results of the XENON1T DM search with the two science runs are inferred based on the background predictions, which are reported in section 4.4.4.

4.4.1 Surface background

Several experiments [287, 288] have demonstrated that detector surfaces exposed to ambient air during construction phase are contaminated by a large amount of radon progeny, in particular ^{210}Pb. With a 22 years half-life, ^{210}Pb decays constantly within the lifetime of the XENON1T experiment. For dark matter searches, ion recoils of ^{206}Pb from ^{210}Po alpha decays, β-decays and the resulting X-rays and Auger electrons of ^{210}Pb are particularly important. Due to incomplete knowledge of LXe properties and detector physics in presence of PTFE, as well as complicated decay structures, a full model including the relevant physics processes is not yet achieved in XENON1T. Instead, a data-driven approach is adopted to predict the event distribution.

As uncertainties in the position reconstruction are quasi-symmetrical, surface events are reconstructed nearly symmetrically around the PTFE TPC boundary. Events falsely reconstructed outside the TPC are used to model the background distribution in S2, $cS2_b$, S1, and z space, with a kernel-density-estimation method, producing a distribution

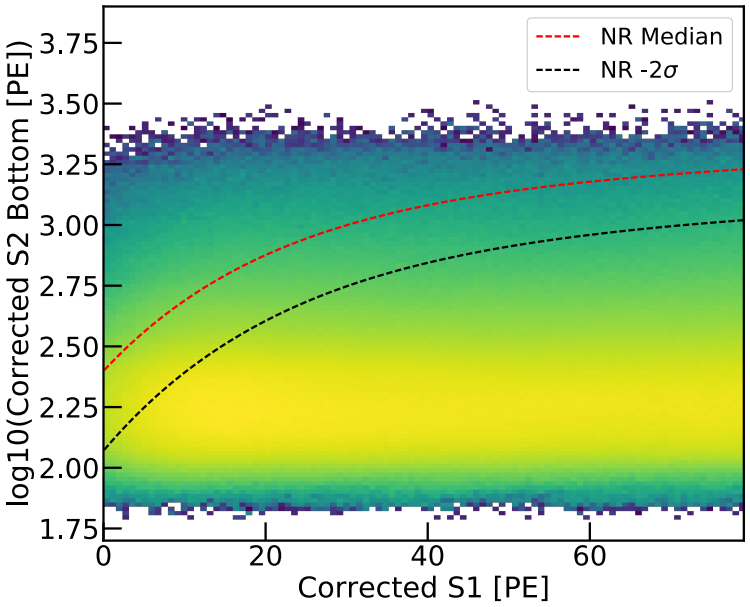

Figure 4.16: Spectrum of the surface background in cS1 and $\mathrm{Log}_{10}(\mathrm{cS2}_b)$. The NR reference region is evidenced between the NR median and -2σ quantile lines, marked in red and black lines, respectively.

$f_{Surf(1)}(\mathrm{cS1},\ \mathrm{cS2}_b,\ \mathrm{S2},\ z)$. The projection in $\mathrm{cS2}_b$ and cS1 space is shown in figure 4.16. Due to significant charge losses, surface background overlaps with the nuclear recoil region of interest (between NR median and -2σ line). In contrast, the r distribution provides excellent rejection power (as can be seen in figure 4.15).

The position reconstruction uncertainty depends mainly on the (uncorrected) S2 signal amplitude (see section 4.1.1). To construct the distribution of surface background in r and S2 space, low energy events originating at the PTFE reflectors are selected with S2 and S1 values below the NR blinded region as well as ^{210}Po α-decays. In each S2 slice, the radial distribution of the control-sample events is fitted, including an uncertainty band estimated by varying fitting methods. The bi-dimensional distribution of surface background, denoted as $f_{Surf(2)}(r,\ \mathrm{S2})$, is then folded with $f_{Surf(1)}(\mathrm{cS1},\ \mathrm{cS2}_b,\ \mathrm{S2},\ z)$ to form a complete model of surface background as $f_{Surf}(\mathrm{cS2},\ \mathrm{cS1},\ \mathrm{S2},\ r,\ z)$, including the uncertainty in the radial distribution. The normalization of the surface background is constrained by the bulk of the distribution in DM search data shown in figure 4.15.

4.4.2 Accidental coincidences

The accidental coincidence (AC) of uncorrelated S1 and S2 (referred to as lone-S1 and lone-S2, respectively) is another background component considered in XENON1T. Lone-S1s and -S2s originate from energy depositions in non-active regions of the detector, where the scintillation or ionization signal is lost. For example, an energy deposition in the region below-cathode will not produce an ionization signal, and a deposited energy very close to the gate may see its scintillation signal blocked by the electrode mesh or

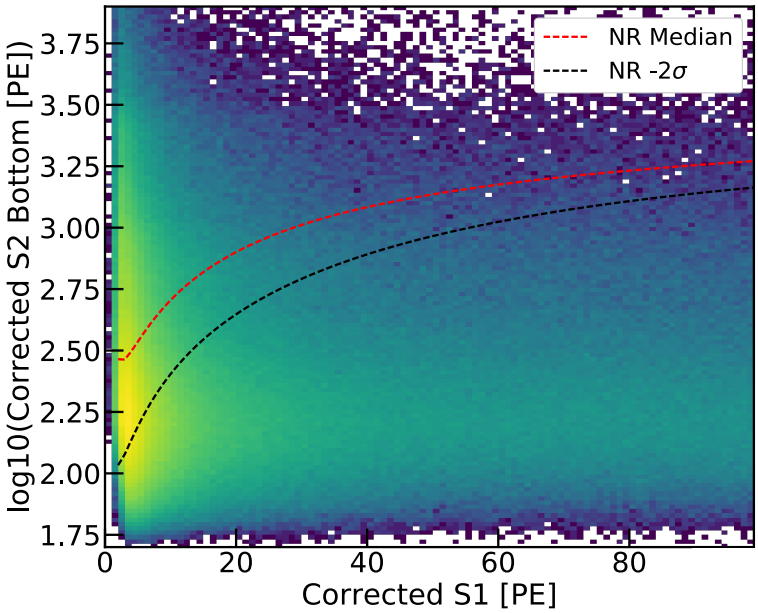

Figure 4.17: Spectrum of the AC background in cS1 and $\mathrm{Log}_{10}(\mathrm{cS2}_b)$. The highlighted reference region lies between the NR median and -2σ quantile lines, marked in red and black lines, respectively.

hidden inside the almost-coincident and larger S2 signal.

The lone-S1 sample is obtained by searching for S1s in the time window before the large primary S1 in each digitized event waveform. The lone-S2 population is extracted using events without S1 found in the digitized waveform, or with the reconstructed z position larger than the maximum drift time. The event selections involving S1 (S2) are excluded for obtaining lone-S1 (lone-S2) samples. Because of the lack of correlation between lone-S1s and lone-S2s, the reconstructed positions of ACs are considered uniform in the active volume. Sampling and randomly pairing the lone-S1 and -S2 distributions yields the (cS1, $\mathrm{cS2}_b$) distribution of the AC background, where the signal correction and event selections that are related to S1 and S2 correlation with event position, such as the selection based on S2 width versus drift time and S1 fraction on top PMTs versus drift time, are applied. The AC model is validated against data outside the DM search ROI.

The AC rate follows $R_{AC} = R_{l-s1} \times R_{l-s2} \times \Delta t$, where R_{l-s1} and R_{l-s2} are the rates of lone-S1s and lone-S2s, respectively. Δt is the coincidence window, which is fixed to the maximum drift time of XENON1T TPC (674 µs for SR0 and 727 µs for SR1). The lone-S1 rate is determined as $R_{l-s1} = 0.9 \pm 0.2\,\mathrm{Hz}$, where the uncertainty comes from differing rates of single electron S2 and dark counts in the event time window preceding the primary S1. The estimated lone-S2 rate is $R_{l-s2} = 2.6 \pm 0.1\,\mathrm{mHz}$. The resulting predicted AC rate in ROI for SR0 and SR1 combined is therefore $0.6 \pm 0.1\,(\mathrm{t \cdot y})^{-1}$. As shown in figure 4.17, the AC distribution is concentrated at low cS1, very relevant in the search for light WIMPs.

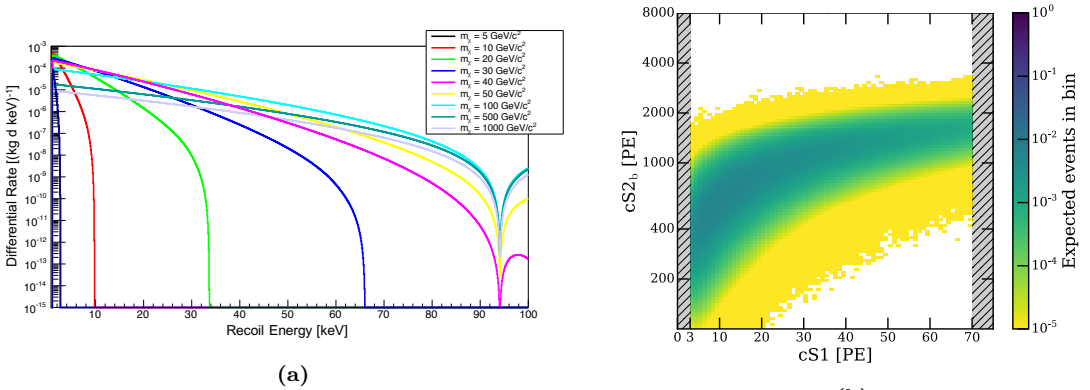

(a) **(b)**

Figure 4.18: (a) Differential rate expected in a xenon target by WIMP-nucleon spin-independent interactions under the assumption of a standard DM galactic halo [289] and the Helm nuclear form factor [293], which is responsible for the reduced rate at ∼94 keV. The recoil energy spectra induced by WIMP of masses from 5 GeV/c^2 to 1 TeV/c^2, with cross section $\sigma_{SI} = 2 \times 10^{-45}$ cm^2, are shown in different colors. (b) The XENON1T dark matter signal model in the (cS1, cS2$_b$) space of a 200 GeV/c^2 WIMP. The spectral shape of light ($\lesssim$ 20 GeV/c^2) WIMPs shrinks towards the lowest portion of the cS1 range. The model of a 6 GeV/c^2 WIMP is very similar to the CNNS model (figure 3.22b), while the shape in the energy space is almost identical among heavy WIMPs.

4.4.3 Adopted WIMP signal model

The dark matter model assumes WIMP elastically scattering off nuclei of the LXe target via spin-independent (SI) interaction with cross section σ_{SI}. A standard DM isothermal halo [289] is considered, in which trapped WIMPs have a Maxwell-Boltzmann velocity distribution. In the assumed astrophysical model, the local dark matter density is $\rho_\chi = 0.3\,\mathrm{GeV/cm^3}$ [290], the most probable WIMP velocity is equal to $v_0 = 220\,\mathrm{km/s}$ [291] with a cut-off corresponding to the galactic escape velocity $v_{esc} = 544\,\mathrm{km/s}$ [291]. The differential rate of WIMP SI interactions in a target medium of mass number A is given by [292]:

$$\frac{dR}{E_R} = \frac{\rho_\chi\,\sigma_{SI}\,A^2}{2\mu_p^2\,m_\chi}\,F^2(q)\int_0^{v_{max}}\frac{f(|\vec{v_\chi}+\vec{v_E}|)}{v}\,\mathrm{d}v, \tag{4.6}$$

where μ_p is the proton-WIMP reduced mass, m_χ the WIMP mass, $f(|\vec{v_\chi}+\vec{v_E}|)$ the distribution of the composition of WIMP and Earth's velocity $v_E = 232\,\mathrm{km/s}$ in the Milky Way, and $v_{max} = v_{esc}+v_E$. The Helm form factor [293] $F(q)$ is assumed to correct for diffractive effects that reduce the nuclear cross section as a function of the transferred momentum q in the WIMP-nucleon recoil. The expected recoil energy spectrum of DM is therefore dependent on the WIMP mass, as shown in figure 4.18a.

The DM signal model in the observable space (shown in figure 4.18b) is built based on the NR response model illustrated in section 3.3 and assuming uniform distribution in the fiducial volume. The uncertainty of the DM signal model is propagated from the determination of NR response model into a rate uncertainty of 15% (3%) for WIMPs of 6 (200) GeV/c^2 mass.

4.4.4 Background predictions for the XENON1T DM search

All the background components and the WIMP NR signal are modelled as unbinned probability density functions in the three main analysis dimensions: cS1, $cS2_b$ and the radial coordinate r. Additionally, in order to take into account the dependency of the neutron background from the vertical coordinate z (with particular reference to the neutron-X distortion mainly influencing the bottom edge of TPC), events are categorized as being inside or outside the 0.65 t core mass (described in section 4.3.1).

Table 4.1 summarizes the expectation value of each background in the combined exposure (278.8 days) of the two XENON1T science runs. The final inference on the unblinded dataset is performed exploiting the full parameter space. In table 4.1, the background predictions are also presented in specific sub-ranges of the energy space and fiducial volume, where DM signal is expected while specific backgrounds are suppressed. A reference NR signal region is defined between the median and -2σ quantile of 200 GeV/c^2 WIMP model in the (cS1, $cS2_b$) space, which contains only a 0.3% of residual ER background contribution due to the small overlap between the ER and NR band distributions. The 0.9 t fiducial volume with a more strict radial bound ($r < 34.6$ cm), with respect to the full 1.3 t FV ($r < 42.8$ cm), contains a negligible contamination of surface background which is confined to higher radii. The inner core volume (0.65 t) contains a highly reduced event contribution from radiogenic neutrons. Although the ER rate is estimated from measurements of α-decays activities from the ^{222}Rn progeny, dark matter search data provide the most stringent constraint. The ER rate normalization is therefore derived from the likelihood fit on the unblinded data since it is left as a free parameter. Electronic recoils due to intrinsic ^{214}Pb β-decays are the major background in any of the restricted NR signal reference sub-spaces. The expected number of events from a 200 GeV/c^2 WIMP, assuming a SI cross section equal to 10^{-46} cm^2 (approximately the lowest excluded cross section for this mass before XENON1T results), is also shown in table 4.1 for comparison.

4.5 Statistical inference on unblinded data

The statistical interpretation of the observed XENON1T data is performed under the hypothesis test approach to determine confidence intervals on the parameter of interest for DM search, the WIMP-nucleon SI cross section. The background-only (or null) hypothesis H_0 and the signal hypothesis H_σ, dependent on the WIMP cross section σ, are based on the models and expectation values described in the previous section. The definition of the test statistic used, the procedure to compute discovery significances and confidence intervals are described in section 4.5.1. The specific likelihood function used in the analysis of the collected XENON1T data in the 1 tonne×year exposure of the combined runs SR0 and SR1 is presented in section 4.5.2. The WIMP search is "blinded" and "salted" to avoid fine-tuning biases based on observed data in the expected signal region. The unblinded and de-salted XENON1T data in the region of interest for

Fiducial Volume	1.3 t	1.3 t	0.9 t	0.65 t
Energy Region	Full	NR Ref.	NR Ref.	NR Ref.
ER	627 ± 18	1.6 ± 0.3	1.1 ± 0.2	0.6 ± 0.1
Neutron	1.4 ± 0.7	0.8 ± 0.4	0.4 ± 0.2	0.14 ± 0.07
CNNS	0.05 ± 0.02	0.03 ± 0.01	0.02 ± 0.01	0.01
AC	0.6 ± 0.1	0.13 ± 0.03	0.08 ± 0.02	0.05 ± 0.01
Surface	106 ± 8	4.8 ± 0.4	0.02	0.01
Total Background	735 ± 20	7.4 ± 0.6	1.6 ± 0.3	0.8 ± 0.1
WIMP ($\sigma_{SI} = 10^{-46}\,\mathrm{cm}^2$)	7.6 ± 0.2	3.6 ± 0.1	2.47 ± 0.07	1.77 ± 0.05

Table 4.1: Predicted number of background events for the XENON1T WIMP search in the combined 278.8 days exposure of the two science runs. The full analysis space is defined as cS1 $\in$ (3, 70) PE, cS2$_b$ $\in$ (50, 8000) PE and inside the 1.3 t fiducial volume (described in section 4.3.1). Background expectation values of each component are reported also in the NR signal reference region (between the median and -2σ quantile of 200 GeV/c^2 WIMP model in the (cS1, cS2$_b$) space) and in the 0.9 t and 0.65 t sub-volumes. The expected number of dark matter signal events is reported for comparison relatively to 200 GeV/c^2 WIMP mass and WIMP-nucleon SI cross section equal to $10^{-46}\,\mathrm{cm}^2$. Uncertainties smaller than 0.005 are not shown.

DM search are shown and discussed in section 4.5.3 along with the results of the final statistical inference on the WIMP hypothesis.

4.5.1 Statistical interpretation framework

Test statistic The profile log-likelihood ratio is used as the test statistic both for confidence intervals and discovery assessments. The likelihood $L(\sigma, \boldsymbol{\theta}|\boldsymbol{x})$ is a function of the signal strength σ, corresponding to the WIMP-nucleon SI cross section in this case, and a number of nuisance parameters $\boldsymbol{\theta}$ given the measured set of outcomes $\boldsymbol{x}$ of an observable:

$$L(\sigma, \boldsymbol{\theta}|\boldsymbol{x}) = \prod_k \prod_{i=1}^{N_k} p_k(x_i^k|\sigma, \boldsymbol{\theta}). \tag{4.7}$$

The index k runs over separate measurements, for example different calibration and dark matter search datasets, and the index i runs over the N_k independent observations x_i^k, which are assumed to follow the probability density function (PDF) $f_k(x|\sigma, \boldsymbol{\theta})$. The test statistic is the profiled log-likelihood ratio

$$q(\sigma) = -2 \log \frac{L(\sigma, \hat{\hat{\boldsymbol{\theta}}})}{L(\hat{\sigma}, \hat{\boldsymbol{\theta}})}, \tag{4.8}$$

where $\hat{\sigma}, \hat{\boldsymbol{\theta}}$ are the unconditional maximum likelihood estimators (MLE) of signal and nuisance parameters, while $\hat{\hat{\boldsymbol{\theta}}}$ are the nuisance parameters that maximize the likelihood with the condition that the signal strength is σ (conditional MLE). To avoid un-physical regions, the best-fit signal $\hat{\sigma}$ is constrained to be non-negative.

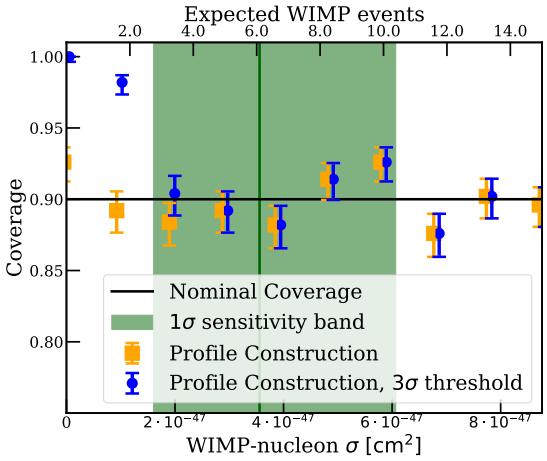

Figure 4.19: Coverage of confidence intervals constructed using the Feldman-Cousins profile construction as a function of the WIMP-nucleon SI cross section for 1 tonne×year search of a 50 GeV/c^2 WIMP. Errorbars indicate 1σ confidence intervals around the best estimate. Orange squares show the result using the profile construction, while the blue circles show the coverage including the 3σ threshold for reporting upper limits. The green line and band highlight the sensitivity and 1σ band of expected exclusion upper limits.

Confidence intervals Confidence intervals may be considered as a repeated hypothesis test performed at each value of the parameter of interest. A signal hypothesis H_σ is tested against the data computing the p-value of the observed test statistic $q(\sigma)$ under such hypothesis. Given the low background of XENON1T, analytic approximations of the test statistic expected distribution [294] do not hold. Therefore, the distribution of $q(\sigma)$ is computed using toy MC simulations of the background and signal models, where the auxiliary measurements related to each nuisance parameter are also varied per toy MC data sample.

The confidence interval is computed with a Feldman-Cousins (FC) construction [295] in the profile likelihood, including all σ for which $q(\sigma) < q_\alpha(\sigma)$, where the acceptance threshold $q_\alpha(\sigma)$ is the $1-\alpha$th percentile of the test statistic distribution. As in the case of a standard FC construction, this will provide one- or two-sided confidence intervals depending on the data, and thus avoids the flip-flopping under-coverage associated with switching between one- and two-sided tests. For a 90% confidence interval (i.e. $\alpha = 0.1$, which is the choice for the XENON1T DM analysis), coverage at $\sigma = 0$ will lead to a two-sided interval in 10% of cases in the absence of signal. For the XENON1T DM analysis, decision is made to use a higher excess reporting threshold, so that only the upper edge of the confidence interval will be reported if the discovery significance is lower than 3σ. This leads to over-coverage at low signals, with an example shown in figure 4.19 affecting limits below the 1σ sensitivity band.

In the case of a downwards fluctuation of observed data, a 15% power-constraint would be applied to set a lower threshold below which upper limits would not be set, as proposed in [296].

Discovery significance and sensitivity The discovery significance based on the actually observed data can be calculated distinctly with respect to the FC confidence interval construction, choosing to run a test to reject the background-only hypothesis (as described in section A.1.3). In this case, the test-statistic is evaluated at the null-hypothesis, $q_0 = q(\sigma = 0)$, whose distribution under H_0 is denoted as $f(q_0|H_0)$. The significance of a given observed test statistic q_0^{obs} on data can be written in terms of p-value as

$$p_{H_0} = \int_{q_0^{obs}}^{\infty} f(q_0|H_0)\ dq_0. \tag{4.9}$$

The local discovery significance above is computed for a single signal hypothesis. To compute a global discovery significance, the distribution of the most significant p-value for any hypothesis is estimated with toy Monte Carlo simulations, and compared with the result from data.

Conversely, the sensitivity of XENON1T in the DM search presented in this work is computed using the test-statistic $q(\sigma)$ and testing the signal hypothesis H_σ on simulated toy MC pseudo experiments, based on the final XENON1T signal and background models, analogously to the method described in [135, 297].

4.5.2 The XENON1T likelihood function

The log-likelihood used in the spin-independent analysis is a sum of extended un-binned likelihoods for the two science runs, extended un-binned likelihoods for ER calibration data and terms expressing ancillary measurements of nuisance parameters θ_m:

$$\begin{aligned} \log L_{\text{total}}(\sigma, \boldsymbol{\theta}) = &\sum_{\text{SR}} \log L_{\text{SR sci}}(\sigma, \boldsymbol{\theta}) \\ &+ \sum_{\text{SR}} \log L_{\text{SR cal}}(\boldsymbol{\theta}) \\ &+ \sum_{\text{m}} \log L_{\text{m}}(\theta_m). \end{aligned} \tag{4.10}$$

The index SR runs over data-taking periods, SR0 and SR1, and L_{sci}, L_{cal} are the likelihood terms for the dark matter search data and ^{220}Rn calibration data, respectively. Ancillary measurements of nuisance parameter θ_m are included in $L_{\text{m}}(\theta_m)$. The un-binned likelihoods take the form:

$$L_{\text{SR sci}}(\sigma, \boldsymbol{\theta}) = \text{Pois}(N_{\text{SR}}|\ \mu_{\text{tot}}(\sigma, \boldsymbol{\theta})) \cdot \prod_{i=1}^{N_{\text{SR}}} \left[\sum_c \frac{\mu_c(\sigma, \boldsymbol{\theta})}{\mu_{\text{tot}}(\sigma, \boldsymbol{\theta})} \cdot f_c(\boldsymbol{x}_i|\boldsymbol{\theta}) \right], \tag{4.11}$$

where the index i runs over events in the relevant science or calibration dataset, and $\mu_{\text{tot}}(\sigma, \boldsymbol{\theta}) = \sum_c \mu_c(\sigma, \boldsymbol{\theta})$, with the index c indicate each signal or background component expectation, $\mu_c(\sigma, \boldsymbol{\theta})$ which may be a function of nuisance parameters, or a nuisance parameter itself. The PDFs, $f_c(\boldsymbol{x}_i|\boldsymbol{\theta})$, for each component are functions of the analysis

coordinates $\boldsymbol{x}_i = (\mathrm{cS1_i}, \mathrm{cS2_i}, \mathrm{r_i})$ and are evaluated for each event in the likelihood. The calibration likelihood $\log L_{\mathrm{SR\ cal}}(\boldsymbol{\theta})$ utilizes a smaller volume, $r < 36.94\,\mathrm{cm}$, and depends only on the cS1 and cS2 dimensions, since the events of interest are uniformly distributed in space and with the smaller radial edge the surface background contamination is removed. The additional spatial binning that distinguish the inner core volume (0.65 t) from the rest of the 1.3 t FV, is technically implemented as combination of two separate un-binned likelihoods, analogous to equation (4.11), where the relative expectations inside and outside the core mass are determined using the (r, z) distribution of the different components.

Nuisance parameters The signal and background models, consisting of expectation values and distributions in analysis space depend on several nuisance parameters. Expectation values for all the modelled backgrounds in the science data as well as AC and ER rates in the ^{220}Rn calibration likelihood are all constrained by a nuisance parameter that reflect their uncertainty. The rate of radiogenic neutrons is considered correlated between science runs, while all other background rates enter separately in the SR0 and SR1 likelihoods.

The neutron and CNNS rates are constrained by ancillary measurements expressed as Gaussian likelihoods, given a true expectation value μ_c and measurement uncertainty σ_c as central value and width, respectively. The signal expectation is dependent on the WIMP mass, the signal acceptance and a multiplicative factor, ϵ_{SR}, expressing the uncertainty of the signal expectation for a fixed cross section, which in turn depends on mass, ranging from 0.15 at $6\,\mathrm{GeV/c^2}$ to 0.03 at $200\,\mathrm{GeV/c^2}$. The accidental coincidence rate $\mu_{AC\ \mathrm{SR}}$ is measured as lying between two extreme estimates and is assigned a uniform PDF between the lower and upper reference. No auxiliary measurements are assigned to ER and surface background rates as their high statistics in the science data sample constrains them. In the case of surface background, the fact that the part of the distribution that mostly would affect the inference is blinded, at low cS1 and radius, motivates the conservative assumption of not imposing an auxiliary constraint.

In addition to uncertainties on the rates, the ER and surface background PDFs also have shape uncertainties. For the surface background, the main uncertainty is the distribution in the inner parts of the detector, leading to choosing the slope of the radial distribution as a shape uncertainty. The science data fit finally constrains the radial dependency of the surface background. The nuisance parameters γ_{er} and Δr, governing the photon yield and recombination fluctuations, in the detector response model (described in section 3.3) are propagated to the likelihood acting as shape uncertainties to the ER background model.

A mis-modelling term, or "safeguard", proposed in [298], is added to the ER background model. It consists of a signal-like component added or subtracted to the nominal ER model. This modification is motivated by the importance of the ER model for the final inference, and the idea that a spurious signal-like over- or under-estimation in the background will have the greatest impact, giving spuriously strong limits or significant

excesses, respectively. Moreover, the ER model is simultaneously fitted to calibration data, which allows the safeguard component to be constrained by the much higher (approximately 10 times for SR0 and SR1) statistics of the calibration dataset. The ER background PDF with the inclusion of the safeguard term is written as

$$f_{\mathrm{ER}}(\boldsymbol{x}|\alpha,\boldsymbol{\theta}_{\mathrm{ER}}) = \beta\cdot[(1-\alpha)\cdot f_{\mathrm{ER\ nominal}}(\boldsymbol{x}|\boldsymbol{\theta}_{\mathrm{ER}}) + \alpha\cdot f_{\mathrm{signal}}(\boldsymbol{x})]\,, \tag{4.12}$$

where α is the safeguard nuisance parameter. If the mis-modeling term causes the PDF to be negative, it is truncated to 0. The normalization of the PDF in the analysis space is ensured by the factor β, which is a function of α and nuisance parameters that affect the ER distribution $\boldsymbol{\theta}_{\mathrm{ER}}$.

4.5.3 The XENON1T dataset and final results

The XENON1T data are unblinded after the background and signal models are fixed, as well as the statistical interpretation method. In addition to blinding, a salting procedure is performed injecting an undisclosed number and class of fake events in order to protect against fine-tuning of models or selection criteria in the post-unblinding phase.

Unblinded dataset The XENON1T dataset is unveiled in figures 4.20, 4.21 and 4.22, showing the unblinded data after de-salting, which found two injected ^{241}AmBe salt events, randomly selected, which had not motivated any further scrutiny of the analysis method. A total of 14 events is found in the NR signal reference region (between the median and -2σ quantile of the 200 GeV/c^2 WIMP signal distribution in the (cS1, cS2$_b$) space) in the full 1.3 t fiducial volume and 2 of them lay within both the 0.9 t and 0.65 t inner volumes. The observed number of events in the 1.3 t FV indicates an excess over the expected background of 7.4 ± 0.6 events. However, it is important to notice that the inference on the measured dataset is performed in the full parameter space and taking into account the distribution of each event in it.

The 1D projection in the cS2$_b$ signal space is shown in the bottom panel of figure 4.20 with data in the 1.3 t FV and in the 0.9 t volume, where the surface background distributed at very low cS2$_b$ is suppressed.

The best-fit models of backgrounds and signal on the full XENON1T dataset are exploited to assign a relative probability to single events to be compatible with each of the models in the likelihood function. In figures 4.20 and 4.22 such probabilities are shown through pie charts assigned to each observed event, considering as reference the signal model of a 200 GeV/c^2 WIMP, for which the best-fit cross section is 4.7×10^{-47} cm^2 (corresponding to 3.6 events in the full ROI). Small charts (mainly single-colored) correspond to unambiguously background-like events, while events where the WIMP probability is >1% are enlarged for visibility (with increasing sizes corresponding to 1%, 5%, 10%, 20% probabilities). Three events show a WIMP probability larger than 20% and none of them is located in the center of the TPC, as can be seen in the (x, y) projection in figure 4.22 (left panel). One is close to the bottom edge of the FV (see

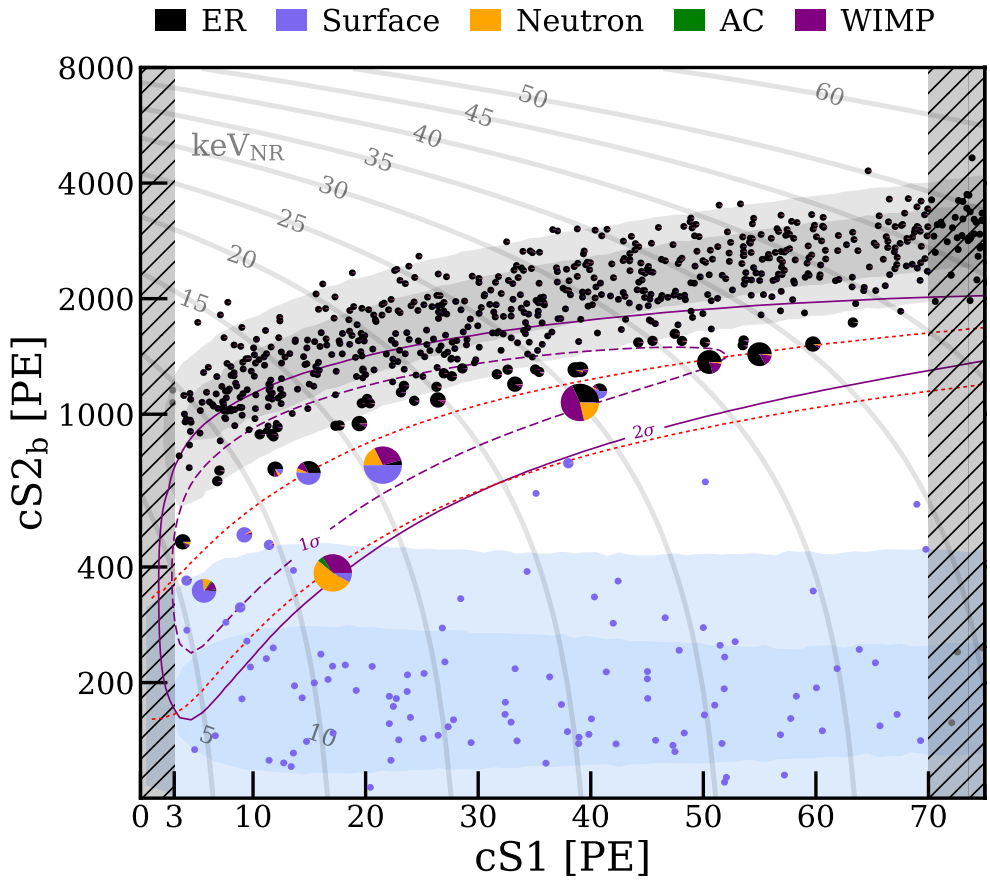

Figure 4.20: The XENON1T unblinded dataset for dark matter search with the combination of the two science runs (SR0 and SR1) for a total exposure of 278.8 d and within 1.3 t fiducial LXe target mass. The distribution in the energy space (cS1,cS2$_b$) of events that pass all selection criteria, described in section 4.3, is shown. Events are drawn as pie charts representing the relative probabilities of the background and signal components for each event, with the color code given in the legend, under the best-fit model for 200 GeV/c^2 WIMP signal and the resulting best-fit cross section $\sigma = 4.7 \times 10^{-47}$ cm^2. Shaded regions show the projection of the ER (grey) and surface (blue) background components. The 1σ (purple dashed) and 2σ (purple solid) percentiles of the 200 GeV/c^2 WIMP signal are overlaid for reference. The NR signal reference region is defined between the two red dotted lines. Grey lines show isoenergy contours in NR energy. Vertical shaded regions are outside the ROI.

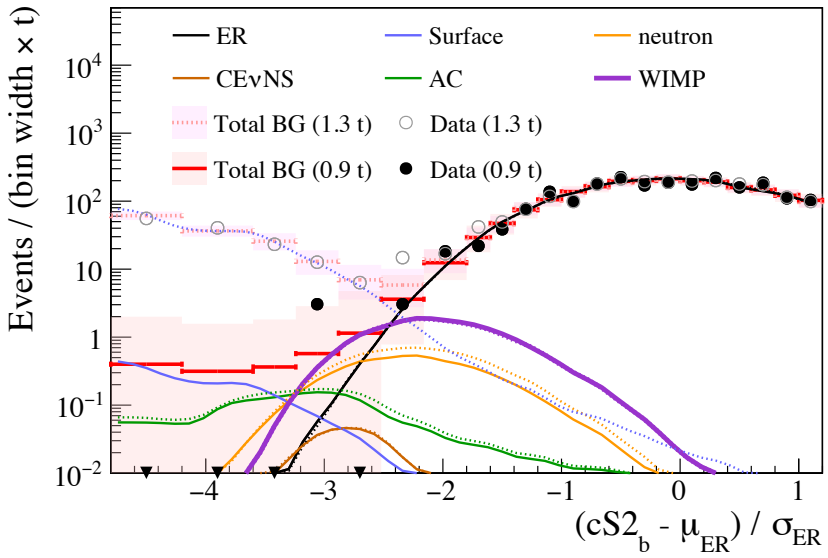

Figure 4.21: Background and 200 GeV/c^2 WIMP signal best-fit predictions, assuming $\sigma = 4.7 \times 10^{-47}$ cm^2, compared to the XENON1T DM search data in the 0.9 t (solid lines and markers) and 1.3 t (dotted lines and hollow markers) fiducial masses. The horizontal axis is the projection along the ER mean (μ_{ER}), normalized to the ER band 1σ quantile (σ_{ER}). Shaded bands indicate the 68% Poisson probability region for the total background expectations.

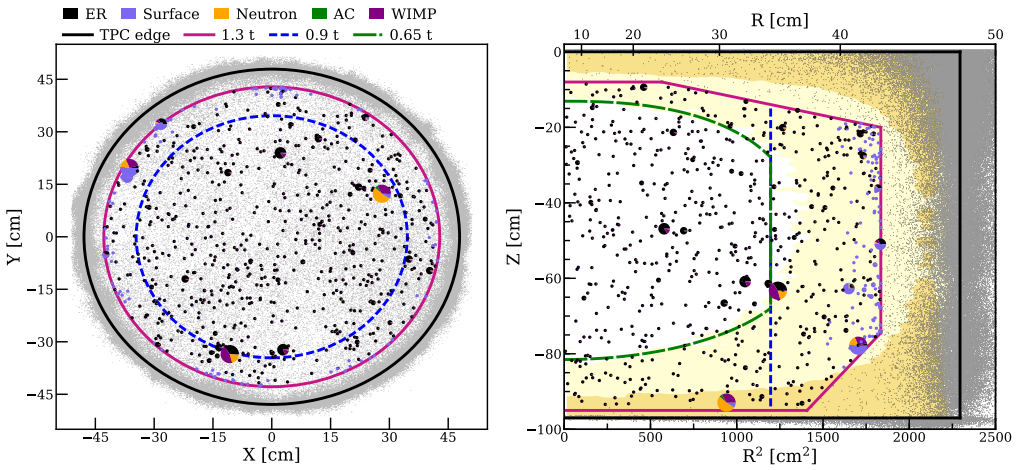

Figure 4.22: Spatial distributions of the XENON1T DM search data. Events are drawn as pie charts with the same marker description as in figure 4.20. Grey points are events reconstructed outside the fiducial mass. The TPC boundary (black line), the 1.3 t fiducial mass (magenta), the maximum radius of the reference 0.9 t mass (blue dashed), and the 0.65 t core mass (green dashed) are shown. Yellow shaded regions display the 1σ (dark) and 2σ (light) probability density percentiles of the radiogenic neutron background component.

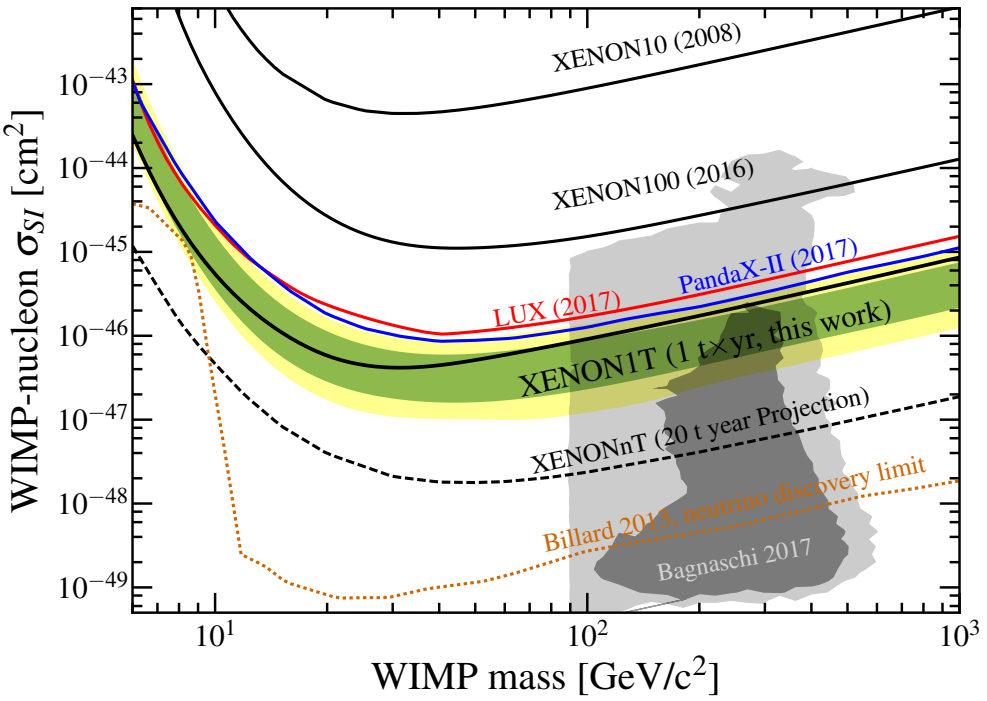

Figure 4.23: The 90% confidence level upper limit on WIMP-nucleon spin-independent cross section from the XENON1T 1 tonne×year search with the 1σ (green) and 2σ (yellow) sensitivity bands. Previous world-best results from LUX [110] and PandaX-II [111] experiments are shown for comparison. Results from past and future detectors of the XENON DM Project are drawn as black solid lines (XENON10 [134] and XENON100 [105]) and dashed line (XENONnT projected sensitivity in 20 t×y exposure [135]). The neutrino discovery limit [138] (orange) is also shown for reference, as well as a supersymmetric DM model [299] constrained by accelerator experiments, astrophysical observations and direct detection searches.

figure 4.22, right) and below the bulk NR distribution in the (cS1, cS2$_b$) space (see figure 4.20), both properties compatible with the expected neutron-X contribution to background. A second event is located at large radius where the surface background is dominant, even though the position in the energy space is displaced from the bulk of surface background model and falls inside the NR band. The third WIMP-like event shows, instead, almost equal compatibility also with the ER and neutron background models.

Results of statistical inference The profile likelihood analysis on the measured data with XENON1T in the science runs SR0 and SR1 indicates no significant excess with respect to the background expectation at any WIMP mass in the directly scanned range from 6 GeV/c^2 to 1 TeV/c^2. The FC construction of the confidence interval on the WIMP-nucleon SI cross section returns a 90% confidence level upper limit, which is shown in figure 4.23.

The limit falls within the calculated sensitivity across all masses, weaker with respect

to the median sensitivity for WIMP masses larger than $30\,\mathrm{GeV/c^2}$ and stronger at low masses. This result, with 1 tonne×year exposure (278.8 live-days and 1.3 t target mass), improves the current most stringent constraints on WIMPs $>6\,\mathrm{GeV/c^2}$, with the lowest cross section value excluded at $4.1 \times 10^{-47}\,\mathrm{cm^2}$ for WIMPs of mass $30\,\mathrm{GeV/c^2}$.

The calculation of the discovery significance based on the best-fit background model finds a p-value of 0.28, 0.41 and 0.22 at 6, 50 and $200\,\mathrm{GeV/c^2}$, respectively. Therefore, the local discovery significance is lower than 0.8σ across the whole WIMP mass range tested. If the background-only local p-value is calculated on a simple Poisson plus Gaussian uncertainty statistics in the NR reference region (where a numerical excess of events is observed), the result gives a rejection significance of $\sim 1.9\sigma$, not significant enough to trigger modification in the background model, fiducial boundary or alternate signal models. Such a choice is conservative as the observed excess anyway results in a weaker exclusion limit with respect the expected median sensitivity.

The 2σ sensitivity band spans one order of magnitude in the WIMP cross section space, as a consequence of the large random variability of observed upper limits due to statistical fluctuation of the background (which is usually extremely low in rare-event searches). Besides the actual limit obtained with the present DM search, the XENON1T median sensitivity, which is not affected by the aforementioned variability, is about 7.0 times better than previous most sensitive experiments to $>50\,\mathrm{GeV/c^2}$ WIMPs (LUX [110] and PANDAX-II [111]). The imminent XENONnT upgrade with increased target LXe mass of 6 tonnes (the commissioning phase foreseen in 2019) will improve upon the XENON1T results by about one order of magnitude.

Summary

The search for dark matter continues. Strong and numerous evidences suggest the existence of dark matter and have triggered comprehensive experimental efforts of the scientific community (chapter 1). No clear discovery has been established so far in experiments at colliders, nor in those exploiting direct and indirect detection techniques.

The XENON Collaboration focuses on direct search for WIMPs, the most natural and popular DM candidate. With the currently operating XENON1T experiment, unprecedented sensitivity to WIMP-nucleon interaction has been achieved among all dark matter detectors (chapter 2). XENON1T is the first ton-scale LXe dual-phase TPC with its 3.2 t xenon mass (of which 2.0 t are contained in the active volume). From November 2016 to February 2018, XENON1T collected dark matter search data for 278.8 live-days, resulting from the combination of the two science runs SR0 (32.1 d) and SR1 (246.7 d), for a 1 t×y exposure WIMP search (discussed in this work). The XENON1T detector represents the current stage of the XENON Dark Matter Project that started in 2007 with the prototype TPC XENON10, followed by XENON100, both providing world-best constraints on WIMP-nucleon cross section. Proceeding on the path already marked of target mass increases and background reductions, the upgrade of XENON1T, named XENONnT, will quickly replace its predecessor by 2019. XENONnT will feature about 8 t (6 t) total (active) LXe mass and aims at lowering the (already ultra-low) background level by a factor 10 to boost the sensitivity by a further order of magnitude.

The ER background in XENON1T (section 3.1), indeed, is the lowest background ever achieved in a direct detection dark matter experiment. In the low energy region of interest for WIMP searches, the measured ER differential rate is

$$82^{+5}_{-3}(\text{syst}) \pm 3(\text{stat})\,(\text{t}\cdot\text{y}\cdot\text{keV})^{-1},$$

stable over the data taking period. This measurement agrees with the expectation from MC simulations, that are also able to correctly predict the ER spectrum at higher energies (up to few MeV), as deduced from the good matching between simulated and measured spectrum. Within the 1.3 t fiducial volume in which the DM search is carried out, the ER background rate is dominated by intrinsic sources: β-decays of ^{214}Pb (part of the ^{222}Rn decay chain) and ^{85}Kr (isotope present in ^{nat}Kr) account for 75% and 11% of the total, respectively (while double-beta decay of ^{136}Xe contributes to just

1%). The ^{nat}Kr/Xe concentration, monitored with RGMS measurements, is reduced by three orders of magnitude during early XENON1T operation by means of online cryogenic distillation, reaching an average 0.66 ± 0.11 ppt during SR0 and SR1. The ^{222}Rn concentration is kept under control through a screening campaign to accurately select detector materials with low ^{222}Rn emanation. Online ^{222}Rn distillation was also tested by operating the cryogenic distillation column in reverse mode. This approach will be fully exploited in XENONnT. The $\sim 10\,\mu$Bq/kg activity of ^{214}Pb is constrained by measuring the rate of ^{218}Pb α-decay ($12.6 \pm 0.8\,\mu$Bq/kg) and ^{214}BiPo delayed coincidence ($5.1 \pm 0.5\,\mu$Bq/kg). The ER background expectation for the 1 t×y WIMP search is constrained by data and amounts to 627 ± 18 (1.6 ± 0.3) events in the full (NR reference) analysis space.

The NR background (section 3.2) due to cosmogenic neutrons is suppressed thanks to the passive water shield and the active Cherenkov veto provided by the Muon Veto system. The contribution of coherent neutrino-nucleus scattering is estimated with MC simulations (taking into account the recently measured CNNS cross section by the COHERENT experiment) and it corresponds to 3% of the total NR background budget, which is dominated by radiogenic neutrons. The expectation value of neutron background is 1.4 ± 0.7 (0.14 ± 0.07) events in the 1.3 t FV (inner core 0.65 t volume and NR reference region). PMT components are responsible for $\sim$ 50% of the radiogenic neutron background as estimated form MC simulations. The neutron background model includes also the neutron-X population, with at least one additional scatter in the region below-cathode (sensitive only to the primary scintillation light) besides the single scatter in the fiducial volume. The distribution in the signal space (S1, S2) of neutron-X events is distorted due to lower S2/S1 ratio. This class of events contributes to 14% of the total neutron background budget, affecting in particular the bottom region of the TPC. The final prediction of radiogenic neutron background is also constrained by the measurement of 9 NR multiple scatter events in XENON1T data that, taking into account the best estimate of the single-to-multiple scatter ratio, provides a scaling factor to the purely MC prediction of $1.5^{+0.9}_{-0.6}$.

The ER and NR background models, and NR WIMP signal as well, are finally obtained through the detector signal response model (section 3.3), which describes the light and charge signals generation and propagation across the detector in order to establish the relationship between the recoil energy and the observed S1 and S2 signals. Runs with internal ^{220}Rn and external neutron sources are conducted to collect calibration data for low energy ER and NR interactions, respectively. The XENON1T model for ER and NR interactions is simultaneously fitted to calibration data. The derived overlap between the ER and NR bands corresponds to a residual 0.3% ER contamination in the reference NR region defined between the NR median and the -2σ quantile.

Additional background components in XENON1T are accidental pile-ups of spurious S1 and S2 signals, and surface events (section 4.4). The expected background due to accidental coincidences is evaluated based on the lone-S1, -S2 rates, obtaining a prediction of 0.6 ± 0.1 events. Due to the finite position reconstruction resolution, ER

events happening at the lateral PTFE reflector surface have a non-null probability to be reconstructed inside the FV. Such events present abnormally small S2 since part of the ionization electrons are captured at the surface and do not contribute to the charge signal. The surface background model, built with data-driven methods, overlaps with the NR region in particular at the lowest energies inducing a background expectation of 106 ± 8 (0.02) events in the 1.3 t FV (inner 0.9 t volume and NR reference region).

The spatial dependency of detector's response is mainly calibrated with an intense ^{83m}Kr source of mono-energetic gamma lines at low energy, periodically diffused in the LXe volume, in order to define proper corrections to the S1 and S2 signals on event-by-event basis (section 4.1). We observe a distortion of the electric drift field which requires an effective correction of the reconstructed event position, based on the reconstructed position distribution of ^{83m}Kr events which are uniformly distributed in the TPC. Such correction is also time-dependent as a consequence of continuous charge accumulation on the TPC wall responsible for drift field distortion. Both S1 and S2 signals are corrected for the collection efficiency of primary and secondary scintillation light. The charge signal is further corrected for the measured electron lifetime, whose evolution during SR0 and SR1 is modelled, with an average value of $\sim 650\,\mu$s corresponding to ~ 0.5 ppb concentration of electronegative impurities that capture free electrons during their drift.

The time stability of signals is monitored with several mono-energetic lines present in the detector for long periods (section 4.2). During SR0, light and charge yields are monitored with de-excitation gamma lines of ^{129m}Xe and ^{131m}Xe isotopes, activated during neutron calibration runs, and are found stable within 0.6% and 0.9%, respectively. In the longer SR1, other sources are also exploited to monitor the signal stability, such as ^{83m}Kr, external gammas and ^{222}Rn. All the measurement agrees with a light yield stable within 0.2% and with a slight increase of the charge yield by about 5% over the whole SR1 period. Effective correction for the observed charge yield variation is not necessary as its size is not large enough to produce a significant effect on the ER model determination.

Several selection criteria are imposed to data (section 4.3) to ensure data quality and reject un-physical events, leading to a WIMP signal acceptance of $\sim 96\%$ ($\sim 93\%$) for S1 (S2) signal. The total XENON1T efficiency for WIMP search as a function of energy takes into account also the detection efficiency, dominated by a 3-fold PMT coincidence condition. The region of interest is defined in the signal space as cS1$\in(3,\ 70)$ PE and cS2$_b\in(50,\ 8000)$ PE.

The portion of analysis space where WIMP signal is expected with highly reduced ER contamination, referred to as NR reference region, is kept blinded until the analysis methods, background and signal models are fixed. Unblinded data reveal 14 events in the full 1.3 t FV within the previously blinded region, 2 of which contained in the inner 0.9 t volume free of surface background. The final inference on the WIMP-nucleon spin-independent cross section σ_{SI} is conducted exploiting a likelihood function parametrized in four dimensions: cS1, cS2$_b$ (signal space), r and z (spatial coordinates). The sys-

tematic uncertainties related to the normalization and shape of the background and signal models are included as nuisance parameters. A confidence interval on σ_{SI} is obtained via Feldman-Cousin construction in order to get an exclusion limit or two-sided interval (implying discovery) depending on the likelihood-based statistical test on data, avoiding the flip-flop problem due to the a priori decision on reporting upper limit only. The profile likelihood analysis (section 4.5) reports no significant excess over the expected background and exclusion limits are obtained for the WIMP mass range $(6,\ 1000)\,\mathrm{GeV/c^2}$. Local discovery significance is found lower than 0.8σ at any WIMP mass, not significant enough to claim discovery even though a small excess is observed. The resulting upper limits on σ_{SI} improve the previous most stringent constraints for WIMP heavier than $8\,\mathrm{GeV/c^2}$. The minimum is found at

$$4.1 \times 10^{-47}\,\mathrm{cm^2} \text{ for } 30\,\mathrm{GeV/c^2} \text{ WIMP.}$$

The obtained limit curve shows upper (lower) $\sim 1\sigma$ fluctuation with respect to the expected median sensitivity at high (low) WIMP masses. The XENON1T sensitivity reached in this $1\,\mathrm{t}\times\mathrm{y}$ DM search improves upon the best sensitivity of other LXe TPC detectors by a factor ~ 7.

The next phase of the XENON Dark Matter Project, XENONnT, is already under construction at LNGS. The commissioning of the increased TPC is expected to start by 2019. With this upgrade, the sensitivity will improve by one order of magnitude in 5 years of data acquisition, and the XENON Collaboration aims to stay at the forefront of the dark matter search rush in the next years.

Appendix A

Projected WIMP discovery potential

Direct experiments searching for WIMPs have been producing dramatic improvements in the last decade covering more than 3 orders of magnitude in the WIMP cross section parameter space, as in the case of the XENON DM Project from the first world-leading XENON10 [134] results to the current best limit of XENON1T [109] (presented in this work). Noble-liquid dual-phase TPCs with liquid xenon target have proven the best sensitivity to WIMPs so far. Although no evidence for DM signal has been found, great efforts are ongoing to keep scanning lower WIMP cross sections. Figure 1.10 shows the un-tested parameter space, below the current world-best WIMP exclusion limit from XENON1T [109], along with the projected sensitivities of future noble-liquid experiments (LZ [136], XENONnT [135], DARWIN [140], using LXe, and DarkSide-20k [300], using liquid Argon) that will approach the neutrino discovery limit [138] drawn in grey.

The sensitivity curves assess the level at which an experiment, given the predicted background and assumed exposure, is expected to be able to set exclusion limits on the WIMP-nucleon SI cross section (as a function of the WIMP mass) with, typically, 90% confidence level. The sensitivity of XENONnT (dashed blue curve in figure 1.10) and XENON1T, before the actual realization of the experiment, is studied in [135, 297]. On the other side, one can also wonder what is the expected capability of an experiment to claim WIMP discovery, besides the power in excluding DM. The sensitivity calculation is based on hypothesis test to reject the signal hypothesis (which includes the background and WIMP models), while the rejection of the background-only hypothesis is related to discovery. The discovery potential of XENON1T, based on the preliminary background expectations exploited to estimate also the sensitivity before the detector construction [135], is presented in section A.1. Discovery limits are evaluated in terms of WIMP-nucleon cross section below which rejection of the background-only hypothesis can not be achieved with a given significance (e.g. 3 or 5σ). In order to put a constraint on the WIMP mass and cross section in case of discovery, a bi-dimensional profile likelihood analysis needs to be performed. The expected performance of XENON1T in

reconstructing the WIMP parameters is studied in section A.2.

The evolution of the potential to WIMP discovery in the long-term perspective assuming the ultimate scenario for Xe-based DM detectors is studied in section A.3, where all the backgrounds but the CNNS component are supposed to be suppressed and discovery limits are evaluated as a function of increasing exposure.

A.1 Discovery potential of XENON1T

The XENON1T discovery potential extends the projected sensitivity studies in [135,297] for the benchmark exposure of 2 tonne·year. The physical model considered (see section A.1.1) is based on preliminary Monte Carlo background predictions, fully described in [135]. The latest MC background predictions for the DM search with XENON1T (discussed in chapter 4) are presented in sections 3.4 and 4.4, and have been updated mainly following more precise information about detector response characterization (section 3.3) and constraints derived from measurements with collected XENON1T data (see sections 3.1.2 and 3.2.5). The expected discovery limits, presented in section A.1.3, are estimated with the profile likelihood approach (see section A.1.2) testing the rejection of the background-only hypothesis by simulating a large number of MC datasets based on the XENON1T physical model.

A.1.1 Physical model

The XENON1T physical model used to study the DM discovery potential is composed by the signal, due to WIMP-nucleon spin-independent interaction, and the ER and NR backgrounds, originated by known particles producing a single (electronic or nuclear) recoil inside the fiducial volume. The standard ER and NR backgrounds are considered. The ER background is mainly caused by radioactive contaminants intrinsic to the LXe target (^{222}Rn, ^{85}Kr) and also by external gammas from detector materials and solar neutrinos (see section 3.1 for a detailed description). Neutrons and CNNS neutrinos contribute to the NR background (see section 3.2). The WIMP signal model assumes standard properties of the local DM halo, as described in section 4.4.3, to calculate the expected recoil energy spectrum for each WIMP mass in the range from 6 to 1000 GeV/c^2 (see figure 4.18a).

The parameter space features the prompt scintillation signal S1 and an idealized discrimination variable Y, which is a simplification of the usual discrimination parameter $\log_{10}$(S2/S1) used in XENON100 data analysis [301]. The background and signal models in the S1 observable space are shown in figure A.1. They are obtained by converting the expected recoil energy spectra into the observable S1 signal via the modelling of the detector signal response described in [135], which is mainly driven by the light and charge yield models extracted by XENON100 [302] and other direct measurements for NRs and by the NEST v0.98 model [254,303] for ERs. Moreover, the XENON1T model in this study is restricted to a super-elliptical fiducial volume (FV) containing 1 tonne

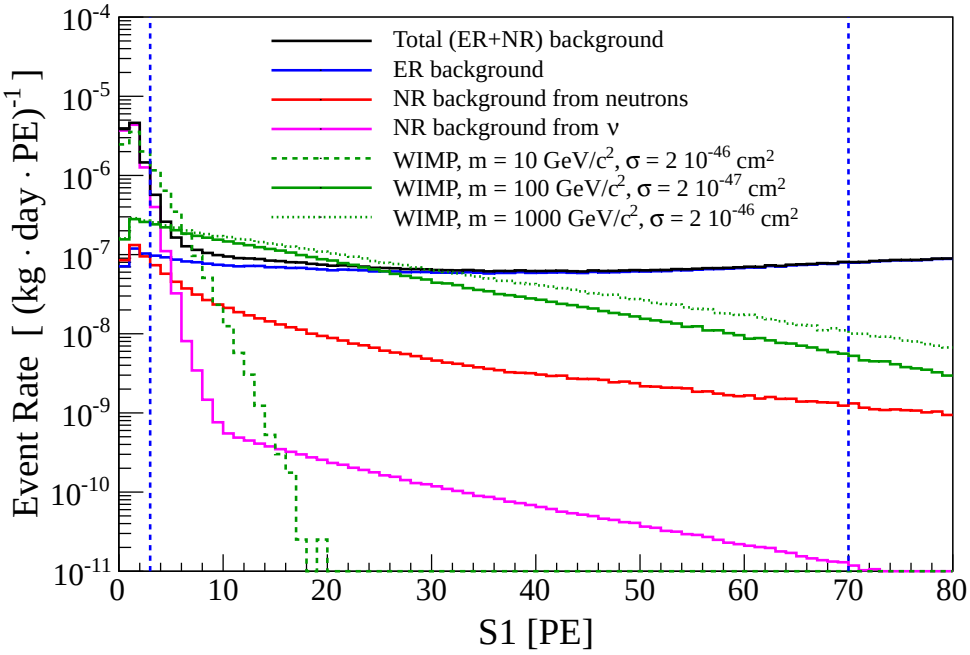

Figure A.1: S1 distribution of the total background (black) and of specific components: ERs (blue), NRs from neutrons (red) and CNNS (magenta). The expected WIMP NR signal spectrum is shown (green) for 10 (dashed), 100 (solid) and 1000 GeV/c^2 (dotted) mass with cross section of 2×10^{-46}, 2×10^{-47} and 2×10^{-46} cm^2, respectively. The vertical dashed lines delimit the (3, 70) PE region of interest for DM search. These spectra assume a 99.75% ER rejection with a flat 40% NR acceptance (see text).

LXe target mass.

The probability density functions (PDFs) of both ER and NR backgrounds are assumed to be Gaussian in the Y discrimination parameter space, with a separation that reproduces the discrimination performance achieved in XENON100 [192], namely 99.5, 99.75, 99.9% ER rejection power with 50, 40, 30% acceptance to NRs, respectively. The Y distribution of the ER model has central value $\mu = 0$ and $\sigma = 1$, while for the NR model (which applies also to the WIMP signal) $\mu = -2.58$ and $\sigma = 0.92$. The spectra in figure A.1 assume an ER rejection cut at the 99.75% quantile of the ER distribution in Y, giving a selection of the parameter space where the WIMP signal is expected with ER suppression. However, the statistical method used in this work exploits a profile likelihood analysis on the whole data sample without any hard cut on the ER population (see section A.1.2).

The expectation values, i.e. the expected number of observed events, of each component of the XENON1T model are calculated from the integral of the S1 spectra in the region of interest (3, 70) PE multiplied by the assumed experiment running time and the fiducial mass. The background (and signal) expectations in 2 tonne·year exposure are reported in table A.1. The ER rate takes into account early assumptions made

	No ER discrimination	99.75% ER discrimination
Background		
ER (μ_{ER})	258	0.65
Neutrons	1.10	0.44
CNNS	1.18	0.47
Total NR (μ_{NR})	2.28	1.55
Signal (μ_{sig})		
10 GeV/c^2 WIMP ($\sigma = 2 \times 10^{-46}$ cm^2)	4.63	1.85
100 GeV/c^2 WIMP ($\sigma = 2 \times 10^{-47}$ cm^2)	7.13	2.85
1 TeV/c^2 WIMP ($\sigma = 2 \times 10^{-46}$ cm^2)	8.85	3.54

Table A.1: Number of expected events without and with 99.75% ER discrimination (giving 40% NR acceptance) in a 2 years long science run assuming 1 t fiducial mass and in the ROI for WIMP search of (3, 70) PE in the S1 parameter space. Background expectations are based on preliminary MC predictions, described in [135], under the assumption of 1 µBq/kg ^{222}Rn and 0.2 ppt ^{85}Kr concentrations contributing to the ER background.

about the concentration of intrinsic contaminants at the level of 1 µBq/kg for ^{222}Rn and 0.2 ppt for ^{85}Kr (see section 3.1 for a detailed discussion about ER background sources and their estimated contribution based on XENON1T measurements).

The main uncertainty in the NR model considered [302] is due to the relative scintillation efficiency in LXe, $\mathcal{L}_{\text{eff}}$, which parametrizes the photon yield for NRs. Other, sub-dominant, systematic uncertainties come from the indetermination in the NR charge yield, $\mathcal{Q}_y$, and from the uncertainty in the predicted ER and NR background rates of 10% and 20%, respectively. The uncertainties from the NEST model [254] on the light and charge yields for ERs are much smaller than those related to NRs. Therefore, shape uncertainties on the ER background model are neglected.

A.1.2 Statistical model

The statistical framework adopted to study the XENON1T discovery potential makes use of the profile likelihood approach. The spectral shapes in the S1 space of the XENON1T model components (signal and backgrounds) are defined as PDFs, called f_{sig}, f_{ER}, f_{NR} for the signal, the ER and NR backgrounds, respectively, where f_{sig} is intended to vary with the WIMP mass. The expectation values for each component are named μ_{sig}, μ_{ER} and μ_{NR}. The Gaussian PDFs in the Y parameter space are indicated by g_{ER}, for the ER background, and g_{NR}, for the WIMP signal and NR background. The analysis is performed through an unbinned and extended likelihood function, meaning that simulated data are sampled from the functions f_c and g_c (where c indicate a specific component) and each event is identified by a point in the unbinned (S1,Y) bi-dimensional space. The parameter of interest (POI) is the signal strength μ_{sig} which is proportional to the WIMP-nucleon cross section σ. The extended likelihood

function is defined as

$$L(\sigma) = \text{Pois}(N_{obs}|\mu_{tot}) \cdot \prod_{i=1}^{N_{obs}} P(S1_i, Y_i) = \frac{e^{-\mu_{tot}}}{N_{obs}!} \cdot \prod_{i=1}^{N_{obs}} \mu_{tot} \cdot P(S1_i, Y_i), \tag{A.1}$$

where N_{obs} is the total number of observed events, $\mu_{tot} = \mu_{sig} + \mu_{ER} + \mu_{NR}$, $S1_i$ and Y_i are the measured values in the two observables for the i-th event. The probability of each event $P(S1_i, Y_i)$ can be expressed in terms of the model components:

$$\begin{aligned} P(S1_i, Y_i) = \frac{1}{\mu_{tot}} \big[& \mu_{sig} \cdot f_{sig}(S1_i) \cdot g_{NR}(Y_i) \\ & + \mu_{ER} \cdot f_{ER}(S1_i) \cdot g_{ER}(Y_i) \\ & + \mu_{NR} \cdot f_{NR}(S1_i) \cdot g_{NR}(Y_i) \big]. \end{aligned} \tag{A.2}$$

Systematic uncertainties are introduced in the likelihood through nuisance parameters. The dominant systematics due to $\mathcal{L}_{\text{eff}}$ indetermination, especially at very low NR energies, does not significantly affects the spectral shapes of neutron, CNNS and WIMP models, as shown in [297]. Therefore, only the variation in the expected number of events is affected by the considered uncertainties, as it is assumed also in [304]. Modifying $\mathcal{L}_{\text{eff}}$ to its $\pm 2\sigma$ values induces a variation up to a factor 4 of the expectation value for CNNS and 6 GeV/c^2 WIMPs, while for the neutron background and 50 GeV/c^2 WIMPs the variation is about 10%. All the systematic uncertainties are parametrized through normal constraints added to the likelihood function, with the nuisance parameters which in turn affect the expectation values of model components. The nuisance parameters are named $\theta_{\mathcal{L}}$, $\theta_{\mathcal{Q}}$, θ_{NR}, θ_{ER} relatively to $\mathcal{L}_{\text{eff}}$, $\mathcal{Q}_y$ and the uncertainty on the ER and NR background rate predictions. The complete log-likelihood function is then written as

$$\begin{aligned} -2 \ln L(\sigma; \boldsymbol{\theta}) = & \, 2 \left[\mu_{sig}(\sigma; \theta_{\mathcal{L}}, \theta_{\mathcal{Q}}) + \mu_{ER}(\theta_{ER}) + \mu_{NR}(\theta_{\mathcal{L}}, \theta_{\mathcal{Q}}, \theta_{NR}) \right] \\ & - 2 \sum_{i=1}^{N_{obs}} \ln \Big\{ \left[\mu_{sig}(\sigma; \theta_{\mathcal{L}}, \theta_{\mathcal{Q}}) \cdot f_{sig}(S1_i) \cdot g_{NR}(Y_i) \right] \\ & \qquad + \left[\mu_{ER}(\theta_{ER}) \cdot f_{ER}(S1_i) \cdot g_{ER}(Y_i) \right] \\ & \qquad + \left[\mu_{NR}(\theta_{\mathcal{L}}, \theta_{\mathcal{Q}}, \theta_{NR}) \cdot f_{NR}(S1_i) \cdot g_{NR}(Y_i) \right] \Big\} \\ & + (\theta_{\mathcal{L}} - \theta^0_{\mathcal{L}})^2 + (\theta_{\mathcal{Q}} - \theta^0_{\mathcal{Q}})^2 + (\theta_{ER} - \theta^0_{ER})^2 + (\theta_{NR} - \theta^0_{NR})^2, \end{aligned} \tag{A.3}$$

where $\boldsymbol{\theta} = (\theta_{\mathcal{L}}, \theta_{\mathcal{Q}}, \theta_{ER}, \theta_{NR})$ and the last term expresses the Gaussian constraints on the nuisance parameters, with θ^0 describing the nominal value (e.g. $\theta^0_{\mathcal{L}} = 0$ corresponds to the median $\mathcal{L}_{\text{eff}}$ in the assumed model [302]).

A.1.3 Discovery limit calculation

The significance of a new process, in a frequentist approach, is estimated with hypothesis test of the null hypothesis H_0 (background only) against the alternative H_σ

which includes both background and signal. The test statistic commonly used for such statistical inference on a given dataset is the profile likelihood ratio:

$$\lambda(\sigma) = \frac{L(\sigma, \hat{\hat{\boldsymbol{\theta}}})}{L(\hat{\sigma}, \hat{\boldsymbol{\theta}})}, \tag{A.4}$$

where $\hat{\sigma}$ and $\hat{\boldsymbol{\theta}}$ are the best-fit values that maximize the likelihood, called maximum likelihood estimators (MLE), and $\hat{\hat{\boldsymbol{\theta}}}$ is the conditional MLE of the nuisance parameters assuming the value σ for the parameter of interest.

To assess the discovery potential of XENON1T, we test the background only hypothesis, on simulated datasets based on the XENON1T physical model, and try to reject it. The test statistic to evaluate agreement of data with the H_0 hypothesis is defined as [294]

$$q_0 = \begin{cases} -2\ln\lambda(0) \\ 0 \end{cases} = \begin{cases} -2\ln\frac{L(0,\hat{\hat{\boldsymbol{\theta}}})}{L(\hat{\sigma},\hat{\boldsymbol{\theta}})} & \text{if } \hat{\sigma} \geq 0 \\ 0 & \text{if } \hat{\sigma} < 0 \end{cases} \tag{A.5}$$

The case $q_0 = 0$ indicates the maximum agreement with the background-only hypothesis H_0, i.e. $\hat{\sigma} = 0$. If the maximum likelihood estimator $\hat{\sigma}$ of σ is found to be negative, this cannot be considered as an indication of disagreement with H_0 due to the presence of a signal and hence q_0 is set to 0.

In order to evaluate the rejection significance of the hypothesis H_0, it is necessary to know the expected distribution of the test statistic under such hypothesis, i.e. the PDF $f(q_0|H_0)$. The PDF is evaluated by generating a large number of toy MC datasets under the H_0 hypothesis and computing each time the value of the profile likelihood ratio test statistic q_0. The observed value q_0^{obs} from a generic dataset can then be used to evaluate how much it is far from 0 (indicating the maximum agreement with H_0). If $q_0^{obs} > 0$, the rejection of the null hypothesis H_0 can be claimed with a significance given by (1-p), where p is the p-value defined as the integral of $f(q_0|H_0)$ above q_0^{obs}:

$$p = \int_{q_0^{obs}}^{\infty} f(q_0|H_0)\ dq_0. \tag{A.6}$$

To evaluate the discovery potential, it is also necessary to compute the PDF of the test statistic q_0 under several signal hypotheses H_σ, assuming different values of $\sigma > 0$. Then the median of each $f(q_0|H_\sigma)$ is taken to perform an hypothesis test over H_0 in order to calculate the expected discovery potential of the experiment. For a fixed significance level, e.g. 99%, the discovery limit is set at the value of the POI such that H_0 is rejected with (1-p)=99% significance. This also means that for higher values of σ, XENON1T would be able to claim discovery with even larger significance. A discovery potential curve is obtained by setting the discovery limit for different WIMP masses. Larger quantiles of $f(q_0|H_\sigma)$ can be also considered besides the median. For example, the 90% quantile corresponds to 90% probability to discover a signal with cross section σ with the fixed 99% significance threshold, while the median discovery limit corresponds to 50% probability of a 99% significant discovery.

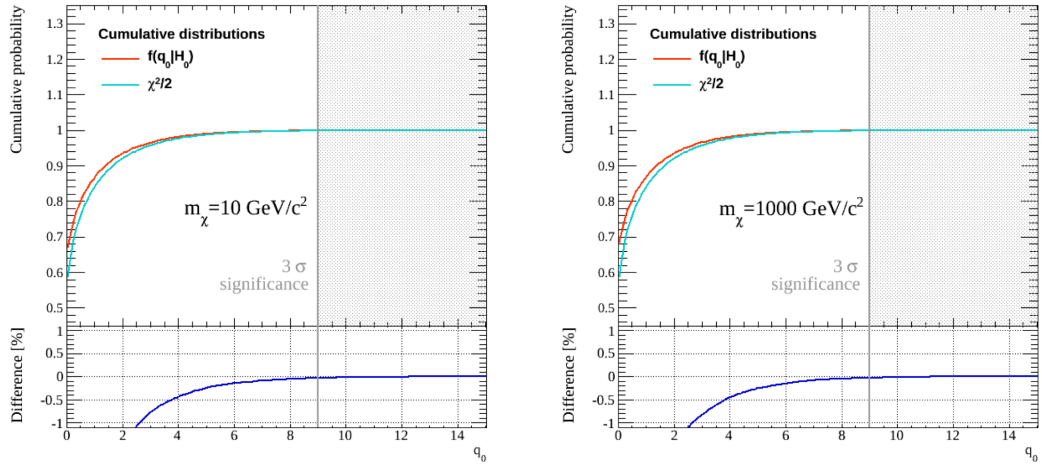

Figure A.2: Cumulative distribution of the profile likelihood ratio test statistic PDF $f(q_0|H_0)$ generated from 10^6 toy MC data samples (orange) and of the asymptotic distribution $\chi^2/2$ (cyan) for 10 (left) and 1000 GeV/c^2 WIMP mass (right). The grey vertical line indicates $q_0 = 9$, corresponding to a significance level of 3σ in the asymptotic approximation.

A total exposure of 2 t·y is fixed to evaluate the XENON1T discovery potential curve. The expected test statistic PDFs under signal (background) hypothesis are computed by simulating 10^4 (10^6) toy MC datasets.

Test of asymptoticity Based on the Wilks theorem [305] and the Wald approximation [306], it has been demonstrated that the PDF of the likelihood ratio, more precisely $-2\ln\lambda(\sigma)$, approaches a noncentral chi-square distribution for 1 degree of freedom when the data sample size is large. In particular, if the asymptotic limit holds, $f(q_0|H_0)$ follows a half-chi-square distribution $\chi^2/2$. Moreover, a simple relationship holds between the significance of rejection of H_0 and the test statistic q_0 in this case:

$$Z = \sqrt{q_0}, \tag{A.7}$$

where Z represents the number of standard deviations for a Gaussian distribution corresponding to the one-sided definition of p-value. Hence, $Z = 3$ corresponds to $p = 0.00135$ or to a significance of $1 - 0.00135 = 99.865\%$.

The validity of the asymptotic limit under the configuration used is tested by comparing the distribution $f(q_0|H_0)$ computed from 10^6 MC data samples (in 2 t·y exposure) to the $\chi^2/2$ distribution, for different WIMP masses, as shown in figure A.2. The two cumulative density functions (CDFs) differ for small q_0, but the discrepancy is highly reduced at $q_0 = 9$. The p-value computed at $q_0 = 9$ is evaluated for several WIMP masses with a $\sim 10\%$ uncertainty related to the number of generated toy MC datasets N_{toys} taken as $\sqrt{N}/N_{toys}$, where N is the fraction of datasets giving $q_0 > 9$. The difference with respect to $p = 0.135\%$, given by the $\chi^2/2$ distribution, is found equal to 27, 19, 22% for WIMP mass of 6, 50, 500 GeV/c^2 respectively.

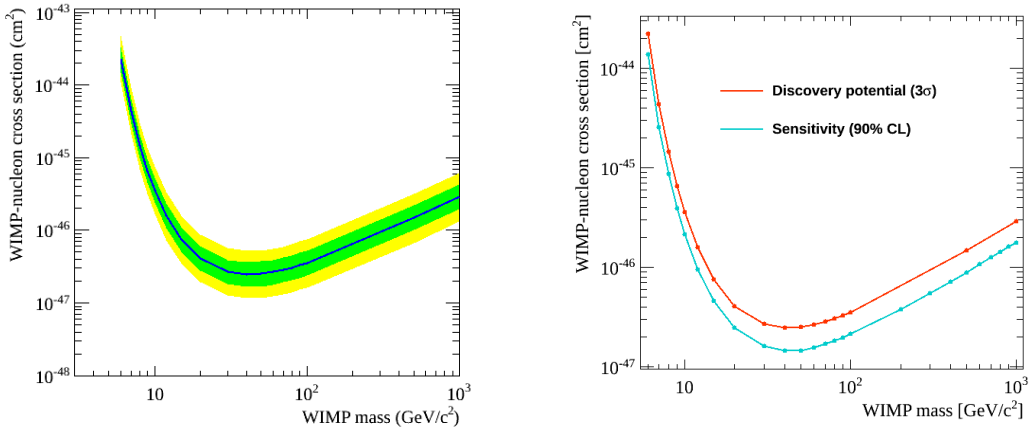

(a) **(b)**

Figure A.3: XENON1T discovery potential at 3σ significance in 2 tonne·year exposure (assuming 1 t fiducial volume) calculated with the simple likelihood approach in which systematic uncertainties are neglected. The median discovery limit (blue line) is shown together with the 1 and 2σ bands (green and yellow, respectively) which are driven by statistical fluctuations only. (b) Comparison between the median discovery limit (cyan) and the sensitivity curve (exclusion limit) at 90% confidence level (red) calculated assuming the same physical model and likelihood function for the benchmark exposure of 2 tonne·year.

Discovery limits at 3σ significance We first consider the case where no nuisance parameters are introduced in the likelihood function, meaning that the test statistic is based on a simple likelihood ratio

$$q_0 = \begin{cases} -2\ln\frac{L(\sigma=0)}{L(\hat{\sigma})} & \text{if } \hat{\sigma} \geq 0 \\ 0 & \text{if } \hat{\sigma} < 0. \end{cases} \tag{A.8}$$

The discovery significance is fixed at 3σ, corresponding to the rejection of H_0 with 99.865% confidence level. The median discovery limit obtained over the WIMP mass range from 6 to 1000 GeV/c^2 is shown in figure A.3a with the 1 and 2σ uncertainty bands. For comparison, the median discovery limit curve is drawn in figure A.3b along with the median sensitivity (exclusion upper limits) at 90% confidence level (CL) with the same likelihood ratio approach, following the method described in [297]. Across all WIMP masses, the 90% CL exclusion limit is a factor $\sim$2 better in terms of WIMP-nucleon cross section values probed, with respect to the 3σ significance discovery limit.

With the introduction of the nuisance parameters $\boldsymbol{\theta}$, the profile likelihood ratio test statistic takes the form of equation (A.5). The discovery limit curve under the complete treatment of systematic uncertainties is shown in figure A.4a, from which the enlargement of the 1 and 2σ bands is evident due to the introduction of nuisance parameters. The median discovery potentials at 3σ significance calculated with the simple likelihood ratio and with the complete profile likelihood are compared in figure A.4b. The two discovery limits coincide for signals from WIMPs of mass larger than 30 GeV/c^2. The

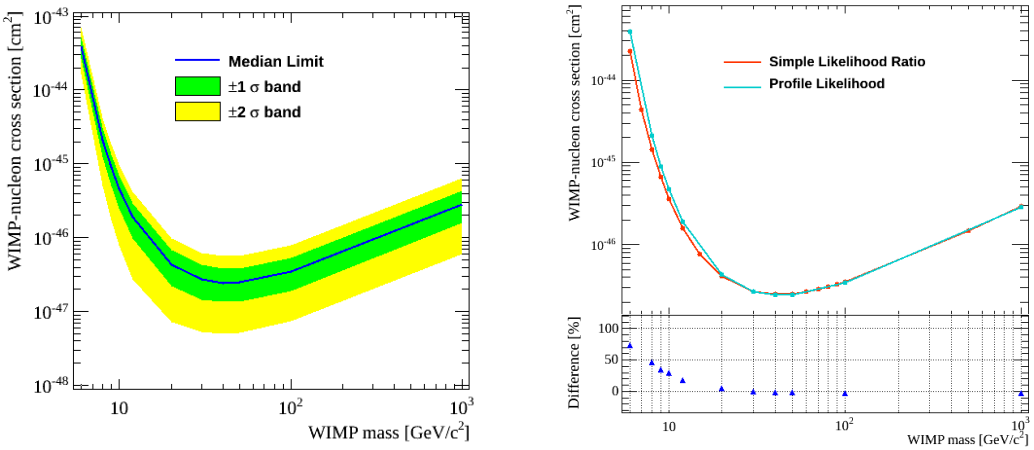

(a) (b)

Figure A.4: XENON1T discovery potential at 3σ significance in 2 tonne·year exposure (assuming 1 t fiducial volume) calculated with the profile likelihood approach in which systematic uncertainties on the NR relative scintillation efficiency $\mathcal{L}_{\text{eff}}$, the NR charge yield $\mathcal{Q}_y$ and on the predicted ER and NR background rates are introduced through nuisance parameters. The median discovery limit (blue line) is shown together with the 1 and 2σ bands (green and yellow, respectively) which are driven by the combination of statistical and systematic uncertainties, resulting larger than those shown in figure A.3a. (b) Comparison between the median discovery limit at 3σ significance in 2 tonne·year exposure calculated with the complete profile likelihood treatment (cyan) and with the simple likelihood approach (red). The introduction of nuisance parameters cause a worsening of the median discovery limit at low WIMP masses since the dominant systematic uncertainty from $\mathcal{L}_{\text{eff}}$ is significant in the low recoil energy region where the expected spectra of CNNS background and light WIMPs are confined.

uncertainty on the NR light yield at low energies, which mostly affects CNNS and light WIMPs, causes the worsening up to about 70% observed at 6 GeV/c^2 WIMP mass (see also table A.2), in addition to the widening of the 1 and 2σ bands. The minimum of the 3σ discovery potential curve of XENON1T is achieved at 2.5×10^{-47} cm^2 for 40 GeV/c^2 WIMP mass. If a larger quantile of $f(q_0|H_\mu)$ is considered, instead of the 50% corresponding to the median limit, the discovery potential is shifted to higher cross sections. At the minimum, 40 GeV/c^2 WIMP mass, the discovery potential weakens by a factor 1.7 (2.4) if the 90% (99%) quantile of the expected discovery limit band is considered as reference, as shown in table A.2.

A.2 WIMP parameter reconstruction with XENON1T

The discovery potential describes which is the smallest signal (or WIMP-nucleon cross section value) that would allow XENON1T to claim discovery with a certain significance level. In case of discovery, the interest will first move to the understanding the basic properties of the observed signal. In this section, we study what would be the XENON1T capability to reconstruct the WIMP mass and its cross section. The expected WIMP parameter reconstruction performance with XENON1T is evaluated

3σ Discovery Limit on WIMP-Nucleon SI Cross Section [cm^2]				
WIMP Mass	Simple Likelihood	Profile Likelihood		
[GeV/c^2]	50%	50%	90%	99%
6	2.2×10^{-44}	3.9×10^{-44}	5.9×10^{-44}	8.0×10^{-44}
40	2.5×10^{-47}	2.5×10^{-47}	4.2×10^{-47}	6.1×10^{-47}
1000	2.9×10^{-46}	2.9×10^{-46}	4.8×10^{-46}	7.2×10^{-46}

Table A.2: XENON1T discovery limits at 3σ significance level in 2 t·y exposure for 6, 40 and 1000 GeV/c^2 WIMP mass obtained from the profile likelihood analysis and the simple likelihood calculation (where systematic uncertainties are neglected). The profile likelihood discovery potential is reported for the median (50%), 90% and 99% upper quantiles of the discovery limits distribution shown in figure A.4a.

from simulated MC datasets, based on the physical model described in section A.1.1, and using an extension of the profile likelihood framework exploited to compute the discovery potential (see section A.1.2).

A.2.1 Confidence regions definition

In the study of discovery potential the cross section σ was the only parameter of interest for the likelihood function, with the limit calculation repeated for each tested WIMP mass. In order to infer the basic WIMP parameters from a dataset containing a significant signal, the likelihood function is set to have 2 parameters of interest: the WIMP-nucleon SI cross section σ and the WIMP mass m_χ. The signal expectation value and S1 shape feature a continuous dependence on the WIMP mass, in this case, and the bi-dimensional extension of the likelihood function (A.3) can be written as

$$\begin{aligned}
-2\ln L(m_\chi, \sigma; \boldsymbol{\theta}) = & \, 2\left[\mu_{sig}(m_\chi, \sigma; \theta_\mathcal{L}, \theta_\mathcal{Q}) + \mu_{ER}(\theta_{ER}) + \mu_{NR}(\theta_\mathcal{L}, \theta_\mathcal{Q}, \theta_{NR})\right] \\
& - 2\sum_{i=1}^{N_{obs}} \ln\Big\{ \left[\mu_{sig}(m_\chi, \sigma; \theta_\mathcal{L}, \theta_\mathcal{Q}) \cdot f_{sig}(S1_i|m_\chi) \cdot g_{NR}(Y_i)\right] \\
& \qquad + \left[\mu_{ER}(\theta_{ER}) \cdot f_{ER}(S1_i) \cdot g_{ER}(Y_i)\right] \\
& \qquad + \left[\mu_{NR}(\theta_\mathcal{L}, \theta_\mathcal{Q}, \theta_{NR}) \cdot f_{NR}(S1_i) \cdot g_{NR}(Y_i)\right] \Big\} \\
& + (\theta_\mathcal{L} - \theta^0_\mathcal{L})^2 + (\theta_\mathcal{Q} - \theta^0_\mathcal{Q})^2 + (\theta_{ER} - \theta^0_{ER})^2 + (\theta_{NR} - \theta^0_{NR})^2.
\end{aligned} \tag{A.9}$$

Both the POIs, σ and m_χ, affect the expected number of signal events μ_s as the cross section σ acts as an overall scaling factor, and because for different WIMP masses the shape and the normalization of the S1 WIMP spectrum changes.

Asimov dataset To study the parameter reconstruction performance achievable, we would need to simulate a large number of toy MC datasets (with a given injected signal) and fit them by maximizing the likelihood function in order to take into account

statistical fluctuations. However, under the asymptotic approximation, the construction of likelihood contours for a particular dataset provides the equivalent information, as suggested in [294]. Such a dataset, called Asimov dataset, is defined such that when one uses it to evaluate the MLE for all parameters, one obtains the true parameter values. Because in the XENON1T statistical model we have event-by-event spectral information (S1 and Y) and the likelihood used is unbinned, the Asimov dataset must contain a number of events (signal and backgrounds) equal to the expectation values, and distributed in S1 and Y as the known spectra as well. The expectation values can be fractional, hence the corresponding number of generated events in the Asimov dataset is taken as the closest integer. For all the n events of a specific type (signal, ER or NR background) in the data sample, the relative PDFs in both S1 and Y spaces are taken into account by dividing them into n slices so that the probability of each slice is the same (i.e. $1/n$). Hence, the extracted values of S1 (and Y) to be associated to the events namely correspond to the quantiles $[1/n\ ,\ 2/n\ ,\ \ldots\ , 1]$. If only one event from a given model component is generated, its S1 and Y are taken as the most probable values. Finally, the set of Y values sampled is shuffled randomly in order to preserve the assumed de-correlation between the S1 and Y observables.

Maximum likelihood confidence regions Simulated toy datasets, with desired true values of WIMP mass and number of signal events are generated assuming $2\,\mathrm{t}\cdot\mathrm{y}$ exposure. For a given MC dataset, the 2 parameters of interest (m_χ, σ) are estimated from their MLE, which are the values $\hat{m}_\chi$ and $\hat{\sigma}$ that maximize the likelihood function (A.9). Bi-dimensional confidence regions in the (m_χ, σ) space are computed via likelihood scan. In the large sample approximation, the region that covers the true value at $1-\gamma$ confidence level, is constructed by finding the values of POIs (m_χ, σ) at which the log-likelihood function decreases by $\Omega_\gamma/2$ [307]:

$$\ln L(m_\chi, \sigma) \;=\; \ln L_{max} - \Omega_\gamma/2, \tag{A.10}$$

where $L_{max} = L(\hat{m}_\chi, \hat{\sigma})$. For two fitted parameters of interest, the correspondence between Ω_γ and the confidence level is:

$1-\gamma$	Ω_γ
68.3%	2.30
90%	4.61
95%	5.99
99%	9.21

(A.11)

A.2.2 Expected reconstruction performances

Similarly to the study of the discovery potential, we consider the simple case where no nuisance parameters $\boldsymbol{\theta}$ are introduced in the likelihood function (A.9). Figure A.5 shows the confidence regions obtained for three different sets of true values (m_χ^*, σ^*) from the likelihood fit of toy MC pseudo-experiments. The true cross section values are chosen

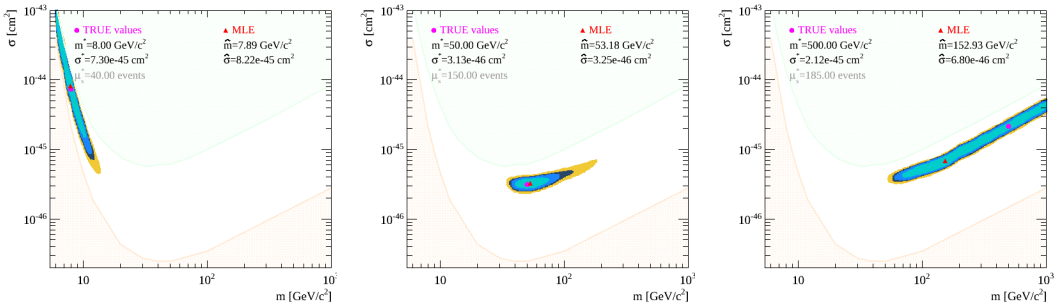

Figure A.5: Confidence regions in the WIMP mass-cross section parameter space calculated with bi-dimensional likelihood scan, neglecting systematic uncertainties in the likelihood function (A.9), on simulated toy MC datasets assuming 2 t·y exposure for three sets of true values, marked with a magenta dot: (a) 8 GeV/c^2 and 7.3×10^{-45} cm^2; (b) 50 GeV/c^2 and 3.1×10^{-46} cm^2; (c) 500 GeV/c^2 and 2.1×10^{-45} cm^2. The contours with 1σ (68.3%), 90%, 95% and 99% confidence level are shown in cyan, blue, navy and yellow areas, respectively. The maximum likelihood estimators ($\hat{m}_\chi$,$\hat{\sigma}$) of WIMP mass and cross section are marked with a red triangle. True cross section values are chosen to be between the LUX exclusion limit [308] (drawn as green line and high transparency shaded area above) and the XENON1T discovery limit (orange line and high transparency shaded area beneath), calculated in section A.1.3.

within the region between the LUX exclusion limit [308] and the median XENON1T discovery potential curve with 3σ significance computed in section A.1.3. The capability to set a confidence interval on the WIMP mass becomes weaker for increasing masses. Above $m_\chi \sim 100$ GeV/c^2, WIMP spectroscopy is not feasible due to the degeneracy of WIMP spectra in the region of interest.

When the nuisance parameters are considered in the likelihood function, the MLE $\hat{m}_\chi$ and $\hat{\sigma}$ are computed from the unconditional maximum likelihood

$$L_{max}(m_\chi, \sigma, \boldsymbol{\theta}) = L(\hat{m}_\chi, \hat{\sigma}, \hat{\boldsymbol{\theta}}), \tag{A.12}$$

where m_χ, σ and $\boldsymbol{\theta}$ are all free parameters in the maximization of the likelihood over a given dataset. The bi-dimensional confidence regions, in the presence of nuisance parameters, are based on the value of the conditional likelihood function. The nuisance parameters are profiled out for each point in the (m_χ, σ) space by calculating the conditional maximum likelihood $L(m_\chi, \sigma, \hat{\hat{\boldsymbol{\theta}}})$, where $\hat{\hat{\boldsymbol{\theta}}}$ is the conditional MLE for fixed values of m_χ and σ. The confidence regions are then computed by evaluating the variation of $L(m, \sigma, \hat{\hat{\boldsymbol{\theta}}})$ in the POI space with respect to the unconditional maximum likelihood (A.12).

Profile likelihood contours for different WIMP signals calculated over the related Asimov datasets are shown in figure A.6, aside the likelihood contours obtained by a simple likelihood analysis on the same datasets. As expected, the impact of the systematic uncertainties is more significant at low WIMP masses, while above ~ 30 GeV/c^2 becomes negligible. The profile likelihood confidence regions are enlarged in particular

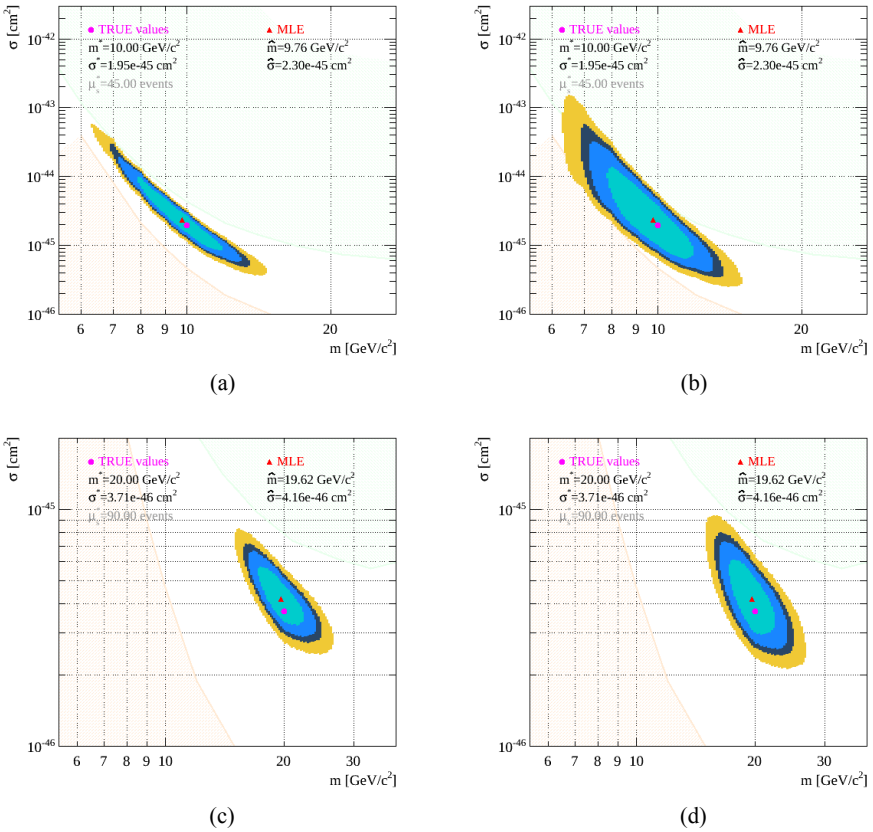

Figure A.6: Confidence regions in the WIMP mass-cross section parameter space calculated with bi-dimensional profile likelihood scan, that takes into account systematic uncertainties, (right panels) compared to the contours obtained with a simple likelihood analysis (left panels) on the same simulated Asimov datasets. Assumed true values are WIMP mass of 10 (a-b) and 20 $\mathrm{GeV/c^2}$ (c-d) with cross section of 2.0×10^{-45} and 3.7×10^{-46} $\mathrm{cm^2}$, respectively. The exposure is fixed at 2 t·y. The color code of contours at different confidence level is the same as in figure A.5.

in the cross section projection, while the constraint on the WIMP mass is only slightly reduced, even at the lowest masses. This behaviour is a consequence of the fact that the considered systematics only affect the normalization of the S1 spectrum and not its shape.

A.3 Discovery potential evolution with exposure

Great efforts and huge improvements have been achieved in the direct WIMP search throughout the last decade. Several experiments have been reducing the allowed parameter space by setting exclusion limits on the WIMP-nucleon SI cross section. At the current stage of the WIMP search history, there are about three orders of magnitude still to be probed before hitting the "neutrino floor" [138], as shown in figure 1.10.

The irreducible CNNS background for non-directional detectors will limit the discovery potential of noble-liquid direct detection experiments in the ultimate scenario of very large target mass and maximal background reduction.

In this section we focus on the WIMP discovery potential evolution as a function of the increasing exposure of Xe-based direct detection experiments. We consider the ultimate background scenario where only the irreducible NR background due to neutrinos (CNNS), assuming that external backgrounds from radioactive contaminants in detector materials and intrinsic xenon contaminations can be dropped thanks to larger Xe mass shielding the internal fiducial volume and improved xenon purification. The physical model used (see section A.3.1) relies on the expected recoil energy spectra of signal and background, following a phenomenological approach proposed in [138]. Two WIMP mass regimes are tested, computing the discovery limits (with the profile likelihood method described in A.1.3) for 6 and 100 $\mathrm{GeV/c^2}$ WIMP mass at different exposures (see section A.3.2).

A.3.1 Physical model and likelihood function

The background model consists in the recoil energy spectrum induced by CNNS interactions due to astrophysical neutrinos (solar, atmospheric and from Supernovae). The WIMP signal model assumes a standard DM halo, as done in section A.1.1 and detailed in section 4.4.3. The analysis space is mono-dimensional in the recoil energy of NR interactions of signal and background in a LXe target (therefore the smearing of S1 and S2 observable signals is not taken into account in this case). The parameter of interest is again the WIMP-nucleon SI cross section σ. We consider one nuisance parameter θ related to the systematic uncertainty on the neutrinos fluxes, which affects the expected number of background events μ_b. A Gaussian constraint on the nuisance parameter is imposed, so that $\theta = 1$ corresponds to 1σ deviation from the central value of μ_b:

$$\mu_b = \mu_b^0 \cdot (1 + \xi \cdot \theta), \tag{A.13}$$

where μ_b^0 is the nominal number of expected CNNS events and ξ is the assumed relative systematic uncertainty. The log-likelihood function for this study can be expressed as

$$\begin{aligned} -2 \ln L(\sigma;\theta) = & \, 2\left[\mu_{sig}(\sigma) + \mu_b(\theta)\right] \\ & - 2 \sum_{i=1}^{N_{obs}} \ln\left[\mu_{sig}(\sigma) \cdot f_{sig}(E_i) + \mu_b(\theta) \cdot f_b(E_i)\right] \\ & + (\theta - \theta^0)^2, \end{aligned} \tag{A.14}$$

where E is the recoil energy and $f(E)$ is the PDF given by the spectrum of WIMP signal or CNNS background.

The calculation of discovery potential is carried out exploiting the profile likelihood ratio test statistic, defined in equation (A.5), to estimate 3σ significance discovery limits at the 90% quantile of the expected distribution.

A.3.2 Discovery potential projections

In this section, we report on the calculated evolution of the discovery potential as a function of the total exposure for a fixed WIMP signal model, hence a fixed WIMP mass. The sensitivity (and the discovery potential as well) of XENON1T and other xenon-based DM detectors is highly reduced for light WIMPs with mass of few GeV/c^2. For this reason, two cases of 6 and 100 GeV/c^2 mass are considered, assuming an idealized low energy threshold (100 eV) for 6 GeV/c^2 mass and higher threshold (4 keV) for 100 GeV/c^2 WIMP, following the approach used in [138].

The discovery limit calculation is repeated over a wide range of exposures by simulating $\mathcal{O}(10^5)$ toy MC datasets to estimate the expected PDF of the test statistic under both the signal and null hypotheses. This is referred to as "frequentist" calculation.

In the large sample limit, where datasets have a large number of events, as in the case of large exposures, the distributions of the test statistic q_0 under any given hypothesis can be predicted analytically, as discussed in previous sections. Given the simple relationships holding between the discovery significance Z_0 and the test statistic q_0, in equation (A.7), it is sufficient to compute the value of q_0 under the Asimov dataset ($q_{0,A}$) to estimate the significance of the rejection of a given background-only hypothesis H_0. Since we want to use the 90% quantile of the $f(q_0|H_\sigma)$ distribution, corresponding to $N = -1.28\sigma$ deviation from the median, to estimate the discovery limit, the significance can be calculated as [294]:

$$Z_0(N) = \sqrt{q_{0,A}} + N. \tag{A.15}$$

The discovery limit at $Z_0 = 3$ significance and at the 90% quantile of the signal hypothesis, is therefore equal to the cross section σ, for which the $q_{0,A}$ value, corresponding to that specific H_σ hypothesis, satisfies the condition

$$q_{0,A} = (Z - N)^2 = (3 + 1.28)^2 = 18.33\ . \tag{A.16}$$

The discovery potential, under the asymptotic limit assumption, can be calculated by generating only the Asimov dataset for each signal hypothesis H_σ (described in section A.2.1), computing the test statistic $q_{0,A}$ on it and finding the cross section σ for which $q_{0,A} = 18.33$.

Low mass and low threshold We study the discovery potential to a 6 GeV/c^2 WIMP signal within a region of interest defined in the interval (0.1, 100) keV of the recoil energy space. In this configuration, the dominant component of CNNS background comes from ^{8}B solar neutrinos. The uncertainty on ^{8}B and *hep* neutrinos flux is 14% [243]. Therefore, we assume a systematic uncertainty on the background expectation value of $\xi = 14\%$. The signal and background PDFs are shown in figure A.7a

The evolution of discovery potential to 6 GeV/c^2 WIMPs obtained with the "frequentist" calculation (cyan) is shown in figure A.7b, where it is compared to the analogous calculation in [138] (black). There is good agreement except at the highest exposures,

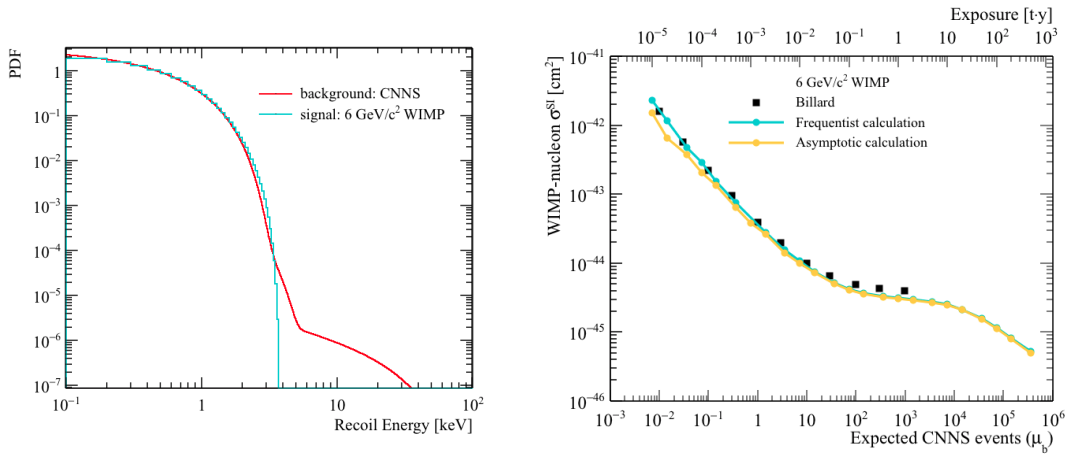

(a) **(b)**

Figure A.7: (a) Normalized recoil energy spectrum of $6\,\mathrm{GeV/c^2}$ WIMP signal (cyan) and CNNS background (red), mostly due to ^{8}B solar neutrinos, in the (0.1, 100) keV energy window. The spectral shapes are almost indistinguishable below $\sim 3\,\mathrm{keV}$, above which the *hep* neutrinos component changes the CNNS spectrum. (b) Evolution of discovery limits at 3σ significance level and 90% quantile of the expected distribution as a function of exposure (upper x-axis) for $6\,\mathrm{GeV/c^2}$ WIMP. The asymptotic (yellow) and frequentist (cyan) calculations of discovery potential are compared to results in [138] (black). The lower x-axis shows the expected number of CNNS events corresponding to the exposures in the upper x-axis.

where the calculated discovery limit eventually keeps improving at exposure $\gtrsim 10\,\mathrm{t\cdot y}$ (such a trend is discussed at the end of this section). The result from the asymptotic calculation is overlaid (yellow), showing that the asymptotic approximation is not valid at very low exposures, when $\mu_b \lesssim 10$ events.

High mass and high threshold The discovery potential for $100\,\mathrm{GeV/c^2}$ WIMPs with an energy threshold of 4 keV, calculated in the asymptotic approximation is shown in figure A.8b. The CNNS background components playing a role above the 4 keV threshold are *hep* solar neutrinos, atmospheric (*atm*) and neutrinos from diffuse Supernovae (*dsnb*). Three nuisance parameters are introduced in the likelihood function in order to take into account the different systematic uncertainty in the flux of neutrinos from different sources: $\xi_{hep} = 14\%$, $\xi_{atm} = 20\%$ and $\xi_{dsnb} = 50\%$. The summed spectral shape, shown in figure A.8a (red), is taken as the background PDF. Similar trend is observed with respect to the low WIMP mass case, with good agreement with results in [138] and improvement of discovery limits at very large exposures.

Impact of systematics and spectral shape The impact of systematic uncertainties on the background prediction is studied evaluating the evolution of discovery potential assuming different systematics on the CNNS expectation value for $6\,\mathrm{GeV/c^2}$ WIMP (see figure A.9a). The uncertainty $\mu_b \cdot \xi$ affects the improvement of the discovery limit

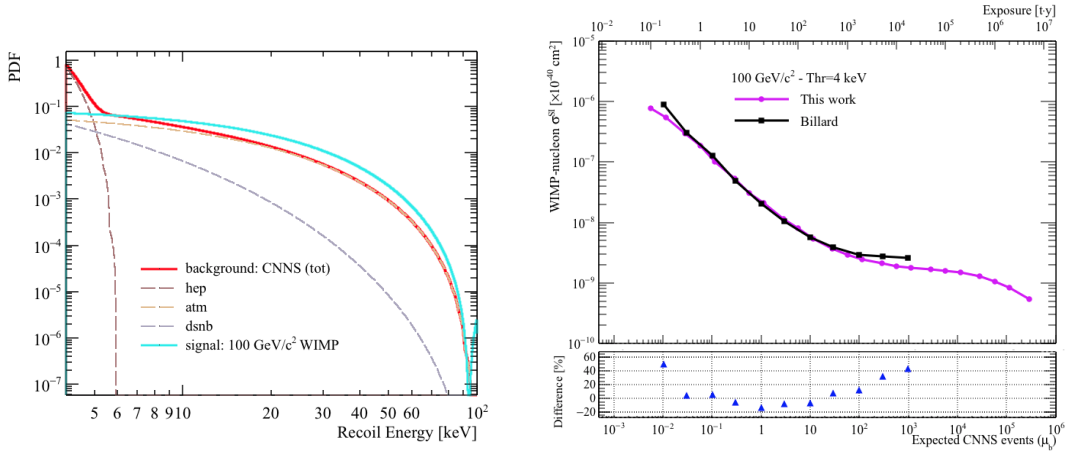

(a) **(b)**

Figure A.8: (a) Normalized recoil energy spectrum of 100 GeV/c^2 WIMP signal (cyan) and CNNS background (red), with isolated contributions from *hep* solar neutrinos, atmospheric neutrinos (*atm*) and from diffuse Supernovae (*dsnb*) in dashed lines, in the (4, 100) keV energy window. (b) Evolution of discovery limits at 3σ significance level and 90% quantile of the expected distribution as a function of exposure for 100 GeV/c^2 WIMP. The asymptotic calculation of discovery potential (magenta) is compared to results in [138] (black).

when it becomes comparable with the statistical uncertainty $1/\sqrt{\mu_b}$ on the predicted number of background events. At large exposures, where the systematics $\mu_b\xi$ becomes dominant over $1/\sqrt{\mu_b}$, the limit shows a constant trend as the required number of signal events over the background to claim discovery is proportional to μ_b. Depending on the amplitude of the normalization uncertainty, the plateau for the achievable discovery limit appear at higher cross section and therefore at smaller exposures.

However, after the plateau (between approximately 10 and 10^4 expected CNNS events in figure A.7b), discovery limits show improvement. Such behaviour can be attributed to the slight difference between the signal and background spectral shape (see figure A.7a). In fact, if the exposure is sufficiently large, and equivalently μ_b, the high energy tail of the background spectrum can effectively contribute to the observed population of background events. For such events the signal and background probability significantly differ. Hence, fluctuations in the background normalization (governed by ξ) can no longer account for the presence of signal events. The discrimination power between signal and background begins to play a role only at very large exposures.

To test this hypothesis, we compare the results of figure A.7b with the discovery limits obtained neglecting the spectral shape information in the profile likelihood. We consider a simple counting analysis, where the likelihood function is given by the probability to observe N events when $\mu_b + \mu_s$ are expected multiplied by the Gaussian constraint on the nuisance parameter:

$$L(\mu_{sig};\theta) = \text{Pois}(N|\mu_{sig} + \mu_b(\theta)) \cdot \text{Gaus}(\theta;0,1). \tag{A.17}$$

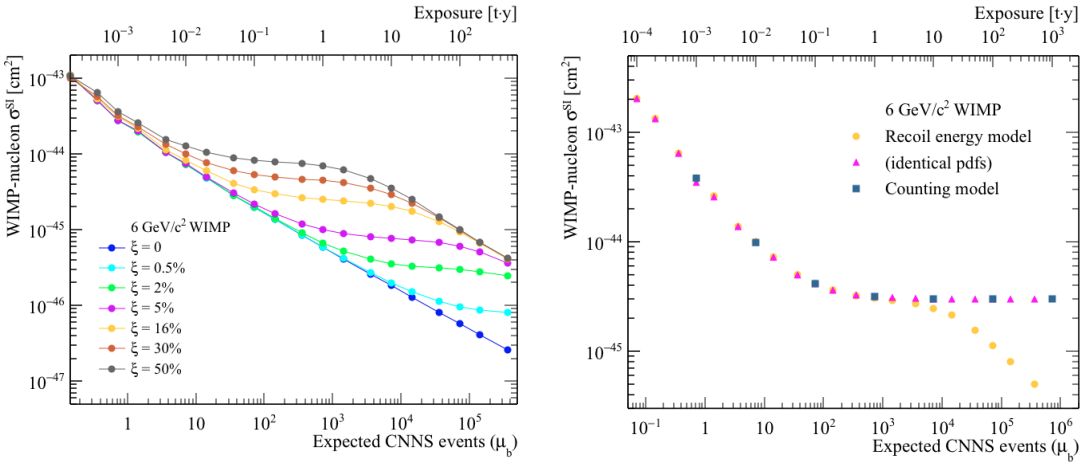

Figure A.9: (a) Evolution of discovery limits at 3σ significance level and 90% quantile for $6\,\mathrm{GeV/c^2}$ WIMP, from asymptotic calculation, for different assumptions about the systematic uncertainty in the predicted CNNS background rate. Relative uncertainties on the CNNS expectation value, from 0 to 50%, are considered and shown with different colors. (b) Discovery potential improvement, for $6\,\mathrm{GeV/c^2}$ WIMP, as a function of exposure. Yellow dots corresponds to the calculation made in figure A.7b, while pink triangles represent the discovery limit obtained by assuming an identical PDF for signal and background in the profile likelihood analysis. The calculation carried out with a counting experiment model, where the spectral information is completely dropped, is shown as blue squares. This result demonstrates that the further improvement in discovery potential, after the plateau due to systematics in the CNNS prediction, is attributable to tiny differences in the spectral shape of WIMP signal and CNNS background.

In principle, such configuration is equivalent to consider the complete likelihood model, defined in equation (A.14), in which the signal and background spectra have identical shape. If the PDFs of signal and background are indistinguishable, the discovery limit on the WIMP cross section scales as [138]

$$\sigma_{Disc} \propto \frac{\sqrt{\mu_b + (\xi\mu_b)^2}}{\mu_b} = \sqrt{\frac{1+\xi^2\mu_b}{\mu_b}}. \tag{A.18}$$

When systematics dominate over statistical uncertainty, i.e. $\xi^2\mu_b \gg 1$, the discovery limit flattens becoming constant with increasing exposure, as $\sigma_{Disc} \propto \xi$ and no further improvement is possible.

Figure A.9b compares the evolution of discovery limits obtained with the simple counting model (blue) and artificially assigning the $6\,\mathrm{GeV/c^2}$ WIMP PDF to the background model (pink) to the result of figure A.8b with the complete profile likelihood treatment. If spectral shapes are not taken into account, a plateau is encountered as predicted by equation (A.18). The systematic uncertainty on the background normalization becomes irrelevant when the exposure is so large that a sensible number background events is expected in the sub-dominant region of the recoil energy spectrum

that differs from the WIMP signal. It should be noted that in this study no uncertainty on the spectral shapes is taken into account. Even tiny shape uncertainties on both WIMP signal and CNNS background could therefore play a role in the ultimate DM search at large exposures when the CNNS expectation value approaches $\sim 10^4$ events.

Bibliography

[1] N. Aghanim et al. Planck 2018 results. VI. Cosmological parameters. *e-Print: arXiv:1807.06209 [astro-ph.CO]*, 2018. (p.7), (p.10), (p.15)

[2] G. Bertone and D. Hooper. A History of Dark Matter. *Submitted to: Rev. Mod. Phys.*, 2016. (p.7)

[3] A. Boveia and C. Doglioni. Dark matter searches at colliders. *Annual Review of Nuclear and Particle Science*, 68(1):429–459, 2018. (p.8)

[4] E. E. Barnard and A. C. Ranyard. Structure of the Milky Way. *Knowledge: An Illustrated Magazine of Science*, 17:253, 1894. (p.8)

[5] W. T. Kelvin. *Baltimore lectures on molecular dynamics and the wave theory of light*. CJ Clay and Sons, 1904. (p.8)

[6] H. Poincare. The Milky Way and the Theory of Gases. *Popular Astronomy*, 14:475–488, 1906. (p.8)

[7] J. C. Kapteyn. First attempt at a theory of the arrangement and motion of the sidereal system. *The Astrophysical Journal*, 55:302, 1922. (p.8)

[8] F. Zwicky. Die rotverschiebung von extragalaktischen nebeln. *Helvetica Physica Acta*, 6:110–127, 1933. (p.8)

[9] E. Hubble and M. L. Humason. The velocity-distance relation among extra-galactic nebulae. *The Astrophysical Journal*, 74:43, 1931. (p.9)

[10] G. R. Burbidge and E. M. Burbidge. The Hercules Clusters of Nebulae. *The Astrophysical Journal*, 130:629, 1959. (p.10)

[11] S. Smith. The mass of the Virgo cluster. *The Astrophysical Journal*, 83:23, 1936. (p.10)

[12] F. Zwicky. On the masses of nebulae and of clusters of nebulae. *The Astrophysical Journal*, 86:217, 1937. (p.10)

[13] S. D. M. White et al. The baryon content of galaxy clusters: a challenge to cosmological orthodoxy. *Nature*, 366(6454):429, 1993. (p.10)

[14] M. F. Struble and H. J. Rood. A compilation of redshifts and velocity dispersions for ACO clusters. *The Astrophysical Journal Supplement Series*, 125(1):35, 1999. (p.10)

[15] F. C. Brandt. A spectroscopic study of the motions in Messier 33. *Monthly Notices of the Royal Astronomical Society*, 129:309, 1965. (p.11)

[16] A. V. Zasov et al. Dark matter in galaxies. *Physics-Uspekhi*, 60(1):3, 2017. (p.11)

[17] K. C. Freeman. On the disks of spiral and S0 galaxies. *The Astrophysical Journal*, 160:811, 1970. (p.11)

[18] J. F. Navarro et al. The structure of cold dark matter halos. *The Astrophysical Journal*, 462:563, 1996. (p.11)

[19] N. Okabe et al. LoCuSS: the mass density profile of massive galaxy clusters at z=0.2. *The Astrophysical Journal Letters*, 769(2):L35, 2013. (p.12)

[20] R. Massey et al. The dark matter of gravitational lensing. *Reports on Progress in Physics*, 73(8):086901, 2010. (p.12)

[21] C. Davidson. A determination of the deflection of light by the sun's gravitational field, from observations made at the total eclipse of May 29, 1919. *Phil. Trans. R. Soc. Lond. A*, 220(571-581):291–333, 1920. (p.12)

[22] R. Gavazzi et al. The sloan lens ACS survey. IV. The mass density profile of early-type galaxies out to 100 effective radii. *The Astrophysical Journal*, 667(1):176, 2007. (p.12), (p.13)

[23] Y. Mellier. Probing the universe with weak lensing. *Annual Review of Astronomy and Astrophysics*, 37(1):127–189, 1999. (p.13)

[24] R. Mandelbaum et al. Galaxy halo masses and satellite fractions from galaxy–galaxy lensing in the Sloan Digital Sky Survey: stellar mass, luminosity, morphology and environment dependencies. *Monthly Notices of the Royal Astronomical Society*, 368(2):715–731, 2006. (p.13)

[25] D. M. Goldberg and D. J. Bacon. Galaxy-galaxy flexion: Weak lensing to second order. *The Astrophysical Journal*, 619(2):741, 2005. (p.13)

[26] D. Clowe et al. Weak lensing mass reconstruction of the interacting cluster 1E0657-558: Direct evidence for the existence of dark matter. *The Astrophysical Journal*, 604(2):596, 2004. (p.13), (p.14)

[27] A. Einstein. Explanation of the perihelion motion of mercury from the general theory of relativity. *Sitzungsber. Preuss. Akad. Wiss. Berlin (Math. Phys.)*, 1915:831–839, 1915. (p.14)

[28] S. Foreman and D. Scott. What do gas-rich galaxies actually tell us about modified newtonian dynamics? *Physical review letters*, 108(14):141302, 2012. (p.14)

[29] J. G. De Swart et al. How dark matter came to matter. *Nature Astronomy*, 1(3):0059, 2017. (p.15)

[30] A. A. Penzias and R. W. Wilson. A measurement of excess antenna temperature at 4080 Mc/s. *The Astrophysical Journal*, 142:419–421, 1965. (p.15)

[31] R. H. Dicke et al. Cosmic Black-Body Radiation. *The Astrophysical Journal*, 142:414–419, 1965. (p.15)

[32] D. J. Fixsen. The temperature of the cosmic microwave background. *The Astrophysical Journal*, 707(2):916, 2009. (p.15)

[33] J. A. Frieman et al. Dark Energy and the Accelerating Universe. *Annual Review of Astronomy and Astrophysics*, 46(1):385–432, 2008. (p.15)

[34] E. W. Kolb and M. S. Turner. The early universe. *Front. Phys.*, 69:1–547, 1990. (p.16)

[35] M. Milgrom. A modification of the newtonian dynamics as a possible alternative to the hidden mass hypothesis. *The Astrophysical Journal*, 270:365, 1983. (p.16)

[36] M. Milgrom. A Modification of the Newtonian Dynamics - Implications for Galaxy Systems. *The Astrophysical Journal*, 270:371, 1983. (p.16)

[37] J. Bekenstein and M. Milgrom. Does the missing mass problem signal the breakdown of Newtonian gravity? *The Astrophysical Journal*, 286:7–14, 1984. (p.16)

[38] J. D. Bekenstein. Relativistic gravitation theory for the modified Newtonian dynamics paradigm. *Physical Review D*, 70(8):083509, 2004. (p.17)

[39] S. Capozziello and M. De Laurentis. Extended theories of gravity. *Physics Reports*, 509(4-5):167–321, 2011. (p.17)

[40] E. Verlinde. On the Origin of Gravity and the Laws of Newton. *Journal of High Energy Physics*, 2011(4):29, 2011. (p.17)

[41] M. M. Brouwer et al. First test of Verlinde's theory of emergent gravity using weak gravitational lensing measurements. *Monthly Notices of the Royal Astronomical Society*, 466(3):2547–2559, 2017. (p.17)

[42] B. P. Abbott et al. GW170817: observation of gravitational waves from a binary neutron star inspiral. *Physical Review Letters*, 119(16):161101, 2017. (p.17)

[43] B. P. Abbott et al. Observation of gravitational waves from a binary black hole merger. *Physical review letters*, 116(6):061102, 2016. (p.17)

[44] A. Goldstein et al. An ordinary short gamma-ray burst with extraordinary implications: Fermi-GBM detection of GRB 170817a. *The Astrophysical Journal Letters*, 848(2):L14, 2017. (p.17)

[45] B. P. Abbott et al. Gravitational waves and gamma-rays from a binary neutron star merger: GW170817 and GRB 170817A. *The Astrophysical Journal Letters*, 848(2):L13, 2017. (p.17)

[46] J. Sakstein. Disformal theories of gravity: from the solar system to cosmology. *Journal of Cosmology and Astroparticle Physics*, 2014(12):012, 2014. (p.18)

[47] J. Sakstein and B. Jain. Implications of the neutron star merger GW170817 for cosmological scalar-tensor theories. *Physical review letters*, 119(25):251303, 2017. (p.18)

[48] T. Baker et al. Strong constraints on cosmological gravity from GW170817 and GRB 170817A. *Physical review letters*, 119(25):251301, 2017. (p.18)

[49] P. Creminelli and F. Vernizzi. Dark Energy after GW170817 and GRB170817A. *Physical review letters*, 119(25):251302, 2017. (p.18)

[50] S. Boran et al. GW170817 falsifies dark matter emulators. *Physical Review D*, 97(4):041501, 2018. (p.18)

[51] Y. B. Zeldovich. The theory of the large scale structure of the universe. In *Symposium-International Astronomical Union*, volume 79, pages 409–421. Cambridge University Press, 1978. (p.18)

[52] J. P. Ostriker and P. J. Peebles. A numerical study of the stability of flattened galaxies: or, can cold galaxies survive? *The Astrophysical Journal*, 186:467–480, 1973. (p.19)

[53] V. Springel et al. Simulations of the formation, evolution and clustering of galaxies and quasars. *Nature*, 435(7042):629, 2005. (p.19)

[54] M. Boylan-Kolchin et al. Resolving cosmic structure formation with the Millennium-II Simulation. *Monthly Notices of the Royal Astronomical Society*, 398(3):1150–1164, 2009. (p.19), (p.20)

[55] C. J. Hogan. Warm Dark Matter. In *Current Topics in Astrofundamental Physics: The Cosmic Microwave Background*, pages 345–353. Springer, 2001. (p.19)

[56] C. Alcock et al. The MACHO project: microlensing results from 5.7 years of large magellanic cloud observations. *The Astrophysical Journal*, 542(1):281, 2000. (p.21)

[57] P. Tisserand et al. Limits on the Macho Content of the Galactic Halo from the EROS-2 Survey of the Magellanic Clouds. *Astronomy & Astrophysics*, 469(2):387–404, 2007. (p.21)

[58] A. S. Szalay and G. Marx. Neutrino rest mass from cosmology. *Astronomy and Astrophysics*, 49:437–441, 1976. (p.21)

[59] Y. Akrami et al. Planck 2018 results. I. Overview and the cosmological legacy of Planck. *e-Print: arXiv:1807.06205*, 2018. (p.21)

[60] P. J. E. Peebles. The origin of galaxies and clusters of galaxies. *Science*, 224(4656):1385–1391, 1984. (p.21)

[61] P. Madau et al. High-redshift galaxies in the Hubble Deep Field: colour selection and star formation history to z $\sim$ 4. *Monthly Notices of the Royal Astronomical Society*, 283(4):1388–1404, 1996. (p.21)

[62] J. R. Bond and A. S. Szalay. The collisionless damping of density fluctuations in an expanding universe. *The Astrophysical Journal*, 274:443–468, 1983. (p.21)

[63] R. D Peccei and H. R. Quinn. CP conservation in the presence of pseudoparticles. *Physical Review Letters*, 38(25):1440, 1977. (p.22)

[64] V. B. Klaer and G. D. Moore. The dark-matter axion mass. *Journal of Cosmology and Astroparticle Physics*, 2017(11):049, 2017. (p.22)

[65] R. J. Creswick et al. Theory for the direct detection of solar axions by coherent Primakoff conversion in germanium detectors. *Physics Letters B*, 427(3-4):235–240, 1998. (p.22)

[66] V. Anastassopoulos et al. New CAST limit on the axion–photon interaction. *Nature Physics*, 13(6):584, 2017. (p.22)

[67] A. Derevianko et al. Axio–electric effect. *Physical Review D*, 82(6):065006, 2010. (p.22)

[68] E. Aprile et al. First axion results from the XENON100 experiment. *Physical Review D*, 90(6):062009, 2014. (p.22)

[69] N. Du et al. Search for Invisible Axion Dark Matter with the Axion Dark Matter Experiment. *Physical review letters*, 120(15):151301, 2018. (p.22)

[70] S. Dodelson and L. M. Widrow. Sterile neutrinos as dark matter. *Physical Review Letters*, 72(1):17, 1994. (p.22)

[71] N. Yoshida et al. Early structure formation and reionization in a warm dark matter cosmology. *The Astrophysical Journal Letters*, 591(1):L1, 2003. (p.22)

[72] A. Kusenko. Sterile neutrinos: the dark side of the light fermions. *Physics Reports*, 481(1-2):1–28, 2009. (p.22)

[73] E. Bulbul et al. Detection of an unidentified emission line in the stacked X-ray spectrum of galaxy clusters. *The Astrophysical Journal*, 789(1):13, 2014. (p.22)

[74] O. Ruchayskiy et al. Searching for decaying dark matter in deep XMM–Newton observation of the Draco dwarf spheroidal. *Monthly Notices of the Royal Astronomical Society*, 460(2):1390–1398, 2016. (p.22)

[75] O. Urban et al. A Suzaku search for dark matter emission lines in the X-ray brightest galaxy clusters. *Monthly Notices of the Royal Astronomical Society*, 451(3):2447–2461, 2015. (p.22)

[76] F. A. Aharonian et al. Hitomi constraints on the 3.5 keV line in the Perseus galaxy cluster. *The Astrophysical Journal Letters*, 837(1):L15, 2017. (p.22)

[77] S. Dimopoulos and H. Georgi. Solution of the gauge hierarchy problem. *Physics Letters B*, 117(5):287–290, 1982. (p.22)

[78] W. De Boer. Grand unified theories and supersymmetry in particle physics and cosmology. *Progress in Particle and Nuclear Physics*, 33:201–301, 1994. (p.22)

[79] I. Aitchison. *Supersymmetry in particle physics: an elementary introduction*. Cambridge University Press, 2007. (p.22)

[80] T. Falk et al. Heavy sneutrinos as dark matter. *e-Print: arXiv hep-ph/9409270*, 1994. (p.23)

[81] J. L. Feng et al. Superweakly interacting massive particles. *Physical review letters*, 91(1):011302, 2003. (p.23)

[82] S. A. Bonometto et al. Mixed dark matter from axino distribution. *Physical Review D*, 49(8):3918, 1994. (p.23)

[83] L. Covi et al. Axinos as dark matter. *Journal of High Energy Physics*, 2001(05):033, 2001. (p.23)

[84] D. J. H. Chung et al. Superheavy dark matter. *Physical Review D*, 59(2):023501, 1998. (p.23)

[85] V. Berezinsky et al. Ultrahigh energy cosmic rays without Greisen-Zatsepin-Kuzmin cutoff. *Physical Review Letters*, 79(22):4302, 1997. (p.23)

[86] H. Cheng et al. Kaluza-Klein dark matter. *Physical Review Letters*, 89(21):211301, 2002. (p.23)

[87] T. Kaluza. Zum unitätsproblem der physik. *Sitzungsberichte der Königlich Preußischen Akademie der Wissenschaften (Berlin)*, pages 966–972, 1921. (p.23)

[88] R. N. Mohapatra et al. Mirror matter as self-interacting dark matter. *Physical Review D*, 66(6):063002, 2002. (p.23)

[89] C. Boehm and P. Fayet. Scalar dark matter candidates. *Nuclear Physics B*, 683(1-2):219–263, 2004. (p.23)

[90] N. Arkani-Hamed et al. The littlest higgs. *Journal of High Energy Physics*, 2002(07):034, 2002. (p.23)

[91] A. De Rújula et al. Charged dark matter. *Nuclear Physics B*, 333(1):173–194, 1990. (p.23)

[92] D. N. Spergel and P. J. Steinhardt. Observational evidence for self-interacting cold dark matter. *Physical Review Letters*, 84(17):3760, 2000. (p.23)

[93] B. Audren et al. Strongest model-independent bound on the lifetime of Dark Matter. *Journal of Cosmology and Astroparticle Physics*, 2014(12):028, 2014. (p.24)

[94] L. Roszkowski et al. WIMP dark matter candidates and searchescurrent status and future prospects. *Reports on Progress in Physics*, 2018. (p.24)

[95] T. Nihei et al. Towards an accurate calculation of the neutralino relic density. *Journal of High Energy Physics*, page 063, 2001. (p.25)

[96] G. Jungman et al. Supersymmetric dark matter. *Physics Reports*, 267(5):195–373, 1996. (p.26)

[97] P. Gondolo. Phenomenological introduction to direct dark matter detection. *e-Print: arXiv hep-ph/9605290*, 1996. (p.26)

[98] M. W. Goodman and E. Witten. Detectability of certain dark-matter candidates. *Physical Review D*, 31(12):3059, 1985. (p.27)

[99] A. Drukier and L. Stodolsky. Principles and applications of a neutral-current detector for neutrino physics and astronomy. *Phys. Rev. D*, 30:2295–2309, 1984. (p.27)

[100] A. K. Drukier et al. Detecting cold dark-matter candidates. *Phys. Rev. D*, 33:3495–3508, 1986. (p.28)

[101] D. N. Spergel. Motion of the Earth and the detection of weakly interacting massive particles. *Phys. Rev. D*, 37:1353–1355, 1988. (p.28)

[102] R. Bernabei et al. The DAMA/LIBRA apparatus. *Nucl. Instrum. Meth.*, A592:297–315, 2008. (p.29)

[103] R. Bernabei et al. The annual modulation signature for dark matter: DAMA/LIBRA-phase1 results and perspectives. *Advances in High Energy Physics*, 2014, 2014. (p.29)

[104] R. Bernabei et al. First model independent results from DAMA/LIBRA-phase2. *e-Print: arXiv:1805.10486*, 2018. (p.29)

[105] E. Aprile et al. XENON100 dark matter results from a combination of 477 live days. *Physical Review D*, 94(12):122001, 2016. (p.29), (p.31), (p.37), (p.56), (p.63), (p.124)

[106] E. Aprile et al. Search for Event Rate Modulation in XENON100 Electronic Recoil Data. *Phys. Rev. Lett.*, 115(9):091302, 2015. (p.29), (p.38)

[107] E. Aprile et al. Search for Electronic Recoil Event Rate Modulation with 4 Years of XENON100 Data. *Phys. Rev. Lett.*, 118(10):101101, 2017. (p.29), (p.38)

[108] E. Aprile et al. First Dark Matter Search Results from the XENON1T Experiment. *Phys. Rev. Lett.*, 119:181301, 2017. (p.29), (p.53), (p.63), (p.70), (p.73), (p.74), (p.82), (p.85), (p.86)

[109] E. Aprile et al. Dark Matter Search Results from a One Tonne×Year Exposure of XENON1T. *Phys. Rev. Lett.*, 121(11):111302, 2018. (p.29), (p.31), (p.56), (p.74), (p.85), (p.91), (p.131)

[110] D. S. Akerib et al. Results from a search for dark matter in the complete LUX exposure. *Phys. Rev. Lett.*, 118(2):021303, 2017. (p.29), (p.31), (p.124), (p.125)

[111] X. Cui et al. Dark matter results from 54-ton-day exposure of PandaX-II experiment. *Physical review letters*, 119(18):181302, 2017. (p.29), (p.31), (p.56), (p.63), (p.102), (p.124), (p.125)

[112] R. Agnese et al. New Results from the Search for Low-Mass Weakly Interacting Massive Particles with the CDMS Low Ionization Threshold Experiment. *Phys. Rev. Lett.*, 116(7):071301, 2016. (p.29)

[113] K. Abe et al. Direct dark matter search by annual modulation in XMASS-I. *Phys. Lett.*, B759:272–276, 2016. (p.29)

[114] G. Adhikari et al. Initial performance of the COSINE-100 experiment. *European Physical Journal C*, 78:107, 2018. (p.30)

[115] P. Montini. Dark matter search with the SABRE experiment. 2018. (p.30)

[116] S. P. Ahlen et al. Limits on Cold Dark Matter Candidates from an Ultralow Background Germanium Spectrometer. *Phys. Lett.*, B195:603–608, 1987. (p.30)

[117] C. E. Aalseth et al. CoGeNT: A Search for Low-Mass Dark Matter using p-type Point Contact Germanium Detectors. *Phys. Rev.*, D88:012002, 2013. (p.30)

[118] Q. Yue et al. Limits on light WIMPs from the CDEX-1 experiment with a p-type point-contact germanium detector at the China Jingping Underground Laboratory. *Phys. Rev.*, D90:091701, 2014. (p.30)

[119] G. K. Giovanetti et al. A Dark Matter Search with MALBEK. *Phys. Procedia*, 61:77–84, 2015. (p.30)

[120] F. Mayet et al. A review of the discovery reach of directional Dark Matter detection. *Phys. Rept.*, 627:1–49, 2016. (p.30)

[121] J. B. R. Battat et al. First background-free limit from a directional dark matter experiment: results from a fully fiducialised DRIFT detector. *Phys. Dark Univ.*, 9-10:1–7, 2015. (p.30)

[122] Q. Riffard et al. First detection of radon progeny recoil tracks by mimac. *Journal of Instrumentation*, 12(06):P06021, 2017. (p.30)

[123] J. Monroe and DMTPC Collaboration. Status and prospects of the DMTPC directional dark matter experiment. In *American Institute of Physics Conference Series*, volume 1441, pages 515–517, 2012. (p.30)

[124] R. Agnese et al. Projected Sensitivity of the SuperCDMS SNOLAB experiment. *Phys. Rev.*, D95(8):082002, 2017. (p.30)

[125] E. Armengaud et al. Performance of the EDELWEISS-III experiment for direct dark matter searches. *JINST*, 12(08):P08010, 2017. (p.30)

[126] G. Angloher et al. Results on low mass WIMPs using an upgraded CRESST-II detector. *The European Physical Journal C*, 74(12):1–6, 2014. (p.30)

[127] G. Angloher et al. The COSINUS project: perspectives of a NaI scintillating calorimeter for dark matter search. *The European Physical Journal C*, 76(8):441, 2016. (p.30)

[128] R. Agnese et al. Silicon Detector Dark Matter Results from the Final Exposure of CDMS II. *Phys. Rev. Lett.*, 111(25):251301, 2013. (p.30)

[129] R. Agnese et al. Maximum Likelihood Analysis of Low Energy CDMS II Germanium Data. *Phys. Rev.*, D91:052021, 2015. (p.30)

[130] G. Angloher et al. Results from 730 kg days of the CRESST-II Dark Matter search. *European Physical Journal C*, 72:1971, 2012. (p.30)

[131] G. Angloher et al. Results on low mass WIMPs using an upgraded CRESST-II detector. *Eur. Phys. J.*, C74(12):3184, 2014. (p.30)

[132] C. Amole et al. Dark matter search results from the PICO-60 CF_3I bubble chamber. *Phys. Rev.*, D93(5):052014, 2016. (p.30)

[133] C. Amole et al. Improved dark matter search results from PICO-2L Run 2. *Phys. Rev.*, D93(6):061101, 2016. (p.30)

[134] J. Angle et al. First Results from the XENON10 Dark Matter Experiment at the Gran Sasso National Laboratory. *Phys. Rev. Lett.*, 100:021303, 2008. (p.31), (p.124), (p.131)

[135] E. Aprile et al. Physics reach of the XENON1T dark matter experiment. *Journal of Cosmology and Astroparticle Physics*, 2016(04):027, 2016. (p.31), (p.42), (p.47), (p.54), (p.58), (p.73), (p.93), (p.119), (p.124), (p.131), (p.132), (p.134)

[136] B. J. Mount et al. LUX-ZEPLIN (LZ) Technical Design Report. *e-Print: arXiv:1703.09144*, 2017. (p.31), (p.131)

[137] P. Agnes et al. DarkSide-50 532-day Dark Matter Search with Low-Radioactivity Argon. *e-Print: arXiv:1802.07198*, 2018. (p.31)

[138] J. Billard et al. Implication of neutrino backgrounds on the reach of next generation dark matter direct detection experiments. *Physical Review D*, 89(2):023524, 2014. (p.31), (p.67), (p.68), (p.124), (p.131), (p.143), (p.144), (p.145), (p.146), (p.147), (p.148)

[139] D. C. Malling et al. After LUX: the LZ program. *e-Print: arXiv:1110.0103*, 2011. (p.31)

[140] J. Aalbers et al. DARWIN: towards the ultimate dark matter detector. *JCAP*, 1611:017, 2016. (p.31), (p.131)

[141] C. E. Aalseth et al. The DarkSide Multiton Detector for the Direct Dark Matter Search. *Adv. High Energy Phys.*, 2015:541362, 2015. (p.31)

[142] J. Calvo et al. Status of ArDM-1t: First observations from operation with a full ton-scale liquid argon target. *e-Print: arXiv:1505.02443*, 2015. (p.31)

[143] D. S. Akerib et al. Results on the Spin-Dependent Scattering of Weakly Interacting Massive Particles on Nucleons from the Run 3 Data of the LUX Experiment. *Phys. Rev. Lett.*, 116(16):161302, 2016. (p.31)

[144] P. Gondolo and J. Silk. Dark matter annihilation at the galactic center. *Phys. Rev. Lett.*, 83:1719–1722, 1999. (p.32)

[145] M. Mateo. Dwarf galaxies of the Local Group. *Ann. Rev. Astron. Astrophys.*, 36:435–506, 1998. (p.32)

[146] T. E. Jeltema et al. Gamma Rays from Clusters and Groups of Galaxies: Cosmic Rays versus Dark Matter. *Phys. Rev.*, D80:023005, 2009. (p.32)

[147] A. A. Abdo et al. Constraints on Cosmological Dark Matter Annihilation from the Fermi-LAT Isotropic Diffuse Gamma-Ray Measurement. *JCAP*, 1004:014, 2010. (p.32)

[148] D. J. Thompson et al. Calibration of the Energetic Gamma-Ray Experiment Telescope (EGRET) for the Compton Gamma-Ray Observatory. *Astrophys. J. Suppl.*, 86:629–656, 1993. (p.32)

[149] W. B. Atwood, , et al. The Large Area Telescope on the Fermi Gamma-Ray Space Telescope Mission. *The Astrophysical Journal*, 697:1071–1102, 2009. (p.32), (p.34)

[150] J. Aleksić et al. Performance of the MAGIC stereo system obtained with Crab Nebula data. *Astroparticle Physics*, 35:435–448, 2012. (p.32)

[151] J. Holder et al. Status of the VERITAS Observatory. *AIP Conf. Proc.*, 1085:657–660, 2009. (p.32)

[152] F. Aharonian et al. Observations of the Crab Nebula with H.E.S.S. *Astron. Astrophys.*, 457:899–915, 2006. (p.32)

[153] M. Actis et al. Design concepts for the Cherenkov Telescope Array CTA: an advanced facility for ground-based high-energy gamma-ray astronomy. *Experimental Astronomy*, 32:193–316, 2011. (p.32)

[154] M. L. Ahnen et al. Limits to Dark Matter Annihilation Cross-Section from a Combined Analysis of MAGIC and Fermi-LAT Observations of Dwarf Satellite Galaxies. *JCAP*, 1602(02):039, 2016. (p.33)

[155] H. Abdallah et al. Search for dark matter annihilations towards the inner Galactic halo from 10 years of observations with H.E.S.S. *Phys. Rev. Lett.*, 117(11):111301, 2016. (p.33)

[156] A. Albert et al. Searching for Dark Matter Annihilation in Recently Discovered Milky Way Satellites with Fermi-LAT. *Astrophys. J.*, 834(2):110, 2017. (p.33)

[157] P. A. R. Ade et al. Planck 2015 results. XIII. Cosmological parameters. *Astron. Astrophys.*, 594:A13, 2016. (p.33)

[158] E. Charles et al. Sensitivity Projections for Dark Matter Searches with the Fermi Large Area Telescope. *Phys. Rept.*, 636:1–46, 2016. (p.33)

[159] J. Carr et al. Prospects for Indirect Dark Matter Searches with the Cherenkov Telescope Array (CTA). *PoS*, ICRC2015:1203, 2016. (p.33)

[160] Gary Steigman, Basudeb Dasgupta, and John F. Beacom. Precise Relic WIMP Abundance and its Impact on Searches for Dark Matter Annihilation. *Phys. Rev.*, D86:023506, 2012. (p.33)

[161] Joseph Silk and Mark Srednicki. Cosmic Ray anti-Protons as a Probe of a Photino Dominated Universe. *Phys. Rev. Lett.*, 53:624, 1984. [,269(1984)]. (p.33)

[162] S. W. Barwick et al. Cosmic ray positrons at high-energies: A New measurement. *Phys. Rev. Lett.*, 75:390–393, 1995. (p.33)

[163] J. Chang et al. An excess of cosmic ray electrons at energies of 300-800 GeV. *Nature*, 456:362–365, 2008. (p.33)

[164] J. Abraham et al. Properties and performance of the prototype instrument for the Pierre Auger Observatory. *Nucl. Instrum. Meth.*, A523:50–95, 2004. (p.33)

[165] H. Kawai et al. Telescope array experiment. *Nucl. Phys. Proc. Suppl.*, 175-176:221–226, 2008. (p.34)

[166] P. Picozza et al. PAMELA: A Payload for Antimatter Matter Exploration and Light-nuclei Astrophysics. *Astropart. Phys.*, 27:296–315, 2007. (p.34)

[167] M. Aguilar et al. First Result from the Alpha Magnetic Spectrometer on the International Space Station: Precision Measurement of the Positron Fraction in Primary Cosmic Rays of 0.5–350 GeV. *Phys. Rev. Lett.*, 110:141102, 2013. (p.34)

[168] O. Adriani et al. An anomalous positron abundance in cosmic rays with energies 1.5-100 GeV. *Nature*, 458:607–609, 2009. (p.34)

[169] M. Ackermann et al. Measurement of Separate Cosmic-Ray Electron and Positron Spectra with the Fermi Large Area Telescope. *Physical Review Letters*, 108(1):011103, 2012. (p.34)

[170] S. Profumo. Dissecting cosmic-ray electron-positron data with Occam's Razor: the role of known Pulsars. *Central Eur. J. Phys.*, 10:1–31, 2011. (p.34)

[171] M. Aguilar et al. Antiproton Flux, Antiproton-to-Proton Flux Ratio, and Properties of Elementary Particle Fluxes in Primary Cosmic Rays Measured with the Alpha Magnetic Spectrometer on the International Space Station. *Phys. Rev. Lett.*, 117(9):091103, 2016. (p.34)

[172] S. Torii. The CALorimetric Electron Telescope (CALET): a High-Energy Astroparticle Physics Observatory on the International Space Stati. *PoS*, ICRC2015:581, 2016. (p.34)

[173] F. Gargano. DAMPE space mission: first data. In *25th European Cosmic Ray Symposium (ECRS 2016) Turin, Italy, September 04-09, 2016*, 2017. (p.34)

[174] R. A. Ong et al. The GAPS Experiment to Search for Dark Matter using Low-energy Antimatter. *PoS*, ICRC2017:914, 2018. (p.34)

[175] L. M. Krauss et al. Solar system constraints and signatures for dark-matter candidates. *Phys. Rev. D*, 33:2079–2083, 1986. (p.34)

[176] S. Adrian-Martinez et al. Limits on Dark Matter Annihilation in the Sun using the ANTARES Neutrino Telescope. *Phys. Lett.*, B759:69–74, 2016. (p.34)

[177] M. G. Aartsen et al. Search for annihilating dark matter in the Sun with 3 years of IceCube data. *Eur. Phys. J.*, C77(3):146, 2017. (p.34)

[178] K. Choi et al. Search for neutrinos from annihilation of captured low-mass dark matter particles in the Sun by Super-Kamiokande. *Phys. Rev. Lett.*, 114(14):141301, 2015. (p.34)

[179] A. V. Avrorin et al. Current status of the BAIKAL-GVD project. *Nucl. Instrum. Meth.*, A725:23–26, 2013. (p.34)

[180] M. G. Aartsen et al. PINGU: A Vision for Neutrino and Particle Physics at the South Pole. *J. Phys.*, G44(5):054006, 2017. (p.34)

[181] T. Yano. Astrophyisical Neutrino at Hyper-Kamiokande. *PoS*, ICRC2017:954, 2018. (p.34)

[182] R. Coniglione. The KM3NeT neutrino telescope. *J. Phys. Conf. Ser.*, 632:012002, 2015. (p.34)

[183] S. Chatrchyan et al. The CMS Experiment at the CERN LHC. *JINST*, 3:S08004, 2008. (p.34)

[184] G. Aad et al. The ATLAS Experiment at the CERN Large Hadron Collider. *JINST*, 3:S08003, 2008. (p.34)

[185] P. J. Fox et al. Missing Energy Signatures of Dark Matter at the LHC. *Phys. Rev.*, D85:056011, 2012. (p.34)

[186] Qing-Hong Cao et al. Effective Dark Matter Model: Relic density, CDMS II, Fermi LAT and LHC. *JHEP*, 08:018, 2011. (p.34)

[187] Qian-Fei Xiang et al. Searches for dark matter signals in simplified models at future hadron colliders. *Phys. Rev.*, D91:095020, 2015. (p.34)

[188] A. M Sirunyan et al. Search for dark matter produced with an energetic jet or a hadronically decaying W or Z boson at $\sqrt{s} = 13$ TeV. *JHEP*, 07:014, 2017. (p.34)

[189] E. Aprile et al. Design and performance of the XENON10 dark matter experiment. *Astroparticle Physics*, 34(9):679–698, 2011. (p.37)

[190] J. Angle et al. First results from the XENON10 dark matter experiment at the Gran Sasso National Laboratory. *Physical Review Letters*, 100(2):021303, 2008. (p.37)

[191] J. Angle et al. Limits on spin-dependent WIMP-nucleon cross sections from the XENON10 experiment. *Physical review letters*, 101(9):091301, 2008. (p.37)

[192] E. Aprile et al. The XENON100 dark matter experiment. *Astroparticle Physics*, 35(9):573–590, 2012. (p.37), (p.46), (p.102), (p.133)

[193] E. Aprile et al. Dark Matter Results from 225 Live Days of XENON100 Data. *Phys. Rev. Lett.*, 109(181301), 2012. (p.37), (p.42)

[194] E. Aprile et al. Limits on spin-dependent WIMP-nucleon cross sections from 225 live days of XENON100 data. *Physical review letters*, 111(2):021301, 2013. (p.37)

[195] E. Aprile et al. First Axion Results from the XENON100 Experiment. *Phys. Rev.*, D90(6):062009, 2014. [Erratum: Phys. Rev.D95,no.2,029904(2017)]. (p.38)

[196] E. Aprile et al. Exclusion of Leptophilic Dark Matter Models using XENON100 Electronic Recoil Data. *Science*, 349(6250):851–854, 2015. (p.38)

[197] E. Aprile et al. Low-mass dark matter search using ionization signals in XENON100. *Phys. Rev.*, D94(9):092001, 2016. [Erratum: Phys. Rev.D95,no.5,059901(2017)]. (p.38)

[198] E. Aprile et al. Search for WIMP Inelastic Scattering off Xenon Nuclei with XENON100. *Phys. Rev.*, D96(2):022008, 2017. (p.38)

[199] E. Aprile et al. Effective field theory search for high-energy nuclear recoils using the XENON100 dark matter detector. *Phys. Rev.*, D96(4):042004, 2017. (p.38)

[200] E. Aprile et al. Search for magnetic inelastic dark matter with XENON100. *JCAP*, 1710(10):039, 2017. (p.38)

[201] E. Aprile et al. Search for Bosonic Super-WIMP Interactions with the XENON100 Experiment. *Phys. Rev.*, D96(12):122002, 2017. (p.38)

[202] E. Aprile. The XENON1T dark matter search experiment. In *Sources and Detection of Dark Matter and Dark Energy in the Universe*, pages 93–96. Springer, 2013. (p.38)

[203] E. Aprile et al. The XENON1T dark matter experiment. *The European Physical Journal C*, 77(12):881, 2017. (p.38), (p.92), (p.103)

[204] K. D. Hill and A. G. Steele. The triple point of xenon. *Metrologia*, 42(4):278, 2005. (p.38)

[205] E. Aprile and T. Doke. Liquid xenon detectors for particle physics and astrophysics. *Reviews of Modern Physics*, 82(3):2053, 2010. (p.39)

[206] E. Aprile et al. Observation of anticorrelation between scintillation and ionization for MeV gamma rays in liquid xenon. *Physical Review B*, 76(1):014115, 2007. (p.41)

[207] M. Yamashita et al. Scintillation response of liquid Xe surrounded by PTFE reflector for gamma rays. *Nuclear Instruments and Methods in Physics Research A*, 535:692–698, 2004. (p.43)

[208] P. Barrow et al. Qualification Tests of the R11410-21 Photomultiplier Tubes for the XENON1T Detector. *JINST*, 12(01):P01024, 2017. (p.44)

[209] L. Baudis et al. Performance of the Hamamatsu R11410 Photomultiplier Tube in cryogenic Xenon Environments. *JINST*, 8:P04026, 2013. (p.45)

[210] K. Lung et al. Characterization of the Hamamatsu R11410-10 3-Inch Photomultiplier Tube for Liquid Xenon Dark Matter Direct Detection Experiments. *Nucl. Instrum. Meth.*, A696:32–39, 2012. (p.45)

[211] E. Aprile et al. Lowering the radioactivity of the photomultiplier tubes for the XENON1T dark matter experiment. *The European Physical Journal C*, 75(11):546, 2015. (p.45), (p.49)

[212] E. Aprile et al. Material radioassay and selection for the XENON1T dark matter experiment. *The European Physical Journal C*, 77(12):890, 2017. (p.45), (p.49), (p.58), (p.59), (p.66)

[213] E. Aprile et al. Conceptual design and simulation of a water Cherenkov muon veto for the XENON1T experiment. *JINST*, 9:P11006, 2014. (p.48), (p.50), (p.68)

[214] M. Aglietta et al. Muon 'Depth intensity' relation measured by LVD underground experiment and cosmic ray muon spectrum at sea level. *Phys. Rev.*, D58:092005, 1998. (p.48)

[215] L. Baudis et al. Gator: a low-background counting facility at the Gran Sasso Underground Laboratory. *Journal of Instrumentation*, 6:8010, 2011. (p.48), (p.59)

[216] G. Heusser et al. Giove: a new detector setup for high sensitivity germanium spectroscopy at shallow depth. *The European Physical Journal C*, 75(11):531, 2015. (p.48), (p.59)

[217] G. Heusser et al. Low-level germanium gamma-ray spectrometry at the μBq/kg level and future developments towards higher sensitivity. *Radioactivity in the Environment*, 8:495–510, 2006. (p.48), (p.59)

[218] G. Zuzel and H. Simgen. High sensitivity radon emanation measurements. *Applied Radiation and Isotopes*, 67(5):889 – 893, 2009. 5th International Conference on Radionuclide Metrology - Low-Level Radioactivity Measurement Techniques ICRM-LLRMT'08. (p.49)

[219] E. Aprile et al. Removing krypton from xenon by cryogenic distillation to the ppq level. *The European Physical Journal C*, 77(5):275, 2017. (p.49), (p.54), (p.60), (p.63)

[220] S. Rosendahl et al. A novel ^{83m}Kr tracer method for characterizing xenon gas and cryogenic distillation systems. *JINST*, 9(10):P10010, 2014. (p.49)

[221] Sebastian Lindemann and Hardy Simgen. Krypton assay in xenon at the ppq level using a gas chromatographic system and mass spectrometer. *The European Physical Journal C*, 74(2):2746, 2014. (p.49), (p.63)

[222] E. Aprile et al. Online ^{222}Rn removal by cryogenic distillation in the XENON100 experiment. *Eur. Phys. J.*, C77(6):358, 2017. (p.50)

[223] C. Geis et al. Optical response of highly reflective film used in the water Cherenkov muon veto of the XENON1T dark matter experiment. *JINST*, 12(06):P06017, 2017. (p.50)

[224] A. Manalaysay et al. Spatially uniform calibration of a liquid xenon detector at low energies using ^{83m}Kr. *Review of Scientific Instruments*, 81(7):073303–073303, 2010. (p.52)

[225] L. W. Kastens, S. B. Cahn, A. Manzur, and D. N. McKinsey. Calibration of a liquid xenon detector with ^{83}Kr^{m}. *Phys. Rev. C*, 80:045809, 2009. (p.52), (p.92)

[226] V. Hannen et al. Limits on the release of Rb isotopes from a zeolite based ^{83m}Kr calibration source for the XENON project. *Journal of Instrumentation*, 6:10013, 2011. (p.52)

[227] R. F. Lang et al. A ^{220}Rn source for the calibration of low-background experiments. *JINST*, 11(04):P04004, 2016. (p.52)

[228] E. Aprile et al. Results from a calibration of XENON100 using a source of dissolved radon-220. *Phys. Rev. D*, 95:072008, 2017. (p.52), (p.92)

[229] R.F. Lang et al. Characterization of a deuterium–deuterium plasma fusion neutron generator. *Nuclear Instruments and Methods in Physics Research Section A: Accelerators, Spectrometers, Detectors and Associated Equipment*, 879:31 – 38, 2018. (p.52), (p.92), (p.103)

[230] J. Dobson. Overview and status of LUX-ZEPLIN, 2016. Presented at Identification of Dark Matter 2016 (iDM2016). (p.54)

[231] E Aprile et al. Dark matter results from 100 live days of XENON100 data. *Physical Review Letters*, 107(13):131302, 2011. (p.55), (p.60)

[232] DS Akerib, HM Araújo, X Bai, AJ Bailey, J Balajthy, E Bernard, A Bernstein, A Bradley, D Byram, SB Cahn, et al. Radiogenic and muon-induced backgrounds in the lux dark matter detector. *Astroparticle Physics*, 62:33–46, 2015. (p.56), (p.63)

[233] M Berger. XCOM: photon cross sections database. *http://www.nist.gov/pml/data/xcom/index.cfm*, 2010. (p.58)

[234] S. Agostinelli et al. GEANT4 - A simulation toolkit. *Nuclear Instruments and Methods in Physics Research*, A506(3):250–303, 2003. (p.58), (p.70), (p.93)

[235] S. A. Bruenner. *Mitigation of 222Rn induced background in the XENON1T dark matter experiment*. PhD thesis, University of Heidelberg, 2017. (p.60)

[236] N. M. Rupp. On the detection of 222Rn with miniaturized propotional counters: background, sensitivity studies and results for XENON1T, 2017. Master thesis, University of Heidelberg. (p.60)

[237] X. Du et al. An atom trap system for practical 81 Kr dating. *Review of Scientific Instruments*, 75(10):3224–3232, 2004. (p.60), (p.64)

[238] M. Selvi. Review of Monte Carlo simulations for backgrounds from radioactivity. *AIP Conf. Proc.*, 1549:213–218, 2013. (p.61)

[239] J. B. Albert et al. Improved measurement of the $2\nu\beta\beta$ half-life of ^{136}Xe with the EXO-200 detector. *Phys. Rev.*, C89(1):015502, 2014. (p.61)

[240] O. A. Ponkratenko et al. Event generator DECAY4 for simulating double-beta processes and decays of radioactive nuclei. *Physics of Atomic Nuclei*, 63(7):1282–1287, 2000. (p.61)

[241] J. Kotila and F. Iachello. Phase space factors for double-β decay. *Phys. Rev.*, C85:034316, 2012. (p.61)

[242] J. N. Bahcall et al. New solar opacities, abundances, helioseismology, and neutrino fluxes. *Astrophys. J.*, 621:L85–L88, 2005. (p.61)

[243] A. M. Serenelli et al. Solar models with accretion. I. Application to the solar abundance problem. *Astrophys. J.*, 743:24, 2011. (p.61), (p.69), (p.145)

[244] K. A. Olive et al. Review of Particle Physics. *Chin. Phys.*, C38:090001, 2014. (p.61)

[245] S. Lindemann. *Intrinsic 85Kr and 222Rn Backgrounds in the XENON Dark Matter Search*. PhD thesis, University of Heidelberg, 2013. (p.64)

[246] Jiunn-Wei Chen et al. Low-energy electronic recoil in xenon detectors by solar neutrinos. *Phys. Lett.*, B774:656–661, 2017. (p.64)

[247] D. Akimov et al. Observation of coherent elastic neutrino-nucleus scattering. *Science*, page 0990, 2017. (p.67), (p.69)

[248] D. Mei and A. Hime. Muon-induced background study for underground laboratories. *Phys. Rev.*, D73:053004, 2006. (p.67)

[249] A. Rocchetti. Monte Carlo simulation of the XENON1T experiment and First comparison with the Muon Veto data, 2016. Master thesis, University of Bologna. (p.68)

[250] P. Sorensen and K. Kamdin. Two distinct components of the delayed single electron noise in liquid xenon emission detectors. *Journal of Instrumentation*, 13(02):P02032, 2018. (p.70)

[251] W. B. Wilson et al. Sources: a code for calculating (α, n), spontaneous fission, and delayed neutron sources and spectra. *Radiation protection dosimetry*, 115(1-4):117–121, 2005. (p.72)

[252] W. B. Wilson et al. SOURCES-4A. Technical report, Technical Report LA-13639-MS, Los Alamos, 1999. (p.73)

[253] R. Lemrani et al. Low energy neutron propagation in MCNPX and GEANT4. *Nucl. Instrum. Meth.*, A560:454–459, 2006. (p.73)

[254] M Szydagis, N Barry, K Kazkaz, J Mock, D Stolp, M Sweany, M Tripathi, S Uvarov, N Walsh, and M Woods. Nest: a comprehensive model for scintillation yield in liquid xenon. *Journal of Instrumentation*, 6(10):P10002, 2011. (p.80), (p.132), (p.134)

[255] B. Lenardo et al. A global analysis of light and charge yields in liquid xenon. *IEEE Trans. Nucl. Sci*, 62(3387):1412–4417, 2015. (p.80), (p.81), (p.82), (p.83)

[256] D. S. Akerib et al. Tritium calibration of the LUX dark matter experiment. *Physical Review D*, 93(7):072009, 2016. (p.80), (p.81), (p.82)

[257] J. Thomas and D. A. Imel. Recombination of electron-ion pairs in liquid argon and liquid xenon. *Physical Review A*, 36(2):614, 1987. (p.81)

[258] E. Aprile et al. Response of the XENON100 dark matter detector to nuclear recoils. *Physical Review D*, 88(1):012006, 2013. (p.81), (p.83)

[259] E. Aprile et al. Signal yields of keV electronic recoils and their discrimination from nuclear recoils in liquid xenon. *Physical Review D*, 97(9):092007, 2018. (p.82)

[260] D. Huang. Ultra-low Energy Calibration of LUX detector using 127Xe Electron Capture. *Bulletin of the American Physical Society*, 60, 2015. (p.81), (p.82)

[261] E. M. Boulton et al. Calibration of a two-phase xenon time projection chamber with a 37Ar source. *Journal of Instrumentation*, 12(08):P08004, 2017. (p.81), (p.82)

[262] M. Szydagis et al. Noble Element Simulation Technique v2.0, 2018. (p.82)

[263] L. W. Goetzke et al. Measurement of light and charge yield of low-energy electronic recoils in liquid xenon. *Physical Review D*, 96(10):103007, 2017. (p.81)

[264] E. Aprile et al. Scintillation response of liquid xenon to low energy nuclear recoils. *Physical Review D*, 72(7):072006, 2005. (p.83)

[265] E. Aprile et al. Simultaneous measurement of ionization and scintillation from nuclear recoils in liquid xenon for a dark matter experiment. *Physical review letters*, 97(8):081302, 2006. (p.83)

[266] E. Aprile et al. New measurement of the relative scintillation efficiency of xenon nuclear recoils below 10 keV. *Physical Review C*, 79(4):045807, 2009. (p.83)

[267] G. Plante et al. New measurement of the scintillation efficiency of low-energy nuclear recoils in liquid xenon. *Physical Review C*, 84(4):045805, 2011. (p.83)

[268] P. Sorensen et al. The scintillation and ionization yield of liquid xenon for nuclear recoils. *Nuclear Instruments and Methods in Physics Research Section A: Accelerators, Spectrometers, Detectors and Associated Equipment*, 601(3):339–346, 2009. (p.83)

[269] A. Manzur et al. Scintillation efficiency and ionization yield of liquid xenon for monoenergetic nuclear recoils down to 4 keV. *Physical Review C*, 81(2):025808, 2010. (p.83)

[270] D. S. Akerib et al. Low-energy (0.7-74 keV) nuclear recoil calibration of the LUX dark matter experiment using DD neutron scattering kinematics. *e-Print: arXiv:1608.05381*, 2016. (p.83)

[271] C. D. Wagner et al. NIST X-ray Photoelectron Spectroscopy Database, NIST Standard Reference Database 20, Version 3.4 (Web Version). *U. S. Department of Commerce*, 2003. (p.82)

[272] C. H. others Faham. Measurements of wavelength-dependent double photoelectron emission from single photons in VUV-sensitive photomultiplier tubes. *Journal of Instrumentation*, 10(09):P09010, 2015. (p.83)

[273] B. L. Paredes et al. Response of photomultiplier tubes to xenon scintillation light. *Astroparticle Physics*, 102:56–66, 2018. (p.83)

[274] XENON Collaboration. The PAX data processor v6.8.0, 2018. (p.84)

[275] J. Goodman and J. Weare. Ensemble samplers with affine invariance. *Communications in applied mathematics and computational science*, 5(1):65–80, 2010. (p.86)

[276] R. Saldanha et al. Model independent approach to the single photoelectron calibration of photomultiplier tubes. *Nuclear Instruments and Methods in Physics Research Section A: Accelerators, Spectrometers, Detectors and Associated Equipment*, 863:35 – 46, 2017. (p.92), (p.102)

[277] COMSOL Multiphysics. *www.comsol.com*. COMSOL AB, Stockholm, Sweden. (p.94)

[278] S. Nissen. Implementation of a fast artificial neural network library (fann). Technical report, Department of Computer Science University of Copenhagen (DIKU), 2003. http://fann.sf.net. (p.93)

[279] B. E. J. Pelssers. Position reconstruction and data quality in xenon, 2015. Master thesis, University of Utercht - Nikhef. (p.93)

[280] F. V. Massoli. *The XENON1T experiment: Monte Carlo background estimation and sensitivity curves study*. PhD thesis, University of Bologna, 2015. (p.93)

[281] K. Ni et al. Preparation of Neutron-activated Xenon for Liquid Xenon Detector Calibration. *Nucl. Instrum. Meth.*, A582:569–574, 2007. (p.97), (p.103)

[282] C. E. Dahl. *The physics of background discrimination in liquid xenon, and first results from Xenon10 in the hunt for WIMP dark matter*. PhD thesis, Princeton U., 2009. (p.100)

[283] J. B. Albert et al. Search for Neutrinoless Double-Beta Decay with the Upgraded EXO-200 Detector. *Phys. Rev. Lett.*, 120(7):072701, 2018. (p.102)

[284] D. S. Akerib et al. Signal yields, energy resolution, and recombination fluctuations in liquid xenon. *Phys. Rev.*, D95(1):012008, 2017. (p.102)

[285] P. Barrow et al. Qualification tests of the R11410-21 photomultiplier tubes for the XENON1T detector. *Journal of Instrumentation*, 12(01):P01024, 2017. (p.102)

[286] R. B. Firestone et al. The 8th edition of the Table of Isotopes. In *Proceedings of the 9th International Symposium on Capture gamma-ray spectroscopy and related topics. V. 2*, 1997. (p.103), (p.104)

[287] R. Agnese et al. Improved WIMP-search reach of the CDMS II germanium data. *Physical Review D*, 92(7):072003, 2015. (p.112)

[288] P.-A. Amaudruz et al. First results from the DEAP-3600 dark matter search with argon at SNOLAB. *Physical review letters*, 121(7):071801, 2018. (p.112)

[289] J. Binney and S. Tremaine. *Galactic Dynamics: Second Edition*. Princeton University Press, 2008. (p.115)

[290] E. I. Gates et al. The Local halo density. *The Astrophysical Journal Letters*, 449(2):L123, 1995. (p.115)

[291] F. J. Kerr and D. Lynden-Bell. Review of galactic constants. *Monthly Notices of the Royal Astronomical Society*, 221(4):1023–1038, 1986. (p.115)

[292] F. Donato et al. Effects of galactic dark halo rotation on WIMP direct detection. *Astroparticle Physics*, 9(3):247–260, 1998. (p.115)

[293] R. H. Helm. Inelastic and elastic scattering of 187-MeV electrons from selected even-even nuclei. *Physical Review D*, 104(5):1466, 1956. (p.115)

[294] G. Cowan et al. Asymptotic formulae for likelihood-based tests of new physics. *The European Physical Journal C-Particles and Fields*, 71(2):1–19, 2011. (p.118), (p.136), (p.141), (p.145)

[295] G. J. Feldman and R. D. Cousins. A Unified approach to the classical statistical analysis of small signals. *Phys. Rev.*, D57:3873–3889, 1998. (p.118)

[296] G. Cowan et al. Power-Constrained Limits. *e-Print: arXiv:1105.3166*, 2011. (p.118)

[297] P. Di Gangi. Study of the sensitivity of the XENON1T experiment with the profile likelihood method, 2015. Master thesis, University of Bologna. (p.119), (p.131), (p.132), (p.135), (p.138)

[298] N. Priel et al. A model independent safeguard against background mismodeling for statistical inference. *JCAP*, 1705(05):013, 2017. (p.120)

[299] E. Bagnaschi et al. Likelihood Analysis of Supersymmetric SU(5) GUTs. *Eur. Phys. J.*, C77(2):104, 2017. (p.124)

[300] C. E. Aalseth et al. DarkSide-20k: A 20 tonne two-phase LAr TPC for direct dark matter detection at LNGS. *Eur. Phys. J. Plus*, 133:131, 2018. (p.131)

[301] E. Aprile et al. Analysis of the XENON100 Dark Matter Search Data. *Astropart. Phys.*, 54:11–24, 2014. (p.132)

[302] E. Aprile et al. Response of the XENON100 Dark Matter Detector to Nuclear Recoils. *Phys. Rev.*, D88:012006, 2013. (p.132), (p.134), (p.135)

[303] M. Szydagis et al. Enhancement of NEST capabilities for simulating low-energy recoils in liquid xenon. *Journal of Instrumentation*, 8(10):C10003, 2013. (p.132)

[304] E. Aprile et al. Likelihood Approach to the First Dark Matter Results from XENON100. *Phys. Rev.*, D84:052003, 2011. (p.135)

[305] S. S. Wilks. The Large-Sample Distribution of the Likelihood Ratio for Testing Composite Hypotheses. *Annals Math. Statist.*, 9(1):60–62, 1938. (p.137)

[306] A. Wald. Tests of statistical hypotheses concerning several parameters when the number of observations is large. *Transactions of the American Mathematical society*, 54(3):426–482, 1943. (p.137)

[307] G. Cowan. *Statistical data analysis*. Oxford University Press, 1998. (p.141)

[308] D. S. Akerib et al. Improved Limits on Scattering of Weakly Interacting Massive Particles from Reanalysis of 2013 LUX Data. *Phys. Rev. Lett.*, 116(16):161301, 2016. (p.142)